

University of Alberta

Geochronology, Petrography, Geochemical Constraints, and Fluid
Characterization of the Buriticá Gold Deposit, Antioquia Department,
Colombia.

by

Guillaume Lesage

A thesis submitted to the Faculty of Graduate Studies and Research
in partial fulfillment of the requirements for the degree of

Master of Science

Earth and Atmospheric Sciences

©Guillaume Lesage

Fall, 2011

Edmonton, Alberta

Permission is hereby granted to the University of Alberta Libraries to reproduce single copies of this thesis and to lend or sell such copies for private, scholarly or scientific research purposes only. Where the thesis is converted to, or otherwise made available in digital form, the University of Alberta will advise potential users of the thesis of these terms.

The author reserves all other publication and other rights in association with the copyright in the thesis and, except as herein before provided, neither the thesis nor any substantial portion thereof may be printed or otherwise reproduced in any material form whatsoever without the author's prior written permission.

Abstract

Buriticá is a low- to intermediate-sulfidation epithermal gold deposit located 75 km north of Medellín, in Colombia. It is hosted by the Buriticá andesite porphyry, a shallow intrusive rock dated at 7.41 ± 0.40 Ma ($^{40}\text{Ar}/^{39}\text{Ar}$ on hornblende), which intrudes the Cretaceous Cañasgordas Group and Buriticá stock.

Gold mineralization is associated with a proximal sericite-adularia and a distal epidote-rich propylitic alteration, and is hosted in two different sets of veins respectively striking and dipping around $072^\circ/87^\circ\text{S}$ and $105^\circ/87^\circ\text{S}$. Hydrothermal sericite yields an age of 7.74 ± 0.08 Ma.

Sulfur isotope and fluid inclusion data indicate that a hot and saline fluid ($>300^\circ\text{C}$, average 5.5 wt.% NaCl equiv.) of magmatic origin mixed with a cooler and less saline meteoric fluid. Boiling conditions were observed in quartz crystals coeval with the timing of gold mineralization, therefore boiling is believed to be the main control on gold precipitation.

Acknowledgements

I would like to thank Jeremy Richards, whose supervision and advice during this project have been very important and much appreciated. Jeremy was very patient with me as I was perfecting my English writing skills, and his comprehensive reviews of my manuscript greatly improved it.

Field and research expenses were financed by Continental Gold of Colombia Inc. and in part by the Society of Economic Geologists. $^{40}\text{Ar}/^{39}\text{Ar}$ geochronological analyses were conducted by Terry Spell, from at the Nevada Isotope Geochronology Laboratory. Sulfur isotope analyses were conducted by Stephen Taylor, from the Isotope Science Laboratory of the University of Calgary. X-ray diffraction analyses were conducted by Diane Caird, from the University of Alberta. Lithochemical analyses were conducted at Activation Laboratories Ltd. in Ancaster, Ontario. Finally, fluid inclusion analyses were conducted by myself at the University of Alberta. Thanks Jeremy for letting me use your lab.

Thanks to all the Continental Gold geologists who helped me while I was mapping in the field: Stuart Moller, Alejandro Murillo, Jimmy Torres, Mauricio Cruz. Elkin—thank you for having carried my heavy samples around in the mountains. My fellow graduate students and close friends for their scientific input, their positive energy, and for the poker nights: Jean-François Gagnon, Neil Fernandes, Alberto Reyes, Stefan Lalonde, Tyler Hauck, Kurt Borth, Catherine Johnson, Shawna White, Hilary Corlett, Jamie Kraft, and all the others.

I would also like to mention all those people who contributed to this project by making my life in Edmonton more fun and interesting, namely Marie-Maude Pontbriand, Francis O'Brien, Jonathan Lavoie-Lapointe, Gabriel Trahan, Alexandra Prescott, Audrey Roy, Cybelle Morin. Thanks for being there.

Table of Contents

1.	Introduction	1
2.	Tectonic History of Colombia	4
3.	Ore Deposits of Colombia	14
4.	Buriticá Historical Background	16
5.	Regional Geologic Setting	17
6.	Buriticá Deposit Geology	21
6.1.	Volcanic and sedimentary rocks	21
6.2.	Plutonic rocks	24
6.3.	Breccia	30
6.4.	Alteration	32
6.5.	Structural setting	36
6.6.	Mineralized veins	39
6.7.	Mineralization Paragenesis	40
7.	Analytical Methods	46
7.1.	X-ray diffraction methods	46
7.2.	Lithogeochemical methods	46
7.3.	Geochronology methods	47
7.4.	Sulfur Isotope Methods	48
7.5.	Fluid Inclusion methods	49
8.	Results	50
8.1.	Lithogeochemistry	50
8.2.	Geochronology	57
8.3.	Sulfur Isotope Analyses	60
8.4.	Fluid Inclusions	61
9.	Discussion	70
9.1.	Timing and tectonic setting of the Buriticá porphyry and gold deposit	70
9.2.	Characteristics of ore-forming fluids in the Buriticá gold deposit	72
9.2.1.	<i>Importance of boiling for gold mineral precipitation</i>	73
9.3.	Classification of the Buriticá gold deposit	74
9.4.	Comparison with other late Miocene gold deposits in Colombia	76
9.4.1.	<i>La Colosa porphyry gold deposit characteristics</i>	76
9.4.2.	<i>Marmato epithermal gold deposit characteristics</i>	78
9.4.3.	<i>Similarities with the Buriticá epithermal gold deposit</i>	80

9.5.	Models for formation of late Miocene gold deposits in Colombia	81
9.6.	Mineral exploration implications	82
10.	Conclusion	83
	References	85
	Appendix A: Sample Descriptions and Locations	99
	Appendix B: Petrographic Descriptions	111
	Appendix C: X-Ray Diffraction Data	126
	Appendix D: Structural Data	130
	Appendix E: Lithochemical Data	136
	Appendix F: Ar-Ar Data	148
	Appendix G: Fluid Inclusion Data	152

List of Tables

Table 7-1.	Measured standard data.	49
Table 8-1.	Sulfide crystallization temperatures calculated from sulfur isotope fractionation between coeval galena and sphalerite.	60
Table 8-2.	Comparative table of fluid inclusion homogenization temperatures (Stage 1 average per sample) vs. sulfur isotopes crystallization temperatures for the same samples.	69
Table 9-1.	Middle Cauca metallogenic belt deposit summary table.	77

List of Figures

Figure 1-1.	Geological provinces of South America, and geographic locations, main deposit types, and sizes of major gold belts.	2
Figure 1-2.	Geological provinces of Colombia and geographic locations of major Miocene gold deposits.	3
Figure 2-1.	Litho-tectonic map of the Northern Andes.	5
Figure 2-2.	Paleogeographic reconstruction of the Archean cratons between the Neoproterozoic and the Late Carboniferous.	7
Figure 2-3.	Schematic cross-sections depicting the closure of a back-arc basin.	9
Figure 2-4.	Major Mesozoic and Cenozoic intrusive rocks of Colombia.	13
Figure 3-1.	Metallogenic belts of Colombia.	15
Figure 4-1.	Underground geology map of the Yaragua mine level 1.	18
Figure 5-1.	Regional geology map of the Buriticá area and its surroundings.	20
Figure 6-1.	Detailed geology map of the Buriticá area.	22
Figure 6-2.	Barroso Formation outcrop photos.	24
Figure 6-3.	Buriticá stock outcrop photos.	26
Figure 6-4.	Buriticá stock hand sample photos and thin section photomicrographs.	28
Figure 6-5.	Buriticá andesite porphyry hand sample photos and thin section photomicrographs.	29
Figure 6-6.	Yaragua breccia hand sample photos.	31
Figure 6-7.	Photos of alteration facies in the Buriticá stock and andesite porphyry in hand specimen.	33
Figure 6-8.	Transmitted light photomicrographs of alteration facies in the Buriticá stock and andesite porphyry.	34
Figure 6-9.	Photos of structural features observed in the Buriticá area.	37
Figure 6-10.	Structural data measured in the Buriticá area, plotted on the lower hemisphere of an equal-area stereographic net.	38
Figure 6-11.	Mineralized vein paragenesis.	40
Figure 6-12.	Transmitted light photomicrographs of Stage 1 sphalerite crystals showing color zonation from dark brown and yellow to late light yellow sphalerite.	41

Figure 6-13. Photos of the San Antonio and Centena veins in hand specimen.	42
Figure 6-14. Reflected light photomicrographs of Stage 1 and Stage 2 vein minerals.	43
Figure 6-15. Reflected light photomicrographs of Stage 3 vein minerals.	45
Figure 8-1. Total alkali ($\text{Na}_2\text{O} + \text{K}_2\text{O}$) versus silica diagram.	51
Figure 8-2. Harker diagrams.	52
Figure 8-3. Chondrite-normalized REE diagram.	54
Figure 8-4. Primitive mantle-normalized extended trace element diagram.	56
Figure 8-5. Apparent $^{40}\text{Ar}/^{39}\text{Ar}$ age spectra for two samples of igneous hornblende.	58
Figure 8-6. Apparent $^{40}\text{Ar}/^{39}\text{Ar}$ age spectra for two samples of hydrothermal sericite.	59
Figure 8-7. Transmitted light photomicrographs of primary fluid inclusions.	63
Figure 8-8. Histogram showing the first melting temperature distribution for fluid inclusions from different host minerals.	65
Figure 8-9. Histograms showing homogenization temperatures and salinity distribution for fluid inclusions from different host minerals.	66
Figure 8-10. Scatter plot of fluid inclusion assemblage average homogenization temperatures vs. average salinity for Stage 1 to Stage 3.	67
Figure 8-11. Scatter plot of homogenization temperatures vs. salinity for fluid inclusions pertaining to four fluid inclusion assemblages from Stage 1 and Stage 2.	68
Figure 9-1. La/Yb versus Sc/Ni diagram showing fields for different tectonic settings.	71

List of Symbols and Abbreviations

Symbol	Description
°C	Degree Celsius
1s.d.	One standard deviation
⁴⁰ Ar*	Radiogenic argon
α	Fractionation factor
Adu	Adularia
Ag	Native silver
amu	Atomic mass unit
Ap	Apatite
Ar	Argon
Au	Native gold
Aug	Augite
Bi	Biotite
Cal	Calcite
CF-EA-IRMS	Continuous flow-isotope ratio mass spectrometry
Chl	Chlorite
cm	Centimeter
Cpy	Chalcopyrite
CRFS	Cauca-Romeral Fault System
deg	Degree
detect.	Detection
Ep	Epidote
equiv.	Equivalent
FUS-ICP	Fusion-inductively coupled plasma
FUS-MS	Fusion-mass spectrometry
g	Gram
Gn	Galena
Hbl	Hornblende
HFSE	High field strenght element
HREE	Heavy rare earth element
IAEA	International Atomic Energy Agency
ICDD	International Center for Diffraction Data
ICP-MS	Inductively coupled mass spectrometry
INAA	Instrumental neutron activation analysis
JCPDS	Joint Committee on Powder Diffraction Standards
km	Kilometer

Symbol	Description
LILE	Large ion lithophile element
LOI	Loss on ignition
LREE	Light rare earth element
m	Meter
Ma	Million years
Mag	Magnetite
mg	Milligram
μm	Micrometer
mm	Millimeter
MSWD	Mean Square Weighted Deviate
n	Number
Or	Orthoclase
P-T-X	Pressure-temperature-composition
Plag	Plagioclase
Por	Pore
ppb	Parts per billion
ppm	Parts per million
Py	Pyrite
Qtz	Quartz
REE	Rare earth element
σ	Standard deviation
s	Second
S	Sulfur
$\sigma_1/\sigma_2/\sigma_3$	Principal structural stresses
Ser	Sericite
Sp	Sphalerite
Stb	Stibnite
TD-ICP	Total digestion-inductively coupled plasma
Te	Tetrahedrite/tennantite
Th	Homogenization temperature
$Th_{L-V(L)}$	Homogenization temperature to the liquid state via a bubble-point transition
T_i	Initial melting temperature
Tm_{clath}	Clathrate final melting temperature
Tm_{CO_2}	CO ₂ final melting temperature
Tm_{ice}	Ice final melting temperature
UTM	Universal Transverse Mercator

Symbol	Description
VCDT	Vienna Canyon Diablo Troilite
wt. %	Weight percent
Xn	Xenolith
XRD	X-ray diffraction

1. Introduction

The focus of this study is the Buriticá gold deposit, located at 6°42.3'N 75°54.3'W, roughly 75 km north of the city of Medellín, in the Antioquia Department of Colombia. Although the presence of gold in the area is believed to have been known since pre-colonial times in the form of hydraulic mining of highly weathered surface material and underground workings along high-grade veins, the geological processes involved and the controls on mineralization are still poorly understood. The Buriticá gold deposit is a structurally controlled epithermal gold deposit associated with the intrusion of a porphyritic andesite intrusive body, on the eastern flank of the Western Cordillera of Colombia.

The first geological study of the area was done in the 1960s by Castro and Feininger (1965), with a focus on possible lead mineralization. The authors did not identify the presence of gold, and concluded that lead mineralization was not economically viable. A vein-hosted gold deposit, however, was discovered in the late 20th century by Grupo de Bullet S.A. Underground mining began in 1992 at the Yaragua mine, located approximately 2 km south of the town of Buriticá. Since its discovery, known gold reserves at the Buriticá deposit have increased significantly (Bargmann and Dominy, 2009).

Colombia's gold deposits represent a large fraction of the known gold mineralization of the Andes (Fig. 1-1), with over 50 million ounces of gold. The Buriticá deposit is located in the Middle Cauca belt, known for its Miocene gold-rich porphyry and epithermal deposits (Sillitoe, 2008). In addition to the Buriticá deposit, the Middle Cauca belt also contains the Marmato and La Colosa deposits (Figs. 1-2), respectively an epithermal Au deposit (reserves of 15.9 Moz Au; Tassinari et al., 2008) and a porphyry Au deposit (inferred resources of 12.9 Moz Au; Gil-Rodriguez, 2010).

The aim of this study is to determine the conditions prevailing in the

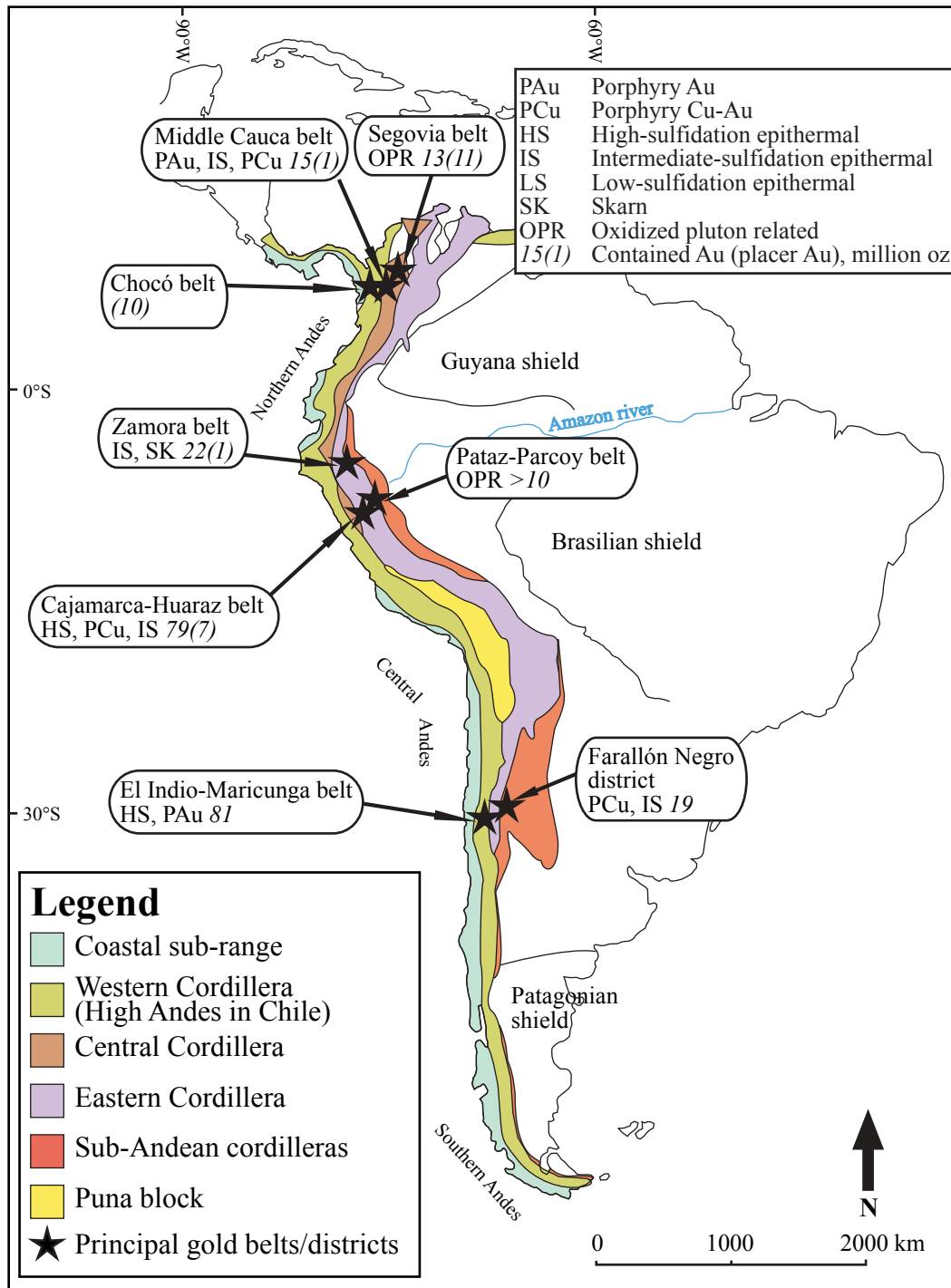


Figure 1-1. Geological provinces of South America, and geographic locations, main deposit types, and sizes of major gold belts (modified from Gansser, 1973; Sillitoe, 2008; WGS 84 latitude-longitude projection).

Buriticá ore-forming system, and to better understand its metallogenic evolution.

A brief introduction to the complex tectonic and metallogenic evolution of Colombia, and an account of the exploration work done so far on the Buriticá

property are first presented. Secondly, the study presents a petrographic description and geochemical characterization of igneous rocks found in the Buriticá area, a detailed vein paragenesis description, geochronological ($^{40}\text{Ar}/^{39}\text{Ar}$) data from magmatic and hydrothermal events, sulfur stable isotope data, and fluid

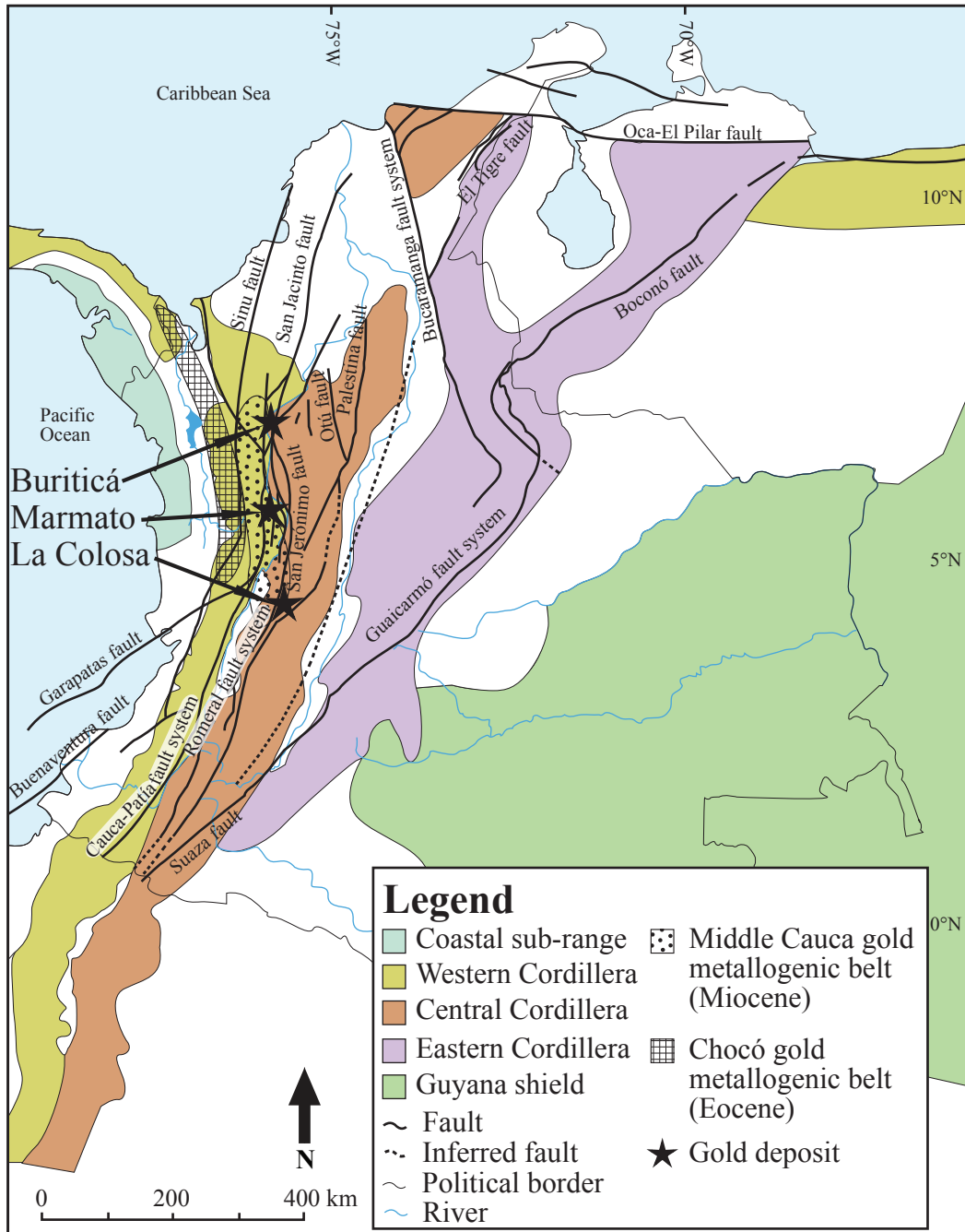


Figure 1-2. Geological provinces of Colombia and geographic locations of major Miocene gold deposits (modified from Gómez Tapias et al., 2007; Ramos and Moreno, 2006; Sillitoe, 2008; WGS 84 latitude-longitude projection).

inclusion data from major mineralized veins of the Buriticá gold deposit. The deposit characteristics are then compared to other gold deposits located in the Middle Cauca belt (Marmato and La Colosa). Finally, a model for the formation of the Buriticá deposit is discussed, and recommendations for further exploration in Colombia are made.

2. Tectonic History of Colombia

The Buriticá gold deposit is located on the eastern edge of the Western Cordillera of Colombia and the of Cañasgordas terrane, approximately 10 km west of its suture zone with the Cajamarca-Valdivia terrane, the Cauca-Romeral fault system (CRFS; Fig. 2-1). The CRFS is a complex series of north- to northeast-trending fault zones formed during the Northern Andean orogeny, the latest of Colombia's orogenic events (Cediel et al., 2003). Movement along faults of the CRFS is characterized by a general right-lateral strike-slip motion (Ego et al., 1995). The Cañasgordas terrane is a Middle Cretaceous to Middle Eocene oceanic terrane accreted during the Miocene as part of this orogeny. The Buriticá deposit is associated with a Late Miocene subduction-related magmatic arc formed to the west of the CRFS.

The Andes are described as a typical cordilleran-type orogeny (Dewey and Bird, 1970), formed by the subduction of oceanic lithosphere below a continental margin. However, based on sectoral differences in tectonic evolution, the Andes can be subdivided into three zones (Gansser, 1973; Shagam, 1975): the Southern, Central, and Northern Andes. The evolution of the Northern Andes records a distinct and very complex geological history involving highly oblique convergence and the interaction of many small tectonic plates through time (Pilger, 1983; Aspden and McCourt, 1986; Aspden et al., 1987; Pindell et al., 1988; Van Thournout et al., 1992; Litherland et al., 1994; Cediel et al., 2003;

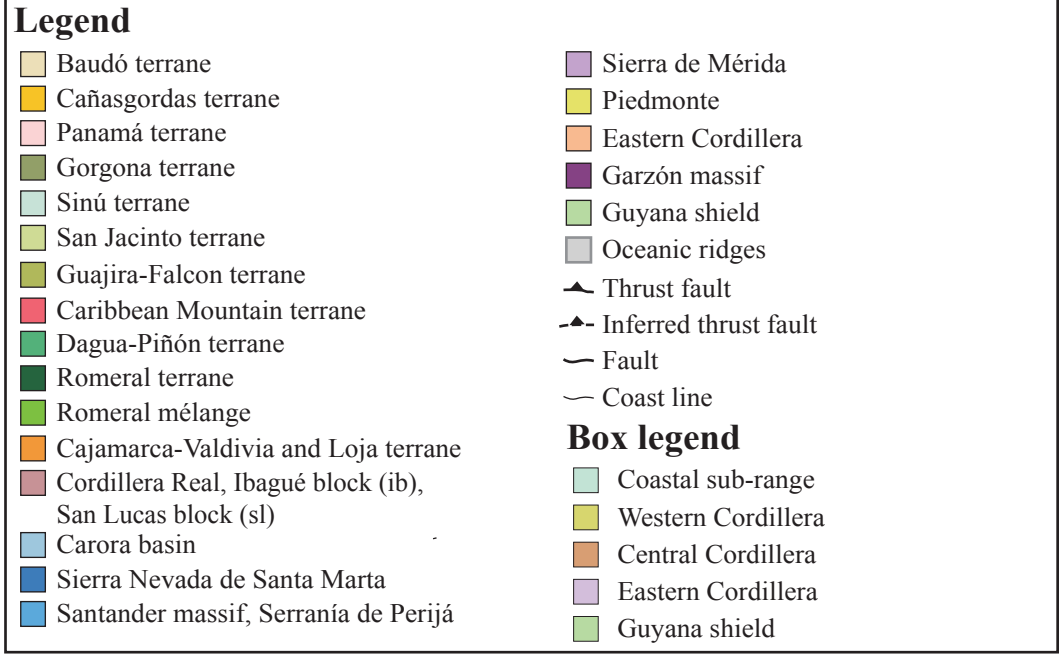
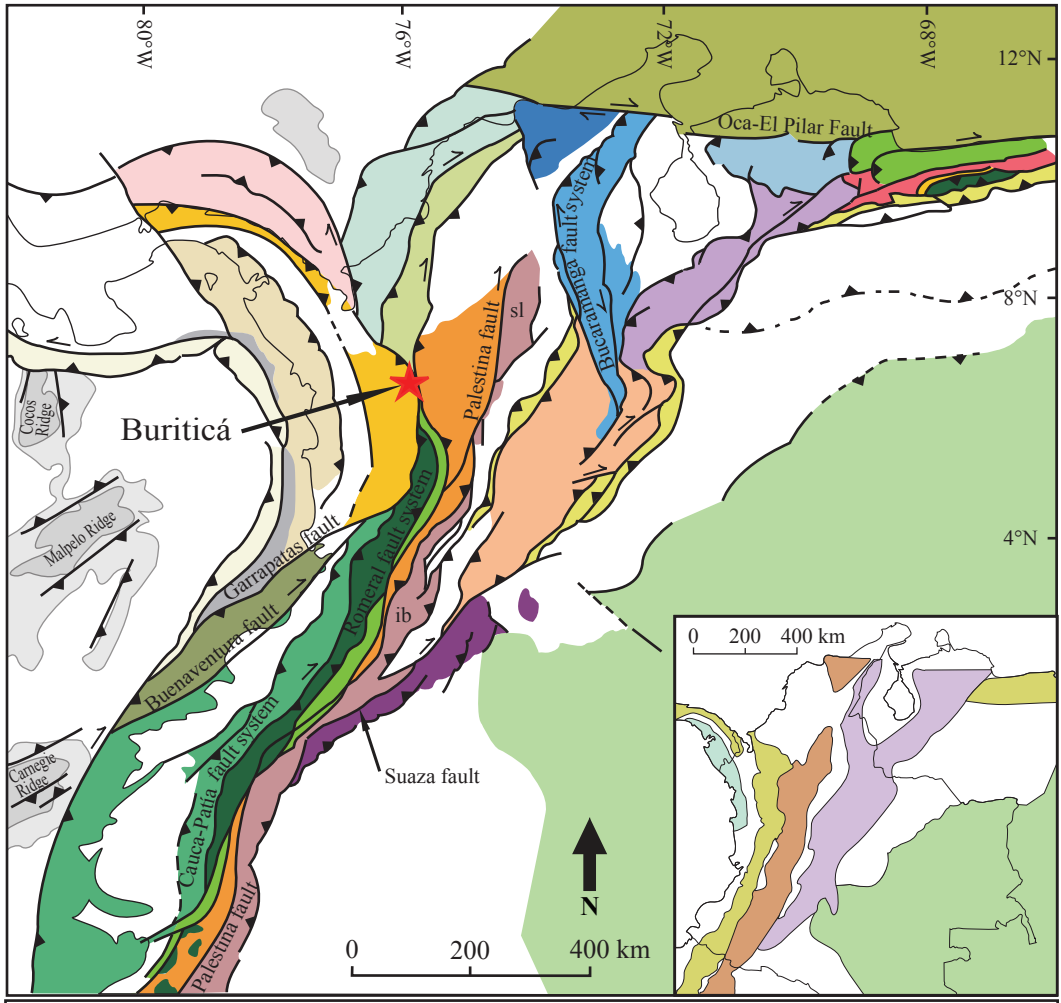


Figure 2-1. Litho-tectonic map of the Northern Andes (modified from Cediel et al., 2003; WGS 84 latitude-longitude projection). Box: Geological provinces of Colombia.

Montes et al., 2005; Acosta et al., 2007).

The Andes of Colombia is part of the Northern Andes, and consists of three cordilleras formed by the accretion of several terranes (Fig. 2-1). Terranes began colliding with the Guyana shield during the Precambrian Grenville orogeny (Hartnady, 1991; Hoffman, 1991), and collisions continue to this day as part of the Northern Andean orogeny (Bürgl, 1967; Campbell, 1974; Irving, 1975; Cediél et al., 2003). The following geological description and tectonic evolution of the various terranes is summarized from Cediél et al. (2003).

The Grenville orogeny (known as Orinoco orogeny in Colombia), spanned from ca. 1350 to 1000 Ma, and culminated with the formation of the supercontinent Rodinia (Fig. 2-2 a). During this orogeny, the eastern margin of Laurentia (modern day North America) and the western margin of Amazonia (modern day South America) collided, thrusting the Chicamocha terrane, a piece of Laurentia, onto the Guyana shield. This terrane now forms the basement of the Eastern Cordillera. These high-grade metamorphic rocks are deeply covered by younger sedimentary rocks in the Eastern Cordillera, but they outcrop along its suture with the Guyana shield in the Sierra Nevada de Santa Marta, the Santander massif, and the Garzón massif. Rodinia was later disrupted during the late Neoproterozoic and Cambrian, with the opening of the Iapetus ocean (Fig. 2-2 b).

Rocks forming the Cajamarca-Valdivia terrane (and its Ecuadorian twin, the Loja terrane) consist of Paleozoic meta-igneous, and marine siliciclastic and volcanoclastic metasedimentary rocks (McCourt et al., 1984; Restrepo et al., 1991; Maya, 1992; Restrepo-Pace, 1992; Toussaint, 1993; Litherland et al., 1994; Maya and González, 1995). Geochemical data suggests two different sources for the sedimentary rocks: an intra-oceanic island arc, and a continental margin. The meta-igneous rocks, observed in the Bolo Azul and Rosario complexes, represent remnants of the island arc.

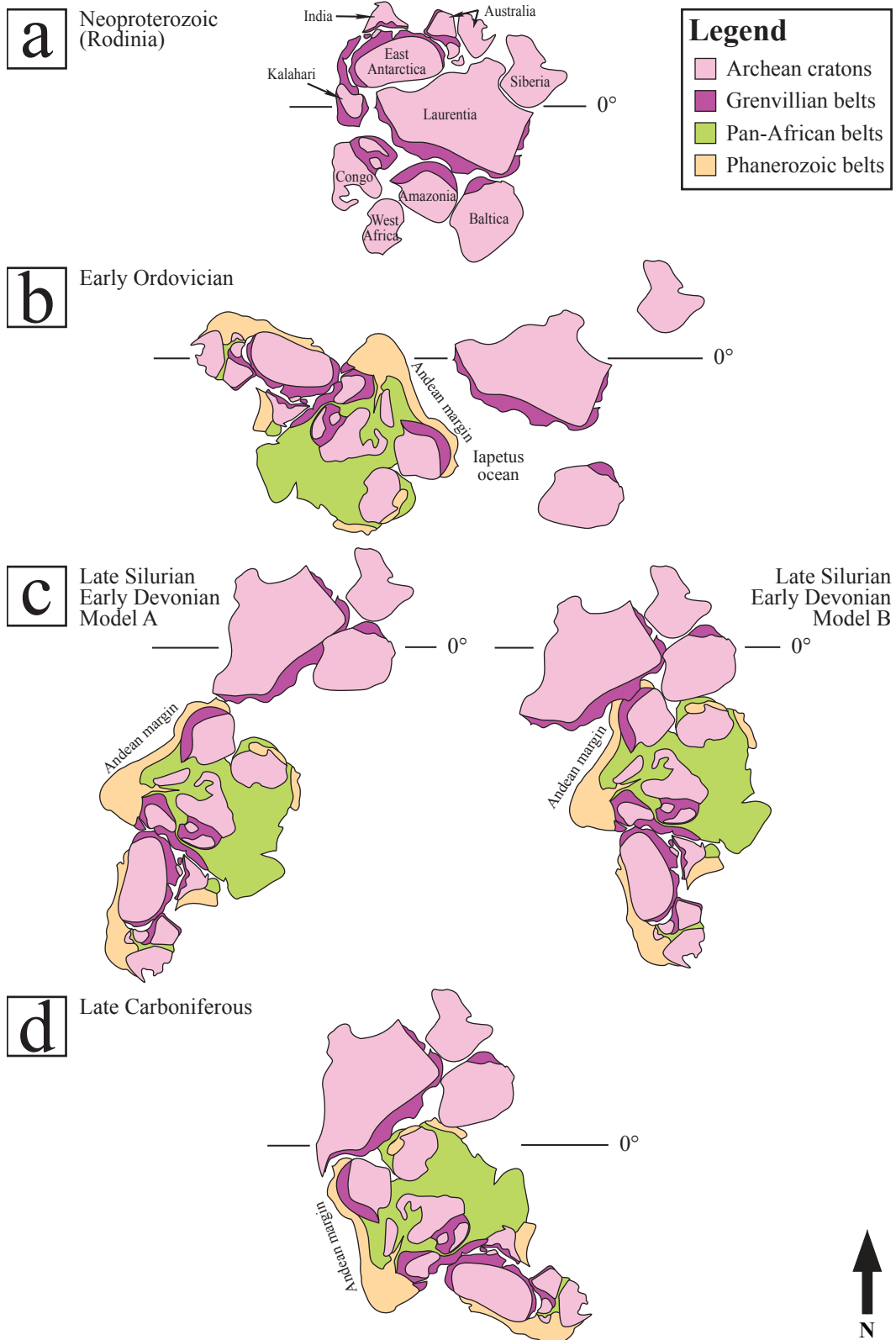


Figure 2-2. Paleogeographic reconstruction of the Archean cratons between the Neoproterozoic and the Late Carboniferous (modified from Hoffman, 1991, and Restrepo-Pace, 1992). Model A is based on Scotese and McKerrow (1990) and model B is based on Kent and Van der Voo (1990).

Two different models (Figs. 2-2 and 2-3) have been described in the literature to account for the closure of this ocean, and for the Cajamarca-Valdivia terrane accretion along the Palestina fault (Kent and Van Der Voo, 1990; Scotese and McKerrow, 1990; see reconstruction in Restrepo-Pace, 1992). According to model A, the South American margin was a convergent active margin with an east-dipping subduction zone causing the formation of a back-arc basin (Fig. 2-3). Closure of the back-arc basin occurred during the Late Silurian and Early Devonian, accreting the Cajamarca-Valdivia terrane to the continental margin. Model A also indicates that collision between North America and South America occurred later, during the Late Carboniferous.

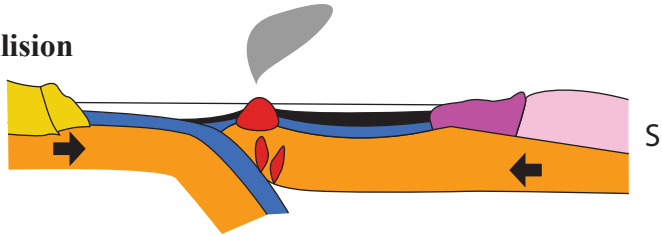
Model B, on the other hand, suggests that accretion of the Cajamarca-Valdivia terrane resulted from the collision of North America and South America during the Late Silurian and Early Devonian (Fig. 2-3). Closure of the Iapetus ocean by collision of North and South America led to the second orogenic event recorded in Colombia (the Quetame orogeny), causing regional metamorphism from lower greenschist to amphibolite facies throughout the country (González, 2001).

Following the Quetame orogeny, a period of north-northeast-oriented extension, located more or less along the modern day Eastern Cordillera, affected Colombia and Venezuela, and lasted from the Late Triassic (229 Ma, La Quinta Formation volcanic rocks) to the Middle Cretaceous (Schubert et al., 1979; Sarmiento-Rojas et al., 2006; Higgs, 2009). Two different hypotheses for this extensional event have been suggested: the first suggests an intracontinental rift associated with the breakup of Pangea (Pindell and Dewey, 1982; Ross and Scotese, 1988; Cediél et al., 2003; Pindell and Kennan, 2009), whereas the second proposes a back-arc extensional origin (Maze, 1984; McCourt et al., 1984; Pindell and Tabbutt, 1995; Meschede and Frisch, 1998). Magmatic activity had a bimodal

Model A: Island arc collision

Early Silurian

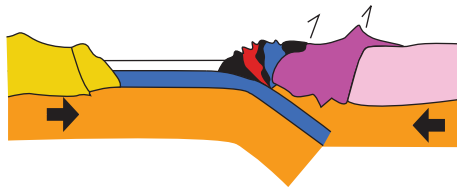
N



S

Late Silurian
Early Devonian

NW

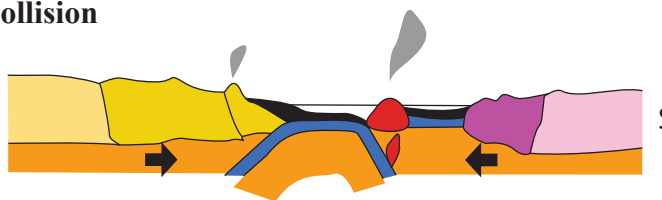


SE

Model B: Continental collision

Early Silurian

N



S

Late Silurian
Early Devonian

NW



SE

Legend

-  Cajamarca-Valdivia terrane
-  Oceanic crust
-  Seafloor sediments
-  Magmatic spreading center
-  Grenville age basement
-  Chicamocha terrane
-  North American craton
-  Guyana shield
-  Mantle

Figure 2-3. Schematic cross-sections depicting the closure of a back-arc basin in an Andean-type convergent boundary for Model A, and in a collisional-type boundary for Model B (modified from Restrepo-Pace, 1992). Not drawn to scale.

alkalic-tholeiitic affinity when the extension was at its maximum during the Early to Middle Cretaceous (Tschanz et al., 1974; Sillitoe et al., 1982; Álvarez, 1983; Dörr et al., 1995), which is consistent with the second hypothesis. However, the first hypothesis is based on evidence of coeval marine sedimentation indicating the formation of a rift basin, a marginal seaway approximately corresponding

to today's Eastern Cordillera and Sierra de Mérida. Pindell and Kennan (2009) suggest that there was no eastward subduction along the Colombian Pacific coast line during Early to Middle Cretaceous time, but that subduction was instead directed westward below the Caribbean tectonic plate, which was migrating eastward to the north of Colombia at the time. The presence of a Middle Cretaceous magmatic arc on the eastern edge of the Caribbean plate is good evidence for this.

Extension stopped shortly after it reached its maximum during the Middle Cretaceous. This was caused by a clockwise rotation of the Farallón oceanic plate around a pole in southern South America from the Late Cretaceous to Eocene, which resulted in a change of plate migration from northward to eastward (Pardo-Casas and Molnar, 1987). This tectonic reorganization initiated east-dipping subduction of the Farallón plate below the newly formed Caribbean plate (the two plates had acted as one before then), and east-dipping subduction of the Caribbean plate below South America (Pindell and Kennan, 2009). In turn, this caused the accretion of several oceanic terranes to the continental margin, and gave way to the Northern Andean orogeny, which is ongoing. This last orogenic event is accountable for modern day topography in Colombia, and results from the interaction between the South American, Farallón-Nazca, and Caribbean tectonic plates. In addition to its changes in direction and velocity, the Farallón plate broke into pieces during the Early Miocene (Pardo-Casas and Molnar, 1987), forming the Cocos and Nazca plates, and complicating the interactions between the different tectonic plates involved in the orogeny.

A large number of small oceanic terranes were accreted to the South American continent during the Northern Andean orogeny. First to be accreted was the Romeral terrane, along the Romeral fault system (Fig. 2-1). The eastern side of this terrane shows various thicknesses of tectonic *mélange*, called the Romeral

mélange. Docking of the terrane occurred during the Early Cretaceous, as evidenced by obducted Jurassic to Early Cretaceous ophiolitic rocks (Wortel and Cloetingh, 1981; Barckhausen et al., 2001), 132–125 Ma blueschist ages from the Central Cordillera (Aspden and McCourt, 1986), and a Middle Cretaceous age for the autochthonous Buga batholith (McCourt and Feininger, 1984). Because of the north-northeast movement of the Farallón plate at the time, the resulting oblique collision had an important transpression component that can be observed in right-lateral displacements along the Romeral fault (Aspden et al., 1987). Accretion of the Romeral terrane also caused a dextral reactivation of the Palestina fault system during the same period (Ego et al., 1995), as well as a general uplift in the Eastern Cordillera recorded by an Aptian erosional unconformity.

Similar evidence for dextral movement along the Early Tertiary Cauca-Patía fault system (Feininger, 1970; De Souza et al., 1984) indicates that the accretion of the Dagua-Piñón terrane must have been caused by a similar mechanism. Important magmatic activity preceded accretion of the Dagua-Piñón terrane, from 90 Ma to 58 Ma, causing the emplacement of many plutonic rocks such as the Antioquia batholith (Ego et al., 1995). The timing of the Dagua-Piñón terrane collision with South America during the Early Eocene is based upon a sudden cessation of magmatic activity shortly after 58 Ma (Maya, 1992), combined with an uplift and erosion period which began at approximately 56 Ma.

Collision between the Gorgona terrane and South America began at ~45 Ma (Cediél and Cáceres, 2000) along the Buenaventura fault (Fig. 2-1). Magmatic activity related to this collision is recorded between 44 Ma and 13 Ma (Kerr and Tarney, 2005), and shows an eastward migration as the Gorgona terrane made its final approach during the Neogene. Middle Miocene uplift in the Central Cordillera and dextral reactivation of the Cauca-Patía fault system are also associated with the docking of the Gorgona terrane.

Deformation of the Gorgona terrane along the Garrapatas fault indicates that the Cañasgordas terrane (or Chocó Arc) began its accretion during the Miocene after the accretion of the Gorgona terrane. This terrane formed on the western edge of the Caribbean plate as an island arc system developed over an east-dipping subduction zone between the Farallón and Caribbean plates (Pindell and Kennan, 2009). This is evidenced by large intrusions such as the Sabanalarga and Mandé batholiths, respectively dated at 97 ± 10 Ma (Maya, 1992) and from 54.7 ± 1.3 Ma to 42.0 ± 0.9 Ma (González et al., 1978). These batholiths were emplaced prior to the Cañasgordas terrane accretion, during the Middle to Late Cretaceous and Paleogene.

Based on deposition of turbidite sequences of continental affinity, accretion of the San Jacinto and Sinú terranes has been dated as Paleocene-Late Eocene and Miocene respectively (Botero, 1975; Göbel and Stibane, 1979). These terranes have played a very small role in the Northern Andean orogeny.

The youngest terrane in Colombia, the Baudó terrane (Fig. 2-1), began to collide with South America during the Late Miocene, and the collision is ongoing. This terrane is associated with a belt of 8–6 Ma autochthonous intrusive rocks located within 50 km to 100 km west of the Cauca-Romeral fault system (Cediel et al., 2003). The Buriticá deposit is hosted in the Cañasgordas terrane, and gold mineralization is thought to be related to this Late Miocene subduction-related continental arc (Fig. 2-4).

In addition to the Farallón (Nazca)–South America collision, interaction with the Caribbean oceanic plate played an important role in the modern evolution of the Northern Andes. Although still debated, the most commonly accepted origin for the Caribbean plate is that it formed as normal oceanic lithosphere within the Pacific, but was thickened to become an oceanic plateau during the Middle to Late Cretaceous when it drifted over the Galapagos hot spot. It then

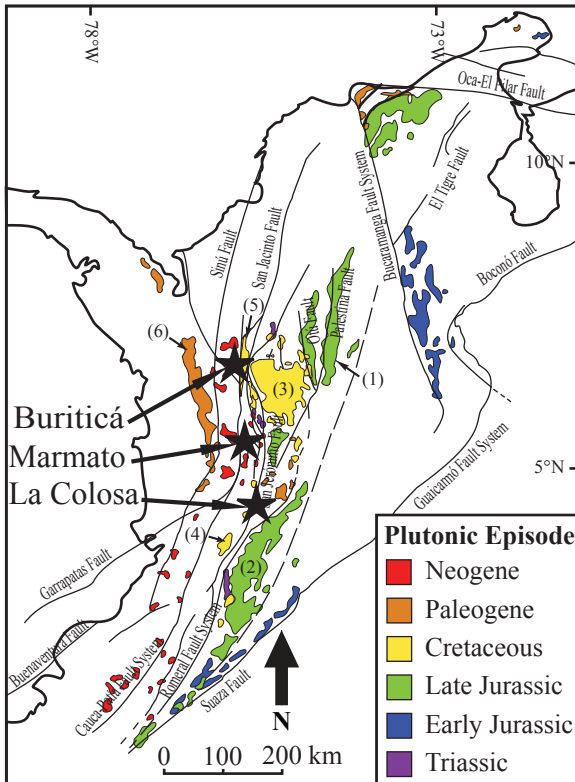


Figure 2-4. Major Mesozoic and Cenozoic intrusive rocks of Colombia. (1) Segovia batholith, (2) Ibagué block, (3) Antioquia batholith, (4) Buga batholith, (5) Sabanalarga batholith, (6) Mandé batholith (modified from Aspden et al., 1987).

passed into the gap between North and South America to arrive at its current location (Aspden et al., 1987; Maya, 1992).

Mann (1995) associated the Caribbean Mountain and the Guajira-Falcon terranes (Fig. 2-1) with the Romeral terrane based on geochronological, compositional, and tectonic similarities. As such, their collision with South America would have occurred in the Middle Cretaceous. Their current location is explained by dextral displacement along the

Oca-El Pilar fault, induced by the

eastward migration of the Caribbean plate (Fig. 2-1).

The northern end of the Eastern Cordillera started drifting to the northwest along the Bucaramanga fault (Fig. 2-1) during the Middle to Late Cretaceous. This resulted in significant uplift in the Santander Massif and the Guajira-Falcon terrane during the Paleocene, obduction of the Caribbean Mountain terrane onto the South American continent during the Eocene, and Miocene to Recent uplift within the Sierra de Mérida, the Serranía de Perijá, and the Sierra Nevada de Santa Marta (Cediél et al., 2003). Minor Paleogene magmatic activity is also observed in the Sierra Nevada de Santa Marta (Zambrano, 1972; Maresch, 1974) due to convergence between the South America and Caribbean plates (Aspden et al., 1987; Van Der Hilst and Mann, 1994; Taboada et al., 2000).

As outlined by Van Der Hilst and Mann (1994), subduction of the Caribbean oceanic plateau under northwestern South America occurs at a very shallow angle ($\sim 17^\circ$) due to its high buoyancy, which could explain the absence of a well developed magmatic arc in northern Colombia or Venezuela. Pindell and Kennan (2009) came to a different conclusion, and proposed that magmatism is absent from north Colombia because the Caribbean plate is too buoyant to subduct and that the South American plate is instead overthrusting it.

The northwest migration of northeastern Colombia and the north-northeast-oriented collision of the Western Cordillera terranes caused strong transpressive stresses in the Eastern Cordillera during the Miocene and Pliocene. Normal faults previously developed during the rifting episode mentioned above were reactivated, and caused strong uplift of the Eastern Cordillera. Late Miocene reactivation of the Suaza fault and uplift of the Garzón massif (Cediél et al., 2003) also coincided with the arrival of the Carnegie ridge, an aseismic ridge of thickened crust, in the subduction zone on the western coast of Ecuador (Van Der Wiel, 1991). Because of the ridge's high buoyancy, the angle of subduction of the oceanic slab flattened, causing stress in the overlying craton, and uplift in the massif.

3. Ore Deposits of Colombia

Cordilleran-type orogenies are a fertile environment for many kinds of ore deposits due to the magmatic activity associated with them. The Northern Andes record important subduction and extension-related magmatism throughout the Mesozoic and Cenozoic (Fig. 2-4; Aspden et al., 1987). Most deposits found in Colombia are porphyry Cu-(Au-Mo) and epithermal Au-Ag deposits.

Copper and gold deposits are located along six major belts of ages from Jurassic to Neogene (Fig. 3-1). The two easternmost belts, the California district

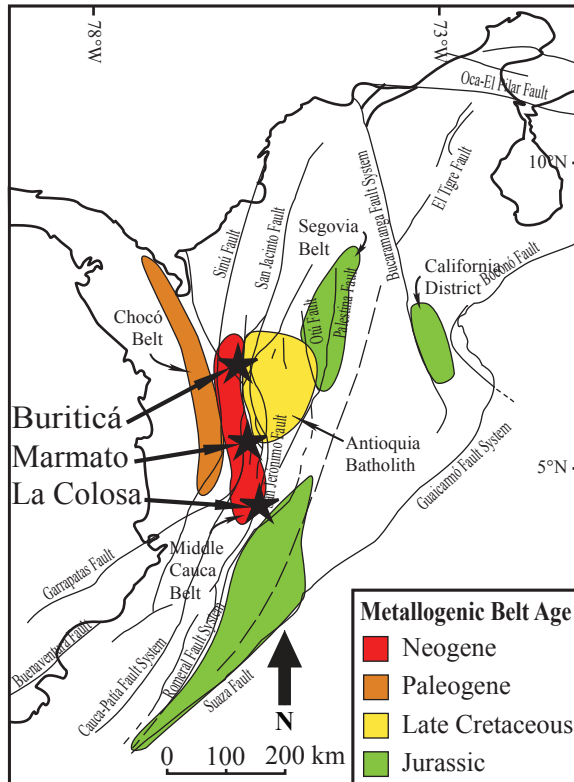


Figure 3-1. Metallogenic belts of Colombia (modified from Sillitoe and Perelló, 2005, and Sillitoe, 2008; WGS 84 latitude-longitude projection).

and Segovia belt located in the Eastern Cordillera, contain porphyry Cu deposits, small skarn deposits associated with intrusive rocks, and oxidized pluton-related Au deposits of Jurassic age (Carlson, 1977; Chiaradia et al., 2008; Mosier et al., 2009). The California district also contains epithermal Au deposits of Cretaceous age, associated with the calc-alkaline plutonic rocks formed during the extension episode that preceded the Northern Andean orogeny.

The younger belts, located along the Central and Western Cordillera, were formed during the Northern Andean orogeny (Sillitoe et al., 1982; Sillitoe, 2008). Cretaceous deposits are associated with the Antioquia batholith and its smaller satellite bodies (Fig. 3-1), and formed as a result of subduction-related magmatism associated with the approach of the Dagua-Piñón terrane. Deposits found in this belt are mostly epithermal Au-Ag, porphyry Cu-Au, and porphyry Au deposits (Sillitoe and Perelló, 2005). Epithermal deposits are characterized by sulfide-rich quartz veins cutting the metamorphic schists of the Cajamarca-Valdivia terrane, and are associated with andesitic and tonalitic intrusions. Porphyry deposits are associated with more felsic intrusions associated with the Antioquia batholith.

Paleogene porphyry Cu-(Au-Mo) deposits such as the Acandí (Álvarez

and Parra, 1979), Pantanos (Álvarez et al., 1983), and Murindó deposits (Guarín and Álvarez, 1977) are located in the Chocó belt (Fig. 3-1). They are associated with allochthonous calc-alkaline batholiths such as the Mandé batholith (Fig. 2-4), which formed in an island-arc setting prior to accretion (González, 2001). Gold deposits found along this belt are primarily placer Au deposits.

Neogene deposits are located along the Cauca-Romeral fault system (Fig. 3-1; Middle Cauca belt), and result from subduction-related magmatism associated with approach of the Baudó terrane during the Miocene. This belt contains epithermal as well porphyry Au deposits (Sillitoe et al., 1982; Aspden et al., 1987). The Buriticá gold deposit is located near the northern end of this belt.

In addition to porphyry- and epithermal-type deposits, a small number of Paleozoic to Cenozoic volcanic-hosted massive sulfide deposits have been identified in the Northern Andes by Carlson (1977), Sillitoe et al. (1982), Rossetti and Colombo (1999), González (2001), Sillitoe and Perelló (2005), Chiaradia et al. (2008), Sillitoe (2008), Tassinari et al. (2008), and Gil-Rodríguez (2010).

4. Buriticá Historical Background

The following summary of historical mineral exploration activities around the village of Buriticá is taken from Bargmann and Dominy (2008, 2009). Gold mineralization is thought to have been recognized in the area since pre-colonial times, as evidenced by old underground workings around high-grade gold veins. However, political tensions and security issues in Colombia have prevented major exploration investments, and limited mine development. Since the mid-1990s, the Colombian political situation has improved significantly and companies are more willing to commit to exploration in the country.

The earliest geological study of the area was done by Castro and Feininger (1965), from the Instituto Colombiano de Geología y Minería (Ingeominas).

The authors evaluated the mineral potential of the Buriticá andesite for lead mineralization, but found out that it was not economically viable. González and Londoño (2002a) more recently published a brief mineralogical description of the Buriticá stock and of the Buriticá andesite.

In 1992, Grupo de Bullet S.A. (Bullet) opened the Yaragua mine, exploiting a high-grade gold-bearing quartz-carbonate vein (the Murcielagos vein; Fig. 4-1), hosted by the Buriticá andesite. It has been producing gold continuously since then, producing 11 694 ounces of gold from 2001 to 2007. Since 2008, the mine has also been exploiting the San Antonio vein. Three levels have been opened in the Yaragua mine: Level One (1484 m elevation), Level Two (1430 m elevation), and Level Three (1370 m elevation). Approximately 400 m of horizontal development along the strike of the vein has been completed to date.

Exploration work has also been conducted by Gran Colombia Resources Ltd. (GCR) since the early 1990s, identifying multiple prospects around the Yaragua mine showing signs of hydrothermal alteration and sulfide mineralization.

Continental Gold of Colombia Inc. (CGC) acquired the Yaragua mine in 2008, along with over 18 910 hectares of land constituting the Buriticá project area. As of the end of 2010, 145 surface drill holes and 54 underground drill holes have been completed, representing a total of 45 000 m of core. An additional 60 000 m is planned to be drilled in 2011. Drilling has identified two new vein zones near the Yaragua mine: the San Antonio vein was found in 2008, and the Veta Sur zone was discovered in 2009. The present study focuses on the Murcielagos and San Antonio veins.

5. Regional Geologic Setting

The Cañasgordas terrane is a Cretaceous oceanic arc composed of

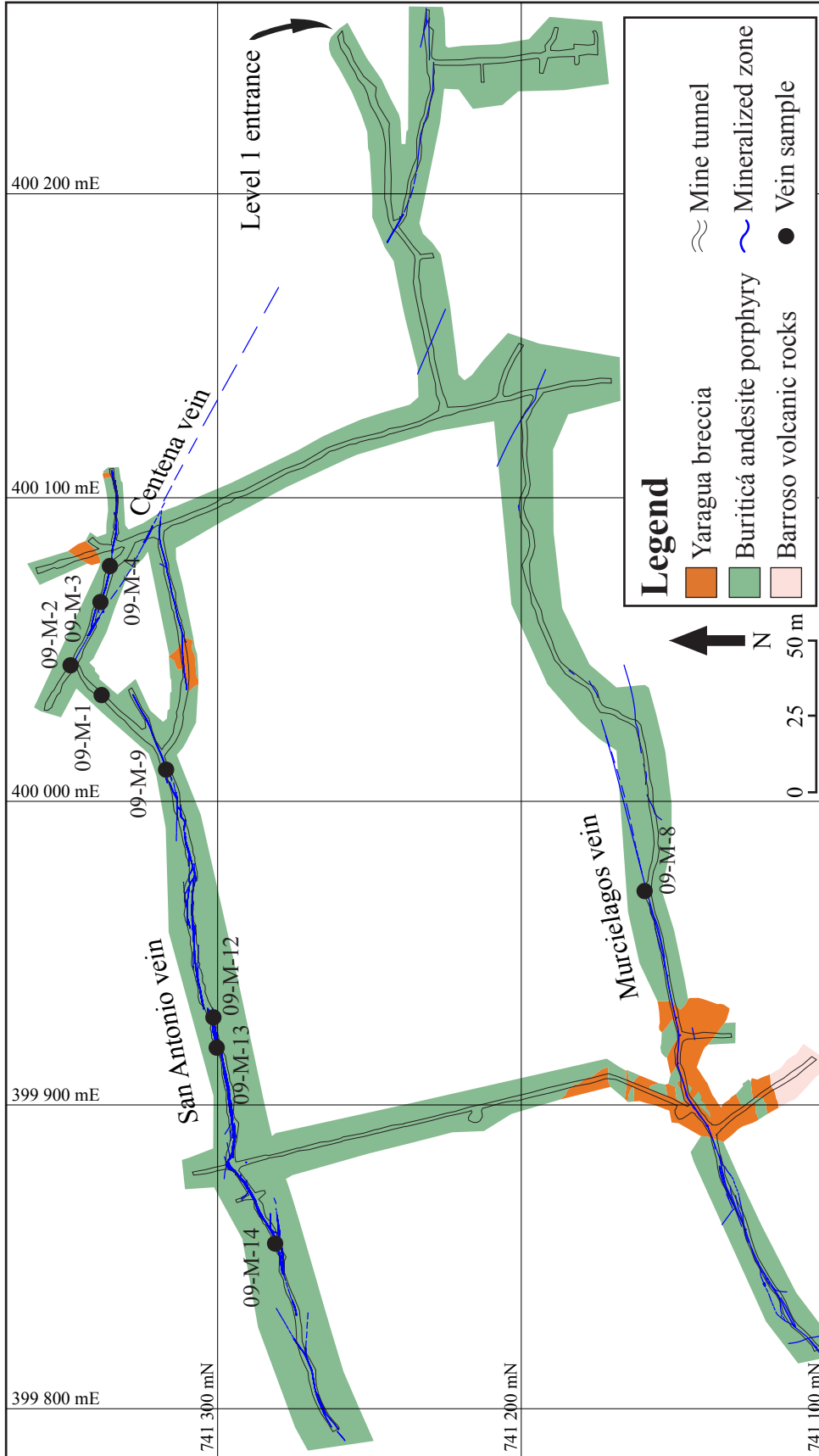


Figure 4-1. Underground geology map of the Yaragua mine level 1, showing the locations of the main mineralized veins and of the vein samples taken (WGS 84 UTM Zone 18N projection; map provided by Continental Gold of Colombia).

three units in the Buriticá area: volcanic and sedimentary rocks of the Barroso Formation, and sedimentary rocks of the Urrao member, part of the Penderisco Formation (Fig. 5-1; Castro and Feininger, 1965; Restrepo and Toussaint, 1976; Álvarez and González, 1978; Etayo et al., 1980; Etayo, 1989; González, 1993). The Barroso volcanic rocks consist of tholeiitic basalts and andesites metamorphosed to the zeolite and prehnite-pumpellyite facies (Álvarez and González, 1978). The sedimentary rocks of the Barroso Formation consist of intercalated lenses of mudstone, chert, siliciclastic, and pyroclastic sediments (González, 2001). Lens thicknesses vary from a few meters to a hundreds of meters. The Penderisco Formation is a 3000 m-thick turbidite sequence deposited over the Barroso Formation in a retrograding basin from continental slope to abyssal plain (Hoyos et al., 1990).

Prior to its accretion, the Cañasgordas terrane was intruded by the calc-alkaline Sabanalarga batholith, a 560 km² dioritic to quartz dioritic intrusive body (González, 2001). K/Ar dating on biotite yielded an age of 97 ± 10 Ma for this pluton (González et al., 1978). The Buriticá stock is considered genetically related to the Sabanalarga batholith on the basis of proximity and similar composition. K/Ar dating on hornblende from the Buriticá stock yielded an age of 91.1 ± 6.4 Ma (Göbel and Stibane, 1979). The age of the Buriticá stock overlaps, within error, with the age of the Sabanalarga batholith, supporting the genetic relation between the two. A series of norites, clinopyroxene-bearing gabbros, and olivine-bearing gabbros, grouped as the Altamira gabbro, intrude the Barroso Formation a few kilometers north of Buriticá, and were dated at 92 Ma (Restrepo and Toussaint, 1976; Maya, 1992).

The Buriticá andesite, which hosts Buriticá gold deposit, has been described by Castro and Feininger (1965), Álvarez and González (1978), and González and Londoño (2002a). It is a mafic porphyritic

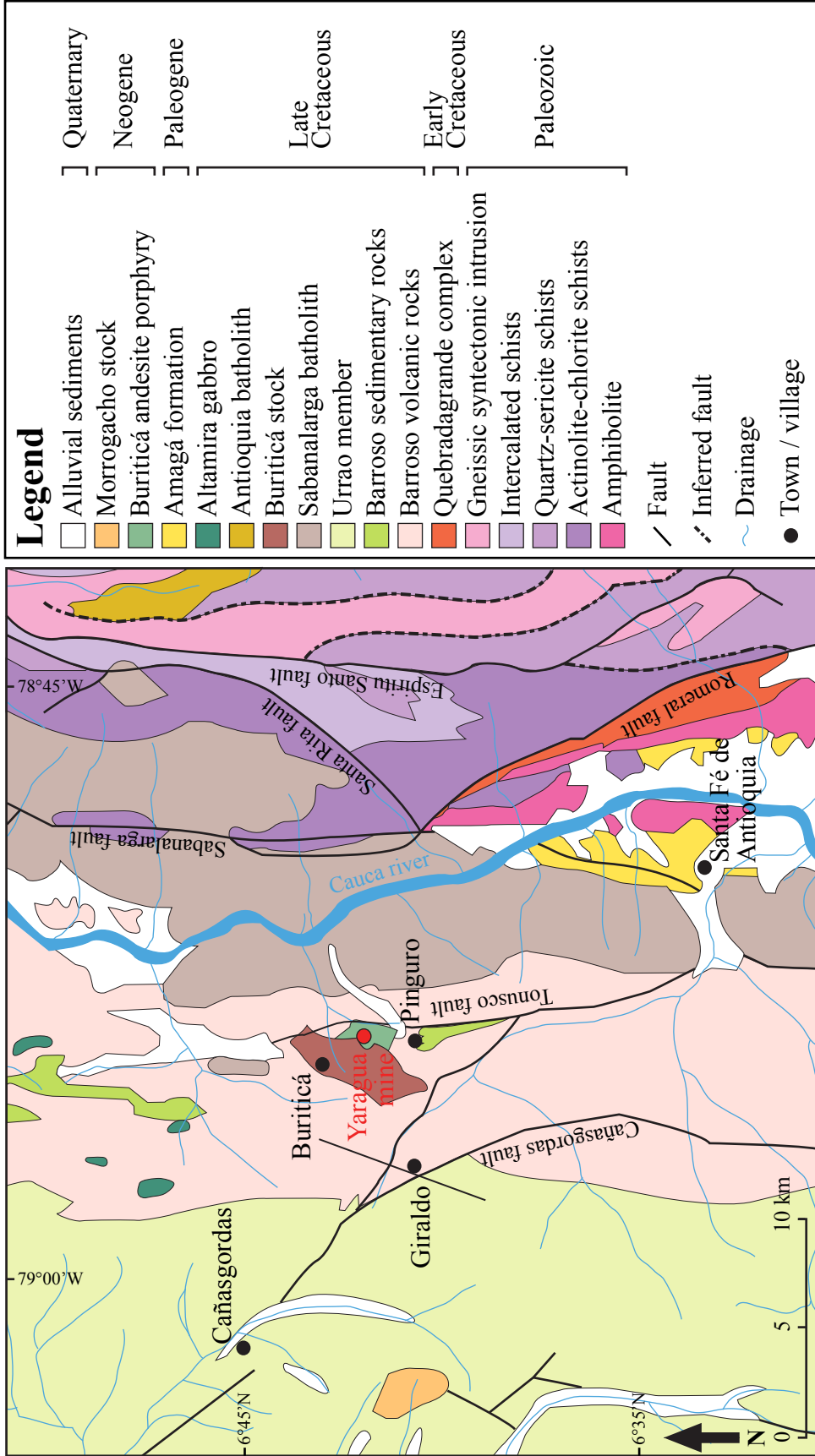


Figure 5-1. Regional geology map of the Buriticá area and its surroundings (modified from González et al., 1999; WGS 84 latitude-longitude projection).

igneous rock that cross-cuts both the Barroso Formation and the Buriticá stock. The age of this unit is still debated. González and Londoño (1998) provided a whole rock K/Ar age of 43.8 ± 4.3 Ma, which would seem to associate it with the Eocene Mandé batholith, and the Chocó metallogenic belt (Sillitoe, 2008) located further to the west (Figs. 1-2 and 3-1). On the basis of similar composition and texture, however, Castro and Feininger (1965) related the Buriticá andesite to other porphyritic bodies found in the Titiribí area, about half way between Buriticá and Marmato (Fig. 1-2). The Titiribí porphyritic rocks have been dated by K/Ar on hornblende at 8.0 ± 0.9 Ma and 7.8 ± 1.0 Ma (González, 1976), which is consistent with the Miocene Middle Cauca metallogenic belt described by Sillitoe (2008).

6. Buriticá Deposit Geology

Detailed mapping was done over a 20 km² area during the summer of 2009 (Fig. 6-1). The map shows the location of the surface samples used for description and analytical purposes. For a detailed description of the surface samples and for petrographic descriptions, see Appendix A and B.

6.1. Volcanic and sedimentary rocks

The oldest rocks in the immediate Buriticá area are those of the Barroso Formation, part of the Cañasgordas group. This formation is characterized by basaltic rocks and associated sedimentary rocks. The basalts are equigranular, fine grained, and composed of euhedral to subhedral lath-shaped plagioclase and prismatic augite. Strong chlorite replacement of mafic minerals, locally associated with epidote alteration, is observed everywhere in this unit. Alteration is associated with small amounts of sulfide minerals, mostly pyrrhotite, and traces of pyrite and chalcopyrite. Abundant quartz-calcite-epidote veining of various thickness and orientation crosscut the unit. Quartz, calcite, and chlorite also fill

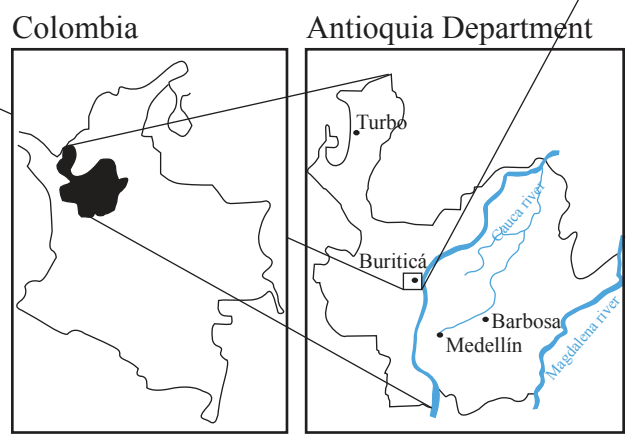
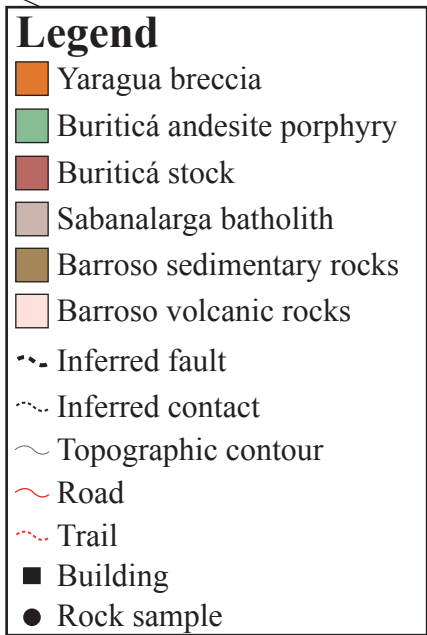
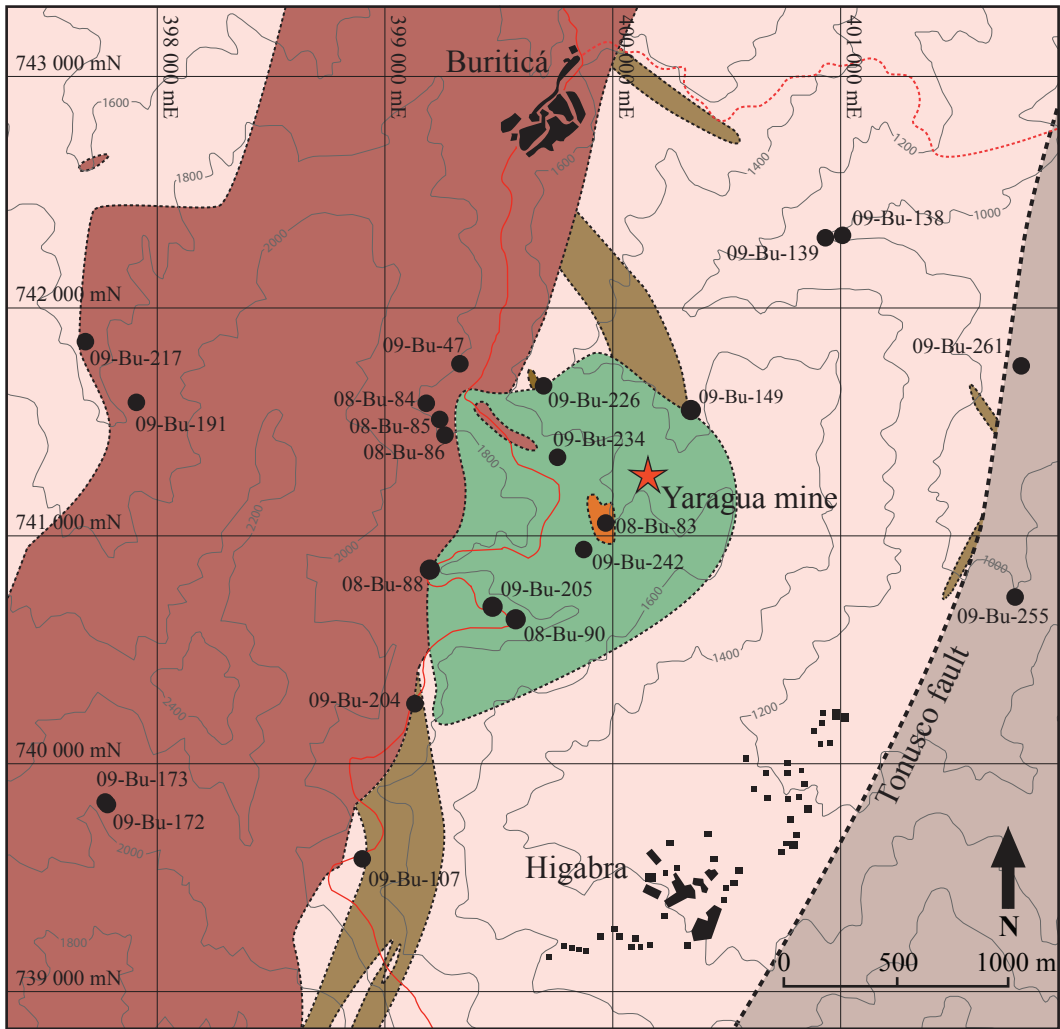


Figure 6-1. Detailed geology map of the Buriticá area showing the location of surface samples (WGS 84 UTM Zone 18N projection).

most vesicles. This alteration is very homogeneous throughout the whole area, and is interpreted as seafloor alteration, unrelated to mineralization.

The basalts of the Barroso Formation represent a thick pile of volcanic rocks, and typically exhibit well developed, younging westward pillow structures (Fig. 6-2 a and b). Way up was determined using pillow shapes and peduncle orientation. A matrix of strongly chloritized and calcite-altered hyaloclastite fills the available room between pillows. Pillows have highly vesicular edges, about 1 cm to 3 cm thick. Vesicle size ranges from 1 mm to 15 mm, and vesicles are locally elongated perpendicular to the pillow surface. Although some vesicles remain empty, most are partially to completely filled with late calcite, quartz, or zeolites.

Lenses of sedimentary rocks were deposited coeval to the basalt. Lens thickness in the study area varies from a few meters up to 230 m. Sediments consist primarily of dark interbedded calcareous mudstone and siltstone (Fig. 6-2 c and d). Bed thickness ranges respectively from 2 cm to 5 cm for the mudstone, and from 10 cm to 30 cm for the siltstone. Thicker siltstone beds commonly have parallel laminations and, rarely, cross-laminations. Way up to the west was determined from cross-laminations as well as from erosive bedding contacts. Although mostly unaltered, this unit is characterized by strong calcite veining. Evidence of folding was seen in the form of asymmetric parasitic folds and will be discussed in further detail later.

Chert beds have also been observed locally on the north side of the Buriticá andesite body (Fig. 6-2 e). Bedding thickness ranges from 5 cm up to 40 cm. Parallel laminations, wavy bedding, and soft sediment deformation are common in this unit (Fig. 6-2 f). The chert is milky white to dark green, very hard and fine-grained. In addition to the chert and siliciclastic rocks, tuff beds have been observed in drill holes, but none were seen during surface mapping.

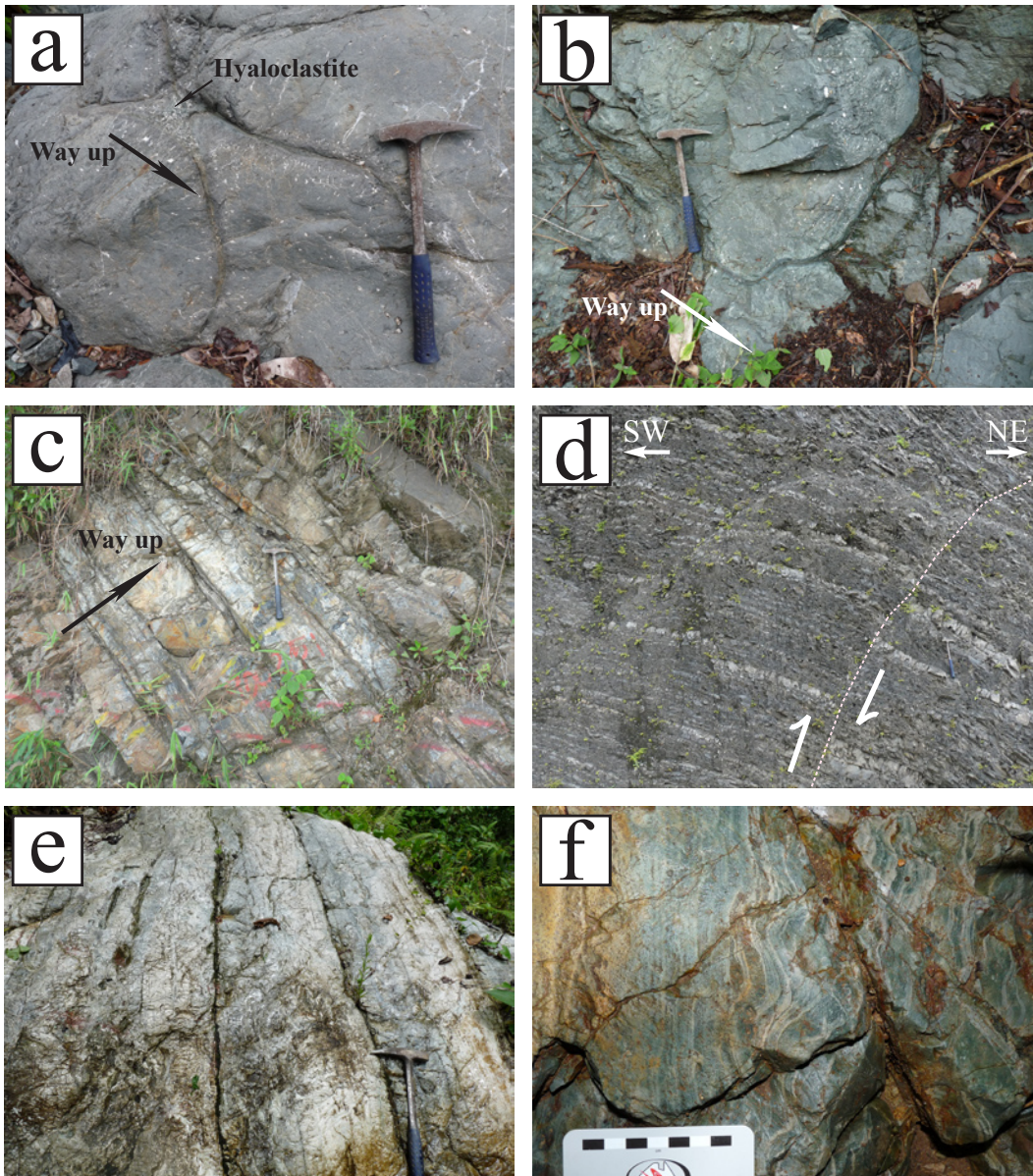


Figure 6-2. Barroso Formation lithologies: (a) vesicular pillow basalt showing hyaloclastite between pillows; (b) vesicular pillow basalt; (c) calcareous siltstone beds showing way up to the west; (d) steeply dipping outcrop surface, calcareous siltstone and mudstone interbeds cut by a series of small north-south faults showing dextral displacement; (e) chert beds showing parallel laminations; (f) close-up view of a chert bed showing parallel laminations and soft sediment deformation.

The Barroso Formation was dated in the Buriticá area using ammonites and foraminifera, yielding ages from Barremian to Albian (Castro and Feininger, 1965; Etayo et al., 1980).

6.2. Plutonic rocks

In addition to the description provided by this study, a brief mineralogical

description of the intrusive rocks of the area is available in González (2001) and González and Londoño (2002a, b).

The contact between the Barroso Formation and the Sabanalarga batholith is located about 1 km east of the Buriticá gold deposit. In the vicinity of the deposit, the Sabanalarga batholith is a massive, fine to medium grained monzogranite. Its primary mineral composition includes 40% quartz, 15% orthoclase, 10% plagioclase, and altered mafic minerals. The studied samples are moderately to strongly altered, and contain 17% chlorite, 15% epidote, 5% sericite, and traces of magnetite, pyrite, and chalcopyrite.

In addition to the strong alteration at the contact with the Barroso Formation, the rock is highly fractured, displays sigmoidal crystals along larger fractures, and abundant quartz recrystallization textures. Based on this evidence, and on a topographic low along the interpreted contact trace, the Barroso–Sabanalarga contact is here interpreted to be faulted, and to represent a strand of the regionally recognized Tonusco fault (Fig. 6-1). This interpretation contrasts with the regional mapping done by González (2001; Fig. 5-1), in which the Tonusco fault cuts the Barroso Formation and represents the eastern contact of the Buriticá andesite porphyry with the Barroso Formation.

The Buriticá stock is an elongate tonalitic intrusive body of approximately 10 to 15 km², and is compositionally similar to the Sabanalarga batholith. Mapping of the Buriticá stock–Barroso Formation contact did not provide enough information to determine the nature of the contact. Wherever exposed, the contact was too altered to give clear evidence to discriminate between an intrusive and a faulted contact. However, the contact strikes at approximately 015°, which is roughly parallel to the faulted Sabanalarga batholith–Barroso Formation contact, and could suggest that it has a structural component. Because exposure is very sparse in the area, the contact outline in Figure 6-1 is mostly interpretive.



Figure 6-3. Buriticá stock: (a) light grey, medium-grained tonalite cut by dark grey glomeroporphyritic andesite dikes; (b) blebs of dark grey glomeroporphyritic andesite in light grey medium grained tonalite matrix: evidence of magma mingling.

The Buriticá stock is primarily composed of equigranular, medium grained hornblende-bearing tonalite. Average mineral composition is 40% quartz, 40% plagioclase, 20% hornblende, and trace amounts of zircon and titanite. Quartz crystals are late in crystallization sequence and form as oikocrysts.

The Buriticá stock shows evidence of magma mingling with a more mafic facies, as shown in Figure 6-3 a and b. This facies occurs both as pinch and swell

dikes or blebs of various sizes intruding the more felsic hornblende-bearing tonalite. Dikes intrude the tonalitic body without preferential orientation. Dike thickness is typically from a few centimeters to around 50 cm, and bleb size is typically in the tens of centimeters range.

The mafic facies is glomeroporphyritic, with plagioclase and augite phenocryst aggregates up to 7 mm across in a microlithic plagioclase-quartz groundmass (Fig. 6-4 e to h). Groundmass represents 65% to 80% of the rock. Individual plagioclase and augite phenocrysts range from 1 mm to 2 mm long for both minerals. Samples 08-Bu-85 and 09-Bu-47 (Fig. 6-4 g and h) contain more plagioclase phenocrysts and more quartz in their groundmass than does sample 09-Bu-172 (Fig. 6-4 e and f).

The youngest igneous rock in the area is the Buriticá andesite porphyry, a 2 km² and at least 500 m thick body, which is located in the Barroso Formation along the eastern Buriticá stock–Barroso Formation contact, and is host to the gold mineralization. The Buriticá andesite is a porphyritic unit, although locally equigranular and fine grained. It contains fine to locally medium grained phenocrysts, and from 50% to 75% microcrystalline groundmass. The groundmass contains plagioclase microliths, and microcrystalline mafic minerals and opaque minerals. Its phenocryst composition is highly variable, but includes plagioclase-augite, plagioclase-augite-biotite, plagioclase-hornblende-augite, plagioclase-hornblende, and plagioclase-only assemblages, with occasional trace amounts of apatite inclusions in mafic minerals (Fig. 6-5). The andesite porphyry also contains small amounts of centimeter-scale sub-angular to angular mafic xenoliths, possibly from the basaltic host rock (Fig. 6-5 c and d). Typically, whenever both augite and hornblende phenocrysts are present in a sample, augite is partially to completely altered to chlorite, whereas hornblende remains quite fresh. Augite crystal edges, and more rarely hornblende crystal edges, are

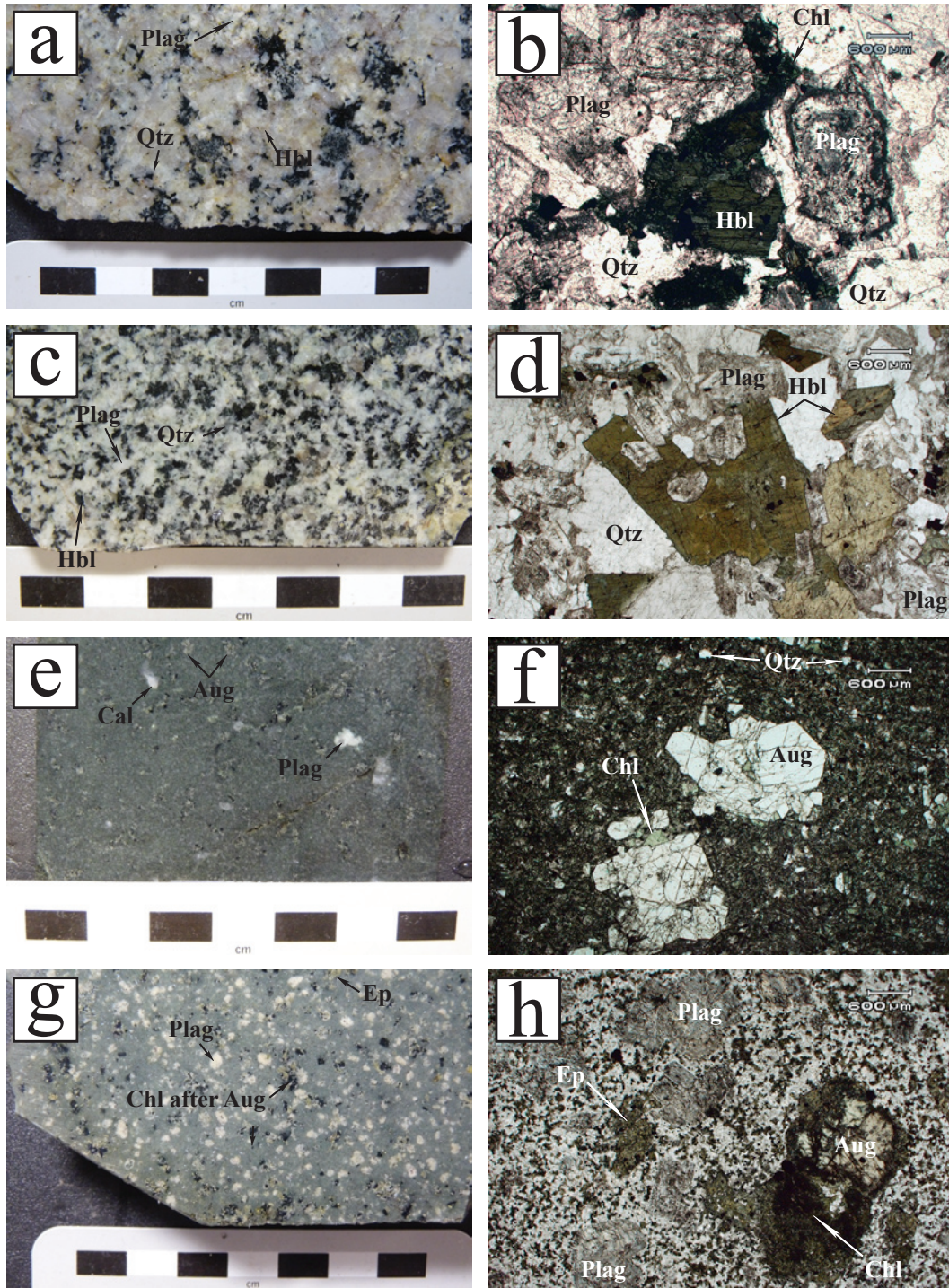


Figure 6-4. Buriticá stock lithologies in hand specimen and thin section (plane-polarized transmitted light): (a) medium-grained hornblende-bearing tonalite (sample 09-Bu-173); (b) photomicrograph of hornblende-bearing tonalite (sample 09-Bu-204); (c) fine- to medium-grained hornblende-bearing tonalite (sample 09-Bu-191); (d) photomicrograph of hornblende-bearing tonalite (sample 09-Bu-191); (e) glomeroporphyritic augite-phyric andesite porphyry intruding the tonalite (sample 09-Bu-172); (f) photomicrograph of glomeroporphyritic augite-phyric andesite porphyry (sample 09-Bu-172); (g) glomeroporphyritic plagioclase-augite-phyric andesite porphyry blebs found in tonalite (sample 09-Bu-47); (h) photomicrograph of glomeroporphyritic plagioclase-augite-phyric andesite porphyry blebs found in tonalite (sample 08-Bu-85). Abbreviations: Aug = augite, Cal = calcite, Chl = chlorite, Ep = epidote, Hbl = hornblende, Plag = plagioclase, Qtz = quartz.

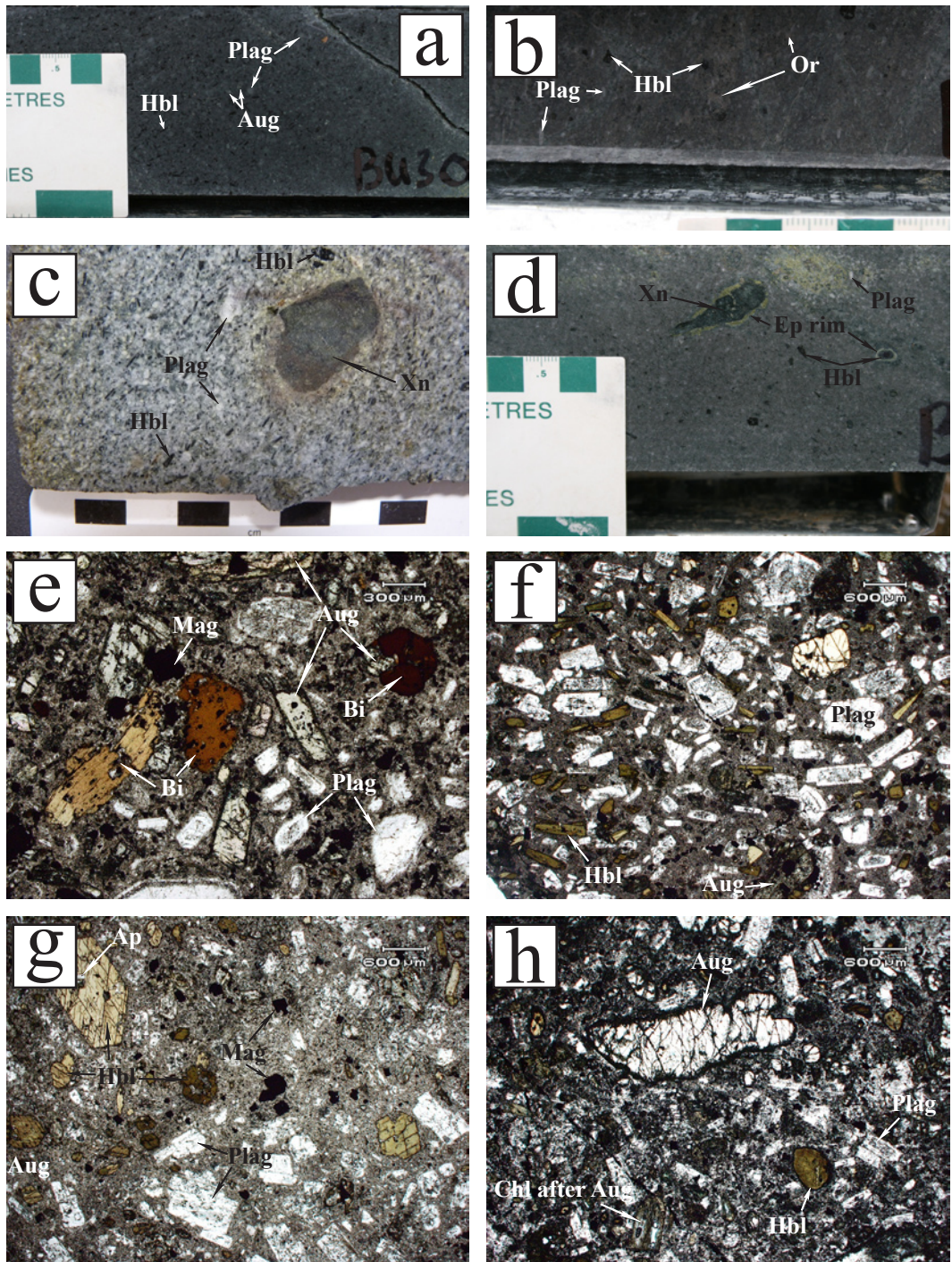


Figure 6-5. Buriticá andesite porphyry lithologies in hand specimen and thin section (plane-polarized transmitted light): (a) plagioclase-hornblende-pyroxene-phyric andesite (sample 08-Bu-30); (b) plagioclase-hornblende-pyroxene-phyric andesite with weak pervasive potassic (orthoclase) alteration (sample 08-Bu-76); (c) mafic xenolith in weakly propylitized plagioclase-hornblende-phyric andesite (sample 09-Bu-205); (d) mafic xenolith in andesite: note thin epidote rims around xenolith and large hornblende phenocrysts in andesite. (e) plagioclase-augite-biotite-phyric andesite (sample 08-Bu-72); (f) plagioclase-hornblende-augite-phyric andesite, trachytic texture (sample 09-Bu-242); (g) plagioclase-hornblende-phyric andesite (sample 09-Bu-205); (h) plagioclase-hornblende-augite-phyric andesite: note thin oxidation rims and rounded augite crystals edges (sample 09-Bu-234). Abbreviations: Ap = apatite, Aug = augite, Bi = biotite, Chl = chlorite, Ep = epidote, Hbl = hornblende, Mag = magnetite, Or = orthoclase, Plag = plagioclase, Xn = xenolith.

locally rounded and do not appear to be in equilibrium with the magma (Fig. 6-5 h). From these observations, the pyroxene-phyric andesite seems to be slightly older than its hornblende-phyric counterpart. Plagioclase-only andesites, on the other hand, are typically seen as late dikes intruding the other andesite facies and exhibiting a well-developed trachytic texture. Trachytic textures are also locally weakly to moderately developed in augite and hornblende-bearing facies (Fig. 6-5 f), indicating flow movements.

Based on the shape and thickness of the Buriticá andesite porphyry body, it is interpreted to be an intrusive unit. Porphyritic texture and microcrystalline groundmass indicate rapid cooling, suggesting that the intrusion was emplaced at a shallow level. According to Álvarez and González (1978) and González (2001), the eastern Buriticá andesite porphyry–Barroso Formation contact is faulted and marks the location of the Tonusco fault. However, no evidence was seen during this study to corroborate this interpretation.

6.3. Breccia

A breccia body called Yaragua breccia is associated with the Buriticá andesite porphyry intrusion (Fig. 6-1). The contact between the massive andesite unit and the breccia unit is transitional. Strong brecciation of the Buriticá andesite porphyry host rock suggests a high-energy magma injection.

The Yaragua breccia is mainly a matrix-supported polymictic breccia, but is locally clast-supported. The breccia contains sub-angular to sub-rounded clasts of all lithologies found in the area (i.e., basalt, chert, diorite/tonalite, and andesite) set in an andesitic matrix (Fig. 6-6). Lobate andesitic clasts are also commonly observed, indicating that they were still hot when the breccia was formed. Clast percentage ranges from 50% to 90%. Average clast size typically ranges from 1 cm to 5 cm, but clasts locally range up to 20 or 25 cm. Outcrop-scale chert blocks were also seen in the Yaragua breccia zone, inside the Buriticá andesite porphyry

body. Clasts are locally aligned along a preferential orientation when observed in drill holes, but the orientation could not be measured because the core is not oriented. This indicates mobilization of the clasts during the brecciation process. According to the nomenclature proposed by Wright and Bowes (1963), the Yaragua breccia is interpreted to be an alloclastic, intrusive breccia.

The size and geometry of the Yaragua breccia body are not well constrained due to a lack of surface exposure. It was mapped at the surface approximately 300 m to the southwest of the mine site in a dry creek bed at an altitude of around 1675 m, and in the southwest part of the underground mine at an altitude of 1484 m. Assuming the breccia observed underground is connected to the breccia seen at the surface, the breccia body is at least 200 m thick and between 100 m and 200 m in diameter.

The Yaragua breccia is typically more altered than the competent

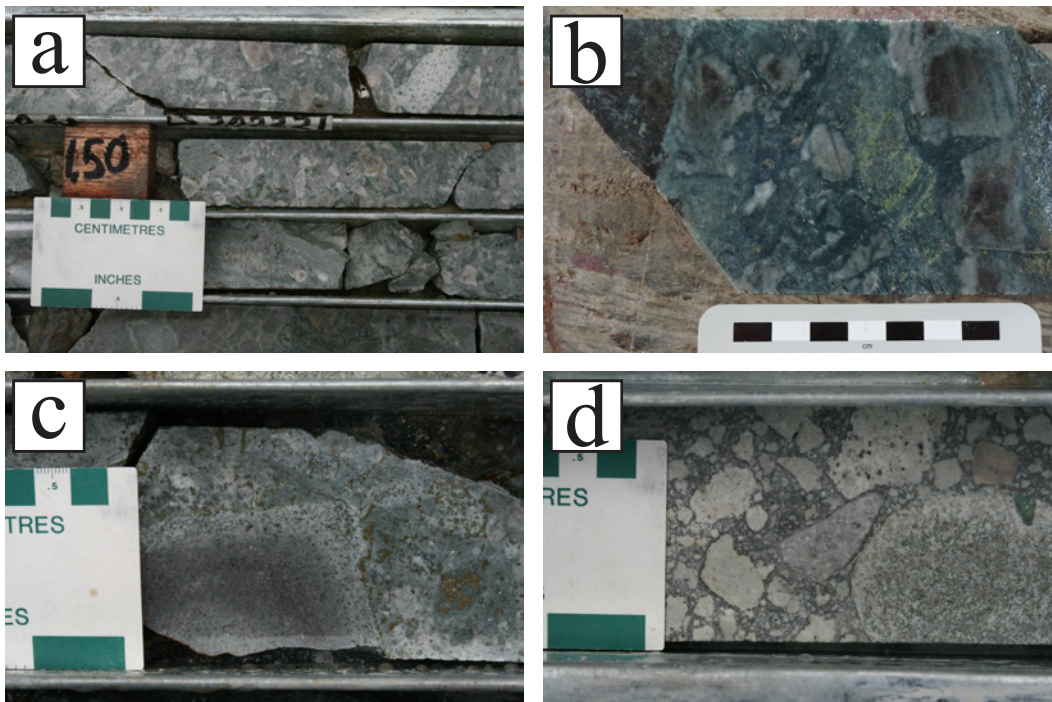


Figure 6-6. Yaragua breccia lithologies in hand specimen: (a) matrix-supported polymictic breccia with andesitic matrix, lobate clasts and preferential alteration of clasts; note alignment of clasts in the upper part of the photo; (b) chert clasts in breccia showing parallel laminations and weak epidote alteration; (c) andesitic clast in breccia with altered edges; sulfides occur in the matrix and in altered clasts; (d) multiple clast lithologies, with strong preferential phyllic alteration of clasts.

surrounding rocks, and generally contains disseminated sulfides, sulfide-rimmed clasts, and gold grades ranging from 0.2 g/t Au to 1.2 g/t Au in the lower grade zones, locally going up to 4.0 g/t Au (Bargmann and Dominy, 2009).

6.4. Alteration

Multiple alteration assemblages can be observed in the vicinity of the Buriticá gold deposit. The oldest and highest temperature alteration observed is a weak potassic alteration associated with the first andesite porphyry intrusion stages. It affects both the tonalitic rocks of the Buriticá stock and the plagioclase-augite-biotite-phyric and plagioclase-augite-phyric facies of the Buriticá andesite porphyry. It is characterized by orthoclase±magnetite±quartz stringers and thin veins in strongly propylitized rocks (Fig. 6-7 a), and locally by medium- to fine-grained poikilitic orthoclase in the rock's groundmass representing up to 15% of the rock (Fig. 6-8 a). Hydrothermal biotite is sometimes present, generally in rocks that already contain magmatic biotite. When present, hydrothermal biotite is fine- to very fine-grained, shreddy and anhedral, and typically represents less than 4% of the altered rock (Fig. 6-8 b). Unlike magmatic biotite, which is euhedral to subhedral and strongly pleochroic from light beige to dark brown, hydrothermal biotite is dark brown and weakly to non pleochroic.

Further away from the intrusion, a chlorite-rich propylitic alteration broadly coeval with potassic alteration is observed. It is marked by strong chlorite alteration of mafic minerals (up to 15% of the rock) and weak to no epidote or carbonate alteration (Fig. 6-8 c and d). Both potassic and propylitic alteration facies are associated with abundant magnetite crystallization (Fig. 6-7 a and b), and with small amounts of sulfides such as pyrite and chalcopyrite, appearing late in the paragenesis. Magnetite crystals are euhedral to subhedral and fine- to very fine-grained, and are either disseminated throughout the rock or located along stockwork veinlets. The country rock was locally highly fractured by the

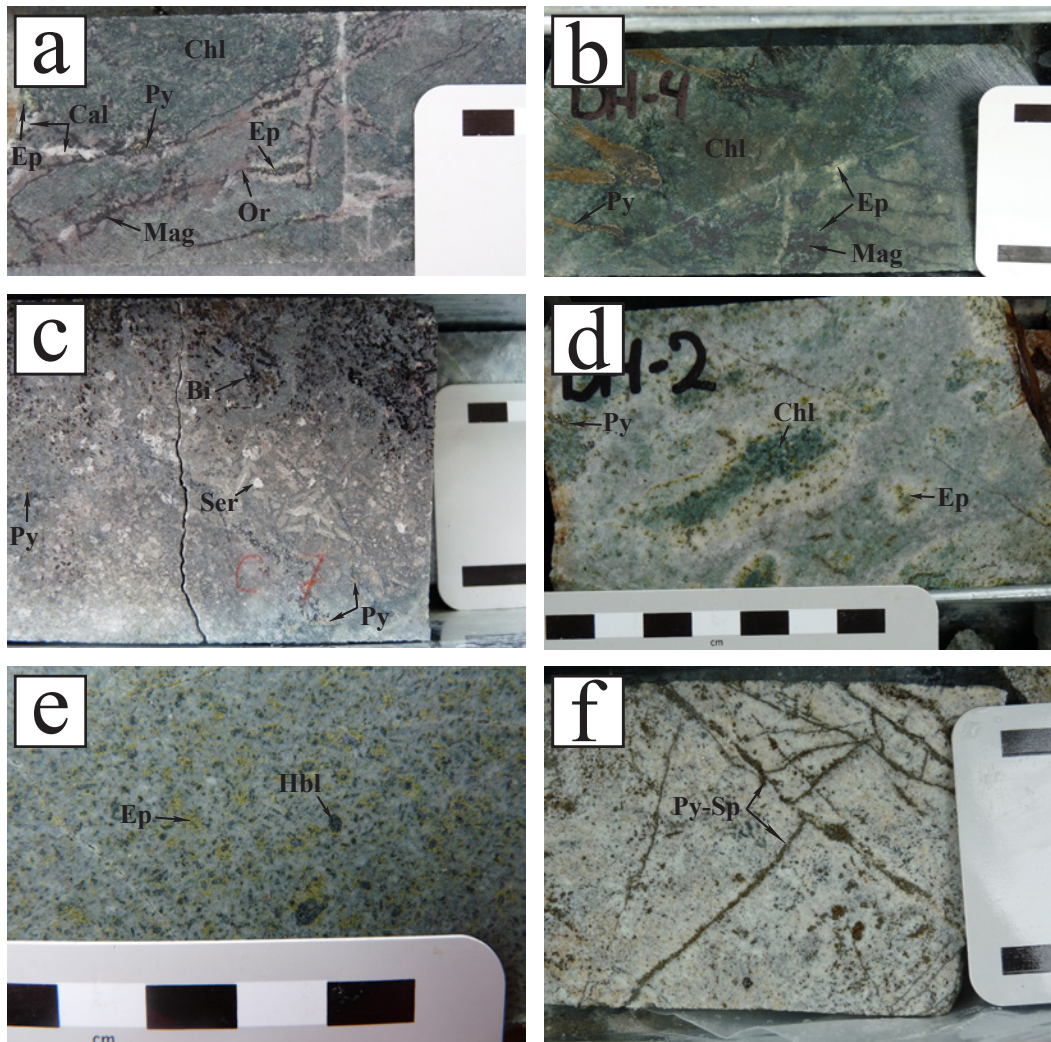


Figure 6-7. Alteration facies in the Buriticá stock and andesite porphyry in hand specimen. (a) strong chlorite alteration and weak epidote alteration in andesite porphyry, orthoclase-magnetite stockwork veinlets, late calcite filling porosity; (b) strong chlorite alteration and weak epidote alteration in andesite, and magnetite-pyrite stockwork veinlets; (c) sericite replacing magmatic biotite, and disseminated pyrite; (d) adularia-sericite alteration overprinting chlorite-rich propylitic alteration in andesite; note epidote-rich zone at the interface between the two alteration facies; (e) moderate adularia-sericite alteration overprinting propylitic (epidote) alteration in andesite; (f) strong adularia-sericite-argillic alteration in andesite, abundant pyrite and sphalerite disseminated throughout the rock and along fractures (sample 09-DH-3). Abbreviations: Bi = biotite, Cal = calcite, Chl = chlorite, Ep = epidote, Hbl = hornblende, Mag = magnetite, Or = orthoclase, Py = pyrite, Ser = sericite, Sp = sphalerite.

hydrothermal fluids and formed a magnetite-cemented breccia. This magnetite breccia, observed only in drill holes, is clast-supported and monomictic, and does not appear to be related to the Yaragua breccia. A few samples from the Buriticá stock and from the Buriticá andesite porphyry have fine-grained disseminated pyrrhotite instead of having magnetite in association with the propylitic alteration.

These two alteration assemblages are not related to any known

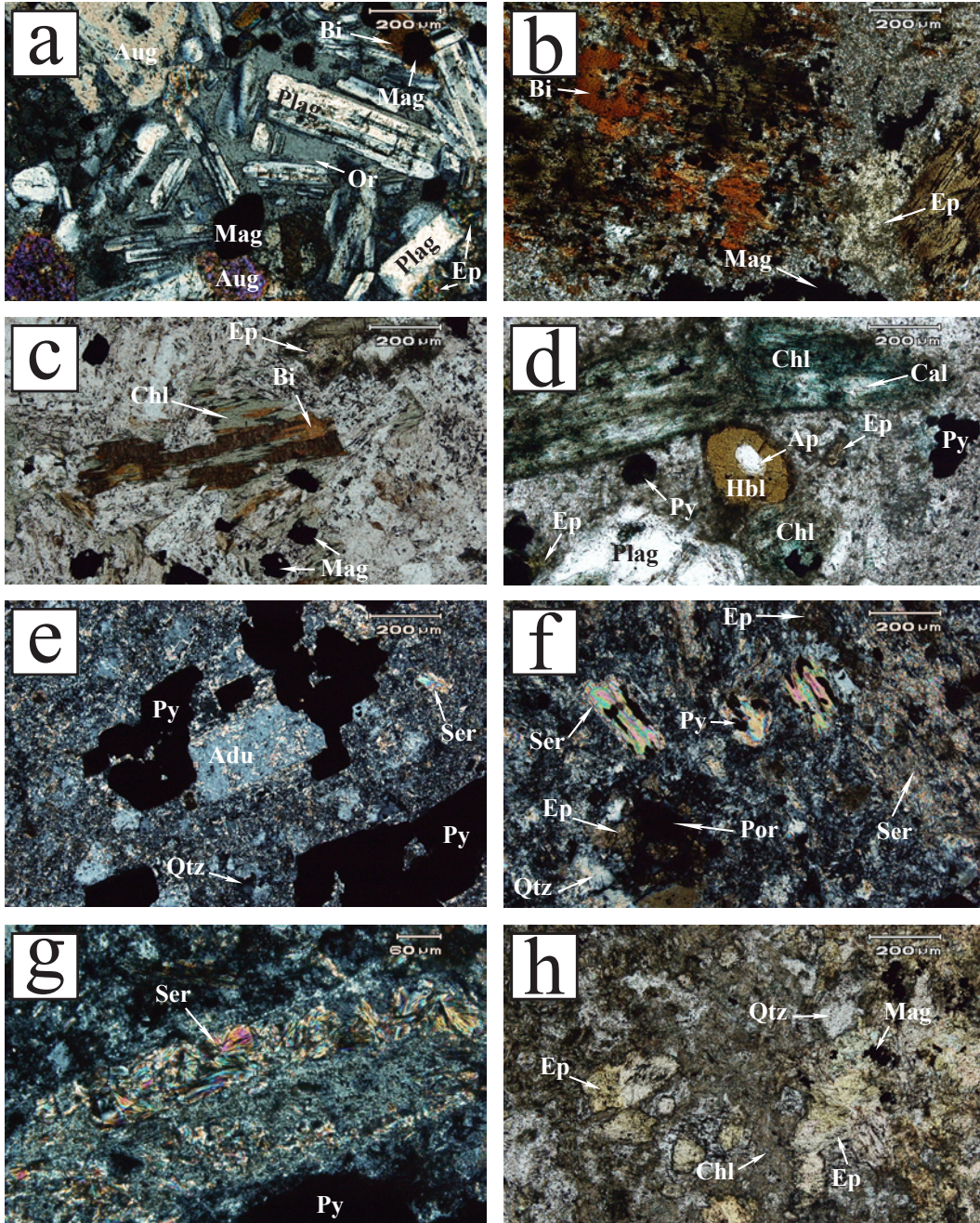


Figure 6-8. Alteration facies in the Buriticá stock and andesite porphyry in thin section (a, e, f, and g: cross-polarized transmitted light; b, c, d, and h: plane-polarized transmitted light): (a) potassic alteration: poikilitic orthoclase crystals, magnetite and secondary biotite (sample 08-Bu-8); (b) potassic alteration: secondary biotite, magnetite, and minor epidote (sample 08-Bu-74); (c) propylitic alteration: chlorite replacement of primary biotite, minor epidote and magnetite (sample 08-Bu-97); (d) propylitic alteration: chlorite-calcite replacement of augite, minor epidote and pyrite (sample 09-Bu-242); (e) adularia-sericite alteration within centimeters of a mineralized vein: euhedral adularia with sericite inclusions, quartz filling porosity and abundant pyrite (sample 09-M-1); (f) adularia-sericite alteration: fine-grained muscovite, very fine sericite and quartz in groundmass, quartz filling porosity and minor epidote (sample 08-Bu-83); (g) adularia-sericite alteration: sericite replacing plagioclase (sample 08-Bu-16); (h) propylitic alteration: abundant epidote, chlorite and quartz, minor magnetite (sample 08-Bu-46). Abbreviations: Adu = adularia, Ap = apatite, Aug = augite, Bi = biotite, Cal = calcite, Chl = chlorite, Ep = epidote, Hbl = hornblende, Mag = magnetite, Or = orthoclase, Plag = plagioclase, Por = porosity, Py = pyrite, Qtz = quartz, Ser = sericite.

mineralization in the Buriticá area, and are likely large-scale alteration related to the Buriticá andesite porphyry intrusive complex. As such, they pre-date the gold mineralization event.

Alteration related to the gold deposit is characterized by proximal adularia-sericite and distal epidote-rich propylitic alteration (Fig. 6-7 c to f). These two alteration styles are believed to represent a chemical gradient away from the veins, with a small overlap at the transition zone between the two styles, where adularia-sericite alteration overprints epidote-rich propylitic alteration (Fig. 6-7 d), indicating that propylitic alteration slightly pre-dates adularia-sericite alteration. It is believed, however, that both of these alteration assemblages are a local effect from the vein fluids, because they are spatially closely related to mineralized structures and are only seen in the Buriticá andesite porphyry and Yaragua breccia units. These two alteration styles locally overprint the potassic and chlorite-rich propylitic alteration mentioned above.

The adularia-sericite alteration is restricted to a few meters around veins and fractures when located in competent rock, but represents the main alteration facies observed in the Yaragua breccia. Stronger and more widespread adularia-sericite alteration occurs in the Yaragua breccia relative to the surrounding competent andesite, likely due to the higher permeability in the breccia, facilitating the flow of hydrothermal fluids. This alteration is characterized by a sericite-adularia-quartz-calcite-dolomite-pyrite-sphalerite assemblage, locally with traces of chalcopyrite and galena.

Within this alteration assemblage, adularia is only found in the most intensely altered zones, whereas sericite is very common even in less altered rocks. When large enough to be identified optically, adularia is fine grained, euhedral, and represents up to 10% to 15% of the rock (Fig. 6-8 e). Adularia has also been identified by X-ray diffraction in some cases where it was too fine

grained to be identified by optical observation. Sericite is commonly observed as inclusions within larger adularia crystals. In addition to occurring as inclusions inside adularia crystals, sericite occurs as microcrystalline elongate crystals in the rock groundmass (Fig. 6-8 e and f), as fine-grained euhedral muscovite crystals up to 0.3 or 0.4 mm long (Fig. 6-8 f), or as plagioclase or biotite replacement (Figs. 6-7 c and 6-8 g). Base metal sulfides occur as subhedral, medium- to very fine-grained disseminated crystals and as fracture filling (Fig. 6-7 h).

Strongly sericite-altered rocks have lost all primary textures, and have been extensively leached with resultant increase of porosity, which was later filled by quartz and carbonates (Fig. 6-8 e and f). Calcite also occurs as a replacement of plagioclase, along with sericite and minor epidote. Quartz and carbonates locally occur as groundmass alteration as well.

X-ray diffraction analysis (XRD) has identified various types of clay minerals such as dickite, kaolinite, and volkonskoite (see Appendix C for detailed XRD results). These clays are interpreted to be supergene minerals, because they are only seen near the surface and within the Yaragua breccia, where permeability is higher. No clays were observed underground, within the mineralized vein adularia-sericite halo.

Distally related to mineralization, propylitic alteration is marked by an epidote-chlorite-calcite-pyrite assemblage, and occurs as either pervasive alteration or mafic mineral replacement. This propylitic alteration is typically not associated with magnetite, and shows less chlorite than epidote (Fig. 6-8 h). However, because the second alteration event (epidote-rich propylitic/adularia-sericite) locally overprints the first alteration event (chlorite-rich propylitic/potassic), rocks sometimes show multiple alteration assemblages.

6.5. Structural setting

This study has outlined several structural features in the Buriticá area

(Appendix D), some of which have a strong control on the Buriticá gold mineralization. An early folding episode has deformed the rocks of the Barroso Formation, as evidenced by asymmetric parasitic folds observed on the north limb of a mudstone lens located to the southeast of the Buriticá andesite porphyry (Fig. 6-9 a). The map pattern and bedding measurements taken throughout the area appear to confirm this folding episode (Figs. 6-1 and 2-13 a). Hinge measurements taken from parasitic folds trend 298° and 277° , and respectively plunge at 58° and 37° . Taking into account that the sediments are younging westward, this would therefore seem to indicate a synclinal fold, gently plunging to the west-northwest, and with its axial plane dipping to the southeast roughly between 40° and 50° (Fig. 6-10 a). No reference to this deformation was found in the literature, but because none of the intrusive bodies in the Buriticá area show evidence of folding, and because the Barroso Formation–Buriticá stock and the Barroso Formation–Sabanalarga batholith contacts are more or less straight, the folding episode likely pre-dates the emplacement of these plutons.

As previously mentioned, the Buriticá area is located very close to the Cauca-Romeral suture zone (CRFS; De Souza et al., 1984; McCourt et al., 1984). Rocks in the area underwent strong faulting and deformation at the time of accretion during the Early Tertiary, and stresses are still active to this day due

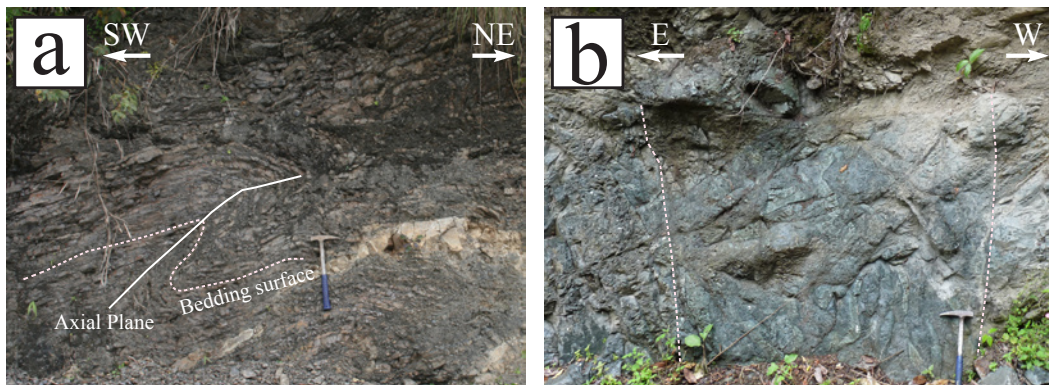


Figure 6-9. Structural features observed in the Buriticá area: (a) parasitic fold observed in mudstone-siltstone (outcrop is vertical and photo is facing to the northwest); (b) meter-scale shear zone containing deformed (elongate) pillow basalt.

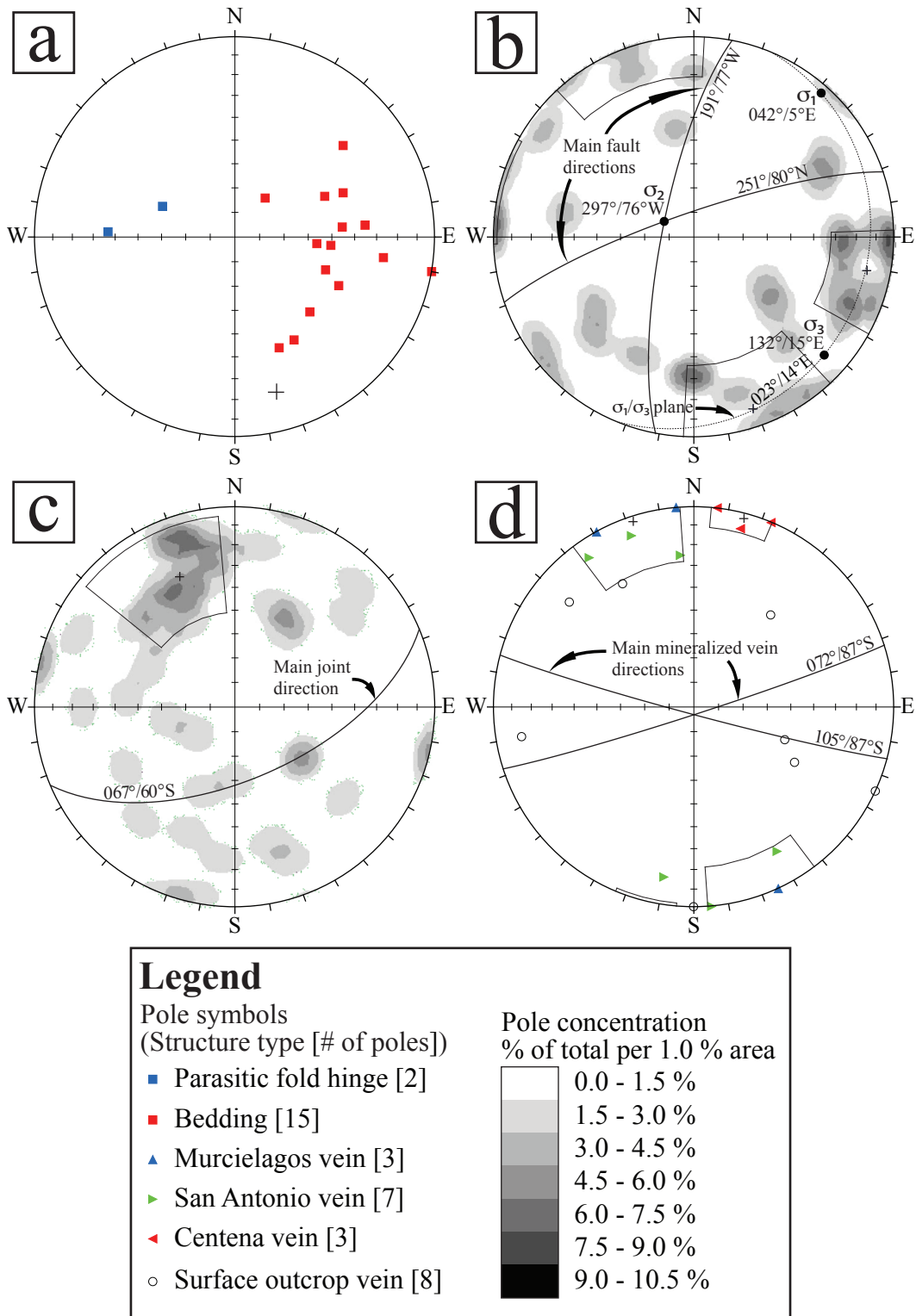


Figure 6-10. Structural data measured in the Buriticá area, plotted on the lower hemisphere of an equal-area stereographic net. (a) bedding poles and parasitic fold hinge; (b) fault pole concentration ($n = 30$), main fault sets and principal stress directions; (c) joint pole concentration ($n = 41$), main joint set direction; (d) mineralized vein poles, main mineralized vein directions. A Fisher distribution was used to plot pole concentration (Fisher, 1953).

to the ongoing plate convergence. Mapping has outlined numerous small, steeply dipping faults and shear zones affecting all the lithologies in the area, which are consistent with young faulting due to the active convergent regime. Two main orientation sets have been identified, respectively striking approximately 191° and 251°, and respectively dipping at 77° to the west and 80° to the north (Fig. 6-10 b). The main 191°-striking fault set is more or less parallel to the Barroso Formation–Sabanalarga batholith contact (Tonusco fault) described earlier, and to the general orientation of the CRFS. Movement along this fault set is dextral strike-slip, which is consistent with the general movement along the CRFS (Ego et al., 1995). The 251°/80°N fault set is interpreted to be conjugate to the main 191°/77°W set. Faults characterizing this conjugate set are typically smaller than those of the north–south set, and display only minor dextral displacement. Deformed basalt pillows have been observed in one of the larger fault zones in the area (Fig. 6-9 b), confirming the transpressive character of the stress regime. Stress directions interpreted from fault orientation (Fig. 6-10 b) indicate near-horizontal southwest-trending σ_1 (042°/5°E) and southeast-trending σ_3 (132°/15°E).

A joint set striking approximately 067°, and dipping 60°S, is associated with the same stress regime (Fig. 6-10 c). The strike and dip of this joint set are fairly similar to those of second main fault set present in the area. The joints are observed in every lithology in the area, although they are better developed in the Barroso Formation than in the other units. This could be due to a rheological difference between the Barroso Formation, the Buriticá stock and Buriticá andesite porphyry, the intrusive rocks being more competent than the rocks of the Barroso Formation.

6.6. Mineralized veins

Known gold mineralization at the Buriticá deposit is hosted in two

different sets of veins with slightly different orientations, respectively striking approximately 072° and 105°, and both dipping to the south between 85° and 90° (Fig. 6-10 d). The largest and most strongly mineralized vein set is the one striking 072°, and includes the San Antonio and Murcielagos veins. In this case too, the strike and dip of this vein set are very close to those of the second major fault set identified in the area. The second vein set, striking 105°, contains the Centena vein (Fig. 4-1). Thicknesses of both vein sets vary locally from 3 cm, up to 20 cm.

6.7. Mineralization Paragenesis

Vein mineralogy is characterized by quartz, calcite, sulfides, and sulfosalts, including chalcopyrite, galena, pyrite, sphalerite, tetrahedrite/tennantite, stibnite, minor native gold and trace amounts of native silver.

Mineral paragenesis has been divided into three different stages (Fig. 6-11). The first stage is a banded quartz-base metal sulfide event characterized by pyrite-chalcopyrite-galena-sphalerite associated with fine grained quartz and trace amounts of tetrahedrite/tennantite, gold and silver. Stage 1 sphalerite shows color banding, with colors from brown to dark yellow. Brown sphalerite

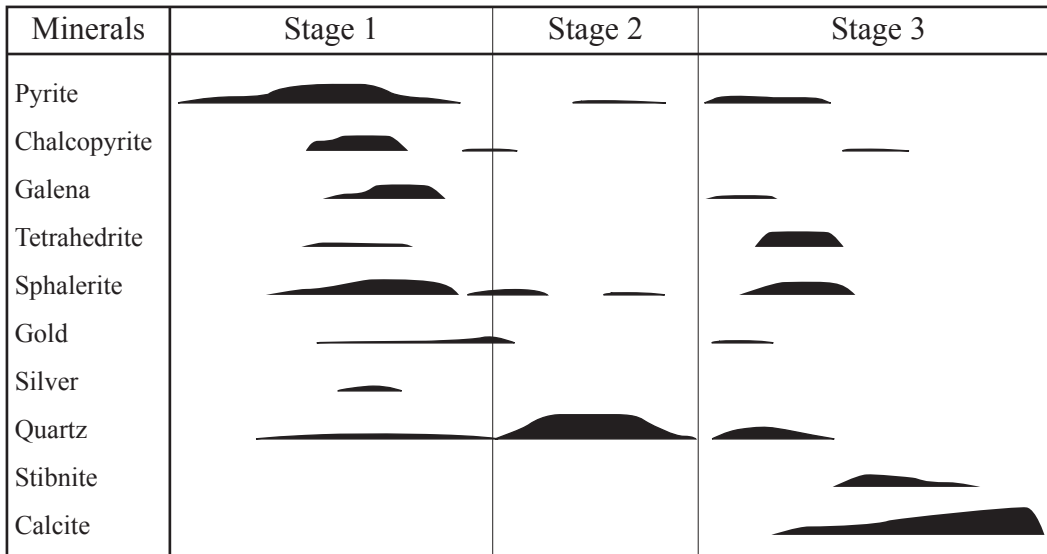


Figure 6-11. Mineralized vein mineral paragenesis.

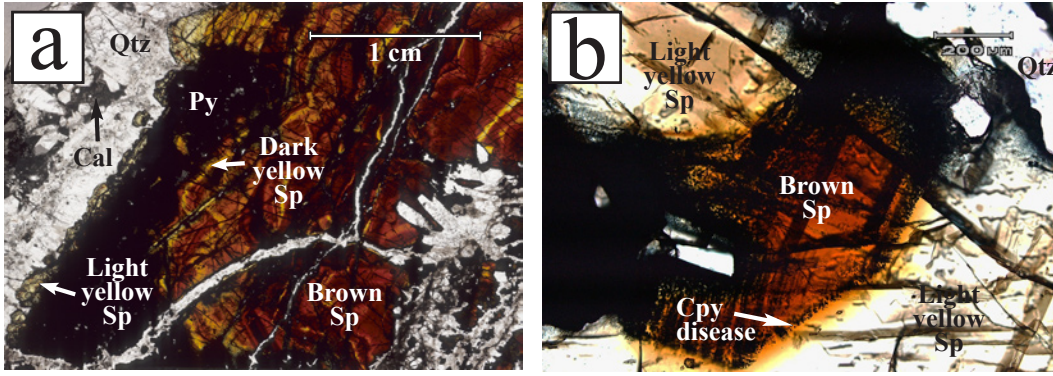


Figure 6-12. Transmitted light photomicrographs of Stage 1 sphalerite crystals showing color zonation from dark brown and yellow to late light yellow sphalerite. Early sphalerite displays more chalcopyrite disease than late sphalerite. Abbreviations: Cal = calcite, Cpy = chalcopyrite, Qtz = quartz, Py = pyrite, Sp = sphalerite.

typically displays strong chalcopyrite disease, whereas it is weaker in dark yellow sphalerite (Fig. 6-12 b). Both sphalerite types are intergrown with galena. After a gap in sphalerite crystallization, light yellow sphalerite formed again towards the end of Stage 1 and continued during Stage 2. Gold mineralization during Stage 1 occurs as fine-grained free gold (average $<300\ \mu\text{m}$, rare millimeter-scale flakes) found between fine-grained quartz crystals, or as inclusions within sulfide minerals (mainly galena, pyrite, and tetrahedrite/tennantite; Figs. 6-13 e and 6-14). Traces of very fine-grained ($<60\ \mu\text{m}$) native silver were deposited during this stage, and are exclusively observed in association with tetrahedrite/tennantite (Fig. 6-14 h).

Stage 2 marks a dramatic decrease in the amount of sulfides, with only pyrite and light yellow sphalerite remaining, and an increase in both quartz grain size and abundance. Quartz from Stage 2 is coarse grained and exhibits vuggy euhedral terminations (Fig. 6-13 c, d, and e); sphalerite is pale yellow and displays various degrees of chalcopyrite disease. Gold is only observed early in this stage, close to the boundary with Stage 1. These first two mineralization stages are particularly well developed in the San Antonio and in the Murcielagos veins.

The third mineralization stage is a calcite-rich event showing brecciation

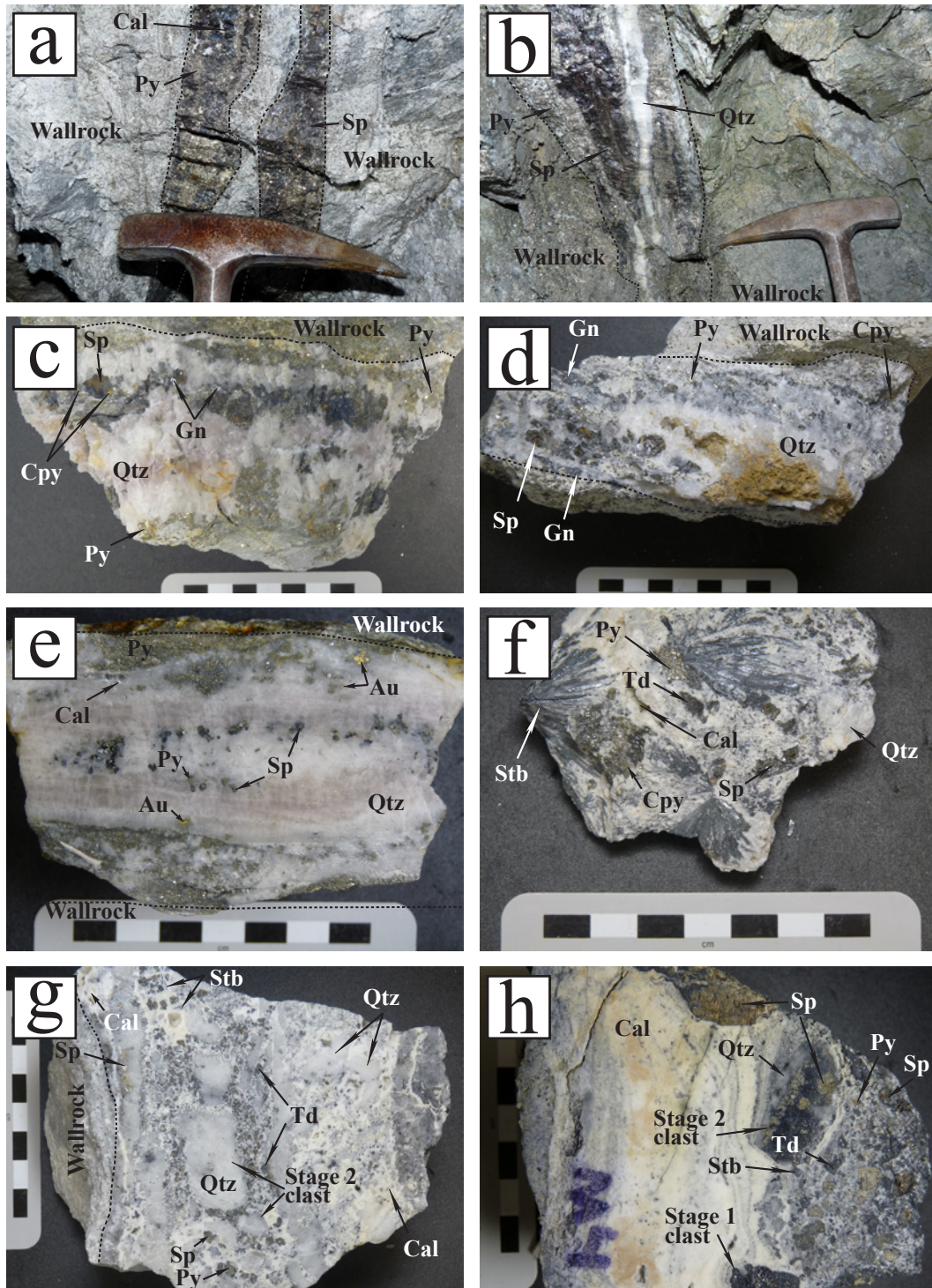


Figure 6-13. San Antonio vein in hand specimen: (a) Yaragua mine level 1; (b) Yaragua mine level 1; (c) well developed quartz-sulfide banding showing Stage 2 coarse-grained quartz in the vein center (sample 09-M-12); (d) well developed banding, vuggy quartz in the vein center (sample 09-M-1); (e) well developed quartz-sulfide banding, early gold associated with fine grained quartz close to vein edges (sample 09-M-13). Centena vein: (f) abundant coarse-grained stibnite, tetrahedrite/tennantite, pyrite and sphalerite in a calcite-quartz matrix (sample 09-M-3); (g) brecciated quartz-sulfide clasts from Stage 2 in a Stage 3 matrix (sample 09-M-3); (h) brecciated quartz-sulfide clasts from Stage 1 and 2 to the right, late banded calcite to the left (sample 09-M-4). Abbreviations: Au = native gold, Cal = calcite, Cpy = chalcocopyrite, Gn = galena, Py = pyrite, Qtz = quartz, Sp = sphalerite, Stb = stibnite, Td = tetrahedrite.

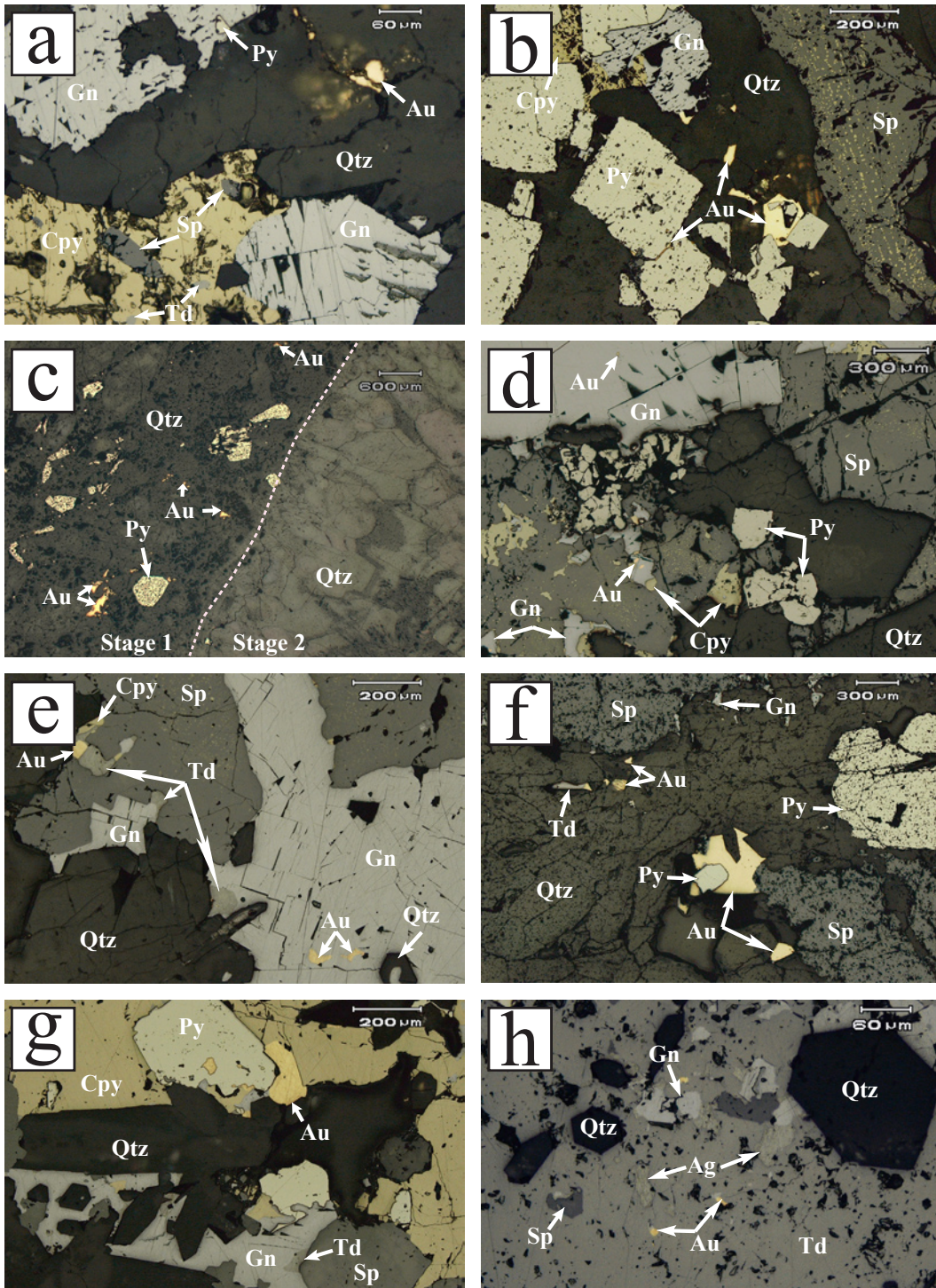


Figure 6-14. Stage 1 and Stage 2 vein minerals in thin section (plane-polarized reflected light): (a) native gold hosted in fine grained quartz (sample 09-M-12); (b) native gold hosted in fine grained quartz and intergrown with pyrite (sample 09-M-12); (c) native gold associated with fine grained Stage 1 quartz; coarse-grained Stage 2 quartz is barren (sample 09-M-13); (d) native gold intergrown with galena (sample 09-GL-2); (e) native gold intergrown with galena and tetrahedrite/tennantite (sample 09-M-14); (f) native gold intergrown with pyrite and tetrahedrite/tennantite (sample 09-M-14); (g) native gold intergrown with pyrite (sample 09-M-14); (h) native gold and native silver intergrown with tetrahedrite/tennantite (sample 09-M-14). Abbreviations: Ag = native silver, Au = native gold, Cpy = chalcopyrite, Gn = galena, Py = pyrite, Qtz = quartz, Sp = sphalerite, Td = tetrahedrite.

textures, and is characterized by an early pyrite-sphalerite-galena-quartz assemblage with trace amounts of gold. Early sulfides are fine to medium grained and subhedral, and intergrown quartz is fine grained and euhedral. Quartz, galena, and pyrite display strong intergrowth textures (Fig. 6-13 g and h), confirming their co-crystallization. This third stage is also characterized by an abundance of antimony-rich minerals (i.e., tetrahedrite/tennantite and stibnite; Fig. 6-15). Pyrite, galena, light yellow sphalerite, tetrahedrite-tennantite, and quartz were co-crystallizing during this stage, although pyrite, galena and quartz started forming a little before the others. Trace amounts of chalcopyrite are found thinly rimming tetrahedrite/tennantite and sphalerite crystals, and Stage 3 sphalerite displays weak to moderate chalcopyrite disease (Fig. 6-15 e and f). Coarse-grained individual stibnite crystals are observed, as well as microcrystalline stibnite needles clustered around galena crystals. Microcrystalline stibnite crystals post-date quartz crystals, and co-crystallized with the calcite matrix (Fig. 6-15 f). Stage 3 minerals are hosted in a very fine-grained calcite matrix, which also contains sphalerite-rich quartz-sulfide clasts, likely broken pieces of Stage 1 and Stage 2 (Fig. 6-15 g and h). The end of Stage 3 is marked by precipitation of microcrystalline calcite bands (Fig. 6-13 h).

Gold in stage 3 occurs as fine-grained free gold (<300 μm), intergrown with early galena (Fig. 6-15 d). This mineralization stage is particularly well developed in the Centena vein, although it is locally seen in both the San Antonio and Murcielagos veins. Recent drilling shows that this stage is also well developed with high-grade mineralization to the southwest of the studied veins, in the Veta Sur area.

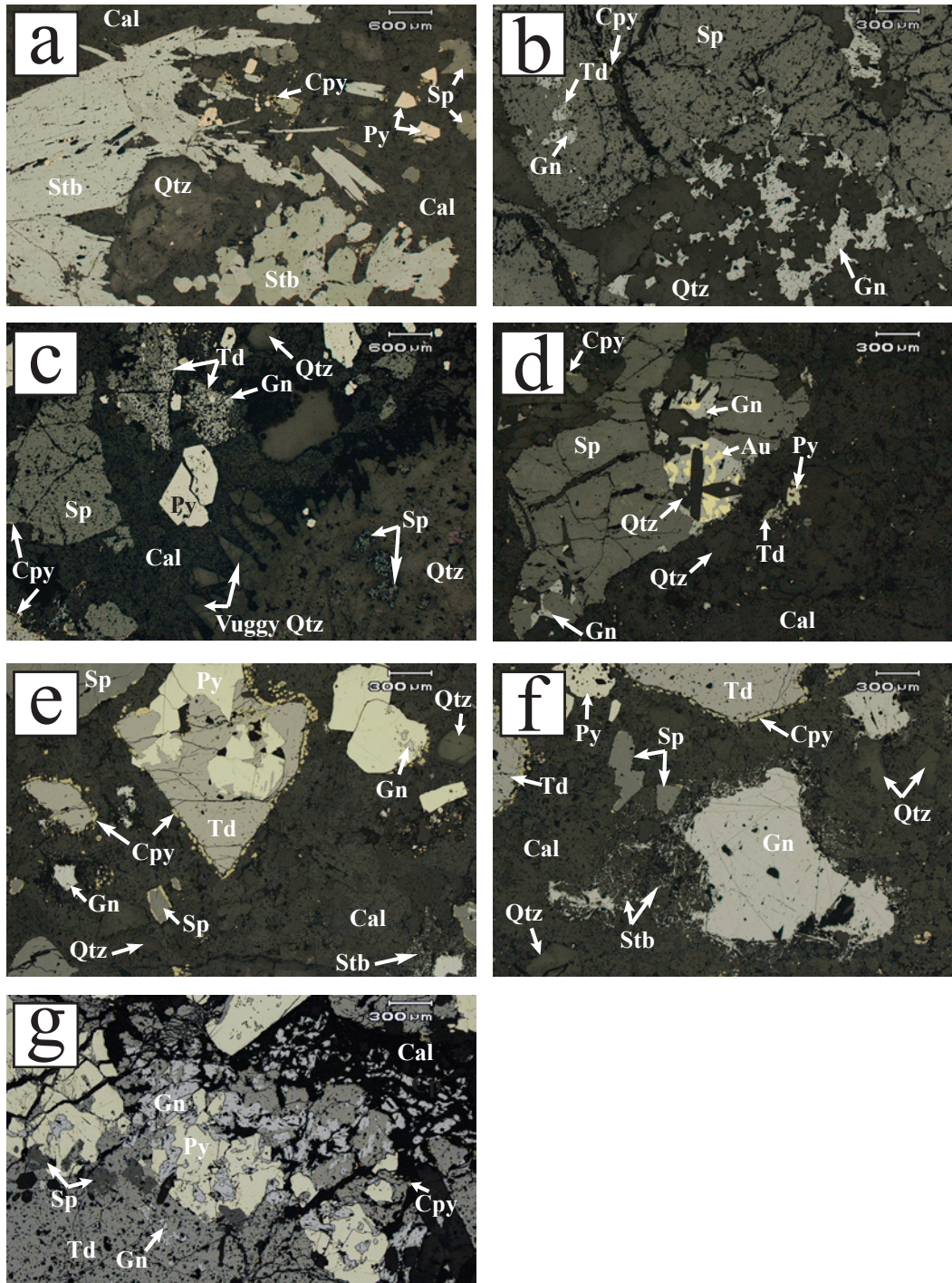


Figure 6-15. Stage 3 vein minerals in thin section (plane-polarized reflected light): (a) coarse grained stibnite, pyrite, sphalerite and quartz in a calcite matrix (sample 09-M-3); (b) early quartz, galena and tetrahedrite/tennantite intergrown, late sphalerite and chalcopyrite (sample 09-M-4); (c) vuggy quartz in the center of the photo, dividing quartz-sulfide filling to the right from calcite-sulfide filling to the left (sample 09-M-3); (d) native gold intergrown with galena and quartz, surrounded by sphalerite and in a calcite matrix (sample 09-M-4); (e) chalcopyrite rims around tetrahedrite/tennantite and sphalerite (sample 09-M-4); (f) very fine grained stibnite needles growing in a calcite matrix and surrounding a galena crystal (sample 09-M-4); (g) tetrahedrite/tennantite, pyrite, and sphalerite intergrown, with late chalcopyrite and calcite (sample 09-M-4). Abbreviations: Au = native gold, Cal = calcite, Cpy = chalcopyrite, Gn = galena, Py = pyrite, Qtz = quartz, Sp = sphalerite, Stb = stibnite, Td = tetrahedrite.

7. Analytical Methods

7.1. X-ray diffraction methods

A set of eleven clay-altered samples were analyzed by Diane Caird, at the X-Ray Diffraction Laboratory of the University of Alberta, to identify which minerals are present when optical identification was too difficult or impossible. The samples were powdered, and analyzed with a Rigaku Geigerflex Powder Diffractometer with a Co tube and a graphite monochromator. Diffraction patterns were matched to specific minerals using the Joint Committee on Powder Diffraction Standards (JCPDS) database published by the International Center for Diffraction Data (ICDD). See Appendix C for detailed results.

7.2. Lithochemical methods

Lithochemical analyses were completed at Activation Laboratories Ltd. in Ancaster, Ontario. A suite of thirty-three samples was chosen, representative of the various igneous rocks present in the Buriticá area. Samples were taken from least altered zones away from mineralization, and from more altered zones related to the vein mineralization, to assess the effects of alteration. Samples were crushed, split, and pulverized with mild steel to a minus 150 mesh. Analytical techniques included fusion-inductively coupled plasma (FUS-ICP) for major elements, and a combination of fusion-mass spectrometry (FUS-MS), fusion-inductively coupled plasma (FUS-ICP), total digestion-inductively coupled plasma (TD-ICP), and instrumental neutron activation analysis (INAA) for trace elements (Actlabs analytical package 4E-Research with ICP-MS). Major elements were analyzed using a 0.2 gram sample material, fused using a lithium metaborate/tetraborate, digested in a 5% nitric acid solution, then analyzed using a Thermo Jarrell-Ash Environ II ICP. For trace elements analyses, samples were either fused, or digested using four acids (hydrofluoric, nitric, perchloric,

and hydrochloric acids), then analyzed using a Perkin Elmer Sciex ELAN 6000, 6100 or 9000 ICP/MS, or a Perkin Elmer Optima 3000 ICP. Samples for INAA consisted of capsules containing an average of 1.5 gram of rock material, irradiated with flux wires at a thermal neutron flux of $7 \times 10^{12} \text{ n cm}^{-2} \text{ s}^{-1}$, and analyzed using a high purity germanium detector after a seven-day decay period. Internal standards, blanks, and duplicates were used for quality control. Results for sample duplicates differ by $<0.5 \text{ wt.}\%$ for major elements and $<1 \text{ ppm}$ for most trace elements. Detection limits are typically in the low ppm to ppb range.

Geochemical diagrams were plotted using Iqpet 2008. For plotting purposes, all major oxide compositions have been normalized to a volatile free basis by normalizing the weight percent values to 100 after subtracting the loss on ignition (LOI) value from the total.

7.3. Geochronology methods

Geochronological analyses were conducted by Dr. Terry Spell, at the Nevada Isotope Geochronology Laboratory, in Las Vegas, Nevada, using a low background MAP215-50 rare gas mass spectrometer, and following a conventional $^{40}\text{Ar}/^{39}\text{Ar}$ step heating method. Hornblende crystals from two fresh intrusive rocks were analyzed to constrain the age of the magmatic events, and sericite crystals from two strongly sericite-altered samples were analyzed to constrain the age of hydrothermal alteration. Samples were crushed using a jaw crusher, and then sieved to obtain the desired size fraction (500 to 1000 μm for hornblende, and 250 to 500 μm for muscovite separation). Amphiboles were further concentrated using bromoform, and a hand magnet was used to remove magnetite from the heavy mineral fraction. Final purification of both hornblende and sericite mineral separates was done by hand picking. Between 50 and 100 micrograms of pure material was separated for each sample.

Samples were irradiated with fast neutrons in a nuclear reactor in order to

convert ^{39}K to ^{39}Ar . They were then heated up to 1400°C over 10 to 14 steps (12 minutes per step) in a high vacuum extraction line using a 20W CO_2 laser, until all gas was released. The age of a sample is calculated using the following equations (Heaman and Ludden, 1991):

$$t = 1/\lambda \cdot \ln[(^{40}\text{Ar}^*/^{39}\text{Ar}) \cdot (J) + 1]$$

and

$$J = (e^{\lambda t_m} - 1) / (^{40}\text{Ar}^*/^{39}\text{Ar})_s$$

Where t is the age of the sample

$\lambda = 5.543 \cdot 10^{-10}$, the total decay constant

$^{40}\text{Ar}^*$ is radiogenic argon

J is a measure of the efficiency of conversion of ^{39}K to ^{39}Ar

t_m is the age of the standard used

$(^{40}\text{Ar}^*/^{39}\text{Ar})_s$ is the ratio measured for the standard

Measurements were corrected for decay during and following irradiation, system blank, atmospheric contamination, and interfering argon isotopes produced by neutron bombardment of Ca and K. Data are reported to $\pm 2\sigma$ uncertainty level.

7.4. Sulfur Isotope Methods

Sulfur isotope analyses were completed by Dr. Stephen Taylor, at the Isotope Science Laboratory of the University of Calgary, Alberta. Isotopic compositions of coeval galena and sphalerite mineral pairs were obtained for six samples from the Murcielagos and San Antonio veins. Samples were crushed by hand, and between 200 and 300 micrograms of homogeneous mineral separates were hand picked. To minimize the risk of inclusions of different sulfides in the hand picked fraction, which would affect the results, only grains smaller than 1 mm were selected. The sulfur isotope ratios ($^{34}\text{S}/^{32}\text{S}$) of the powdered mineral separates were analyzed using a Continuous Flow-Isotope Ratio Mass

Spectrometry (CF-EA-IRMS). Sulfur isotopic ratios were calculated from SO₂ gas produced by combustion of the samples at 1020 °C using a pulse of O₂ gas. Raw isotopic ratios were normalized to the Vienna Canyon Diablo Troilite (VCDT) using the International Atomic Energy Agency (IAEA) S1, S2, and S3 standards. Internal laboratory standards were analyzed every ten samples within each sample set to check for accuracy, which is determined to be ±0.3‰ (1σ).

Precipitation temperatures were calculated from the sulfur isotope fractionation between galena and sphalerite, using the fractionation factor given by Clayton (1981) for temperatures from 100 °C to 600 °C:

$$1000 \cdot \ln \alpha_{\text{gn-sp}} = 0.76 \cdot (10^6/T^2),$$

where α is the fractionation factor, $\alpha = \frac{(S^{34}/S^{32})_{\text{Sp}}}{(S^{34}/S^{32})_{\text{Gn}}}$

and T is the crystallization temperature (in Kelvin).

7.5. Fluid Inclusion methods

Fluid inclusion analyses were undertaken by the author at the University of Alberta. A set of nine gold-bearing vein samples were collected from the Yaragua mine Level 1 (Fig. 4-1). Doubly polished thin sections were prepared at the University of Alberta, and quartz and sphalerite-hosted fluid inclusions from selected chips were analyzed using an Olympus BX50 microscope and a Linkham THMSG600 microthermometric stage. Fluid inclusions were cooled to -150°C, and phase changes were recorded upon reheating until total homogenization temperature (Th) was reached. Sequential freezing (Haynes, 1985) was used when needed to accurately determine temperatures at which phase changes occurred. Calibration was completed before and after the study using pure CO₂ and H₂O standards (Table 7-1). The temperature measurement precision and accuracy is therefore estimated to be ±0.1°C below 0°C,

	Tm _{CO2}	Tm _{ice}	Th _{Crit}
Expected	-56.6°C	0.0°C	374.1°C
Before	-56.6°C	0.1°C	377°C
After	-56.5°C	0.1°C	375°C

Table 7-1. Measured standard data.

$\pm 1^{\circ}\text{C}$ above 100°C , and $\pm 2^{\circ}\text{C}$ above 300°C . An infrared filter was used to prevent heating of the inclusions by the microscope light.

8. Results

8.1. Lithochemistry

Of the 33 samples analyzed for whole rock geochemistry, three samples were from the basalt of the Barroso Formation, one sample was from the Sabanalarga batholith, seven samples were from the medium grained, hornblende-bearing tonalitic facies of the Buriticá stock, four samples were from the glomeroporphyritic, augite-bearing facies of the Buriticá stock, and 18 samples were from the Buriticá andesite porphyry (see Appendix A for sample locations and brief descriptions). Because of the widespread hydrothermal alteration in the area, very few samples were perfectly fresh. Most samples exhibit at minimum a weak propylitic alteration, either from seafloor alteration in the case of the Barroso basalt, or related to the Buriticá andesite porphyry intrusion. A few samples from the Buriticá andesite porphyry show potassic alteration, and some others show adularia-sericite alteration related to gold mineralization. Because alteration strongly modifies the major element chemistry, the most altered samples are identified on the geochemical diagrams to allow for a better petrogenetic interpretation. Geochemical data from igneous rocks of the La Colosa porphyry Au deposit (Gil-Rodriguez, 2010) are plotted in Figures 8-1 to 8-4 for comparison purposes.

The compositions of the igneous rocks of the Buriticá area are plotted on a total alkali-silica classification diagram (Fig. 8-1; Le Bas et al., 1986; Middlemost, 1994). According to this diagram, the Barroso basalts plot in the basalt field, close to the basaltic andesite field (Fig. 8-1 a). The Buriticá stock hornblende-bearing facies plots in the diorite, granodiorite and granite fields,

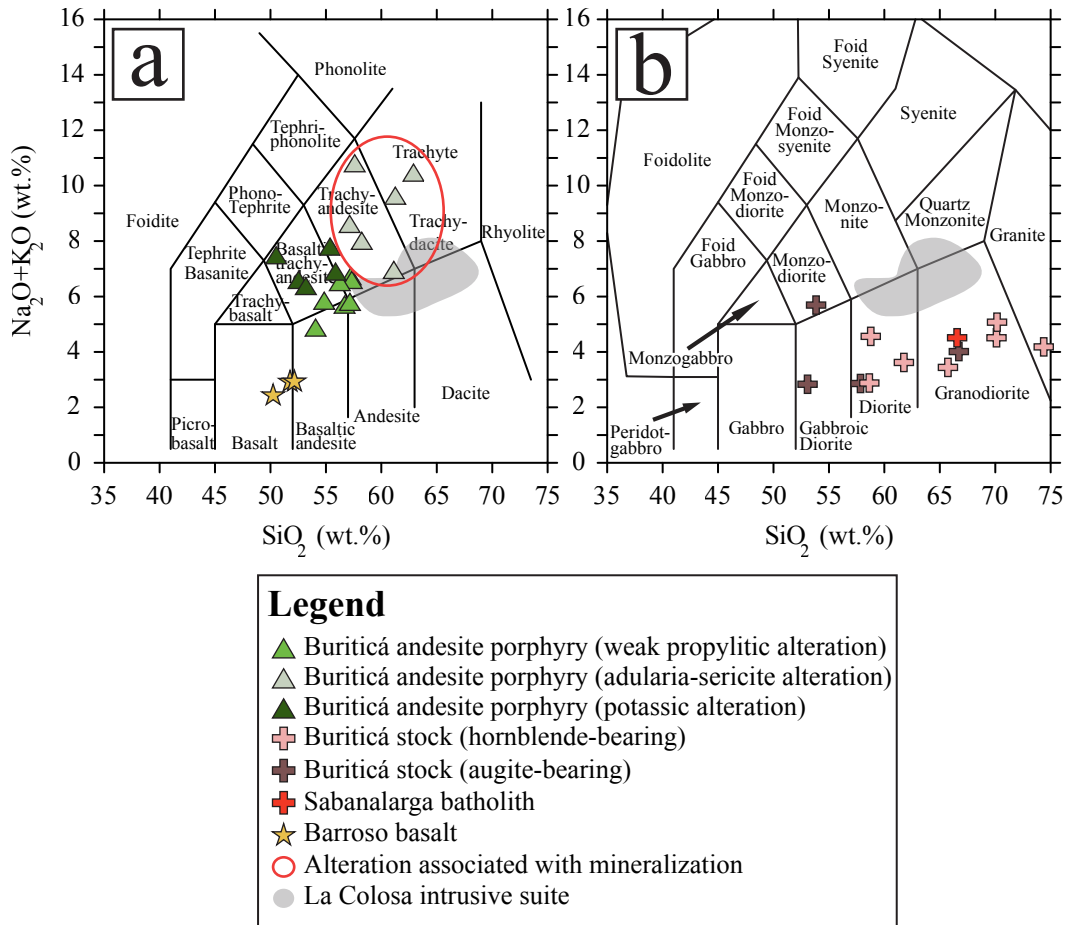


Figure 8-1. Total alkali ($\text{Na}_2\text{O} + \text{K}_2\text{O}$) versus silica diagrams showing the compositions of igneous rocks from the Buriticá area, and using: (a) a volcanic rock classification (LeBas et al., 1986); (b) a plutonic rock classification (Middlemost, 1994). Rocks from the Buriticá andesite porphyry have been plotted according to their alteration style. The compositional range of igneous rocks of the La Colosa deposit is shown in grey (data from Gil-Rodríguez, 2010).

whereas its augite-bearing facies plots in the gabbroic diorite, monzodiorite, diorite and granodiorite fields (Fig. 8-1 b). Weakly propylitized Buriticá andesite porphyry samples straddle the basaltic trachy-andesite, trachy-andesite, basaltic andesite, and andesite fields (Fig. 8-1 a). Potassic alteration distinctly increased the K_2O content of the rocks, but does not appear to have affected the SiO_2 content significantly, whereas rocks showing adularia-sericite alteration appear to have been enriched in both silica and potassium.

Harker diagrams (Fig. 8-2) plot major and minor oxide variations against SiO_2 (wt.%). Two distinct fractionation trends can be identified on these diagrams: one for Barroso basalt and the Buriticá stock, and one for the Buriticá andesite

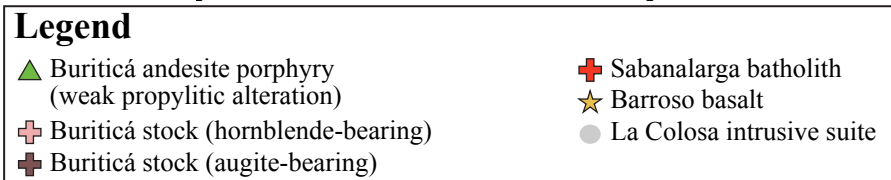
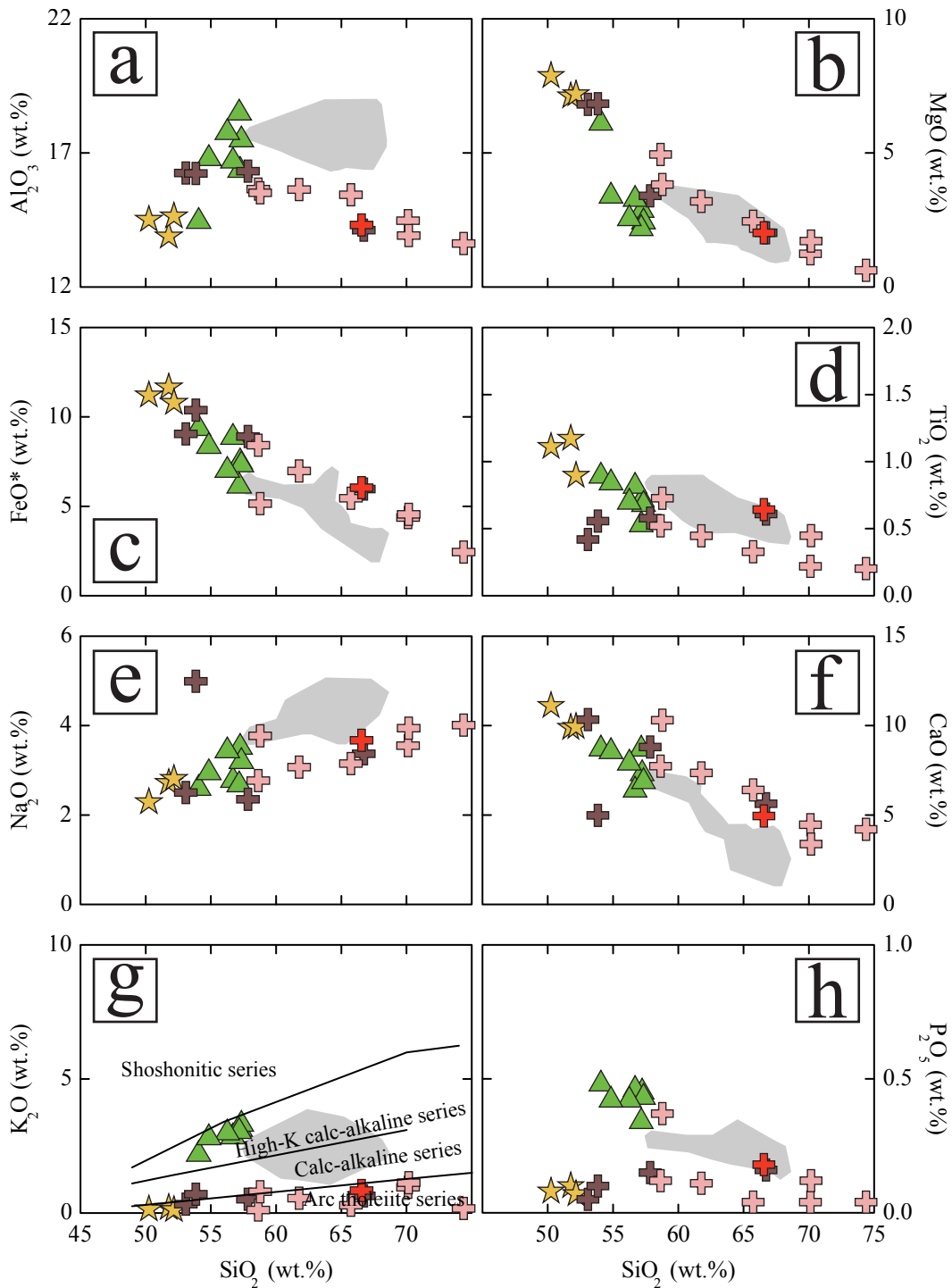


Figure 8-2. Harker diagrams, showing the major oxide variations with silica (SiO₂) content for the igneous rocks present in the Buriticá area. Also shown is the composition range for the igneous rocks of the La Colosa deposit (data from Gil-Rodriguez, 2010). (g) Magmatic series fields from Peccerillo and Taylor (1976).

porphyry. Samples from the Barroso basalt and the Buriticá stock plot in the arc-tholeiitic field, whereas samples from the Buriticá andesite porphyry plot in the high-K calc-alkaline field (Fig. 8-2 g; Iddings, 1892; Peccerillo and Taylor, 1976). Samples from the La Colosa deposit analyzed by Gil-Rodriguez (2010), which were also weakly altered, seem to be on the same trend as the Buriticá andesite porphyry (Figs. 8-1 a and 8-2 g), although they are more evolved and less K-rich.

Trace element data were normalized and plotted on multi-element diagrams for petrogenetic interpretation. All normalized multi-element diagrams were plotted using normalization values from Sun and McDonough (1989). Figures 8-3 and 8-4 respectively show rare earth element (REE) compositions normalized to chondrite concentrations, and trace element compositions normalized to primitive mantle concentrations. Potassic- and adularia-sericite-altered samples are not distinguishable from fresher, weakly propylitized samples on these diagrams, suggesting that alteration has had little effect on trace element concentrations.

In Figure 8-3 a, the Barroso basalt samples show a flat REE pattern, which implies that these are the least evolved of the lithologies found in the area.

The hornblende-bearing facies of the Buriticá stock displays a negative Eu anomaly, indicative of early plagioclase fractional crystallization, because Eu^{2+} substitutes for Ca in calcic plagioclase (Hanson, 1980). Its pattern is slightly depleted in heavy rare earth elements (HREE) relative to light rare earth elements (LREE). The HREE-depleted pattern can be explained by either clinopyroxene and hornblende fractionation during emplacement, or by low degrees of partial melting of a mantle source resulting in higher LREE concentrations. However, assuming that the Barroso basalts and the Buriticá stock are part of the same fractionation trend, hornblende fractionation is the most plausible explanation. HREE depletion over LREE is also visible on the Buriticá andesite porphyry

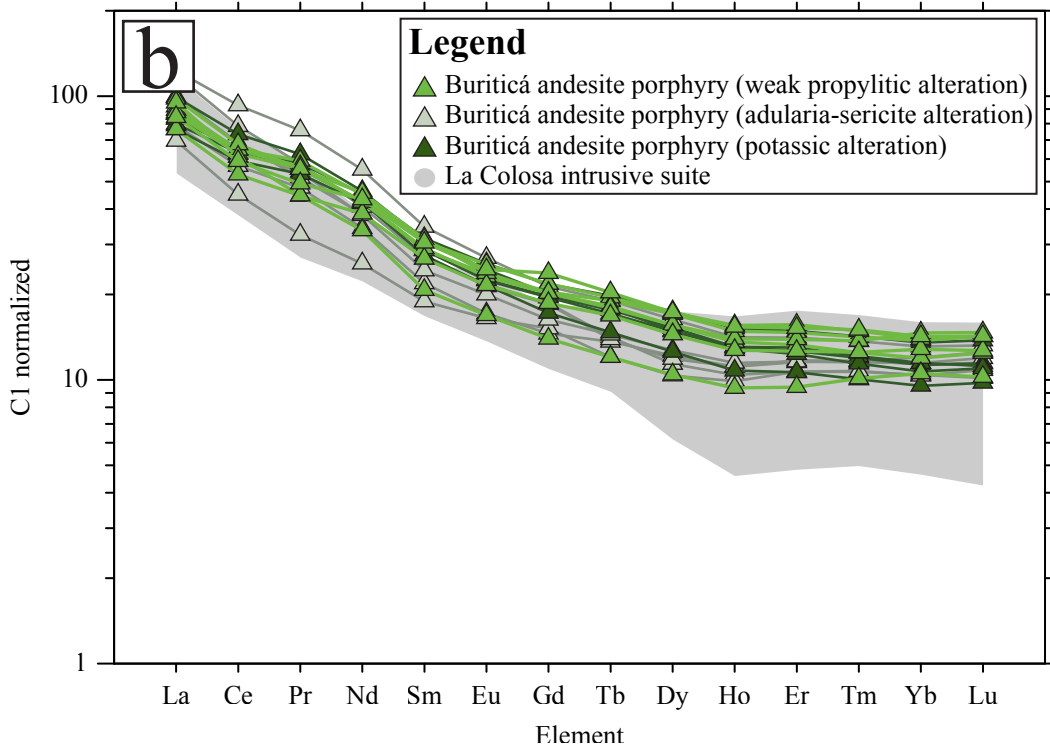
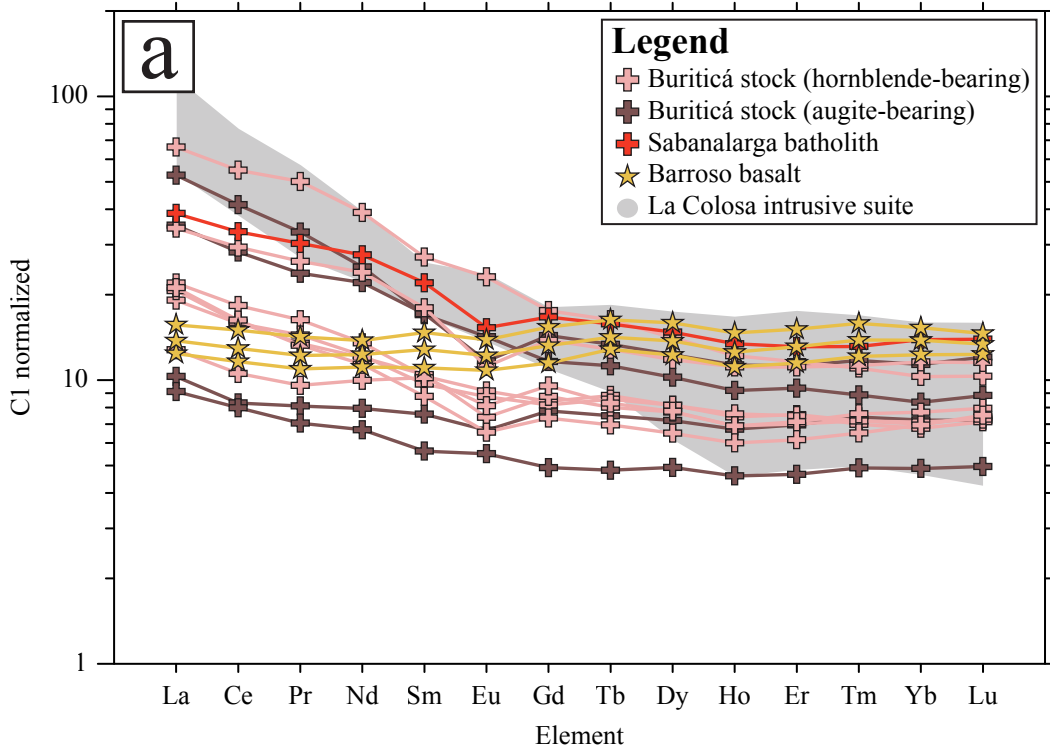


Figure 8-3. Chondrite-normalized REE diagram, showing: (a) profiles for the Barroso basalt, the Sabanalarga batholith, and the Buriticá stock; (b) profiles for the Buriticá andesite porphyry. Also shown in grey is the range of REE compositions for the igneous rocks of the La Colosa deposit (data from Gil-Rodriguez, 2010). C1 normalization values from Sun and McDonough (1989).

pattern.

Of the four samples from the augite-bearing facies of the Buriticá stock, two have relatively flat patterns (samples 09-Bu-172 and 09-Bu-226), and two have patterns similar to the hornblende-bearing facies of the Buriticá stock (samples 08-Bu-85 and 09-Bu-47).

The Buriticá andesite porphyry is more enriched in REE than the other lithologies present in the area, but overlaps the La Colosa compositional range (Fig. 8-3 b). The absence of a Eu anomaly can be explained either by minimal plagioclase fractional crystallization during ascent of the magma, which would be expected from a wet magma such as this one (as evidenced by biotite and hornblende phenocrysts), and/or by an elevated oxygen fugacity (f_{O_2}) in the andesitic magma, which would lead to more Eu^{3+} than Eu^{2+} , and to less Eu substitution in plagioclase. The range of REE patterns from the La Colosa deposit is very similar to that of the Buriticá andesite porphyry, although some samples are more HREE-depleted.

On an extended trace element diagram (Fig. 8-4 a), the Barroso basalts show relatively flat patterns consistent with a primitive arc source. The Sabanalarga batholith and the Buriticá stock, however, display large ion lithophile element (LILE) enrichments and strong negative anomalies for Nb, Ta, and Ti, characteristic of subduction zone magmatism. No Pb data are reported for these rocks because the results were lower than the detection limit (5 ppm).

The Buriticá andesite porphyry trace element patterns are enriched over those of the Buriticá stock, especially in LILE. This likely results from a greater subduction component. Antimony enrichment, although common in subduction-related rocks, is present in unusually high concentrations in the Buriticá stock as well as in the Buriticá andesite porphyry, especially in the most altered samples. Antimony is interpreted to be an important constituent of the hydrothermal fluids

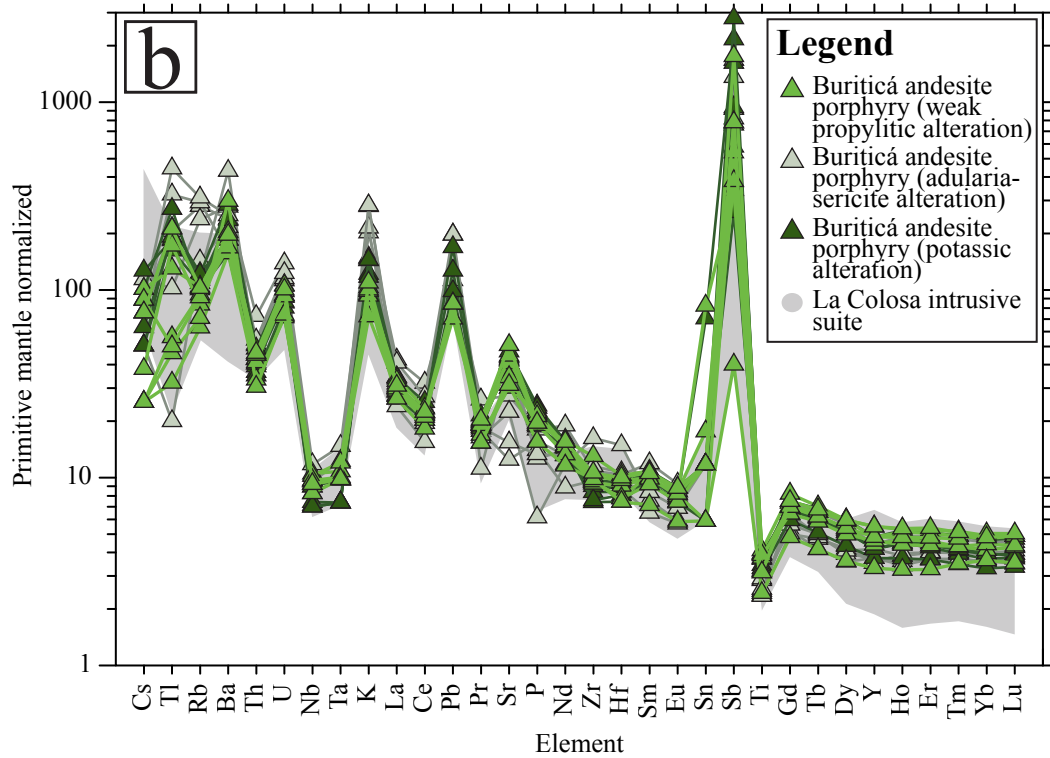
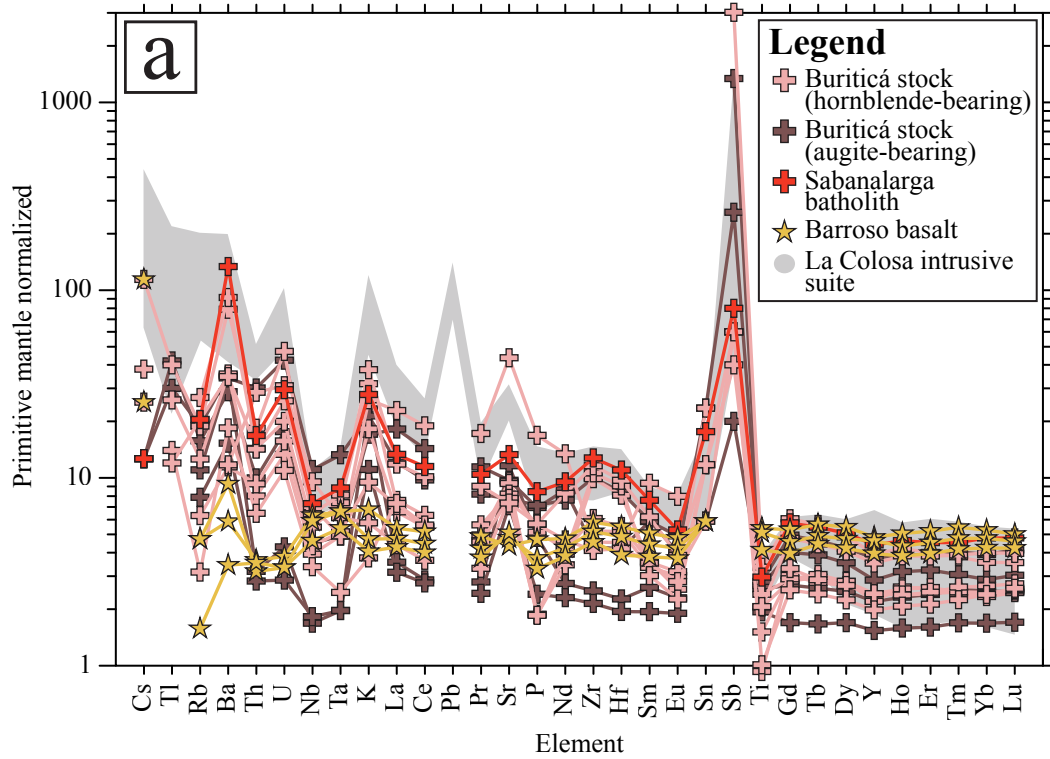


Figure 8-4. Primitive mantle-normalized extended trace element diagram, showing: (a) profiles for the Barroso basalt, the Sabanalarga batholith, and the Buriticá stock; (b) profiles for the Buriticá andesite. Also shown is the range of trace element compositions for igneous rocks from La Colosa deposit (data from Gil-Rodríguez, 2010). See Figure 2-20 for symbol legend. Primitive mantle normalization values from Sun and McDonough (1989).

causing gold mineralization, as evidenced by the large amounts of stibnite in the mineralized veins. The Buriticá andesite porphyry compositions are very similar to those of the La Colosa deposit, except for slightly greater LILE-enrichments in some samples and less HREE-depletion, as noted in Figure 8-3 b.

8.2. Geochronology

Detailed geochronological results are presented in Appendix F. Age spectra obtained from magmatic hornblende are presented in Figure 8-5, those obtained from hydrothermal sericite are presented in Figure 8-6. Plateau ages were determined using a criterion of three or more consecutive steps overlapping in age at the $\pm 2\sigma$ analytical error (95% confidence level), and comprising more than 50% of the total ^{39}Ar released (Fleck et al., 1977). The inverse isochron ages, the number of steps, the initial $^{40}\text{Ar}/^{36}\text{Ar}$ ratio, and the mean square weighted deviates (MSWD) value for each sample are also presented in Figures 8-5 and 8-6 (Roddick, 1978; Dalrymple et al., 1988; Wendt and Carl, 1991).

Analysis of sample 09-Bu-191, hornblende from the Buriticá stock, did not produce a statistically valid plateau or isochron age, and thus no reliable age could be determined (Fig. 8-5 a). The two first steps degassed only about 1% the total ^{39}Ar released, and respectively yielded ages of 465.12 ± 43.02 Ma and 211.71 ± 18.70 Ma. Step nine yielded an age of 85.93 ± 2.10 Ma, representing the youngest of all steps, and is therefore interpreted to be the maximum age for the sample. The spectrum has a mild u-shape, which could suggest that excess argon is present, although the absence of an isochron prevents us from verifying this hypothesis. Assuming there is no excess argon present, the total gas age would be the most reliable age, at 99.0 ± 1.2 Ma. In any case, these data are consistent with the K/Ar age on hornblende previously published by Göbel and Stibane (1979) for the Buriticá stock, at 91.1 ± 6.4 Ma.

Hornblende from sample 09-Bu-205 has been analyzed to determine the

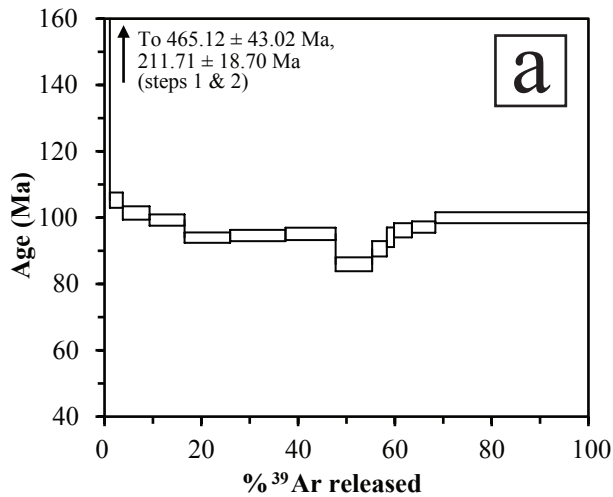
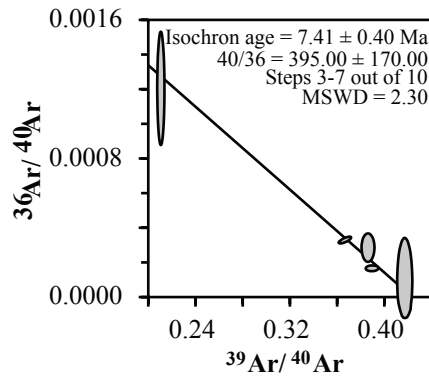
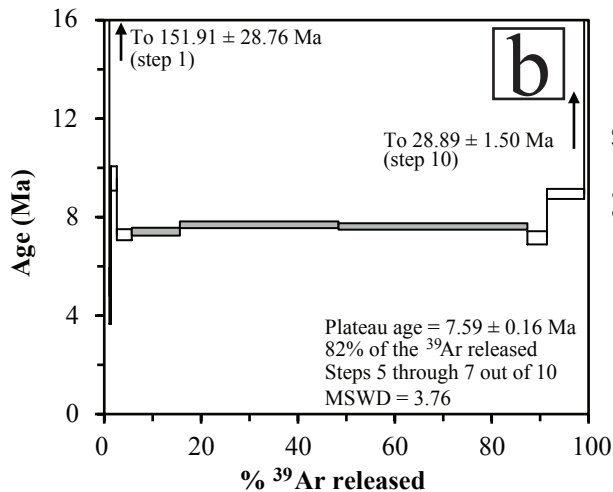


Figure 8-5. Apparent $^{40}\text{Ar}/^{39}\text{Ar}$ age spectra for two samples of igneous hornblende from: (a) the Buriticá stock (sample 09-Bu-191); and (b) the Buriticá andesite porphyry (sample 09-Bu-205). Sample 09-Bu-191 did not yield a valid plateau or isochron age. Sample 09-Bu-205 yielded a poorly defined plateau age; the isochron age is therefore considered more reliable. Complete data are provided in Appendix F.



age of the Buriticá andesite porphyry (Fig. 8-5 b). A plateau age of 7.59 ± 0.16 Ma is defined by steps five through seven, and an isochron age of 7.41 ± 0.40 Ma is defined by steps three through seven. Because the first three and last three steps yield older ages than the plateau (u-shaped spectrum), it is likely that excess argon is present, which is confirmed by the initial $^{40}\text{Ar}/^{36}\text{Ar}$ ratio (395.00 ± 170.00) calculated from the inverse isochron. Because excess argon is present, the isochron age is interpreted as the most reliable. Note also that the MSWD is higher for the plateau age than for the isochron age (respectively, 3.76 and 2.30), which is another indication that the isochron age is more accurate. An isochron is considered statistically valid when its $\text{MSWD} < 2.5$ (Brooks et al., 1972), which is the case here. According to these data, the age of 43.8 ± 4.3 Ma from whole

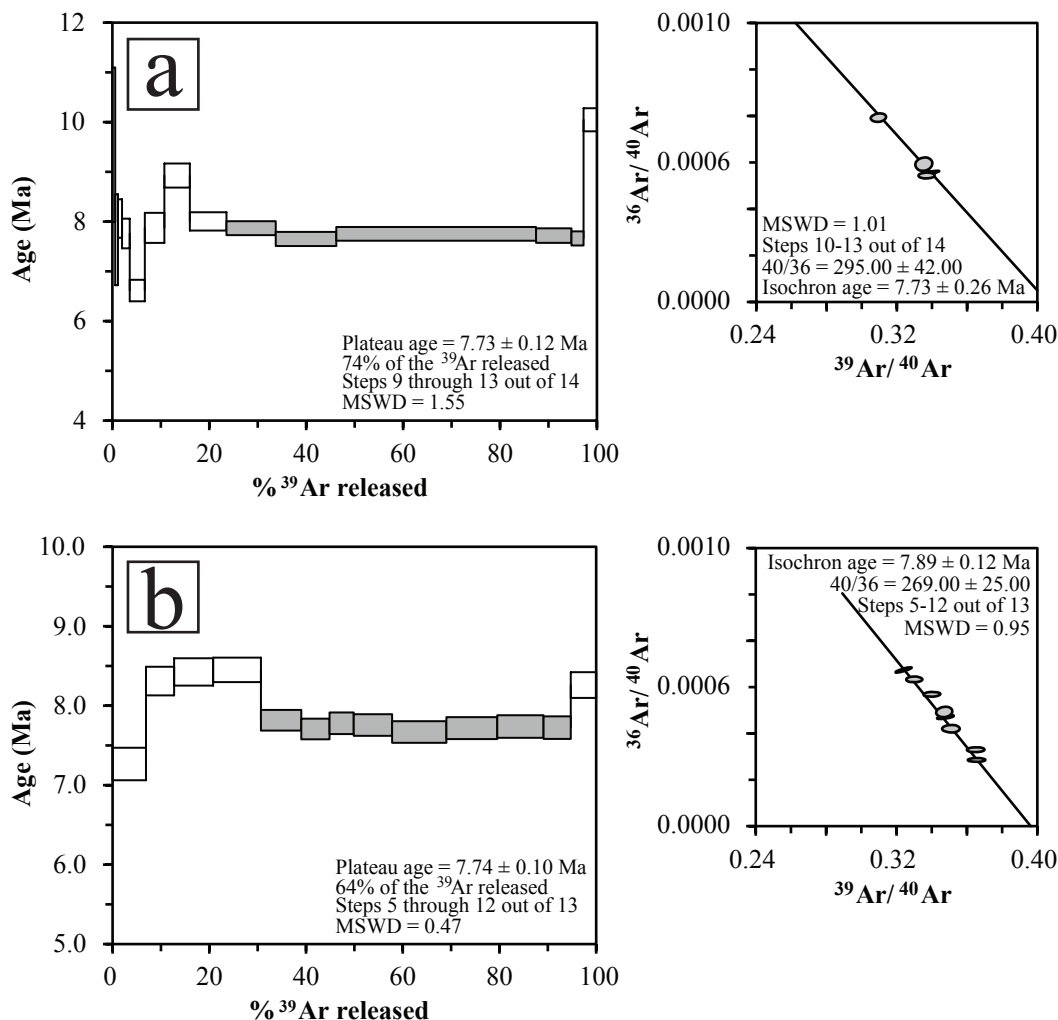


Figure 8-6. Apparent $^{40}\text{Ar}/^{39}\text{Ar}$ age spectra for two samples of hydrothermal sericite from the Buriticá andesite porphyry: (a) sample 08-Bu-16; and (b) sample 08-Bu-83. Sample 08-Bu-16 yielded a poorly defined plateau age, whereas sample 08-Bu-83 yielded a well-defined plateau age. Complete data are provided in Appendix F.

rock K/Ar analysis published by González and Londoño (1998) is wrong, and Castro and Feininger (1965) were right to relate the Buriticá andesite porphyry to the porphyritic rocks in the Titiribí area.

Both samples of sericite from the alteration halo around the mineralized zones yielded similar ages, with well-defined plateaus at 7.73 ± 0.12 Ma and 7.74 ± 0.10 Ma (Fig. 8-6 a and b). Isochron ages are respectively 7.73 ± 0.26 Ma and 7.89 ± 0.12 Ma for the same samples. Spectra shapes and initial $^{40}\text{Ar}/^{36}\text{Ar}$ ratios (295.00 ± 42.00 and 269.00 ± 25.00) confirm that no excess argon is present. A lower initial $^{40}\text{Ar}/^{36}\text{Ar}$ ratio than the atmospheric value for sample 08-Bu-83

($269.00 \pm 25.00 < 295.5$) is unusual and could indicate a partial loss of radiogenic argon (Lanphere and Dalrymple, 1978). In both cases the data points on the isochron plots are tightly distributed, so the plateau ages are considered more reliable. The weighted average calculated from the two plateau gives an age of 7.74 ± 0.08 Ma for hydrothermal alteration. According to these data, the timing of alteration is within error of the timing of magmatism, at 7.41 ± 0.40 Ma.

8.3. Sulfur Isotope Analyses

Sulfur isotopic compositions of sulfide minerals are influenced by a number of factors including pH, oxygen fugacity, sulfur fugacity, and temperature of the solution precipitating the minerals (Ohmoto, 1972). A high oxygen fugacity and a low pH, for example, will both favor ^{32}S over ^{34}S , yielding lower $\delta^{34}\text{S}$.

$\delta^{34}\text{S}$ results and calculated crystallization temperatures for the galena-sphalerite mineral pair are presented in Table 8-1. $\delta^{34}\text{S}$ compositions range from

Sample ID	$\delta^{34}\text{S}$ (‰)	T (°C)
08-GL-2 Gn	-2.1	359 ± 107
08-GL-2 Sp (dark yellow)	-0.2	
09-M-1 Gn	-2.2	419 ± 144
09-M-1 Sp (dark yellow)	-0.6	
09-M-2 Gn	-1.4	385 ± 121
09-M-2 Sp (dark yellow)	0.4	
09-M-8 Gn	-1.9	302 ± 78
09-M-8 Sp (dark yellow)	0.4	
09-M-13 Gn	-2.3	125 ± 25
09-M-13 Sp (brown)	2.5	
09-M-13 Gn	-2.3	338 ± 95
09-M-13 Sp (dark yellow)	-0.2	
09-M-14 Gn	-2.6	113 ± 23
09-M-14 Sp (brown)	2.5	
09-M-14 Gn	-2.6	316 ± 85
09-M-14 Sp (dark yellow)	-0.4	

Table 8-1. Sulfide crystallization temperatures calculated from sulfur isotope fractionation between coeval galena and sphalerite (Gn = galena, Sp = sphalerite).

-2.6 ‰ to -1.4 ‰ for galena, and from -0.6 ‰ to +2.5 ‰ for sphalerite. Although it is impossible to directly determine the source of the sulfur from these data alone, the $\delta^{34}\text{S}$ range is consistent with expected $\delta^{34}\text{S}$ values for sulfides found in porphyry environments, and forming from a mantle source (Ohmoto and Rye, 1979).

The color of sphalerite is controlled by its FeS content, which is a function of temperature, and the sulfur and the oxygen fugacities, which means that the color of sphalerite will likely also be reflected in its sulfur isotopic composition, as is observed in Table 8-1. Dark brown sphalerite from Stage 1 at Buriticá displays abundant chalcopyrite disease and is a great deal more opaque than lighter-colored sphalerite; it therefore likely contains more impurities that could affect its isotopic composition. Based on these observations, yellow sphalerite is considered more reliable as a geothermometer.

Much attention was paid when handpicking sphalerite crystals to discriminate between dark brown and dark yellow sphalerite. Light yellow sphalerite was excluded because it is not coeval with galena. Results show that there is a significant $\delta^{34}\text{S}$ difference between the two sphalerite species, yellow sphalerite having a much lower ^{34}S content than brown sphalerite. According to these results, yellow sphalerite–galena mineral pairs yield crystallization temperatures varying from approximately 300 °C to 420 °C (using the fractionation equation of Clayton, 1981), with an weighted average temperature of 338 ± 80 °C ($n = 6$), whereas brown sphalerite–galena mineral pairs yield temperatures of approximately 110 ± 20 °C and 130 ± 30 °C for the same samples (Table 8-1). The higher temperature set is interpreted to be more reliable for the reasons noted above.

8.4. Fluid Inclusions

A total of 302 quartz- and sphalerite-hosted fluid inclusions from Stage

1 through 3 of the vein paragenesis were analyzed (see Appendix G). Most inclusions found in the samples were primary, although pseudo-secondary and secondary inclusions were also present. Only primary inclusions, typically located within growth zones (Fig. 8-7 a and b), and pseudo-secondary inclusions were analyzed for this study (based on the criteria of Roedder, 1984, and Goldstein, 2003). Regardless of the host mineral, average inclusion size varies between 5 μm and 20 μm . Very few larger inclusions were observed, up to 40 μm . Many of the larger inclusions contain heterogeneously trapped sericite crystals, but no other daughter minerals were observed in any inclusion.

Inclusions that showed evidence of necking or leaking were avoided because they do not represent an isoplethic/isochoric system, which is required for valid microthermometric measurements (Roedder, 1984; Bodnar, 2003). Inclusions located within areas showing recrystallization features (e.g., rounded crystal edges, undulating extinction under cross-polarized light) were also avoided because they have likely experienced post-entrapment modifications and therefore do not represent the original P-T-X conditions. Coarser quartz grains from Stage 2 commonly exhibit secondary inclusions located along fractures that crosscut grain boundaries. These inclusions were not analyzed, because they do not sample the source fluid from which crystals originally formed.

Fluid inclusion assemblages are defined as finely discriminated groups of petrographically associated inclusions, and are composed of inclusions which have all been sealed at the same time (Goldstein and Reynolds, 1994; Goldstein, 2003). Fluid inclusions from the Buriticá deposit belonging to a single fluid inclusion assemblage show relatively constant fluid/vapor phase ratios, with typical liquid-fill percentages ranging from 80% to 90%, indicating that the trapped fluid was homogeneous (Diamond, 2003), and that reequilibration (e.g., necking, stretching, leakage, or refilling) is not likely to have occurred. Evidence

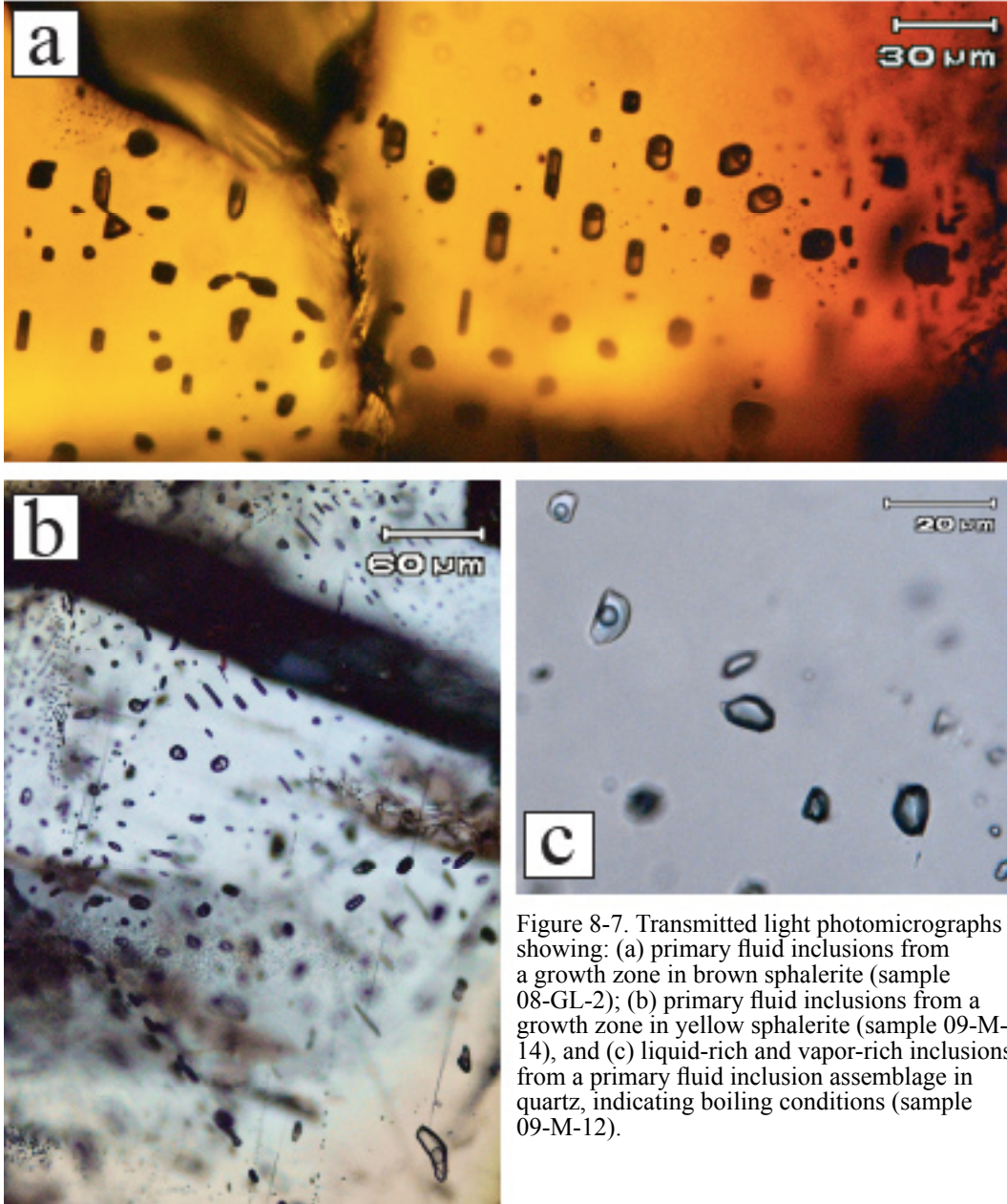


Figure 8-7. Transmitted light photomicrographs showing: (a) primary fluid inclusions from a growth zone in brown sphalerite (sample 08-GL-2); (b) primary fluid inclusions from a growth zone in yellow sphalerite (sample 09-M-14), and (c) liquid-rich and vapor-rich inclusions from a primary fluid inclusion assemblage in quartz, indicating boiling conditions (sample 09-M-12).

of boiling was observed in quartz crystals late during Stage 1 and during Stage 2, as primary vapor-rich inclusions occurring alongside liquid-vapor inclusions in fluid inclusion assemblages (Fig. 8-7 c). Measurements were not performed on most vapor-rich inclusions because it was not possible to precisely determine phase change temperatures. Vapor-rich inclusions were not observed in sphalerite. It is possible, however, that some vapor-rich inclusions were present but were overlooked because they were mistakenly thought to be other types of dark

inclusions such as opaque chalcopyrite.

Of all the analyzed fluid inclusions, only two vapor-rich inclusions from Stage 1 quartz contain a small amount of CO₂, as evidenced by dry ice melting at -56.4°C and -56.3°C respectively. Note that these melting temperatures are slightly above the melting temperature of pure CO₂. Melting of solid CO₂ at temperatures above -56.6°C has not been reported to date in the literature. Melting temperatures above -56.6°C indicate either a thermal lag between the stage and the sample, or a calibration error (Shepherd et al., 1985). None of the other inclusions show evidence of dry ice or clathrate formation, indicating that CO₂ was not present in the system in significant amounts.

Reported eutectic temperatures are -21.1°C for the pure H₂O-NaCl system, -22.9°C for the H₂O-NaCl-KCl system, -33.6°C for the H₂O-MgCl₂ system, and -35.0°C for the H₂O-FeCl₂ system (Borisenko, 1977; Crawford, 1981). First melting temperatures from this study form a bimodal population: (1) a small population with temperatures ranging from -29.0°C to -32.4°C, mostly from brown sphalerite-hosted inclusions from Stage 1 but also some quartz-hosted inclusions from Stage 2; and (2) a large population with temperatures ranging from -21.3°C to -27.6°C, from quartz- and sphalerite-hosted inclusions from Stage 1 through 3 (Fig. 8-8). According to these eutectic temperatures, although NaCl is likely the main salt present in the inclusions, a small amount of KCl is likely present and, in the case of Stage 1 and Stage 2 inclusions, some divalent cations such as MgCl₂ or FeCl₂ are likely present as well.

Fluid salinity was calculated as equivalent weight percent NaCl (wt.% NaCl equiv.) from final ice melting temperatures, using the equation of Bodnar (1993). Fluid salinity ranges from 3.4 to 7.6 wt.% NaCl equiv. for brown sphalerite-hosted inclusions, from 2.1 to 5.9 wt.% NaCl equiv. for yellow sphalerite-hosted inclusions, and from 0.4 to 9.2 wt.% NaCl equiv. for quartz-

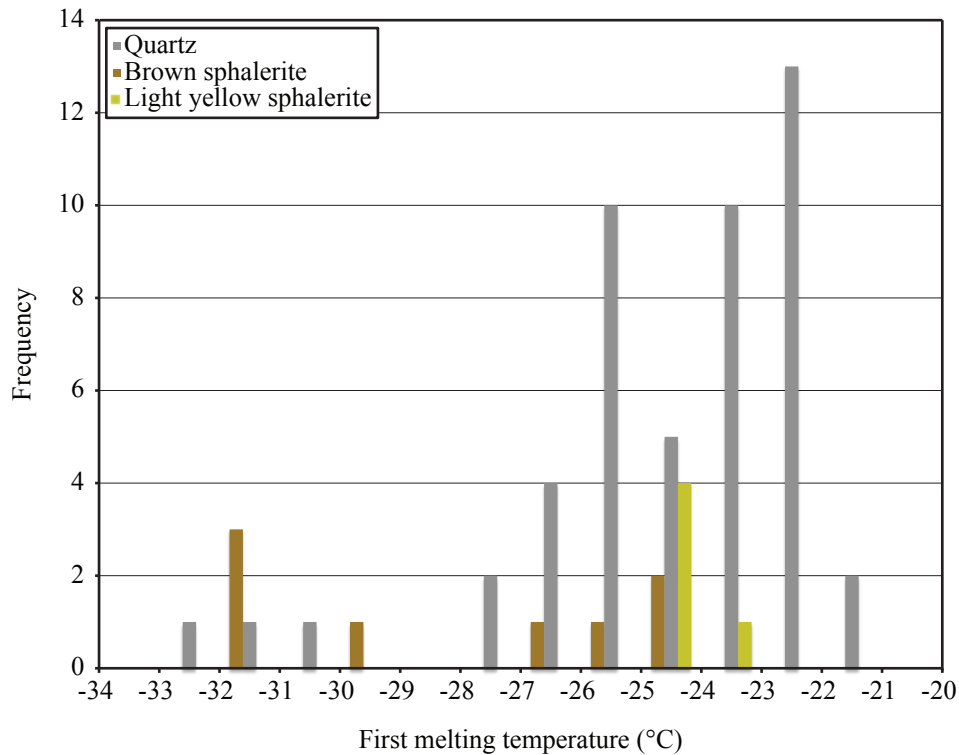


Figure 8-8. Histogram showing the first melting temperature distribution for fluid inclusions from different host minerals.

hosted inclusions, with the exception of one quartz-hosted fluid inclusion assemblage containing between 23.1 and 24.0 wt.% NaCl equiv. (Fig. 8-9 a). Average fluid salinity decreases constantly from Stage 1 to Stage 3 (Fig. 8-10). Homogenization temperatures range from approximately 210°C to 350°C for inclusions in all host minerals and also consistently decrease with time (Figs. 8-9 b and 8-10). Brown sphalerite, which formed exclusively during Stage 1, shows higher homogenization temperatures than yellow sphalerite, which formed from late Stage 1 to Stage 3 (Fig. 8-10). Quartz, on the other hand, formed over the whole range of temperatures. Trends of decreasing homogenization temperatures and salinity are also observed within some fluid inclusion assemblages (Fig. 8-11), especially from Stage 1 and Stage 2. This is good evidence that fluid mixing took place between a hot and saline fluid of possible magmatic origin and cooler, less saline water of possible meteoric origin.

Measured homogenization temperatures represent minimum estimates

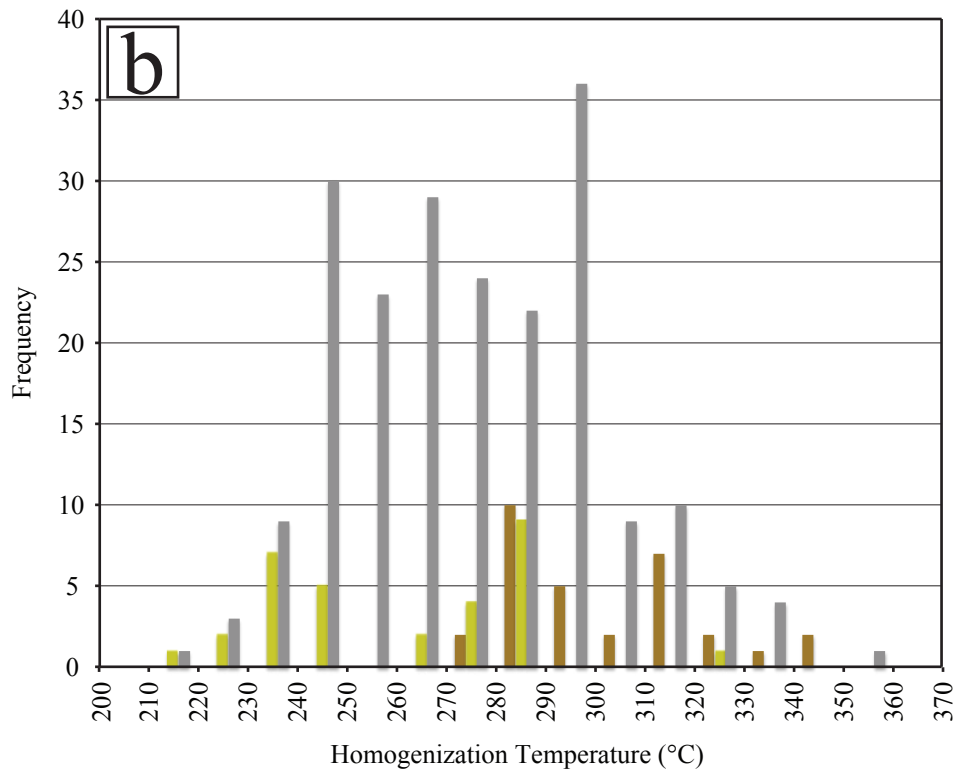
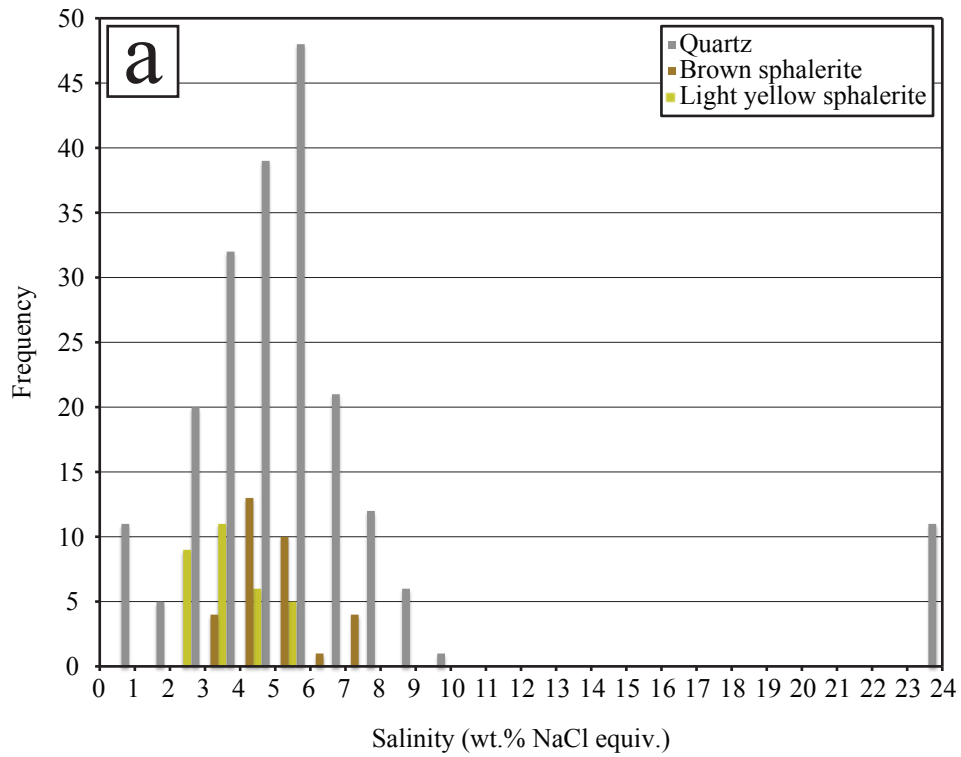


Figure 8-9. Histograms showing homogenization temperatures and salinity distribution for fluid inclusions from different host minerals.

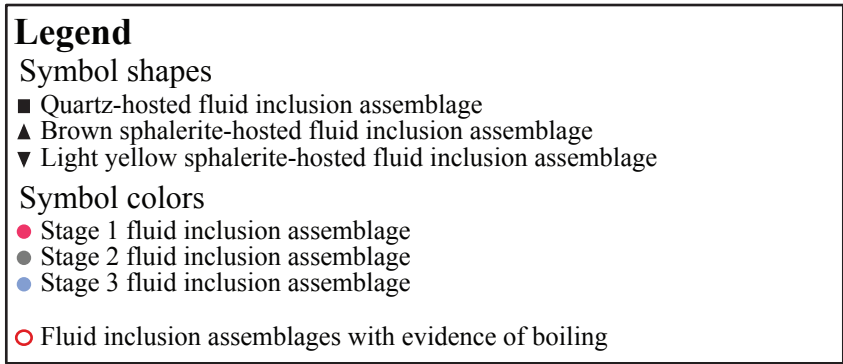
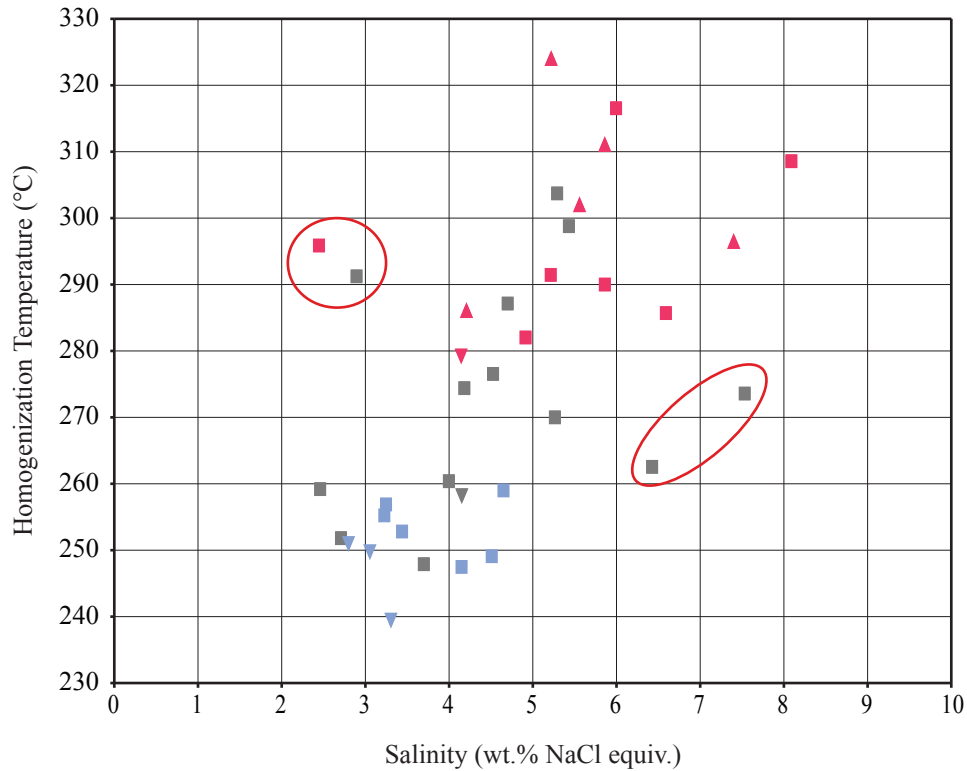


Figure 8-10. Scatter plot of fluid inclusion assemblage average homogenization temperatures vs. average salinity for Stage 1 to Stage 3.

for the actual trapping temperatures unless boiling takes place in the system at the time of entrapment, in which case the measured homogenization temperature represents exactly the trapping temperature. If boiling evidence is absent, a pressure correction is needed in order to obtain real formation temperatures. No evidence of boiling was observed in fluid inclusion assemblages before the end of Stage 1. A pressure correction (Roedder and Bodnar, 1980) is therefore applied using the sulfur isotope data as an independent geothermometer, because

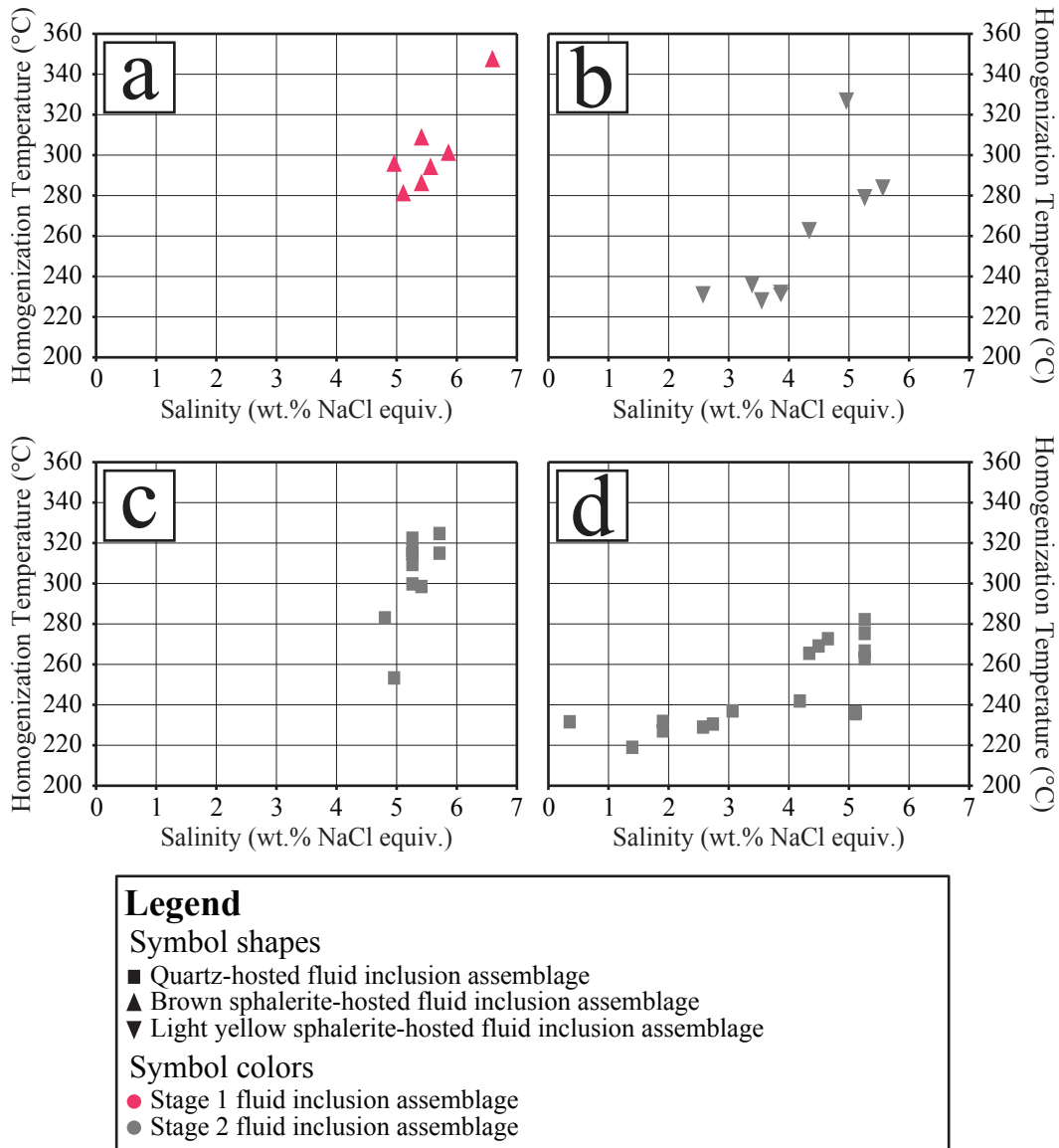


Figure 8-11. Scatter plot of homogenization temperatures vs. salinity for fluid inclusions pertaining to four fluid inclusion assemblages from Stage 1 and Stage 2: (a) 09-M-14, (b) 09-M-14, (c) 09-M-1, and (d) 09-M-13.

the fractionation of stable isotopes is not significantly affected by pressure. Fluid inclusion assemblage average homogenization temperatures for Stage 1 vary between 279°C and 324°C, and salinity varies between 2.4 to 8.1 wt.% NaCl equiv. (Fig. 8-10). Table 8-2 reports the averaged fluid inclusion assemblage salinity and homogenization temperatures, and calculated sulfur isotope fractionation temperatures for three selected samples. According to Table 8-2, the pressure correction required for Stage 1 fluid inclusion homogenization

Sample ID	Salinity	Fluid inclusion temperature (°C)	Sulfur isotope temperature (°C)
09-M-8	6.02	293	300 ± 80
09-M-14	5.80	310	320 ± 90
08-GL-2	5.61	302	360 ± 110

Table 8-2. Comparative table of fluid inclusion homogenization temperatures (Stage 1 average per sample) vs. sulfur isotopes crystallization temperatures for the same samples.

temperatures is likely between 10°C and 50°C. Using an isochore diagram for H₂O-NaCl inclusions having a salinity of 5 wt.% NaCl (Bodnar and Vityk, 1994), pressure at the time of formation for samples 09-M-8 and 09-M-14 is estimated to be approximately 250 bars, whereas it is 700 bars for sample 08-GL-2. The error for these pressures is quite large because the estimated pressure is a function of the calculated sulfide crystallization temperature for each sample, which is greatly affected by the error for the $\delta^{34}\text{S}$ values ($\pm 0.3\%$). Assuming hydrostatic pressure conditions, the calculated depth of formation is approximately 2.5 km for samples 09-M-8 and 09-M-14, and approximately 7 km for sample 08-GL-2. All three vein samples were taken at the same elevation, and sampled the same mineralization stages. The depth of formation of ~2.5 km for Stage 1 is considered more reliable because two of the three samples yielded this result.

Boiling starts at the end of Stage 1 and continues through most of Stage 2, thus fluid inclusions trapped during Stage 2 were trapped under conditions of immiscibility. No pressure correction is therefore needed for these later samples, and the measured homogenization temperatures directly record the trapping temperature (Roedder and Bodnar, 1980). Average homogenization temperatures for Stage 2 fluid inclusion assemblage range between 248°C and 304°C, and salinity ranges between 2.5 and 7.5 wt.% NaCl equiv. (Fig. 8-10). Using the diagram of Haas (1971) and the average salinity and homogenization temperature from boiling fluid inclusion assemblages, and assuming that the system was under hydrostatic pressure conditions, the estimated depth of formation for Stage 2 is

between 1000 m and 550 m below the water table.

Average homogenization temperatures for Stage 3 fluid inclusion assemblages range from 240°C to 259°C, and salinities range from 2.8 to 4.6 wt.% NaCl equiv. (Fig. 8-10). Clear evidence of boiling was not observed in Stage 3, although the brecciation observed in this stage and the very fine grained calcite matrix indicate a high-energy environment and rapid cooling, consistent with boiling. In any case, pressure correction is not possible because an independent geothermometer is not available for this stage. A correction, however, would have likely been less than 50°C, which the maximum correction applied for Stage 1.

9. Discussion

9.1. Timing and tectonic setting of the Buriticá porphyry and gold deposit

Formation of alteration minerals associated with the Buriticá gold deposit (7.74 ± 0.08 Ma) is coeval, within error, with cooling of the Buriticá andesite porphyry intrusion (7.41 ± 0.40 Ma), and postdates reported ages for the Cañasgordas terrane accretion (Early to Middle Miocene, prior to 12 Ma; Cediel et al., 2003).

Geochemical characteristics of magmas can provide information about the tectonic setting in which they formed (Bailey, 1981; Brown et al., 1984; Pearce et al., 1984; Thompson et al., 1984; Harris et al., 1986; Pitcher, 1987). In this case, the Buriticá andesite porphyry magma is of high-K calc-alkaline affinity (Fig. 8-2; Peccerillo and Taylor, 1976). The shoshonitic character of some samples from the Buriticá andesite porphyry is likely due to alteration, but the least-altered samples from the suite nevertheless have a high-K composition. According to the extensive literature on high-K calc-alkaline rocks, such magmas can be generated either in a post-collisional setting from partial melting of chemically-enriched continental lithosphere following crustal thickening, or in a continental arc setting

where the magmas are a mixture of mantle-derived and lower crustal-derived magmas (e.g., Pitcher, 1987; Roberts and Clemens, 1993; Barbarin, 1999; Ferré and Bernard, 2001; Liu et al., 2002; Chen et al., 2003; Yang et al., 2007).

The continental arc nature of the Buriticá andesite porphyry is highlighted by its trace element composition using the orogenic andesite discrimination criteria of Bailey (1981). Using various trace element ratios such as La/Yb and Sc/Ni, Bailey (1981) subdivided orogenic andesites into three different tectonic settings (Fig. 9-1): (1) oceanic island arcs and island arcs partially formed on thin continental crust, and further divided into low-K and “other” andesites; (2) continental arc formed on a continental crust of thin to average thickness; and (3) continental arc formed on thick continental crust (i.e., Andean type). It is interpreted that the calculated ratios for the Buriticá andesite porphyry represent that of the original rock, because all samples plot in a relatively tight group in the continental-arc andesite range, between the fields for arcs developed on average to thick crust.

These geochemical and geochronological data confirm that the Buriticá andesite porphyry is part of a Miocene subduction-related magmatic arc, which consist of a series of relatively small and

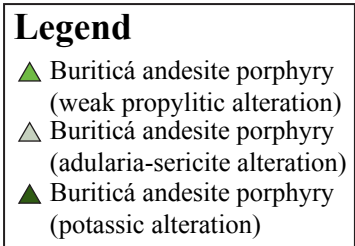
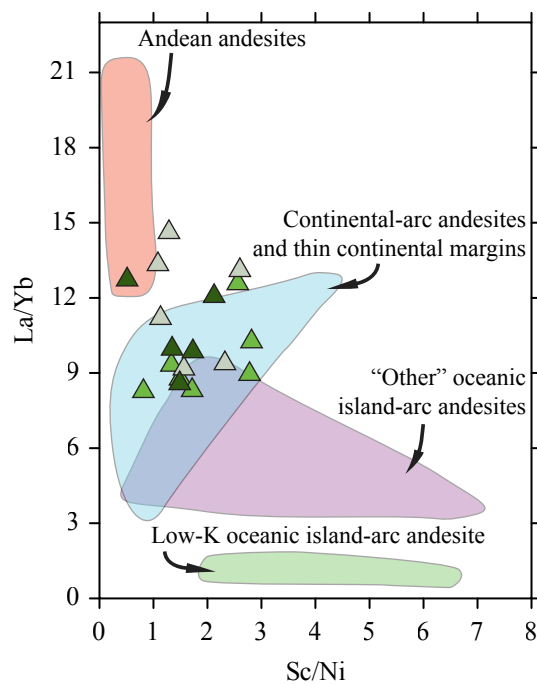


Figure 9-1. La/Yb versus Sc/Ni diagram showing fields for different tectonic settings from Bailey (1981).

isolated plutons that approximately follow the Cauca-Romeral fault system (Fig. 2-4; Aspden et al., 1987).

Mineralized veins were formed shortly after the Buriticá andesite porphyry intrusion, and in the same transpressional tectonic environment. The orientation and dip of the conjugate mineralized vein sets is consistent with the stress field associated with dextral strike-slip motion along the Cauca-Romeral fault system.

9.2. Characteristics of ore-forming fluids in the Buriticá gold deposit

Fluid inclusion and sulfur isotope data indicate that early Stage 1 fluids in the system were relatively high temperature and high salinity (approximately 280°C to 325°C, with a maximum pressure correction of 50°C; 2.45 to 8.09 wt.% NaCl equiv., average of 5.8 wt.% NaCl equiv.), and were likely of magmatic origin (i.e., derived from the Buriticá andesite porphyry). Figure 8-10 reveals a clear fluid evolution trend towards lower temperatures and salinities with time, terminating in Stage 3 at temperatures between approximately 240°C and 260°C (excluding pressure correction), and salinities between 2.80 and 4.65 wt.% NaCl equiv, with an average of 3.6 wt.% NaCl equiv. The ore-forming system is interpreted to have evolved from an early magmatic fluids-dominated system to a late groundwaters-dominated system, with fluid mixing taking place happening throughout the duration of the system, especially during Stage 2 (Figs. 6-11 and 8-11).

The magmatic origin of the fluid is confirmed by the sulfur isotope ratios calculated from sulfide minerals, which range from -2.6 ‰ to 2.5 ‰ and thus overlap with the isotopic compositions found in porphyry systems (typically from -3 ‰ to -1 ‰; Ohmoto and Rye, 1979). The system is thought to have been under hydrostatic pressure conditions from the beginning, at an estimated depth of ~2.5 km. Sulfide minerals, fine-grained quartz, silver and gold precipitated during Stage 1 (Fig. 6-11) because of boiling of the hydrothermal fluid, possibly initiated

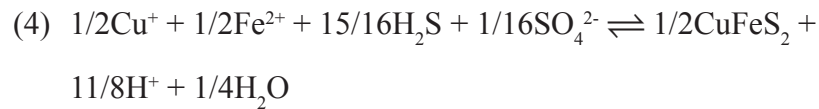
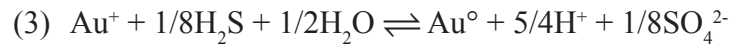
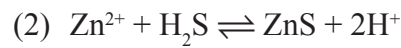
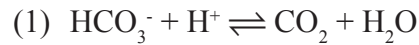
by a sudden depressurization of the system (Fournier, 1999). Boiling is interpreted to have started at some point during Stage 1 and to have carried on during most of Stage 2, and is thought to be the main Au precipitation trigger.

Stage 3 contains a very distinct mineral assemblage, with renewed crystallization of sulfide minerals and gold (after Stage 2 which has only a minor sulfide and gold content), and significant quantities of calcite and antimony-rich minerals, such as stibnite (Fig. 6-11). Stage 3 shows brecciation textures, with Stage 1 and Stage 2 clasts hosted in a very fine-grained calcite-rich matrix. This suggests that Stage 3 was formed in a high-energy environment and that the groundmass minerals cooled rapidly, which would be consistent with a boiling system. The Stage 3 samples used during this study contained only small amounts of gold, but recent drilling has shown zones of Stage 3 mineralization with much higher gold grades. Little information is known about what triggered Stage 3 Au deposition, but we can speculate that it was caused by boiling pulses of late magmatic fluids. Further fluid inclusion work is required on high-grade Stage 3 samples, however, to confirm this hypothesis.

9.2.1. *Importance of boiling for gold mineral precipitation*

Boiling hydrothermal fluids undergo many physical and chemical changes, the most noticeable of which is devolatilization (i.e., loss of gas such as H_2 , CH_4 , CO_2 , H_2S and SO_2). Removing CO_2 and H_2S from solution is a very efficient ore depositional mechanism because it significantly affects the hydrothermal fluid pH, and sulfide stability and oxidation state, respectively (Drummond and Ohmoto, 1985). CO_2 and H_2S have very similar behaviors in an aqueous solution, except that CO_2 is more volatile and typically much more abundant than H_2S in natural hydrothermal systems. CO_2 will thus be exsolved at faster rate than H_2S , and will have a stronger effect on the hydrothermal fluid characteristics. The following equations show some of the main equilibrium reactions pertinent to ore mineral

precipitation from a boiling hydrothermal solution:



Equation (1) shows how the H^+ concentration of the hydrothermal fluid is depleted (i.e., the pH is increased) as CO_2 gas exsolves. An increased pH leads to sulfide mineral precipitation such as sphalerite, chalcopyrite, and pyrite, respectively expressed by equations (2), (4), and (5). Unlike most metals, which are mainly transported as chloride complexes in hydrothermal fluids, gold can be transported as a chloride complex (equation (3)) but is predominantly transported as a bisulfide complex (equation (6); Casadevall and Ohmoto, 1977; Seward, 1973). A pH increase will therefore trigger precipitation of the chloride-complexed gold, but most of the gold, transported as a bisulfide complex, will be precipitated as the H_2S gas is exsolved.

9.3. Classification of the Buriticá gold deposit

Epithermal deposits have been classified using a number of different schemes since the late 1970s (see Simmons et al., 2005, and references therein). Some classification schemes are purely descriptive, and are based on fluid chemistry or alteration and gangue mineralogy (acid sulfate or alunite-kaolinite vs. adularia-sericite; Hayba et al., 1985; Heald et al., 1987; Berger and Henley, 1989). Other schemes are based on the stability of sulfur-bearing minerals (i.e., sulfur and oxygen fugacity), which gives insights into the evolution state of hydrothermal fluids (low- vs. intermediate- or high-sulfidation state; Hedenquist

et al., 2000; Einaudi et al., 2003; Sillitoe and Hedenquist, 2003; Sillitoe, 2008). The original sulfidation classification scheme was divided into the low- (LS) and high-sulfidation (HS) categories (Hedenquist, 1987; White and Hedenquist, 1990; White and Hedenquist, 1995), but an intermediate-sulfidation (IS) category was recently recognized as a hybrid type between the high- and low-sulfidation types (Hedenquist et al., 2000). Gemmell (2004) published a thorough comparison of the low- and intermediate-sulfidation deposit features.

According to the sulfidation-state classification scheme, the Buriticá gold deposit fits somewhere between a low- and an intermediate-sulfidation epithermal deposit (see Table 9-1 for a summary of the deposit characteristics). Characteristics of the Buriticá deposit that can be attributed to both deposit types include:

- (1) Genetic relationship with a calc-alkaline host rock,
- (2) Fluid temperatures between 250°C and 300°C, and showing the possible role of magmatic and meteoric fluids,
- (3) Alteration mineralogy dominated by sericite and quartz, with some adularia in zones of stronger alteration,
- (4) Vein mineralogy dominated by pyrite, sphalerite, galena, tetrahedrite, chalcopyrite, quartz and calcite,
- (5) Crustiform vein banding and vuggy quartz cavities.

Certain characteristics, however, fit only the low sulfidation description:

- (1) No hypogene clays observed anywhere in the deposit,
- (2) Presence of Fe-rich brown sphalerite during the early vein paragenesis.

On the other hand, some characteristics fit the intermediate-sulfidation category better than low-sulfidation:

- (1) Fluid salinity ranging from 0.35 to 9.21 wt.% NaCl equiv.

The fluid inclusion assemblage showing a fluid salinity of approximately 23.50 wt.% NaCl equiv. is excluded because it is considered an outlier. (LS deposits generally have a fluid salinity < 2 wt.% NaCl equiv.; IS deposits have a fluid salinity between 0 and 23 wt.% NaCl equiv.),

- (2) Depth of formation is deeper than typical LS or IS deposit formation, but is closer to the IS depth range (LS deposits usually form between 0 and 300 m; IS deposits usually form between 300 and 800 m),
- (3) Presence of Fe-poor yellow sphalerite during the late vein paragenesis,
- (4) Relatively large quantities of sulfide minerals in the veins (10 to 15 vol.%), which is due to the high salinity of the fluids (LS deposits typically contain only 1 to 2 vol.% of ore minerals; IS deposits contain 5 to 20 vol.% of ore minerals).

9.4. Comparison with other late Miocene gold deposits in Colombia

Sillitoe (2008) described the Miocene Middle Cauca metallogenic belt, which contains a number of gold-rich deposits such as Buriticá, Marmato, and La Colosa (Fig. 3-1 b). Table 9-1 presents a comparison of these three deposits.

9.4.1. *La Colosa porphyry gold deposit characteristics*

The following description of the La Colosa deposit is summarized from Gil-Rodriguez (2010). La Colosa is located in the Central Cordillera of Colombia, and is associated with a series of porphyritic to equigranular Late Miocene medium- to high-K calc-alkaline diorites, quartz diorites, and dacites (Figs. 8-1 and 8-2), which intrude Paleozoic low-grade metamorphic schists and quartzites of the Cajamarca Complex (Maya, 1992). The intrusive rocks hosting the La Colosa deposit are interpreted to have been emplaced at a depth of ~3-4 km based

Deposit name	Gold deposit type	Au Content (Moz)	Deposit age	Host rock	Alteration	Principal mineralization style(s)	Ore minerals	Gangue minerals	Ore fluid	Source(s)
Buriticá	Low/intermediate sulfidation epithermal Au-Ag	---	7.73 ± 0.12 Ma	High-K calc-alkaline, porphyritic andesite stock	Strong proximal sericite+quartz± adularia±calcite, distal propylitic (epidote+chlorite± calcite)	Dilational banded quartz-sulfide-calcite veins, disseminated sulfides, breccias	Pyrite, sphalerite, galena, chalcocopyrite, tetrahedrite, stibnite, native gold	Quartz, calcite	Mixed magmatic-meteoric	---
Marmato	Low/intermediate sulfidation epithermal to mesothermal Au-Ag	15.9	5.6 ± 0.6 Ma	Porphyritic andesite and dacite	Strong proximal sericite+quartz± adularia±calcite, minor kaolinitization	Dilational banded veins, stockwork veins/veinlets, breccias	Pyrite, sphalerite, galena, chalcocopyrite, arsenopyrite, pyrrhotite, stibnite, argentite, native gold, electrum	Calcite, quartz	Mixed magmatic-meteoric	Rodriguez and Warden (1993), Rossetti and Colombo (1999), Tassinari et al. (2008)
La Colosa	Porphyry Au	12.9	8.3 ± 0.2 Ma to 7.3 ± 0.2 Ma	Medium to high-K calc-alkaline, equigranular to porphyritic diorite and quartz diorite stocks	Pervasive proximal potassic (biotite±K-feldspar), weak intermediate argillic (sericite+chlorite± kaolinite±illite), distal propylitic (chlorite+epidote± calcite)	Disseminated sulfides, stockwork veins/veinlets, breccias	Pyrite, magnetite, chalcocopyrite, molybdenite, pyrrhotite	---	Magmatic	Gil-Rodriguez (2010)

Table 9-1. Middle Cauca metallogenic belt deposit summary table.

on thermobarometric data from amphiboles.

Alteration and mineralization styles at La Colosa are typical of porphyry deposits (Sillitoe, 2000; Seedorff et al., 2005). Alteration facies at La Colosa range from potassic to phyllic/argillic, to propylitic. Mineralization is characterized by veinlets and disseminations of ore minerals. Three different intrusive breccia bodies have also been identified, all of which have significant gold mineralization.

The earliest intrusive unit in the La Colosa area was dated at 8.3 ± 0.2 Ma. Early diorites display high gold grades, pervasive potassic alteration characterized by biotite and K-feldspar, and patchy actinolite-albite alteration. Mineralization in these units consists of pyrite, magnetite, chalcopyrite, molybdenite and pyrrhotite.

Intermineral diorites display moderate gold grades, weak argillic alteration characterized by sericite, chlorite and illite, and weak propylitic alteration characterized by chlorite, epidote and calcite. Ore minerals in these units are pyrite, chalcopyrite, and pyrrhotite.

Late diorites, quartz diorites and dacites show very low gold grades, and weak to moderate sericitic and propylitic alteration. Pyrite is the only sulfide mineral present in these units. The latest of all intrusive units is a dacite dike, and was dated at 7.3 ± 0.2 Ma, indicating a lifespan of ~ 1 Ma for the magmatic system.

9.4.2. *Marmato epithermal gold deposit characteristics*

Characteristics of gold deposits in the Marmato district have been described by Rodriguez and Warden (1993), Rossetti and Colombo (1999), and Tassinari et al. (2008). The Marmato district is located on the eastern side of the Cauca fault, on the western edge of the Central Cordillera, and includes several small underground workings such as Plata Fría, La Maria, Aguaceral, La Negra, La Felicia, La Palma, and Marmato Bajo. Mineralization is associated

with porphyritic andesites and dacites of the Combia Formation, which were respectively dated at 7.1 ± 0.2 Ma and 6.3 ± 0.7 Ma (Rodríguez, 1987), and intrude the Paleozoic upper greenschist–lower amphibolite metasedimentary and metavolcanic rocks (e.g., quartz-sericite schist, quartz-biotite schist, graphite schist, amphibolite) of the Arquía Complex (González and Maya, 1995) and the Oligocene-Miocene sedimentary rocks of the Amagá Formation (Van Der Hammen, 1960).

Alteration and mineralization styles in the Marmato district have led people to classify this deposit as an adularia-sericite epithermal gold deposit (Rossetti and Colombo, 1999), as a low-sulfidation deposit (Tassinari et al., 2008), and as an intermediate-sulfidation deposit (Sillitoe, 2008). Ductile deformation was arguably observed in the deeper parts of the Marmato deposit, and has also led some people to characterize this part of the system as mesothermal (Rodríguez and Warden, 1993; Tassinari et al., 2008).

Typical host-rock alteration is marked by a meter-scale zone of sericitization, silicification, and locally minor kaolinitization surrounding the veins. A larger propylitic alteration, characterized by quartz-calcite-chlorite-pyrite-sericite-epidote, is also recognized in the area, but is interpreted to pre-date the gold mineralizing event and to be associated with the emplacement of the Marmato stock.

Mineralization consists of steeply dipping mm- to m-thick veins, extensional veins, as well as stockwork and small breccia zones. Gangue minerals are quartz, calcite, and adularia, whereas ore minerals are mainly pyrite, sphalerite and galena, with minor amounts of chalcopyrite, arsenopyrite, pyrrhotite, stibnite, Ag-sulfosalts, native gold and electrum. Native gold usually occurs as inclusions within sulfide minerals. Disseminated ore minerals are locally observed, but are limited to zones immediately surrounding the mineralized veins (i.e., <1 m from

the veins).

9.4.3. *Similarities with the Buriticá epithermal gold deposit*

The timing of magmatism and related hydrothermal activity at the Buriticá deposit is slightly older than reported ages of the Marmato deposit and younger than the reported age of the La Colosa deposit. In the Marmato district, magmatic activity was dated at ~7–6 Ma (Rodríguez, 1987), and hydrothermal activity was dated at 5.6 ± 0.6 Ma (Tassinari et al., 2008). At La Colosa, the magmatic activity was dated at ~8–7 Ma (Gil-Rodríguez, 2010). The three deposits thus formed within a ~3 m.y. period in the late Miocene, and are all spatially and temporally associated with porphyritic rocks.

No geochemical data are available for the Marmato stock, but according to petrographic descriptions from Rossetti and Colombo (1999), the porphyritic andesites at Marmato and Buriticá are very similar. Alteration, mineralization style, and ore mineralogy are similar too, with alteration dominated by sericite and adularia, accompanied by sulfides such as pyrite, sphalerite, galena, chalcopyrite, and stibnite. Fluid inclusions from the Marmato deposit show an absence of CO₂, yield salinities between 1.6 and 8.1 wt.% NaCl equiv, and homogenization temperatures between 263°C and 331°C. These fluid characteristics are almost identical to those observed during mineralization stages 1 and 2 at the Buriticá deposit.

Gil-Rodríguez (2010) reports geochemical data for the host rock suite at La Colosa. It appears that the La Colosa rocks are more felsic (i.e., more evolved) than the Buriticá andesite porphyry (Figs. 8-1 and 8-2). The porphyry characteristics of the La Colosa deposit, different from the epithermal features observed at Marmato and Buriticá, indicates that it likely represents a deeper level in a similar magmatic-hydrothermal system.

9.5. **Models for formation of late Miocene gold deposits in Colombia**

In a typical subduction tectonic setting, one could expect to find various types of porphyry or epithermal deposits (e.g., Cu, Cu±Au, Cu±Mo, Au, Mo; Sillitoe, 1972; Richards, 2003, 2005; Candela and Piccoli, 2005). The question that arises then is why are so many gold-rich deposits observed in Colombia relative to copper-rich or molybdenum-rich deposits, particularly along the Miocene Middle Cauca belt?

It is generally accepted that metals in porphyry and epithermal systems come from partial melting and oxidation of the asthenospheric mantle wedge and the lithospheric mantle caused by rising water exsolved from a subducting slab (see review by Richards, 2005). Oxidation of the mantle destabilizes sulfide phases to form sulfate. In the absence of a sulfide melt, into which chalcophile and siderophile elements partition strongly, metals are concentrated in the silicate melt fraction.

Gold partitions more strongly than copper into the sulfide phases relative to the silicate melt (Peach et al., 1990). Since Middle Cretaceous time, fluids exsolved from the subducting slab might have contributed to enrich the asthenospheric mantle wedge, the lithospheric mantle and the lower crust in gold relative to copper by oxidizing part of the sulfide melt. According to this hypothesis, subduction-related magmatism prior to the Miocene, even if sporadic, could have preferentially mobilized copper into the silicate melts, and left gold in the residual sulfide phases within the lithospheric mantle and the lower crust (Richards, 2005; Richards, 2009).

Due to a density contrast, ascending mafic magmas are thought to stall at the base of the crust, where they undergo a process of melting and assimilation of the crust, and storage and homogenization (MASH; Hildreth and Moorbath, 1988). The MASH process is an important step in order to concentrate volatiles

(e.g., H₂O, S, Cl) in the evolved melt by fractional crystallization. These volatiles are critical for the efficient partitioning and transport of metals into the fluid phase, for the formation of the hydrothermal system, and thus the formation of a sizable ore deposit.

Upon comparison of the Buriticá deposit with the Marmato deposit, it is clear that the processes involved in both localities are quite similar. Since the timing and host rock geochemistry are relatively identical for the Buriticá and La Colosa deposits, the difference between the two of them may be explained by a faster rate of ascent and a shallower emplacement depth (i.e., in the epithermal environment rather than the porphyry environment) at Buriticá than at La Colosa, likely due to the proximity of the Buriticá deposit to the major crustal faults of the Cauca-Romeral fault system. All three deposits are spatially and temporally associated with the Miocene magmatic arc formed during the approach and subsequent collision of the Chocó arc with South America (Fig. 2-4; Aspden et al., 1987; Pindell and Kennan, 2009).

9.6. Mineral exploration implications

Such similarities between the deposits of the Middle Cauca belt may also mean that their gold endowment is comparable. With known reserves of 15.9 Moz for the Marmato district (Tassinari et al., 2008), and inferred resources of 12.9 Moz for the La Colosa deposit (Gil-Rodriguez, 2010), potential for gold discovery in the Buriticá area is very good.

In the Buriticá area, exploration should focus on subvertical structural features striking between 070° and 105°, because they represent potential extensional jogs associated with the dextral movement along the Cauca-Romeral fault system, where mineralizing fluid would have been focused.

Because both the Marmato and La Colosa deposits are located within the Paleozoic metamorphic rocks of the Central Cordillera, whereas Buriticá

is located within the Mesozoic rocks of the Western Cordillera, it seems that the nature of the country rock is not a major factor in the formation of those deposits. Therefore, all Miocene medium- to high-K calc-alkaline magmatic activity could be prospective for gold mineralization, and should be investigated. Furthermore, the Miocene Middle Cauca metallogenic belt boundaries may have to be expanded to include a larger portion of the Neogene magmatic arc shown in Figure 3-1 b.

10. Conclusion

The Buriticá deposit is a low- to intermediate-sulfidation gold deposit formed between ~8–7 Ma, immediately after the intrusion of the Buriticá andesite porphyry, dated at 7.41 ± 0.40 Ma. Biotite-dominant potassic alteration and chlorite-dominant propylitic alteration were developed during the early stages of the Buriticá andesite porphyry intrusion, but do not carry gold mineralization. Gold is associated with proximal sericite-quartz-adularia alteration and distal epidote-dominant propylitic alteration. Gold is primarily located within banded quartz-sulfide veins, but also occurs with disseminated sulfides within the vein wallrock and within an intrusive breccia called the Yaragua breccia. Mineralized veins are subvertical and strike between 070° and 105° . Structures with these orientations represent extensional zones associated with the prevailing tectonic stress field at the time of the Chocó arc collision, and are consistent with dextral movement along the faults of the Cauca-Romeral fault system.

The Buriticá deposit is hosted by a composite high-K calc-alkaline porphyritic andesite intrusive body. The earliest facies have an augite+plagioclase±biotite phenocryst assemblage, whereas the latest facies have a hornblende+plagioclase and plagioclase-only phenocryst assemblages.

Vein paragenesis at Buriticá can be divided into three different stages.

Mineralization consists of native gold inclusions within sulfides quartz mainly in the first stage, which contains fine-grained quartz, pyrite, sphalerite, galena, tetrahedrite/tennantite, chalcopyrite, and traces of native gold and silver. Stage 2 contains almost exclusively quartz, along with a small amount of sphalerite and pyrite. Stage 3 is characterized by trace amounts of gold, increased sulfide content, abundant calcite and stibnite, and displays brecciation textures.

Sulfur isotope data from early Stage 1 indicate an average sulfide crystallization of approximately 350°C and that sulfur was likely of magmatic origin, which is consistent with the fluid inclusion data. Fluid inclusion analyses indicate that fluid mixing took place during the hydrothermal system, particularly during Stage 2, when a hot and saline fluid (>300°C, average 5.5 wt.% NaCl equiv.) of magmatic origin mixed with a cooler and less saline meteoric fluid. Vapor-rich inclusions indicating boiling conditions were observed in quartz crystals starting at the end of Stage 1 (coeval with the timing of gold mineralization), and are present until well into Stage 2. Boiling is believed to be the main control on gold precipitation.

Similarities between the Buriticá deposit and other deposits of the Middle Cauca metallogenic belt are striking. They include host rock geochemistry, age, alteration facies, ore mineralogy, and fluid characteristics. Because all these deposits have considerable gold endowment, the Buriticá district, still largely unexplored, offers a unique opportunity for gold discovery.

References

- Acosta, J., Velandia, F., Osorio, J., Lonergan, L., and Mora, H., 2007, Strike-slip deformation within the Colombian Andes, *in* Ries, A.C., Butler, R.W.H., and Graham, R.H., eds., *Deformation of the continental crust: The legacy of Mike Coward: Geological Society of London Special Publication*, v. 272, p. 303–309.
- Álvarez, E., and González, H., 1978, *Geología y geoquímica del cuadrángulo Y-7 (Urrao): Ingeominas, Map scale 1:100 000, Informe 1761, 347 p., Medellín.*
- Álvarez, E., and Parra, E., 1979, *Evaluación del prospecto de cobre y molibdeno en las cabeceras del río Muerto, Municipio de Acandí, Departamento del Chóco: Ingeominas, Informe 1791, 203 p., Bogotá.*
- Álvarez, E., Parra, E., Caballero, H., and Nugteren, H., 1983, *Estudio para la justificación de la prefactibilidad en el prospecto de pórfido cuprífero de Pantanos - Pegadorcito, Departamento de Antioquia: Ingeominas, Informe Ecominas, 172 p., Medellín.*
- Álvarez, J.A., 1983, *Geología de la Cordillera Central y el occidente colombiano y petroquímica de los intrusivos granitoides Mesocenoicos: Ingeominas, Boletín Geológico*, v. 26, p. 1–175, Bogotá.
- Aspden, J.A., and McCourt, W.J., 1986, *Mesozoic oceanic terrane in the central Andes of Colombia: Geology*, v. 14, p. 415–418.
- Aspden, J.A., McCourt, W.J., and Brook, M., 1987, *Geometrical control of subduction-related magmatism: The Mesozoic and Cenozoic plutonic history of Western Colombia: Journal of the Geological Society of London*, v. 144, p. 893–905.
- Bailey, J.C., 1981, *Geochemical criteria for a refined tectonic discrimination of orogenic andesites: Chemical Geology*, v. 32, p. 139–154.
- Barbarin, B., 1999, *A review of the relationships between granitoid types, their origins and their geodynamic environments: Lithos*, v. 46, p. 605–626.
- Barckhausen, U., Ranero, C.R., von Huene, R., Cande, S.C., and Roeser, H.A., 2001, *Revised tectonic boundaries in the Cocos Plate off Costa Rica: Implications for the segmentation of the convergent margin and for plate tectonic models: Journal of Geophysical Research*, v. 106, p. 19207–19220.
- Bargmann, C.J., and Dominy, S.C., 2008, *Continental Gold Limited: Buriticá Project Review, NI 43-101 Technical Report: Snowden*, 108 p.

- Bargmann, C.J., and Dominy, S.C., 2009, Continental Gold Limited: Buriticá Gold Project, Geological and Exploration Review: Snowden, 127 p.
- Berger, B.R., and Henley, R.W., 1989, Advances in the understanding of epithermal gold-silver deposits, with special reference to the western United States, *in* Keays, R.R., Ramsay, W.R.H., and Groves, D.I., eds., The geology of gold deposits: The perspective in 1988: Economic Geology, Monograph 6, p. 405–423.
- Bodnar, R.J., 1993, Revised equation and table for determining the freezing point depression of H₂O-NaCl solutions: *Geochimica et Cosmochimica Acta*, v. 57, p. 683–684.
- Bodnar, R.J., 2003, Re-equilibration of fluid inclusions, *in* Samson, I., Anderson, A., and Marshall, D., eds., Fluid inclusions: Analysis and interpretation: Mineralogical Association of Canada, Short Course Handbook, v. 32, p. 213–231.
- Bodnar, R.J., and Vityk, M.O., 1994, Interpretation of microthermometric data for H₂O-NaCl fluid inclusions, *in* DeVivo, B., and Frezzotti, M.L., eds., Fluid inclusions in minerals: Methods and applications: Virginia Polytechnic Institute and State University, p. 117–130, Blacksburg, VA.
- Borisenko, A.S., 1977, Study of the salt composition of solutions in gas-liquid inclusions in minerals by the cryometric method: *Soviet Geology and Geophysics*, v. 17, p. 11–19.
- Botero, G., 1975, Edades radiométricas de algunos plutones colombianos: *Revista de Minería*, v. 27, p. 8336–8342, Medellín.
- Brooks, C., Hart, S.R., and Wendt, T., 1972, Realistic use of two-error regression treatments as applied to rubidium-strontium data: *Reviews of Geophysics and Space Physics*, v. 10, p. 551–577.
- Brown, G.C., Thorpe, R.S., and Webb, P.C., 1984, The geochemical characteristics of granitoids in contrasting arcs and comments on magma sources: *Journal of the Geological Society of London*, v. 141, p. 413–426.
- Bürgl, H., 1967, The orogenesis of the Andean system of Colombia: *Tectonophysics*, v. 4, p. 429–443.
- Campbell, C.J., 1974, Colombian Andes, *in* Spencer, A.M., ed., Mesozoic-Cenozoic orogenic belts: Data for orogenic studies: Geological Society of London Special Publication, v. 4, p. 705–724.
- Candela, P.A., and Piccoli, P.M., 2005, Magmatic processes in the development of porphyry-type ore systems, *in* Hedenquist, J.W., Thompson, J.F.H.,

Goldfarb, R.J., and Richards, J.P., eds., *Economic Geology 100th Anniversary Volume: Society of Economic Geologists*, p. 25–37, Littleton, CO.

- Carlson, G.G., 1977, Geology of the Bailadores, Venezuela, massive sulfide deposit: *Economic Geology and the Bulletin of the Society of Economic Geologists*, v. 72, p. 1131–1141.
- Casadevall, T., and Ohmoto, H., 1977, Sunnyside mine, Eureka mining district, San Juan County, Colorado: Geochemistry of gold and base metal ore deposition in a volcanic environment: *Economic Geology and the Bulletin of the Society of Economic Geologists*, v. 72, p. 1285–1320.
- Castro, N., and Feininger, T., 1965, Geología de la region entre Buriticá y Santa Fe de Antioquia, con especial referencia a la geología económica de un cuerpo andesítico: Ingeominas, Informe interno, p. 1-41, Medellín.
- Cediel, F., and Cáceres, C., 2000, Geological map of Colombia: Geotec Ltd., Third Edition, digital format with legend and tectonostratigraphic chart.
- Cediel, F., Shaw, R.P., and Cáceres, C., 2003, Tectonic assembly of the Northern Andean block, *in* Bartolini, C., Buffer, R.T., and Blickwede, J., eds., *The circum-gulf of Mexico and the Caribbean: Hydrocarbon habitats, basin formation, and plate tectonics: AAPG Memoirs*, v. 79, p. 815–848.
- Chen, B., Jahn, B.M., and Zhai, M.G., 2003, Sr-Nd isotopic characteristics of the Mesozoic magmatism in the Taihang–Yanshan orogen, north China craton, and implications for Archean lithosphere thinning: *Journal of the Geological Society of London*, v. 160, p. 963–970.
- Chiaradia, M., Tripodi, D., Fontboté, L., and Reza, B., 2008, Geologic setting, mineralogy, and geochemistry of the Early Tertiary Au-rich volcanic-hosted massive sulfide deposit of La Plata, Western Cordillera, Ecuador: *Economic Geology and the Bulletin of the Society of Economic Geologists*, v. 103, p. 161–183.
- Clayton, R.N., 1981, Isotopic thermometry, *in* Newton, R.C., Navrotsky, A., and Wood, B.J., eds., *The thermodynamics of minerals and melts: Springer-Verlag*, p. 85–109, Berlin.
- Crawford, M.L., 1981, Phase equilibria in aqueous fluid inclusions, *in* Hollister, L.S., and Crawford, M.L., eds., *Fluid inclusions: Applications to petrology: Mineralogical Association of Canada, Short Course Handbook*, v. 6, p. 75–100.
- Dalrymple, G.B., Lanphere, M.A., and Pringle, M.S., 1988, Correlation diagrams in $^{40}\text{Ar}/^{39}\text{Ar}$ dating: Is there a correct choice?: *Geophysical Research*

Letters, v. 15, p. 589–591.

De Souza, H.A.F., Espinosa, A., and Delaloye, M., 1984, K-Ar ages of basic rocks in the Patia Valley, southwestern Colombia: *Tectonophysics*, v. 107, p. 135–145.

Dewey, J.F., and Bird, J.M., 1970, Mountain belts and the new global tectonics: *Journal of Geophysical Research*, v. 75, p. 2625–2647.

Diamond, L. W., 2003, Systematics of H₂O Inclusions, *in* Samson, I., Anderson, A., and Marshall, D., eds., *Fluid inclusions: Analysis and interpretation: Mineralogical Association of Canada, Short Course Handbook*, v. 32, p. 55–80.

Dörr, W., Grösser, J. R., Rodriguez, G. I., and Kramm, U., 1995, Zircon U-Pb age of the Paramo Rico tonalite-granodiorite, Santander Massif (Cordillera Oriental, Colombia) and its geotectonic significance: *Journal of South American Earth Sciences*, v. 8, p. 187–194.

Drummond, S.E., and Ohmoto, H., 1985, Chemical evolution and mineral deposition in boiling hydrothermal systems: *Economic Geology and the Bulletin of the Society of Economic Geologists*, v. 80, p. 126–147.

Ego, F., Sébrier, M., and Yepes, H., 1995, Is the Cauca-Patia and Romeral fault system left- or right-lateral?: *Geophysical Research Letters*, v. 22, p. 33–36.

Einaudi, M.T., Hedenquist, J.W., and Inan, E.E., 2003, Sulfidation state of fluids in active and extinct hydrothermal systems: Transitions from porphyry to epithermal environments, *in* Simmons, S.F., and Graham, I., eds., *Volcanic, geothermal and ore-forming processes: Rulers and witnesses of processes within the Earth: Society of Economic Geologists Special Publication*, v. 10, p. 285–314.

Etayo, F., 1989, Campanian to Maastrichtian fossils in the northeastern Western Cordillera, Colombia: *Geología Norandina*, v. 11, p. 23–31.

Etayo, F., González, H., and Álvarez, E., 1980, Mid-Albian ammonites from northern Western Cordillera, Colombia: *Geología Norandina*, v. 2, p. 25–30.

Feininger, T., 1970, The Palestina Fault, Colombia: *Geological Society of America Bulletin*, v. 81, p. 1201–1216.

Ferré, E.C., and Bernard, E.L., 2001, Geodynamic significance of early orogenic high-K crustal and mantle melts: Example of the Corsica Batholith: *Lithos*, v. 59, p. 47–67.

- Fisher, R.A., 1953, Dispersion on a Sphere: Proceedings of the Royal Society of London, Series A, v. 217, p. 295–305.
- Fleck, R.J., Sutter, J.F., and Elliot, D.H., 1977, Interpretation of discordant $^{40}\text{Ar}/^{39}\text{Ar}$ age-spectra of Mesozoic tholeiites from Antarctica: *Geochimica et Cosmochimica Acta*, v. 41, p. 15–32.
- Fournier, R.O., 1999, Hydrothermal processes related to movement of fluid from plastic into brittle rock in the magmatic-epithermal environment: *Economic Geology and the Bulletin of the Society of Economic Geologists*, v. 94, p. 1193–1211.
- Gansser, A., 1973, Facts and theories on the Andes: *Journal of the Geological Society of London*, v. 129, p. 93–131.
- Gemmell, B., 2004, Low- and Intermediate-sulfidation epithermal deposits: Center for Ore Deposit and Exploration Studies (CODES), Special Publication, v. 5, p. 57–63.
- Gil-Rodriguez, J., 2010, Igneous petrology of the Colosa gold-rich porphyry system (Tolima, Colombia): Unpublished M.Sc. Thesis, University of Arizona, 51 p., Tucson, AZ.
- Göbel, V., and Stibane, F., 1979, Edad K-Ar en hornblenda de plutones tonalíticos, Cordillera Occidental, Colombia: Universidad Nacional de Colombia, Publicación Especial de Geología, v. 17, 2 p., Medellín.
- Goldstein, R.H., 2003, Petrographic Analysis of Fluid Inclusions, *in* Samson, I., Anderson, A., and Marshall, D., eds., *Fluid inclusions: Analysis and interpretation: Mineralogical Association of Canada, Short Course Handbook*, v. 32, p. 9–53.
- Goldstein, R.H., and Reynolds, T.J., 1994, Systematics of fluid inclusions in diagenetic minerals: *Society of Economic Paleontologists and Mineralogists, Short Course Handbook*, v. 31, 199 p.
- González, H., 1976, Geología del cuadrángulo J-8 (Sonsón): Ingeominas, Informe 1704, 421 p., Medellín.
- González, H., 1993, Mapa geológico generalizado del Departamento de Risaralda: Ingeominas, Map scale 1:200 000, 1 p., Bogotá.
- González, H., 2001, Mapa geológico del Departamento de Antioquia - Memoria explicativa: Ingeominas, Map scale 1:400 000, 240 p., Bogotá.
- González, H., and Maya, M., 1995, Unidades litodémicas de la Ridge Central de Colombia: Ingeominas, *Boletín Geológico*, v. 35, p. 43–57, Bogotá.

- González, H., and Londoño, A., 1998, Edades K/Ar en algunos plutones del Graben del Cauca y norte de la Cordillera Occidental: *Geología Colombiana*, v. 23, p. 117–131.
- González, H., and Londoño, A.C., 2002a, Catálogo de las Unidades Litoestratigráficas de Colombia: Andesita de Buriticá (E₂ab), Cordillera Occidental, Departamento de Antioquia: Comisión Estratigráfica de Ingeominas, 11 p., Medellín.
- González, H., and Londoño, A.C., 2002b, Catálogo de las Unidades Litoestratigráficas de Colombia: Tonalita de Buriticá (K₂tb), Cordillera Occidental, Departamento de Antioquia: Comisión Estratigráfica de Ingeominas, 13 p., Medellín.
- González, H., Restrepo, J.J., Toussaint, J.F., and Linares, E., 1978, Edad radiométrica K-Ar del Batolito de Sabanalarga: Universidad Nacional de Colombia, *Publicación Especial de Geología*, v. 8, p. 1–5, Medellín .
- González, H., Cosslo, U., Maya, Vásquez, E., and Holguín, M., 1999, Mapa geológico del Departamento del Antioquia: Ingeominas, Map scale 1:400,000, 1 p., Medellín.
- Guarín, G., and Álvarez, E., 1977, Geología y geoquímica del proyecto de cobre porfídico del área de Murindó: Ingeominas, Informe Interno, 169 p., Medellín.
- Gutscher, M.A., Malavieille, J., Lallemand, S., and Collot, J.Y., 1999, Tectonic segmentation of the North Andean margin: impact of the Carnegie Ridge collision: *Earth and Planetary Science Letters*, v. 168, p. 255–270.
- Haas, J.L., 1971, The effect of salinity on the maximum thermal gradient of a hydrothermal system at hydrostatic pressure: *Economic Geology and the Bulletin of the Society of Economic Geologists*, v. 66, p. 940–946.
- Hanson, G., 1980, Rare earth elements in petrogenetic studies of igneous systems: *Annual Review of Earth and Planetary Sciences*, v. 8, p. 371–406.
- Harris, N.B.W., Pearce, J.A., and Tindle, A.G., 1986, Geochemical characteristics of collision-zone magmatism, *in* Coward, M.P., and Ries, A.C., eds., *Collision Tectonics: Geological Society of London Special Publication*, v. 19, p. 67–81.
- Hartnady, C.J.H., 1991, Plate tectonics; About turn for supercontinents: *Nature*, v. 352, p. 476–478.
- Hayba, D.O., Bethke, P.M., Heald, P., and Foley, N.K., 1985, Geological, mineralogical, and geochemical characteristics of volcanic-hosted

- epithermal deposits, *in* Berger, B.R., and Bethke, P.M., eds., *Geology and geochemistry of epithermal systems: Society of Economic Geologists, Reviews in Economic Geology*, v. 2, p. 129–168.
- Haynes, F.M., 1985, Determination of fluid inclusion compositions by sequential freezing: *Economic Geology and the Bulletin of the Society of Economic Geologists*, v. 80, p. 1436–1439.
- Heald, P., Foley, N.K., and Hayba, D.O., 1987, Comparative anatomy of volcanic-hosted epithermal deposits: acid-sulfate and adularia-sericite types: *Economic Geology and the Bulletin of the Society of Economic Geologists*, v. 82, p. 1–26.
- Heaman, L., and Ludden, J.N., eds., 1991, *Applications of radiogenic isotope systems to problems in geology: Mineralogical Association of Canada, Short Course Handbook*, v.19, 498 p.
- Hedenquist, J.W., 1987, Mineralization associated with volcanic-related hydrothermal systems in the circum-Pacific basin, *in* Horn, M.K., ed., *Circum-Pacific Energy and Mineral Resources Conference*, 4th, Singapore, 1986, *Transactions: American Association of Petroleum Geologists*, p. 513–524, Tulsa, OK.
- Hedenquist, J.W., Arribas, R.A., and Gonzalez-Urien, E., 2000, Exploration for epithermal gold deposits, *in* Hagemann, S.G., and Brown, P.E., eds., *Gold in 2000: Reviews in Economic Geology*, v. 13, p. 245–277.
- Higgs, R., 2009, Caribbean-South America oblique collision model revised, *in* James, K.H., Lorente, M.A., and Pindell, J.L., eds., *The origin and evolution of the Caribbean plate: Geological Society of London Special Publication*, v. 328, p. 613–657.
- Hildreth, W., and Moorbath, S., 1988, Crustal contributions to arc magmatism in the Andes of Central Chile: *Contributions to Mineralogy and Petrology*, v. 98, p. 455–489.
- Hoffman, P.F., 1991, Did the breakout of Laurentia turn Gondwanaland inside-out?: *Science*, v. 252, p. 1409–1412.
- Hoyos, G., Restrepo, C., and Salazar, J., 1990, *Características sedimentotectónicas de la Formación Penderisco en el sector norte de la Cordillera Occidental, Colombia: Unpublished B.Sc. (Undergraduate) Thesis, Universidad EAFIT*, 290 p., Medellín.
- Iddings, J.P., 1892, The origin of igneous rocks: *Bulletin of the Philosophical Society of Washington*, v. 12, p. 89–213.

- Irving, E.M., 1975, Structural evolution of the northernmost Andes, Colombia: U.S. Geological Survey, Professional Paper, v. 846, p. 1-47.
- Kent, D.V., and Van Der Voo, R., 1990, Palaeozoic palaeogeography from palaeomagnetism of the Atlantic-bordering continents, *in* McKerrow, W.S., and Scotese, C.R., eds., Palaeozoic palaeogeography and biogeography: Geological Society of London Memoirs, v. 12, p. 49–56.
- Kerr, A.C., and Tarney, J., 2005, Tectonic evolution of the Caribbean and northwestern South America: The case for accretion of two Late Cretaceous oceanic plateaus: *Geology*, v. 33, p. 269-272.
- Lanphere, M.A., and Dalrymple, G.B., 1978, The use of $^{40}\text{Ar}/^{39}\text{Ar}$ data in evaluation of disturbed K-Ar systems: US Geological Survey Open-file Report 78-701, p. 241–243.
- Le Bas, M.J., Maitre, R.W., Streckeisen, A., and Zanettin, B., 1986, A chemical classification of volcanic rocks based on the total alkali-silica diagram: *Journal of Petrology*, v. 27, p. 745–750.
- Liu, H.T., Sun, S.H., Liu, J.M., and Zhai, M.G., 2002, The Mesozoic high-Sr granitoids in the northern marginal region of north China craton: Geochemistry and source region: *Acta Petrologica Sinica*, v. 18, p. 257–274.
- Litherland, M., Aspden, J.A., and Jemielita, R.A., 1994, The metamorphic belts of Ecuador: *British Geological Survey Overseas Memoirs*, v. 11, 147 p.
- Mann, P., ed., 1995, Geologic and tectonic development of the Caribbean plate boundary in southern Central America: Geological Society of America, Special Paper, v. 326, 349 p..
- Maresch, W. V., 1974, Plate tectonics origin of the Caribbean mountain system of northern South America: Discussion and proposal: *Geological Society of America Bulletin*, v. 85, p. 669–682.
- Maya, M., 1992, Catálogo de dataciones isotópicas en Colombia: Ingeominas, *Boletín Geológico*, v. 32, p. 135–187, Bogotá.
- Maya, M., and González, H., 1995, Unidades litodemicas en la Cordillera Central de Colombia: Ingeominas, *Boletín Geológico*, v. 35, p. 43–57, Bogotá.
- Maze, W.B., 1984, Jurassic La Quinta Formation in the Sierra de Perija, northwestern Venezuela: Geology and tectonic environment of red beds and volcanic rocks, *in* Bonini, W.E., Hargraves, R.B., and Shagam, R., eds., The Caribbean-South American plate boundary and regional tectonics: Geological Society of America Memoirs, v. 162, p. 263–282.

- McCourt, W.J., and Feininger, T., 1984, High-pressure metamorphic rocks in the Central Cordillera of Colombia: British Geological Survey Report, v. 84, p. 28–35.
- McCourt, W.J., Aspden, J.A., and Brook, M., 1984, New geological and geochronological data from the Colombian Andes: Continental growth by multiple accretion: *Journal of the Geological Society of London*, v. 141, p. 831–845.
- Meschede, M., and Frisch, W., 1998, A plate-tectonic model for the Mesozoic and Early Cenozoic history of the Caribbean plate: *Tectonophysics*, v. 296, p. 269–291.
- Middlemost, E.A.K., 1994, Naming materials in the magma/igneous rock system: *Earth-Science Reviews*, v. 37, p. 215–224.
- Montes, C., Hatcher, R.D., and Restrepo-Pace, P.A., 2005, Tectonic reconstruction of the northern Andean blocks: Oblique convergence and rotations derived from the kinematics of the Piedras–Girardot area, Colombia: *Tectonophysics*, v. 399, p. 221–250.
- Mosier, D.L., Berger, V.I., and Singer, D.A., 2009, Volcanogenic massive sulfide deposits of the world: Database and grade and tonnage models: US Geological Survey Open-file Report 2009-1034, 46 p.
- Ohmoto, H., 1972, Systematics of sulfur and carbon isotopes in hydrothermal ore deposits: *Economic Geology and the Bulletin of the Society of Economic Geologists*, v. 67, p. 551–578.
- Ohmoto, H., and Rye, R.O., 1979, Isotopes of sulfur and carbon, *in* Barnes, H.L., ed., *Geochemistry of hydrothermal ore deposits* (second edition): John Wiley & Sons, p. 509–567, New York.
- Pardo-Casas, F., and Molnar, P., 1987, Relative motion of the Nazca (Farallon) and South American plates since Late Cretaceous time: *Tectonics*, v. 6, p. 233–248.
- Peach, C.L., Mathez, E.A., and Keays, R.R., 1990, Sulfide melt–silicate melt distribution coefficients for noble metals and other chalcophile elements as deduced from MORB: Implications for partial melting: *Geochimica et Cosmochimica Acta*, v. 54, p. 3379–3389.
- Pearce, J.A., Harris, N.B.W., and Tindle, A.G., 1984, Trace element discrimination diagrams for the tectonic interpretation of granitic rocks: *Journal of Petrology*, v. 25, p. 956–983.
- Peccerillo, A., and Taylor, S.R., 1976, Geochemistry of Eocene calc-alkaline

- volcanic rocks from the Kastamonu area, northern Turkey: *Contributions to Mineralogy and Petrology*, v. 58, p. 63–81.
- Pilger, R.H., 1983, Kinematics of the South American subduction zone from global plate reconstructions, *in* Carbé, S.J.R., *Geodynamics of the Eastern Pacific Region, Caribbean and Scotia Arcs*, v. 9, p. 113–125.
- Pindell, J.L., and Dewey, J.F., 1982, Permo-Triassic reconstruction of western Pangea and the evolution of the Gulf of Mexico/Caribbean region: *Tectonics*, v. 1, p. 179–211.
- Pindell, J.L., and Tabbutt, K.D., 1995, Mesozoic-Cenozoic Andean paleogeography and regional controls on hydrocarbon systems, *in* Tankard, A.J., Suárez, S.R., and Welsink, H.J., eds., *Petroleum basins of South America: AAPG Memoirs*, v. 62, p. 101–128.
- Pindell, J.L., and Kennan, L., 2009, Tectonic evolution of the Gulf of Mexico, Caribbean and northern South America in the mantle reference frame: An update, *in* James, K.H., Lorente, M.A., and Pindell, J.L., eds., *The origin and evolution of the Caribbean plate: Geological Society of London Special Publication*, v. 328, p. 1–55.
- Pindell, J.L., Cande, S.C., Pitman, W.C., Rowley, D.B., Dewey, J.F., LaBrecque, J., and Haxby, W., 1988, A plate-kinematic framework for models of Caribbean evolution, *in* Scotese, C.R., and Sager, W.W., eds., *Mesozoic and Cenozoic plate reconstructions: Tectonophysics*, v. 155, p. 121–138.
- Pitcher, W.S., 1987, Granites and yet more granites forty years on: *Geologische Rundschau*, v. 76, p. 51–79.
- Restrepo, J.J., and Toussaint, J.F., 1976, Edades radiométricas de algunas rocas de Antioquia: *Universidad Nacional de Colombia, Publicación Especial de Geología*, v. 6, p. 1–13, Medellín.
- Restrepo, J.J., Toussaint, J.F., González, H., Cordani, U., Kawashita, K., Linares, E., and Patrica, C., 1991, Precisiones geocronológicas sobre el Occidente Colombiano: *Simposio sobre el magmatismo andino y su marco tectónico, Ingeominas*, v. 1, p. 1–21, Manizales.
- Restrepo-Pace, P.A., 1992, Petrotectonic characterization of the Central Andean Terrane, Colombia: *Journal of South American Earth Sciences*, v. 5, p. 97–116.
- Richards, J.P., 2003, Tectono-magmatic precursors for porphyry Cu-(Mo-Au) deposit formation: *Economic Geology and the Bulletin of the Society of Economic Geologists*, v. 96, p. 1515–1533.

- Richards, J.P., 2005, Cumulative factors in the generation of giant calc-alkaline porphyry Cu deposits, in Porter, T.M., ed., Super porphyry copper and gold deposits: A global perspective: Porter Geoscience Consulting Publishing, Linden Park, South Australia, v. 1, p. 7–25.
- Richards, J.P., 2009, Postsubduction porphyry Cu-Au and epithermal Au deposits: Products of remelting of subduction-modified lithosphere: *Geology*, v. 37, p. 247–250.
- Roberts, M.P., and Clemens, J.D., 1993, Origin of high-potassium, calc-alkaline, I-type granitoids: *Geology*, v. 21, p. 825–828.
- Roddick, J.C., 1978, The application of isochron diagrams in ^{40}Ar - ^{39}Ar dating: A discussion: *Earth and Planetary Science Letters*, v. 41, p. 233–244.
- Rodriguez, C., 1987, Informe final de exploración, Etapa 1, Proyecto zonas aledañas a Marmato: Informe Ecominas (unpubl.), Bogotá.
- Rodriguez, C., and Warden, A.J., 1993, Overview of some Colombian gold deposits and their development potential: *Mineralium Deposita*, v. 28, p. 47–57.
- Roedder, E., 1984, Fluid inclusions: Mineralogical Society of America, *Reviews in Mineralogy*, v. 12, 644 p., Washington D.C.
- Roedder, E., and Bodnar, R.J., 1980, Geologic pressure determinations from fluid inclusion studies: *Annual Review of Earth and Planetary Sciences*, v. 8, p. 263–301.
- Ross, M.I., and Scotese, C.R., 1988, A hierarchical tectonic model of the Gulf of Mexico and Caribbean region: *Tectonophysics*, v. 155, p. 139–168.
- Rossetti, P., and Colombo, F., 1999, Adularia-sericite gold deposits of Marmato (Caldas, Colombia): Field and petrographical data, in McCaffrey, K.J.W., Lonergan, L., and Wilkinson, J.J., eds., *Fractures, fluid flow and mineralization: Geological Society of London Special Publication*, v. 155, p. 167–182.
- Sarmiento-Rojas, L.F., Van Wess, J.D., and Cloetingh, S., 2006, Mesozoic transtensional basin history of the Eastern Cordillera, Colombian Andes: Inferences from tectonic models: *Journal of South American Earth Sciences*, v. 21, p. 383–411.
- Schubert, C., Sifontes, R., Velez, V., and Loiza, P., 1979, Formación La Quinta (Jurásico) Andes Merideños: *Geología de la sección tipo: Acta Científica Venezolana*, v. 30, p. 42–55.

- Scotese, C.R., and McKerrow, W.S., 1990, Revised world maps and introduction, *in* McKerrow, W.S., and Scotese, C.R., eds., *Palaeozoic palaeogeography and biogeography: Geological Society of London Memoirs*, v. 12, p. 1–21.
- Seedorff, E., Dilles, J.H., Proffett, J.M., Einaudi, M.T., Zurcher, L., Stavast, W.J.A., Johnson, D.A., and Barton, M.D., 2005, Porphyry deposits: Characteristics and origin of hypogene features, *in* Hedenquist, J.W., Thompson, J.F.H., Goldfarb, R.J., and Richards, J.P., eds., *Economic Geology 100th Anniversary Volume: Society of Economic Geologists*, p. 251–298, Littleton, CO.
- Seward, T.M., 1973, Thiocomplexes of gold and the transport of gold in hydrothermal ore solution: *Geochimica et Cosmochimica Acta*, v. 37, p. 379–399.
- Shagam, R., 1975, The northern termination of the Andes, *in* Nairn, A.E.M., and Stehli, F.G., *The ocean basins and margins, vol. 3: The Gulf of Mexico and the Caribbean: Plenum Press*, p. 325–420, New York.
- Sillitoe, R.H., 1972, A plate tectonic model for the origin of porphyry copper deposits: *Economic Geology and the Bulletin of the Society of Economic Geologists*, v. 67, p. 184–197.
- Sillitoe, R.H., 2000, Gold-rich porphyry deposits: Descriptive and genetic models and their role in exploration and discovery, *in* Hagemann, S.G., and Brown, P.E., eds., *Gold in 2000: Reviews in Economic Geology*, v. 13, p. 315–345.
- Sillitoe, R.H., 2008, Major gold deposits and belts of the North and South American Cordillera: Distribution, tectonomagmatic settings, and metallogenic considerations: *Economic Geology and the Bulletin of the Society of Economic Geologists*, v. 103, p. 663–687.
- Sillitoe, R.H., and Hedenquist, J.W., 2003, Linkages between volcanotectonic settings, ore-fluid compositions, and epithermal precious metal deposits, *in* Simmons, S.F., and Graham, I., eds., *Volcanic, geothermal and ore-forming processes: Rulers and witnesses of processes within the Earth: Society of Economic Geologists Special Publication*, v. 10, p. 315–343.
- Sillitoe, R.H., and Perelló, J., 2005, Andean copper province: tectonomagmatic settings, deposit types, metallogeny, exploration, and discovery, *in* Hedenquist, J.W., Thompson, J.F.H., Goldfarb, R.J., and Richards, J.P., eds., *Economic Geology 100th Anniversary Volume: Society of Economic Geologists*, p. 845–890, Littleton, CO.
- Sillitoe, R.H., Jaramillo, L., Damon, P.E., Shafiqullah, M., and Escovar, R., 1982,

Setting, characteristics, and age of the Andean porphyry copper belt in Colombia: *Economic Geology and the Bulletin of Economic Geologists*, v. 77, p. 1837–1850.

- Simmons, S.F., White, N.C., and John, D.A., 2005, Geological characteristics of epithermal precious and base metal deposits, *in* Hedenquist, J.W., Thompson, J.F.H., Goldfarb, R.J., and Richards, J.P., eds., *Economic Geology 100th Anniversary Volume: Society of Economic Geologists*, p. 485–522, Littleton, CO.
- Shepherd, T.J., Rankin, A.H., and Alderton, D.H.M., 1985, *A practical guide to fluid inclusion studies*: Blackie, 239 p., Glasgow.
- Sun, S.S., and McDonough, W.F., 1989, Chemical and isotopic systematics of oceanic basalts: Implications for mantle composition and processes, *in* Saunders, A.D., Norry, M.J., eds., *Magmatism in ocean basin: Geological Society of London Special Publication*, v. 42, p. 313–345.
- Taboada, A., Rivera, L.A., Fuenzalida, A., Cisternas, A., Philip, H., Bijwaard, H., Olaya, J., and Rivera, C., 2000, Geodynamics of the northern Andes: Subductions and intracontinental deformation (Colombia): *Tectonics*, v. 19, p. 787–813.
- Tassinari, C.C.G., Pinzon, F.D., and Buena Ventura, J., 2008, Age and sources of gold mineralization in the Marmato mining district, NW Colombia: A Miocene-Pliocene epizonal gold deposit: *Ore Geology Reviews*, v. 33, p. 505–518.
- Thompson, R.N., Morrison, M.A., Hendry, G.L., Parry, S.J., Simpson, P.R., Hutchison, R., and O'Hara, M.J., 1984, An assessment of the relative roles of crust and mantle in magma genesis: An elemental approach: *Philosophical Transactions of the Royal Society of London, Series A*, v. 310, p. 549–590.
- Toussaint, J.F., 1993, *Evolución geológica de Colombia: Precámbrico–Paleozóico*: Universidad Nacional de Colombia, 129 p., Medellín.
- Tschanz, C.M., Marvin, R.F., Cruz, B.J., Mehnert, H., and Cebula, G.T., 1974, Geologic evolution of the Sierra Nevada de Santa Marta, northeastern Colombia: *Geological Society of America Bulletin*, v. 85, p. 273–284.
- Van Der Hammen, T., 1960, *Estratigrafía del Terciario y Maestrichtiano continentales y tectogénesis de los Andes Colombianos*: Ingeominas, *Boletín Geológico*, v. 6, p. 67–128, Bogotá.
- Van Der Hilst, R., and Mann, P., 1994, Tectonic implications of tomographic images of subducted lithosphere beneath northwestern South America:

- Geology, v. 22, p. 451–454.
- Van Der Wiel, A.M., 1991, Uplift and volcanism of the SE Colombian Andes in relation to Neogene sedimentation in the Upper Magdalena Valley: PhD Thesis, Landbouwniversiteit, Wageningen, 208 p., The Netherlands.
- Van Thournout, F., Hertogen, J., and Quevedo, L., 1992, Allochthonous terranes in northwestern Ecuador: Tectonophysics, v. 205, p. 205–221.
- Wendt, I., and Carl, C., 1991, The statistical distribution of the mean squared weighted deviation: Chemical Geology, v. 86, p. 275–285.
- White, N.C., and Hedenquist, J.W., 1990, Epithermal environments and styles of mineralization: Variations and their causes, and guidelines for exploration: Journal of Geochemical Exploration, v. 36, p. 445–474.
- White, N.C., and Hedenquist, J.W., 1995, Epithermal gold deposits: Styles, characteristics and exploration: Society of Economic Geologists Newsletter, v. 23, p. 9–13.
- Wortel, R., and Cloetingh, S., 1981, On the origin of the Cocos-Nazca spreading center: Geology, v. 9, p. 425–430.
- Wright, A.E., and Bowes, D.R., 1963, Classification of volcanic breccias: A discussion: Geological Society of America Bulletin, v. 74, p. 79–86.
- Yang, J.H., Fu, Y., Wu, F.Y., Wilde, S.A., Xie, L.W., Yang, Y.H., and Liu, X.M., 2007, Tracing magma mixing in granite genesis: In situ U-Pb dating and Hf-isotope analysis of zircons: Contributions to Mineralogy and Petrology, v. 153, p. 177–190.
- Zambrano, E., Vázquez, E., Duval, B., Latreille, M., and Coffinières, B., 1972, Paleogeographic and petroleum synthesis of western Venezuela: Editions Technip, 62 p., Paris.

Sample ID	Type	Location Description	Collar Coordinate Easting ¹	Collar Coordinate Northing ¹	Collar Elevation (m)	Used for:	Brief Sample Description
08-Bu-04	Core	Hole: BUUY-9 Depth: 21.3 m Azimuth: 53° Dip: -50°	399897	741156	1503	XRD ²	White andesite, intense adularia-sericite alteration, no original texture left, sericite, quartz, milky white feldspar, undifferentiated clays, weak calcite filling of porosity, euhedral fine-grained disseminated pyrite (3%) and sphalerite (0.5%)
08-Bu-07	Core	Hole: BUSY-7 Depth: 79.3 m Azimuth: 307° Dip: -43°	400032	741094	1591	TS ³	Medium to dark greenish grey fine-grained pyroxene-phyric andesite, few larger (medium-grained) plagioclase and pyroxene phenocrysts, few sub-angular to sub-rounded clasts up to 1-2 cm, suspect the larger pyroxene are xenocrysts and not phenocrysts, moderately magnetic, weak chlorite alteration, very fine-grained disseminated pyrrhotite (8%), calcite coating along fractures
08-Bu-08	Core	Hole: BUSY-7 Depth: 131.0 m Azimuth: 307° Dip: -43°	400032	741094	1591	TS	Light pinkish green fine-grained pyroxene-biotite-phyric andesite, equigranular, strongly magnetic, medium to strong chlorite-epidote alteration of mafic minerals, milky white plagioclase, weak potassic alteration (shreddy biotite and pinkish groundmass color), weak calcite alteration and calcite along fractures, trace of very fine-grained disseminated pyrite and chalcopyrite
08-Bu-13	Core	Hole: BUSY-8 Depth: 109.2 m Azimuth: 299° Dip: -60°	400033	741094	1591	GC	Dark greenish grey fine-grained plagioclase-pyroxene-phyric equigranular andesite, moderately magnetic, moderate chlorite alteration of mafic minerals, trace of euhedral fine-grained disseminated pyrite
08-Bu-16	Core	Hole: BUSY-9 Depth: 89.5 m Azimuth: 220° Dip: -46°	400033	741096	1591	Ar-Ar	Light grey plagioclase-phyric andesite, porous rock, intense adularia-sericite alteration, quartz, sericite, strong calcite alteration, calcite and quartz filling porosity, subhedral fine-grained disseminated pyrite (10%), trace of very fine-grained disseminated sphalerite

Sample ID	Type	Location Description	Collar Coordinate Easting ¹	Collar Coordinate Northing ¹	Collar Elevation (m)	Used for:	Brief Sample Description
08-Bu-19	Core	Hole: BUSY-10 Depth: 101.2 m Azimuth: 178° Dip: -49°	400032	741094	1591	GC, TS	Light greenish grey plagioclase-phyric andesite, fine-grained to aphanitic groundmass, euhedral lath-shaped plagioclase phenocrysts up to 6 mm, trachytic texture well developed, moderate adularia-sericite (sericite-quartz) alteration, euhedral fine-grained pyrite (3%) disseminated and along fractures, late calcite infilling porosity
08-Bu-21	Core	Hole: BUSM-2A Depth: 19.7 m Azimuth: 215° Dip: -60°	399915	740682	1777	TS	Light grey to white polymictic breccia with sub-angular to sub-rounded clasts average 1-2 cm up to 8-10 cm in diameter, majority of clasts is andesitic, strong alteration/bleaching, preferential carbonate alteration of clasts, euhedral fine-grained pyrite disseminated throughout the rock and rimming clasts (7%), and euhedral fine-grained disseminated sphalerite (3%)
08-Bu-29	Core	Hole: BUSY-12 Depth: 101.3 m Azimuth: 61° Dip: -75°	399927	741214	1647	GC	Medium to light greenish grey plagioclase-phyric andesite, fine-grained groundmass containing lots of fine stumpy chlorite altered pyroxene, strong chlorite alteration of mafic minerals and weak epidote alteration, moderately magnetic, fine-grained magnetite along fractures, trace of very fine-grained disseminated pyrite
08-Bu-30	Core	Hole: BUSY-13 Depth: 47.7 m Azimuth: 179° Dip: -85°	399780	741150	1752	GC	Medium grey plagioclase-hornblende-phyric andesite, fine-grained to aphanitic groundmass, euhedral stumpy plagioclase and acicular hornblende, phenocrysts are up to 2-3 mm, moderately magnetic, weak chlorite-epidote alteration, euhedral fine-grained disseminated pyrite (1%)
08-Bu-31	Core	Hole: BUSY-13 Depth: 66.9 m Azimuth: 179° Dip: -85°	399780	741150	1752	TS, XRD	White porphyritic andesite, intense adularia-sericite alteration, milky white feldspar, quartz, locally sericite luster, undifferentiated clays, carbonates, medium to fine-grained disseminated galena (10%), pyrite (7%), sphalerite (3%), and chalcopyrite (trace)

Sample ID	Type	Location Description	Collar Coordinate Easting ¹	Collar Coordinate Northing ¹	Collar Elevation (m)	Used for:	Brief Sample Description
08-Bu-32	Core	Hole: BUSY-13 Depth: 120.7 m Azimuth: 179° Dip: -85°	399780	741150	1752	GC	Light grey plagioclase-pyroxene-phyric andesite, fine-grained to aphanitic groundmass, locally clastic texture (sub-rounded clasts up to 2-3 cm), weak trachytic alignment of plagioclase, plagioclase are milky white, moderate sericite-quartz alteration, weak chlorite alteration, fine-grained disseminated pyrite (3-4%)
08-Bu-36	Core	Hole: BUSY-13 Depth: 145.1 m Azimuth: 179° Dip: -85°	399780	741150	1752	GC	Light grey plagioclase-pyroxene-biotite-phyric andesite, fine-grained to aphanitic groundmass, few fine-grained biotite crystals, weakly magnetic, strong chlorite replacement of mafic minerals, strong sericite-quartz alteration, weak calcite alteration, euhedral fine-grained disseminated pyrite (2-3%)
08-Bu-37	Core	Hole: BUSY-13 Depth: 169.2 m Azimuth: 179° Dip: -85°	399780	741150	1752	TS, XRD	White porphyritic andesite, intense adularia-sericite alteration, faint clastic texture preserved, milky white feldspar, quartz, specs of very fine-grained sericite, undifferentiated clays, carbonate, euhedral medium-grained pyrite disseminated and along fractures (5%)
08-Bu-40	Core	Hole: BUSY-13 Depth: 244.3 m Azimuth: 179° Dip: -85°	399780	741150	1752	TS	Light grey to white matrix-supported polymictic breccia, porous rock, intense quartz-calcite alteration, lots of vuggy quartz and calcite/dolomite, although very altered clasts seem to be of andesitic and chert origin, euhedral fine to medium-grained pyrite located preferentially in matrix and andesitic clasts, trace of disseminated sphalerite-galena-chalcopyrite
08-Bu-42	Core	Hole: BUSY-11 Depth: 54.0 m Azimuth: 320° Dip: -51°	399928	741214	1647	TS, XRD	Light greyish white porphyritic andesite, strong adularia-sericite alteration overprinting locally weak chlorite alteration, milky white feldspar, quartz, very fine specs of sericite, trace carbonate, subhedral fine-grained disseminated pyrite (10-15%), trace sphalerite along fractures

Sample ID	Type	Location Description	Collar Coordinate Easting ¹	Collar Coordinate Northing ¹	Collar Elevation (m)	Used for:	Brief Sample Description
08-Bu-46	Core	Hole: BUSY-11 Depth: 126.0 m Azimuth: 320° Dip: -51°	399928	741214	1647	TS	Medium to dark green clast-supported monomictic breccia with sub-angular clasts up 5 cm and magnetite matrix (10%), clasts are plagioclase-phyric andesite, milky white plagioclase, strong pervasive epidote-chlorite alteration, weak calcite alteration, fine-grained pyrite (1%) along fractures
08-Bu-51	Core	Hole: BUUY-10 Depth: 7.8 m Azimuth: 206° Dip: -46°	399897	741156	1503	TS	Clast-supported polymictic breccia with strongly altered porphyritic andesite and chert clasts, andesite clasts are light green and have strong chlorite and sericite alteration, weak calcite along fracture, subhedral fine to medium-grained pyrite (3%) and sphalerite(2%) in matrix
08-Bu-52	Core	Hole: BUUY-10 Depth: 14.9 m Azimuth: 206° Dip: -46°	399897	741156	1503	XRD	White polymictic breccia, intense adularia-sericite alteration, no original texture left, sericite, quartz, undifferentiated clays, euhedral fine-grained sphalerite (5%) and pyrite (3%) along fractures and filling porosity, late calcite filling porosity
08-Bu-58	Core	Hole: BUUY-12 Depth: 12.5 m Azimuth: 10° Dip: -50°	400254	741241	1381	GC	Dark greyish green plagioclase-pyroxene-phyric andesite, fine-grained to aphanitic groundmass, euhedral lath-shaped plagioclase phenocrysts up to 4 mm, weak trachytic alignment of plagioclase developed, strong chlorite alteration of mafic minerals and weak epidote-carbonate alteration, lots of very fine black flaky specs (likely biotite), weakly magnetic, trace of fine-grained disseminated pyrite, this sample looks like a more crystal-rich zone in an overall polymictic clastic/breccia unit
08-Bu-61	Core	Hole: BUUY-12 Depth: 29.7 m Azimuth: 10° Dip: -50°	400254	741241	1381	GC	Dark greenish grey fine-grained to aphanitic plagioclase-pyroxene-phyric equigranular rock, lots of black fine shreddy crystals likely biotite, very strongly magnetic, weak chlorite-epidote alteration, anhedral very fine-grained disseminated pyrite/pyrrhotite? (7%)

Sample ID	Type	Location Description	Collar Coordinate Easting ¹	Collar Coordinate Northing ¹	Collar Elevation (m)	Used for:	Brief Sample Description
08-Bu-70	Core	Hole: BUUY-8 Depth: 70.5 m Azimuth: 345° Dip: -85°	399814	741118	1506	XRD	White porphyritic andesite, intense adularia-sericite alteration, milky white feldspar, quartz, undifferentiated clays, trace fine to very fine-grained sericite, lots of carbonates, euhedral to subhedral medium-grained pyrite (15%) and sphalerite (5%) along fractures
08-Bu-72	Core	Hole: BUUY-11 Depth: 68.0 m Azimuth: 294° Dip: -60°	399897	741156	1503	GC, TS	Medium to dark grey plagioclase-pyroxene-biotite-phyric andesite, aphanitic groundmass, fine-grained phenocrysts with rare ones up to 5-6 mm, moderately magnetic, trace of fine-grained disseminated pyrite
08-Bu-74	Core	Hole: BUUY-13 Depth: 35.8 m Azimuth: 190° Dip: -50°	400256	741257	1384	TS	Light greenish grey plagioclase-pyroxene-biotite-phyric andesite, fine-grained to aphanitic groundmass, euhedral medium to coarse-grained phenocrysts, weakly clastic with sub-rounded clasts up to 1-2 cm, moderately to strongly magnetic
08-Bu-76	Core	Hole: BUUY-13 Depth: 55.8 m Azimuth: 190° Dip: -50°	400256	741257	1384	GC	Dark grey with locally very weak pinkish tinge plagioclase-pyroxene-hornblende-phyric andesite, fine-grained to aphanitic groundmass, euhedral medium-grained phenocrysts up to 4 mm, moderately magnetic, weak potassic and chlorite alteration, fine-grained disseminated magnetite (0.5-1%) and pyrite (trace)
08-Bu-78	Grab	Underground. Yaragua mine Level 2, 2,4 m east of point 218	---	---	1430	GC	White porphyritic andesite, intense adularia-sericite alteration, increased porosity because of alteration, sericite, quartz, milky white feldspar, undifferentiated clays, moderate calcite filling of porosity, euhedral fine to medium-grained disseminated pyrite (10%) and sphalerite (2%)
08-Bu-79	Grab	Underground. Yaragua mine Level 2, point 18 (west side)	---	---	1430	GC, TS	Medium green plagioclase-hornblende-phyric andesite, fine-grained to aphanitic groundmass, strong chlorite-epidote-calcite alteration, weak sericite alteration, euhedral fine-grained disseminated pyrite (3%)

Sample ID	Type	Location Description	Collar Coordinate Easting ¹	Collar Coordinate Northing ¹	Collar Elevation (m)	Used for:	Brief Sample Description
08-Bu-83	Grab	Surface outcrop	399981	741047	1644	Ar-Ar, TS, XRD	Light greyish white porphyritic andesite, intense adularia-sericite alteration, locally more clastic texture, quartz, milky white feldspar, sericite, euhedral fine to medium-grained disseminated pyrite (10%), weak late calcite infilling porosity
08-Bu-84	Grab	Surface outcrop	399183	741584	1655	GC	Dark grey plagioclase-pyroxene-phyric andesite, quartz-rich (very hard) aphanitic groundmass, weakly magnetic, porphyritic texture with euhedral stumpy medium-grained plagioclase and pyroxene phenocrysts, looks fresh, trace of fine-grained disseminated pyrite, interpreted as a porphyritic phase related to the Buriticá Stock and not to the Buriticá Andesite
08-Bu-85	Grab	Surface outcrop	399242	741513	1657	GC, TS	Dark greenish grey glomeroporphyritic plagioclase-pyroxene-phyric tonalite, medium-grained phenocrysts, very hard (quartz-rich) aphanitic groundmass, strong epidote-chlorite alteration of mafic phenocrysts, weakly magnetic
08-Bu-86	Grab	Surface outcrop	399265	741444	1669	GC	Medium greenish grey plagioclase-hornblende-phyric andesite, fine-grained to aphanitic groundmass, porphyritic texture with medium-grained euhedral phenocrysts (acicular hornblende, stumpy plagioclase), moderately magnetic, very weak chlorite-epidote alteration
08-Bu-88	Grab	Surface outcrop	399200	740854	1664	GC	Medium greenish grey plagioclase-hornblende-pyroxene-phyric andesite, fine-grained to aphanitic groundmass, euhedral medium-grained stumpy milky white plagioclase, acicular hornblende, fine stumpy chlorite altered pyroxene, weakly magnetic, moderate chlorite alteration of groundmass

Sample ID	Type	Location Description	Collar Coordinate Easting ¹	Collar Coordinate Northing ¹	Collar Elevation (m)	Used for:	Brief Sample Description
08-Bu-90	Grab	Surface outcrop	399574	740634	1900	TS	Medium brownish grey plagioclase-hornblende-phyric andesite, fine-grained to aphanitic groundmass, porphyritic texture with euhedral medium-grained phenocrysts (acicular hornblende, stumpy plagioclase), hornblende crystals average 3-4 mm but up to 15 mm, weakly to moderately magnetic, oxidized look
08-Bu-93	Core	Hole: BUSY-1 Depth: 30.9 m Azimuth: 241° Dip: -61°	399929	741212	1647	GC, TS	Light greenish white pyroxene-plagioclase-phyric equigranular diorite, moderate sericite alteration, strong epidote-chlorite alteration, weakly magnetic, subhedral fine-grained disseminated pyrite (3%)
08-Bu-96	Core	Hole: BUSY-1 Depth: 136.3 m Azimuth: 241° Dip: -61°	399929	741212	1647	GC, TS	Medium-grained equigranular quartz diorite, milky white subhedral plagioclase, stumpy subhedral pyroxene, few fine-grained quartz, moderate to strong chlorite-calcite replacement of pyroxene, weak epidote disseminated alteration, subhedral fine-grained disseminated pyrite (5%)
08-Bu-97	Core	Hole: BUSY-1 Depth: 159.0 m Azimuth: 241° Dip: -61°	399929	741212	1647	EM	Medium-grained equigranular quartz diorite, milky white subhedral plagioclase, stumpy subhedral pyroxene, few fine-grained quartz and biotite crystals, moderately magnetic, moderate to strong chlorite-calcite replacement of pyroxene, weak epidote disseminated alteration, cut by a one centimeter thick K-feldspar vein, trace of very fine-grained disseminated pyrite
08-GL-02	Grab	Underground. Yaragua mine Level 1, Taken by other so exact location is unknown	---	---	1484	FI	San Antonio vein, 10 cm-wide banded quartz-pyrite-sphalerite-chalcopyrite-galena-gold with coarse-grained vuggy quartz

Sample ID	Type	Location Description	Collar Coordinate Easting ¹	Collar Coordinate Northing ¹	Collar Elevation (m)	Used for:	Brief Sample Description
09-Bu-47	Grab	Surface outcrop	399336	741734	1657	GC, TS	Light greyish green plagioclase-pyroxene-phyric andesite (interpreted as the Buriticá Stock chilled margin), fine-grained to aphanitic quartz-rich groundmass, subhedral rounded plagioclase up to 3-4 mm and euhedral stumpy dark pyroxene up to 2 mm, moderate chlorite alteration of mafic and groundmass and disseminated epidote alteration
09-Bu-107	Grab	Surface outcrop	398934	739629	1946	GC, TS	Dark greenish grey plagioclase-hornblende-phyric andesite, fine-grained to aphanitic groundmass, porphyritic texture with euhedral stumpy plagioclase up to 1-2 mm and euhedral elongate hornblende up to 10 mm, weakly magnetic, strong chlorite-carbonate alteration of mafic minerals, late calcite and quartz infilling of porosity and calcite stringers
09-Bu-138	Grab	Surface outcrop	400969	742212	1054	FI	10 cm-wide quartz-calcite-sphalerite-pyrite vein with trace chalcopyrite in basalt, N45/70
09-Bu-139	Grab	Surface outcrop	400953	742288	1063	GC, TS	Medium to dark grey fine-grained equigranular pillowed basalt, weakly magnetic, moderate chlorite-epidote alteration, trace of euhedral fine-grained pyrite
09-Bu-149	Grab	Surface outcrop	400372	741560	1350	GC, TS	Medium to dark grey fine-grained equigranular pillowed basalt, weakly magnetic, moderate chlorite-epidote alteration, trace of euhedral fine-grained pyrite
09-Bu-172	Grab	Surface outcrop	397820	739793	2055	GC, TS	Medium to dark grey glomeroporphyritic plagioclase-pyroxene-phyric tonalite, glomeroporphyritic up to 6-7 mm in diameter, very hard (quartz-rich) aphanitic groundmass, weakly magnetic, strong chlorite alteration, weak calcite alteration

Sample ID	Type	Location Description	Collar Coordinate Easting ¹	Collar Coordinate Northing ¹	Collar Elevation (m)	Used for:	Brief Sample Description
09-Bu-173	Grab	Surface outcrop	397777	739843	2054	GC, TS	Coarse to locally medium-grained equigranular tonalite, anhedral quartz, euhedral to subhedral plagioclase, anhedral to subhedral pyroxene, fine-grained biotite, interlocking crystals texture, moderate chlorite alteration of mafic minerals, locally small pockets of fine-grained equigranular tonalite/diorite (magma mixing?)
09-Bu-177	Grab	Surface outcrop	397064	739663	2149	EM, GC, TS	Dark greenish grey fine-grained to aphanitic equigranular basalt, fresh to weakly chlorite altered, euhedral to anhedral fine-grained disseminated pyrite (1-3%), taken on the west side of the Buriticá Stock
09-Bu-191	Grab	Surface outcrop	397938	741600	1931	EM, GC, TS	Medium-grained equigranular tonalite, anhedral quartz, euhedral plagioclase, anhedral to subhedral hornblende, moderate chlorite alteration of hornblende, euhedral fine-grained disseminated pyrite (1%)
09-Bu-204	Grab	Surface outcrop	399151	740258	1934	GC, TS	Medium-grained equigranular tonalite, anhedral quartz, euhedral plagioclase, anhedral to subhedral pyroxene, strong chlorite alteration of hornblende, weakly magnetic, trace euhedral fine-grained disseminated pyrite
09-Bu-205	Grab	Surface outcrop	399466	740678	1876	EM, GC, TS	Medium greenish grey plagioclase-hornblende-phyric andesite, fine-grained to aphanitic groundmass, porphyritic texture with euhedral medium-grained phenocrysts (acicular hornblende, stumpy plagioclase), hornblende crystals average 3-4 mm but up to 10 mm, magnetic, locally trachytic texture (especially noticeable from oriented acicular hornblende crystals), few polymictic clasts/xenoliths are present (2-3 cm diameter)
09-Bu-217	Grab	Surface outcrop	397721	741849	1830	FI	30 cm-wide banded quartz-sphalerite-chalcopyrite-pyrite vein in strongly chlorite altered tonalite, late calcite in the center of the vein and infilling porosity, N135/50

Sample ID	Type	Location Description	Collar Coordinate Easting ¹	Collar Coordinate Northing ¹	Collar Elevation (m)	Used for:	Brief Sample Description
09-Bu-226	Grab	Surface outcrop	399724	741673	1527	GC, TS	Medium to dark green plagioclase-pyroxene-phyric andesite, fine-grained to aphanitic groundmass, euhedral plagioclase phenocrysts up to 2 mm, glomeroporphyritic texture with pyroxene crystal aggregates up to 8-10 mm, individual pyroxene crystals are euhedral and up to 1-2 mm, weakly magnetic, strong chlorite-epidote alteration, weak calcite alteration, 5% fine-grained disseminated pyrite (interpreted as a dyke of material similar to that of the dykes cutting the Buriticá Stock)
09-Bu-234	Grab	Surface outcrop	399767	741347	1704	GC, TS	Medium greenish grey plagioclase-pyroxene-hornblende-phyric andesite, fine-grained to aphanitic groundmass, porphyritic texture with euhedral plagioclase laths up to 3 mm and mafic phenocrysts up to 4-5 mm, weakly magnetic, moderate to strong chlorite-epidote alteration, epidote located along fractures, fine-grained pyrite along fractures
09-Bu-242	Grab	Surface outcrop	399945	740924	1679	GC, TS	Light grey plagioclase-hornblende-pyroxene-phyric andesite, fine to aphanitic groundmass, euhedral phenocrysts with elongate hornblende (average size 1-2 mm up to 6 mm), pyroxene (average 1 mm), and plagioclase (up to 3 mm), strong chlorite alteration of pyroxene, weak calcite alteration, subhedral fine-grained disseminated pyrite (5%)
09-Bu-255	Grab	Surface outcrop	401768	740708	1058	GC	Light greenish grey medium-grained equigranular tonalite, anhedral quartz, euhedral plagioclase, subhedral to euhedral (acicular) hornblende, strong chlorite and calcite alteration, trace very fine-grained disseminated pyrite, weak sheared texture (nearby fault?)

Sample ID	Type	Location Description	Collar Coordinate Easting ¹	Collar Coordinate Northing ¹	Collar Elevation (m)	Used for:	Brief Sample Description
09-Bu-261	Grab	Surface outcrop	401788	741730	925	GC, TS	Light greenish grey fine to medium-grained equigranular granite, quartz grains finer grained than feldspar or mafic minerals, weakly magnetic, strong chlorite-magnetite alteration of mafic minerals, moderate epidote alteration of plagioclase, weak calcite alteration, rock is highly fractured with evidence of shear along fractures (sigmoidal crystal shapes)
09-DH-3	Core	Hole: BUSY-31 Depth: 51.2 m Azimuth: 215° Dip: -45°	399915	741355	1655	TS, XRD	White porphyritic andesite, intense adularia-sericite alteration, undifferentiated clays, quartz, milky white feldspar, weak carbonate alteration, subhedral fine-grained pyrite (15%) disseminated and along fractures
09-DH-11	Core	Hole: BUSY-33 Depth: 99.0 m Azimuth: 335° Dip: -81°	399624	740908	1775	XRD	Light grey to white porphyritic andesite, strong adularia-sericite alteration, strong carbonate flooding, undifferentiated clays, quartz, milky white feldspar, trace of very fine-grained sericite, subhedral fine-grained pyrite (15%) disseminated and along fractures, and subhedral medium-grained sphalerite (2%) along fractures
09-M-1	Grab	Underground. Yaragua mine Level 1	400035	741338	1484	FI, SI, TS, XRD	San Antonio vein, 15 cm-wide banded quartz-pyrite-sphalerite-galena-chalcopyrite vein with coarse-grained vuggy quartz and late calcite infilling porosity, and quartz-adularia-sericite altered wallrock, N245/72
09-M-2	Grab	Underground. Yaragua mine Level 1	400045	741349	1484	SI	Centena vein, 30 cm-wide banded quartz-pyrite-galena vein with trace sphalerite, late coarse-grained vuggy quartz, late calcite infilling porosity, highly oxidized, N118/90
09-M-3	Grab	Underground. Yaragua mine Level 1	400066	741339	1484	FI	Centena vein, 10 cm-wide calcite-stibnite breccia vein with sub-angular to sub-rounded quartz-pyrite-sphalerite-galena-chalcopyrite-gold clasts, N110/81

Sample ID	Type	Location Description	Collar Coordinate Easting ¹	Collar Coordinate Northing ¹	Collar Elevation (m)	Used for:	Brief Sample Description
09-M-4	Grab	Underground. Yaragua mine Level 1	400078	741335	1484	FI	Centena vein, 10 cm-wide calcite breccia vein with sub-rounded quartz-pyrite-sphalerite-galena-chalcopryrite-gold clasts, N102/90
09-M-8	Grab	Underground. Yaragua mine Level 1	399970	741160	1484	FI, SI	Murcielagos vein, 15 cm-wide banded quartz-pyrite-galena-chalcopryrite-sphalerite-gold vein, late calcite-rich fluid pulse weakly brecciating the vein and filling porosity, N66/90
09-M-9	Grab	Underground. Yaragua mine Level 1	400011	741317	1484	FI	San Antonio vein, 10 cm-wide banded pyrite-sphalerite-quartz with trace galena and chalcopryrite, and with late calcite infilling porosity, N75/80
09-M-12	Grab	Underground. Yaragua mine Level 1	399929	741303	1484	FI	San Antonio vein, 8-10 cm-wide banded quartz-sphalerite-pyrite-chalcopryrite-galena vein with coarse-grained vuggy quartz/amethyst and late calcite infilling porosity, N270/90
09-M-13	Grab	Underground. Yaragua mine Level 1	399919	741300	1484	FI, SI	San Antonio vein, 4 cm-wide banded quartz-pyrite-sphalerite-galena-chalcopryrite-gold vein, vein is 90% amethyst quartz, N270/90
09-M-14	Grab	Underground. Yaragua mine Level 1	399854	741281	1484	FI, SI	San Antonio vein, 5-6 cm-wide banded quartz-pyrite-sphalerite-galena-chalcopryrite-gold vein with coarse-grained quartz and weak late calcite infilling of porosity, N105/75

¹Collar coordinates are in WGS 84 / UTM zone 18N projection

²XRD = X-ray diffraction sample

³TS = thin section sample

⁴GC = lithochemical sample

⁵Ar-Ar = Ar-Ar geochronology sample

⁶EM = electron microprobe sample

⁷FI = fluid inclusion sample

⁸SI = sulfur isotope sample

Appendix D: Petrographic Descriptions

Sample: 08-Bu-7

Lithology: Plagioclase-Pyroxene-Phyric Andesite

Unit: Buriticá Andesite

Primary Minerals:

Plagioclase (30%) Euhedral, lath-shaped, average 0.5-0.6 mm up to 1.5 mm, polysynthetic twinning, some crystals are zoned, most are aligned along preferential orientation

Augite (20%) Euhedral, stumpy, octagonal, average 0.5 mm up to 1 mm, simple and lamellar twinning, edges of crystals don't look at equilibrium with the groundmass

Apatite (trace) Euhedral, very fine-grained, as inclusions in augite

Groundmass (52%) Fine-grained to microcrystalline

Alteration Minerals:

Chlorite (10%) Very fine-grained, disseminated as small clusters throughout the matrix and along fractures

Epidote (1%) Subhedral, found along fractures

Pyrrhotite (8%) Subhedral, 0.01 to 0.2 mm diameter, strongly anisotropic, seems present both in altered zones and less altered zones of the sample, exhibits different texture (exsolution-like) when associated with chlorite-rich zones

Rusty iron oxides (2%) Anhedral, associated with pyrrhotite-rich zones

Opaque Minerals:

Pyrite (trace) Subhedral, very fine-grained, disseminated

Chalcopyrite (trace) Anhedral, very fine-grained, disseminated

Texture:

Holocrystalline, weakly porphyritic, fine-grained to microlithic plagioclase groundmass, weakly developed trachytic texture, weak propylitic alteration (chlorite-epidote).

Sample: 08-Bu-8

Lithology: Plagioclase-Pyroxene-Biotite-Phyric Andesite

Unit: Buriticá Andesite

Primary Minerals:

Plagioclase (45%) Euhedral, lath-shaped, average 0.4-0.6 mm up to 1 mm, polysynthetic and simple twinning, locally zoned

Augite (25%) Euhedral, stumpy, octagonal, 0.5-1 mm in diameter, very rough looking (altered)

Biotite (5%) Subhedral, 0.2-0.3 mm, light to dark brown, strongly pleochroic and birefringent, locally encloses plagioclase crystals

Apatite (trace) Euhedral, prismatic, very fine-grained, found as inclusions within some augite and biotite crystals

Alteration Minerals:

Orthoclase (15%) Anhedral, medium-grained, occurs as oikocrysts enclosing other minerals, simple twinning

Biotite (3%) Anhedral, 0.1-0.3 mm, dark brown, weakly pleochroic and birefringent

Sericite (1%) Very fine-grained, locally replacing biotite

Chlorite (trace) Very fine-grained, occurs as small clusters disseminated within the rock

Epidote (trace) Very fine-grained, disseminated

Opaque Minerals:

Magnetite (8%) Subhedral, 0.05-0.2 mm, disseminated

Pyrite (trace) Anhedral, very fine-grained, disseminated

Chalcopyrite (trace) Anhedral, very fine-grained, disseminated

Texture:

Holocrystalline, poikilitic texture.

Sample: 08-Bu-16

Lithology: Plagioclase-Phyric Andesite

Unit: Buriticá Andesite

Primary Minerals:

Intense phyllic alteration, no original texture left, very few plagioclase phenocryst relics intensely altered to quartz-sericite-calcite with little plagioclase remnants

Groundmass is microcrystalline and seems very altered, mineral identification is difficult

Alteration Minerals:

Calcite (15%) Anhedral, fine-grained, filling porosity and disseminated clusters in the groundmass, also euhedral calcite along fractures

Quartz (10%) Anhedral, fine-grained, filling porosity

Sericite (7%) Euhedral to subhedral, fine-grained, disseminated and altering plagioclase phenocrysts

Opaque Minerals:

Pyrite (10%) Subhedral, fine-grained, disseminated, locally associated with quartz and filling porosity

Sphalerite (trace) Anhedral, very fine-grained, disseminated

Texture:

Intense phyllic alteration, porous rock (3-4%), few very altered zones so fine-grained mineral identification is not possible.

Sample: 08-Bu-19

Lithology: Plagioclase-Phyric Andesite

Unit: Buriticá Andesite

Primary Minerals:

Plagioclase (25%) Euhedral crystals, medium-grained, trachytic texture, now almost completely altered to a sericite-quartz-calcite assemblage

Groundmass (75%) Microcrystalline, altered plagioclase microliths

Alteration Minerals:

Quartz (8%) Anhedral crystals, fine to very fine-grained, 0.1 mm crystals disseminated throughout groundmass, approx. 40% of altered plagioclase

Sericite (15%) Very fine-grained, alteration of plagioclase, locally larger (0.1-0.3 mm) euhedral crystals

Chlorite (5%) Anhedral, very fine-grained, disseminates patches of chlorite, some patches have a vague stumpy crystal-like shape (could be relics of pyroxene)

Opaque Minerals:

Pyrite (3%) Euhedral crystals, fine-grained, disseminated throughout groundmass and along fractures

Calcite/Dolomite (6%) Anhedral, infilling porosity and within altered plagioclase

Texture:

Holocrystalline, porphyritic, microlithic plagioclase groundmass. Well-developed trachytic alignment of plagioclase phenocrysts. Strong phyllic alteration.

Sample: 08-Bu-21

Lithology: Matrix-supported polymictic breccia

Unit: Yaragua Breccia

Primary Minerals:

Plagioclase (trace) Euhedral to subhedral, 0.5-1.5 mm, located within breccia matrix and porphyritic clasts, polysynthetic twinning, originally 25% of rock but almost all phenocrysts are altered to calcite-sericite-quartz

Matrix (50%) Porphyritic, microcrystalline groundmass (75% of matrix), unable to identify minerals in groundmass

Alteration Minerals:

Quartz (20%) Anhedral, fine-grained, mostly within altered plagioclase, some clasts exclusively made of very fine-grained quartz (possibly recrystallized chert clasts)

Sericite (5%) Subhedral to euhedral, very fine-grained, mostly within altered plagioclase

Dolomite/calcite (20%) Anhedral, fine-grained, mostly replacing plagioclase, locally flooding the matrix and filling porosity

Opaque Minerals:

Pyrite (12%) Subhedral to euhedral, fine-grained, disseminated mostly in matrix and a little in porphyritic clasts (fine-grained quartz-rich clasts don't have pyrite)

Sphalerite (trace) Anhedral, very fine-grained, located specifically in some altered phenocrysts

Texture:

Matrix-supported polymictic breccia, plagioclase-rich porphyritic matrix, most clasts seem to be of same lithology as matrix, some clasts are quartz-rich and very fine-grained (chert?). Intense phyllic alteration, matrix so fine-grained mineral identification is not possible.

Sample: 08-Bu-31

Lithology: Andesite

Unit: Buriticá Andesite

Primary Minerals:

Intense phyllic alteration, no primary mineral nor texture preserved

Alteration Minerals:

Sericite (30%) Euhedral, few fine-grained disseminated crystals, mostly occurs as very fine-grained elongate crystals within the groundmass

Quartz (24%) Anhedral, very fine to fine-grained, disseminated throughout the groundmass and filling porosity

Calcite (19%) Anhedral to subhedral, fine-grained, disseminated throughout the groundmass and filling porosity

Opaque Minerals:

Pyrite (10%) Euhedral to subhedral, medium-grained, disseminated

Sphalerite (15%) Anhedral, very fine to medium-grained, disseminated

Galena (0.5%) Anhedral to subhedral, very fine-grained, associated with sphalerite

Chalcopyrite (trace) Occurs as chalcopyrite disease within sphalerite

Texture:

Intense phyllic alteration, no primary texture preserved, porous (2%).

Sample: 08-Bu-37

Lithology: Matrix-supported polymictic breccia

Unit: Yaragua Breccia

Primary Minerals:

Intense phyllic alteration, no primary mineral nor texture preserved. Very few plagioclase relic now composed of quartz-sericite

Alteration Minerals:

Quartz (35%) Anhedral, locally euhedral open space terminations when filling porosity, very fine to fine-grained, mostly very fine-grained disseminated throughout the groundmass

Sericite (25%) Euhedral to anhedral, very fine-grained, rare fine-grained disseminated crystals, mostly very fine elongate crystals within the groundmass

Calcite (10%) Anhedral to subhedral, fine-grained, filling porosity

Opaque Minerals:

Pyrite (8%) Subhedral, fine to coarse-grained, disseminated, locally filling porosity

Sphalerite (trace) Anhedral, very fine-grained, disseminated

Texture:

Intense phyllic alteration, no primary texture preserved (although there could be a weak clastic texture relic), porous (4-5%), some altered groundmass zones are too fine-grained for mineral identification.

Sample: 08-Bu-40

Lithology: Matrix-supported polymictic breccia

Unit: Yaragua Breccia

Primary Minerals:

Intense alteration, no primary mineral preserved

Alteration Minerals:

Quartz (77%) Subhedral, very fine-grained, granular crystals representing most of the rock, and

fine-grained, vuggy quartz (15%) with euhedral termination along fractures and filling porosity

Calcite (15%) Subhedral, fine-grained, filling porosity, coeval with the vuggy quartz

Opaque Minerals:

Pyrite (5%) Euhedral to subhedral, fine to medium-grained, preferentially located within matrix

Sphalerite (1-2%) Anhedral, fine-grained, preferentially located within matrix

Galena (trace) Anhedral, fine-grained, associated with sphalerite

Chalcopyrite (trace) Anhedral, very fine-grained, associated with sphalerite and occurring as chalcopyrite disease

Texture:

Matrix-supported polymictic breccia with sub-rounded clasts up to 3-4 cm, clasts are highly fractured, porous (1%), lots of vuggy calcite and quartz. Some clasts might have been quartz-rich prior to alteration (chert), but because of the intense alteration, all the quartz now present is interpreted as secondary.

Sample: 08-Bu-42

Lithology: Plagioclase-Phyric Andesite

Unit: Buriticá Andesite

Primary Minerals:

Plagioclase (25%) Euhedral, lath-shaped, 0.5-1 mm, weakly trachytic, undulatory extinction, simple twinning, strongly altered to quartz-sericite

Pyroxene (1%) Euhedral, stumpy, 0.5-1 mm, very altered, only crystals shape is identifiable

Groundmass (50%) Microcrystalline, mineral identification difficult, lots of very fine sericite crystals

Alteration Minerals:

Sericite (25%) Euhedral to subhedral, very fine-grained, located within the groundmass and the altered plagioclase, few fine-grained (0.1-0.3 mm) euhedral sericite crystals disseminated

Quartz (10%) Anhedral, very fine-grained, disseminated throughout the groundmass, located within the altered plagioclase, and filling porosity

Opaque Minerals:

Pyrite (12%) Euhedral to subhedral, fine-grained, disseminated

Sphalerite (trace) Anhedral, very fine-grained, disseminated

Texture:

Holocrystalline, porphyritic with phenocrysts up to 1 mm and microcrystalline groundmass, weakly developed trachytic texture.

Sample: 08-Bu-46

Lithology: Plagioclase-Phyric Andesite

Unit: Buriticá Andesite

Primary Minerals:

Plagioclase (15%) Euhedral crystals, average 1 mm, most of them completely altered

Groundmass mostly contains secondary quartz

Alteration Minerals:

Quartz (52%) Anhedral crystals, very fine-grained, main component of groundmass

Epidote (20%) Granular crystals, fine to very fine-grained, disseminated throughout the groundmass

Chlorite (3%) Acicular crystals, very fine-grained

Calcite (trace) Associated with epidote-rich zones

Opaque Minerals:

Magnetite (10%) Subhedral crystals, disseminated throughout the groundmass and following fractures

Texture:

Holocrystalline, porphyritic. Strong propylitic alteration.

Sample: 08-Bu-51

Lithology: Clast-supported polymictic breccia

Unit: Yaragua Breccia

Primary Minerals:

Plagioclase (5%) Euhedral, 0.3-1 mm, polysynthetic and simple twinning, partially replaced by sericite, located exclusively in porphyritic andesite clasts

Alteration Minerals:

Quartz (50%) Anhedral, very fine-grained, granular, mostly located in quartz-rich clasts (likely recrystallized chert clasts)

Sericite (20%) Subhedral, acicular, very fine-grained, replacing plagioclase and disseminated in porphyritic andesite clast groundmass

Chlorite (15%) Anhedral to subhedral, acicular, very fine-grained, located in porphyritic andesite clast groundmass and in breccia matrix

Epidote (5%) Anhedral, very fine-grained, located in matrix

Calcite (1-2%) Subhedral, fine-grained, in matrix and filling porosity

Opaque Minerals:

Pyrite (3%) Euhedral to subhedral, fine-grained, located in matrix

Sphalerite (3%) Anhedral, fine-grained, located in matrix

Galena (trace) Anhedral, very fine-grained, associated with sphalerite

Chalcopyrite (trace) Anhedral, very fine-grained, occurs as chalcopyrite disease

Texture:

Clast-supported polymictic breccia with angular to sub-rounded clasts up to 3-4 cm, strong phyllic alteration, sericite preferentially in andesitic clasts (alteration of plagioclase), lots of sulfides in matrix.

Sample: 08-Bu-72

Lithology: Plagioclase-Pyroxene-Phyric Andesite

Unit: Buriticá Andesite

Primary Minerals:

Plagioclase (15%) Subhedral to euhedral crystals, lath-shaped zoned crystals, fine-grained, polysynthetic twinning

Augite (12%) Euhedral stumpy crystals, light greenish white, average 0.5 mm, simple twinning

Biotite (5%), Euhedral to subhedral crystals, average 0.5 mm, light to dark brown, strong pleochroism and birefringence

Apatite (trace), Euhedral crystals, fine-grained, prismatic, chadacrysts within augite and plagioclase

Groundmass (60%) Microcrystalline, plagioclase microliths

Alteration Minerals:

Biotite (4%) Anhedral, average 0.1 mm, dark brown, weak pleochroism and birefringence, associates with mafic crystals

Magnetite (3%) Subhedral to anhedral crystals, fine-grained, disseminated throughout the groundmass

Chlorite (1%) Light to dark green, fine to very fine-grained, replacing augite

Sericite (trace) Very fine-grained, associated with most altered parts of the sample

Opaque Minerals:

Pyrite (trace) Associated with most altered parts of the sample

Texture:

Holocrystalline, porphyritic, locally glomeroporphyritic. Biotite and chlorite are replacing mafic crystals. Plagioclase weakly altered. Overall the rock is pretty fresh.

Sample: 08-Bu-74

Lithology: Plagioclase-Pyroxene-Biotite-Phyric Andesite

Unit: Buriticá Andesite

Primary Minerals:

Plagioclase (30%) Euhedral to subhedral, 1-4 mm, polysynthetic twinning, simple twinning, some zoned crystals

Augite (27%) Euhedral to subhedral, stumpy, octagonal, 1-10 mm, simple twinning

Biotite (3-4%) Euhedral, average 0.5 mm up to 1.2 mm, light beige to dark brown, strong pleochroism and birefringence

Groundmass (30%) Microcrystalline, mineral identification difficult, lots of very fine anhedral secondary biotite

Alteration Minerals:

Biotite (2-3%) Anhedral, fine-grained, dark brown, very weak pleochroism and weak birefringence, altering mafic minerals, very fine-grained within groundmass

Epidote (trace) Very fine-grained, traces only

Opaque Minerals:

Magnetite (7%) Subhedral to anhedral, very fine-grained, disseminated crystal clusters and located along fractures

Pyrite (trace) Subhedral, very fine-grained, disseminated

Texture:

Holocrystalline, porphyritic, weak potassic biotite-dominant alteration.

Sample: 08-Bu-79

Lithology: Plagioclase-Hornblende-Phyric Andesite

Unit: Buriticá Andesite

Primary Minerals:

Strong propylitic alteration of the sample, all phenocrysts have been altered from their original minerals. Primary minerals interpreted as being plagioclase and hornblende on the basis of pseudomorph shapes.

Groundmass (75%) Microcrystalline, plagioclase microliths

Alteration Minerals:

Chlorite (10%) Dark green, replacing hornblende

Epidote (5%) Subhedral crystals, locally radial habit, fine-grained, disseminated throughout the groundmass

Sericite (5%) Very fine-grained, replacing plagioclase

Quartz (2%), Very fine-grained, disseminated throughout the groundmass, infilling porosity, and locally concentrated in altered plagioclase

Opaque Minerals:

Pyrite (2%) Euhedral to subhedral crystals, average 0.2 mm, disseminated throughout the groundmass

Calcite (trace) Associated with chlorite

Texture:

Holocrystalline, porphyritic. Plagioclase phenocrysts are completely altered. Mafic phenocrysts completely chlorite altered.

Sample: 08-Bu-83

Lithology: Plagioclase-Phyric Andesite

Unit: Buriticá Andesite

Primary Minerals:

Strong phyllic/argillic alteration of the sample, all phenocrysts have been altered from their original minerals. Few relics of medium-grained plagioclase phenocrysts are seen.

Groundmass (77%) Microcrystalline, quartz and feldspar

Alteration Minerals:

Quartz (10%) Anhedral crystals, fine-grained in groundmass and partially replacing plagioclase phenocrysts, medium-grained filling porosity

Pyrite (6%) Subhedral to anhedral crystals, average 0.1-0.2 mm, disseminated throughout the rock, associated with sericite and epidote clusters

Sericite (4%) Subhedral crystals, average 0.25 mm when individual crystals in groundmass, very fine-grained when partially replacing plagioclase

Epidote (3%) Rounded grains, strong relief, very fine-grained, partially replacing plagioclase and found as clusters within the groundmass

Opaque Minerals:

Hematite (trace)

Texture:

Holocrystalline, porphyritic. Plagioclase phenocrysts completely saussuritized. Alteration increased the rock porosity, which is now filled with quartz.

Sample: 08-Bu-85

Lithology: Porphyritic Tonalite

Unit: Buriticá Stock

Primary Minerals:

Plagioclase (15% phenocrysts, 25% in groundmass) Euhedral to subhedral, 0.5-2.5 mm, simple and polysynthetic twinning, locally zoned crystals, undulatory extinction, occurs as glomeroporhs up to 6-7 mm, also major component of the groundmass (very fine-grained laths)

Quartz (40%) Anhedral, granular, <0.1 mm, component of the groundmass

Augite (likely up to 10%) Only one crystal left, strong epidote-chlorite alteration of mafic phenocrysts, euhedral, average 2-3 mm, simple twinning, occurred as glomeroporhs up to 6-7 mm

Zircon (trace) Euhedral, prismatic, very fine-grained, colorless, strong relief, strongly birefringent, only a few crystals observed as inclusions in plagioclase

Groundmass (75%) Microcrystalline, quartz-plagioclase-epidote-chlorite-magnetite

Alteration Minerals:

Epidote (8% augite replacement, 8% in groundmass) Subhedral to anhedral, very fine-grained, disseminated throughout the groundmass and replacing mafic phenocrysts

Chlorite (2% augite replacement, 1-2% in groundmass) Anhedral to subhedral, acicular, very fine-grained, disseminated throughout the groundmass and replacing mafic phenocrysts

Quartz (trace) Anhedral, very fine-grained, along fractures with chlorite

Calcite (trace) Anhedral, very fine-grained, along fractures with chlorite

Opaque Minerals:

Magnetite (5%) Subhedral to anhedral, few fine-grained disseminated crystals, most of it is very fine-grained and disseminated throughout the groundmass

Chalcopyrite (trace) Anhedral, very fine-grained, only a few disseminated grains

Texture:

Holocrystalline, glomeroporphyritic with crystal aggregates up to 7 mm and microcrystalline groundmass, strong propylitic alteration.

Sample: 08-Bu-90

Lithology: Plagioclase-Hornblende-Pyroxene-Phyric Andesite

Unit: Buriticá Andesite

Primary Minerals:

Plagioclase (10%) Euhedral, stumpy, 0.5-3 mm, simple and polysynthetic twinning, some crystals are zoned, undulatory extinction,

Hornblende (7%) Euhedral to subhedral, average 0.5-2 mm up to 10 mm, brownish green, strongly pleochroic, simple twinning

Augite (3%) Euhedral to anhedral (rounded), average 0.1-0.3 mm up to 1 mm, transparent, non pleochroic, strong birefringence, simple twinning, crystals (principally crystal edges) are altered and don't look at equilibrium with the magma

Groundmass (76%) Cryptocrystalline, mineral identification not possible

Opaque Minerals:

Magnetite (4%) Subhedral, 0.1-0.2 mm, disseminated, also very fine-grained euhedral to subhedral crystals in disseminated in groundmass

Chalcopyrite (trace) Anhedra, very fine-grained, associated with magnetite

Rusty red very fine-grained unidentifiable mineral (trace) Iron oxide?, disseminated in groundmass, associated mostly with mafic minerals

Texture:

Hypocrystalline, porphyritic with locally some hornblende and some plagioclase glomeroporphs, one hornblende phenocryst surrounded by altered pyroxene chunks, pyroxene does not look at equilibrium.

Sample: 08-Bu-93

Lithology: Plagioclase-Pyroxene-Phyric Andesite

Unit: Buriticá Andesite

Primary Minerals:

Plagioclase (45%) Euhedral to subhedral, average 0.5-1 mm, simple and polysynthetic twinning, undulatory extinction, some crystals zoned

Augite (10%) Euhedral, stumpy, octagonal, 0.5-1 mm, simple twinning, strongly altered to chlorite-epidote=calcite

Alteration Minerals:

Orthoclase (15%) Anhedra, 0.3-0.5 mm, undulatory extinction

Chlorite (12%) Anhedra to euhedral, very fine-grained, replacing mafic minerals

Epidote (10%) Anhedra, very fine-grained to fine-grained, altering mafic minerals and along fractures, latest alteration event

Quartz (1-2%) Anhedra, 0.1-0.2 mm, disseminated

Calcite (trace) Anhedra, very fine-grained, associated with epidote and replacing mafic minerals

Biotite (Trace) Euhedral to subhedral, fine-grained, being replaced by sericite, only traces left

Opaque Minerals:

Magnetite (5%) Subhedral, 0.1-0.5 mm, disseminated

Pyrite (3%) Subhedral, 0.2-0.5 mm, associated with sericite

Chalcopyrite (1%) Anhedra, very fine-grained, disseminated, concentrated in fine-grained zones of the rock

Texture:

Holocrystalline, equigranular, multiple alteration events overprinting each other (potassic-phylic-propylitic).

Sample: 08-Bu-96

Lithology: Plagioclase-Pyroxene-Phyric Quartz Diorite

Unit: Buriticá Stock

Primary Minerals:

Plagioclase (50%) Euhedral to subhedral, lath-shaped, 0.3-1 mm, polysynthetic and simple twinning, undulatory extinction

Augite (15%) Euhedral to subhedral, octagonal, stumpy, average size 0.5-1 mm, up to 2 mm, simple twinning, strongly altered to chlorite-calcite

Quartz (5%) Anhedra, 0.1-0.4 mm, late in mineral paragenesis (filling remaining space)

Sphene (2%) Anhedra, fine to very fine-grained, very high relief, colorless, very strong birefringence, very low reflectance, associated with pyrite

Alteration Minerals:

Chlorite (8%) Very fine-grained, replacing augite crystals

Calcite (8%) Anhedra, fine to very fine-grained, mainly replacing augite minerals

Epidote (3%) Anhedra, granular, very fine-grained, disseminated

Opaque Minerals:

Pyrite (7%) Anhedra to subhedral, fine to very fine-grained, disseminated

Texture:

Holocrystalline, equigranular, fine-grained, few medium-grained augite crystals, strong chlorite-

calcite alteration of mafic minerals.

Sample: 08-Bu-97

Lithology: Plagioclase-Pyroxene-Biotite-Phyric Quartz Diorite

Unit: Buriticá Stock

Primary Minerals:

Plagioclase (50%) Euhedral to subhedral, lath-shaped, 0.3-1 mm, polysynthetic and simple twinning, undulatory extinction

Augite (15%) Euhedral to subhedral, octagonal, stumpy, average size 1 mm, up to 4 mm, simple twinning, strongly altered to chlorite-calcite

Quartz (5%) Anhedral, 0.1-0.4 mm, late in mineral paragenesis (filling remaining space)

Biotite (2-3%) Euhedral to subhedral, 0.2-0.6 mm, strongly pleochroic, partially altered to chlorite

Alteration Minerals:

Orthoclase (10%) Anhedral, fine-grained, disseminated throughout the rock, and euhedral, fine-grained, located in a 1 cm thick orthoclase-quartz vein

Chlorite (8%) Very fine-grained, replacing augite crystals and partially altered biotite crystals

Calcite (4%) Anhedral, fine to very fine-grained, replacing augite minerals

Biotite (1-2%) Anhedral, very fine-grained, weakly to non-pleochroic, partially altered to chlorite

Epidote (1-2%) Subhedral, very fine-grained, disseminated

Magnetite (6%) Subhedral, fine to very fine-grained, disseminated, associated with altered mafic minerals

Opaque Minerals:

Pyrite (1%) Anhedral, fine to very fine-grained, disseminated

Chalcopyrite (trace) Anhedral, very fine-grained, disseminated

Texture:

Holocrystalline, equigranular, fine-grained, few medium-grained augite crystals, cut by a 1 cm thick orthoclase(80%)-quartz(20%) vein, strong chlorite-calcite alteration of mafic minerals.

Sample: 09-Bu-47

Lithology: Porphyritic Tonalite

Unit: Buriticá Stock

Primary Minerals:

Phenocrysts (30%) Medium-grained, completely altered from their original mineral

Groundmass (70%) Microcrystalline, anhedral quartz and plagioclase microliths

Alteration Minerals:

Epidote (15%) Fine-grained, replacing phenocrysts

Chlorite (10%) Fine-grained, light to medium green, disseminated throughout groundmass and replacing phenocrysts

Calcite (5%) Associated with epidote

Opaque Minerals:

Hematite (trace) Associated with chlorite

Texture:

Holocrystalline, porphyritic. Strong propylitic alteration.

Sample: 09-Bu-107

Lithology: Plagioclase-Hornblende-Phyric Andesite

Unit: Buriticá Andesite

Primary Minerals:

Plagioclase (1-2%) Euhedral, 1-3 mm, zoned, strongly altered

There are some relics of hornblende crystal shapes, but all have been entirely altered to chlorite-carbonate

Groundmass (83%) Microcrystalline, lots of altered plagioclase microliths

Alteration Minerals:

Calcite/dolomite (6%) Anhedral, fine-grained, replacing hornblende and filling porosity

Quartz (5%) Anhedral, fine-grained, filling porosity
Chlorite (3%) Anhedral, very fine-grained, light to medium green, replacing hornblende

Opaque Minerals:

Magnetite (2%) Subhedral to euhedral, fine-grained, disseminated, some very fine-grained euhedral magnetite disseminated throughout the groundmass
Pyrite (trace) Anhedral to subhedral, very fine-grained, disseminated
Chalcopyrite (trace) Anhedral, very fine-grained, disseminated

Texture:

Holocrystalline, porphyritic with phenocrysts up to 2-3 mm, two xenoliths observed about 2 mm each in diameter, porosity filled with calcite and quartz.

Sample: 09-Bu-139

Lithology: Basalt

Unit: Barroso Basalt

Primary Minerals:

Plagioclase (30%) Euhedral, elongate, 0.1-0.5 mm, lath-shaped
Augite (20%) Subhedral, stumpy, average size 0.1-0.2 mm, up to 0.5-0.6 mm, simple twinning, partially altered to epidote-chlorite

Alteration Minerals:

Chlorite (25%) Anhedral to subhedral, very fine-grained, mainly amygdale and fracture filling along with quartz, also disseminated throughout the rock and partially replacing pyroxene
Epidote (10%) Anhedral to subhedral, very fine-grained, disseminated, partially replacing pyroxene
Quartz (10%) Anhedral to subhedral, fine to very fine-grained, mainly amygdale and fracture filling, also disseminated throughout the rock

Opaque Minerals:

Pyrrhotite (4%) Anhedral, very fine-grained, disseminated
Pyrite (1%) Subhedral, fine-grained, disseminated
Chalcopyrite (trace) Anhedral, very fine-grained, disseminated

Texture:

Holocrystalline, equigranular, intersertal texture, amygdales and few microfractures filled with quartz and chlorite.

Sample: 09-Bu-149

Lithology: Basalt

Unit: Barroso Basalt

Primary Minerals:

Plagioclase (60%) Euhedral, elongate, 0.1-0.5 mm up to 1 mm, lath-shaped, polysynthetic twinning, undulatory extinction
Augite (35%) Subhedral, stumpy, 0.1-0.2 mm, simple twinning observed on a few crystals, almost entirely replaced by chlorite

Alteration Minerals:

Chlorite (30%) Acicular, fine to very fine-grained, strongly replacing mafic minerals, also located along fractures and filling vesicles
Quartz (2-3%) Very fine-grained, located along fractures and filling vesicles
Epidote (trace) Associated with chlorite

Opaque Minerals:

Pyrrhotite (4%) Anhedral, very fine-grained, disseminated
Chalcopyrite (trace) Anhedral, very fine-grained, disseminated
Pyrite (trace) Subhedral, fine-grained, disseminated

Texture:

Holocrystalline, fine-grained, equigranular, strong pervasive chlorite alteration, few chlorite-quartz-filled vesicles (1% of the rock), and fractures.

Sample: 09-Bu-172

Lithology: Glomeroporphyritic Tonalite

Unit: Buriticá Stock

Primary Minerals:

Augite (15%) Euhedral to subhedral, stumpy, 0.5-1.5 mm, simple twinning, occurs mostly as glomeroporphyritic, locally altered to chlorite-carbonate

Quartz (7%) Anhedra, 0.1-0.2 mm, part of groundmass

Plagioclase (60%) Euhedral, lath-shaped, 0.1-0.2 mm long, part of groundmass

Groundmass (80%) Microcrystalline, quartz-plagioclase-chlorite-epidote

Alteration Minerals:

Chlorite (25%) Anhedra to subhedral, very fine-grained, replacing augite phenocrysts and disseminated throughout the groundmass

Epidote (5-8%) Subhedral, very fine-grained, disseminated throughout the groundmass

Calcite/dolomite (5%) Anhedra, variable size, filling porosity and associated with chlorite altering augite phenocrysts

Opaque Minerals:

Pyrrhotite (trace) Anhedra, very fine-grained, disseminated

Chalcopyrite (trace) Anhedra, very fine-grained, disseminated

Texture:

Holocrystalline, glomeroporphyritic with augite phenocrysts aggregates up to 6-7 mm, moderate chlorite-epidote alteration.

Sample: 09-Bu-173

Lithology: Tonalite

Unit: Buriticá Stock

Primary Minerals:

Quartz (50%) Anhedra, average 2.5 mm

Plagioclase (40%) Subhedral, average 1.5-2.5 mm, zoned, polysynthetic and simple twinning, undulatory extinction

Hornblende (18%) Subhedral, acicular, average 1-1.5 mm, medium to dark green, pleochroic, partially altered to chlorite

Alteration Minerals:

Chlorite (10%) Subhedral, very fine-grained, replacing mafic minerals

Opaque Minerals:

Pyrrhotite (1%) Anhedra to subhedral, very fine to fine-grained, associated with altered zones

Chalcopyrite (trace) Anhedra, very fine-grained associated with altered zones

Texture:

Holocrystalline, equigranular, interlocking crystal texture.

Sample: 09-Bu-177

Lithology: Basalt

Unit: Barroso Basalt

Primary Minerals:

Plagioclase (45%) Euhedral to subhedral, elongate, 0.1-0.5 mm up to 0.8 mm, lath-shaped, polysynthetic and simple twinning, undulatory extinction

Augite (30%) Subhedral, prismatic, 0.1-0.3 mm, simple twinning observed on a few crystals, partially replaced by chlorite

Alteration Minerals:

Chlorite (20%) Subhedral, acicular, very fine-grained, replacing mafic minerals, also and filling vesicles

Epidote (1-2%) Anhedra, very fine-grained, disseminated

Quartz (1%) Anhedra, very fine-grained, filling vesicles

Calcite (trace) Anhedra, filling vesicles

Opaque Minerals:

Pyrrhotite (5%) Anhedral, very fine-grained, disseminated
Pyrite (1%) Subhedral, fine-grained, disseminated
Chalcopyrite (trace) Anhedral, very fine-grained, disseminated

Texture:

Holocrystalline, fine-grained, equigranular, few vesicles filled with chlorite, quartz, or calcite.

Sample: 09-Bu-191

Lithology: Tonalite

Unit: Buriticá Stock

Primary Minerals:

Quartz (35%) Anhedral crystals, medium-grained oikocrysts
Plagioclase (35%) Euhedral to locally subhedral crystals, polysynthetic twinning
Hornblende (20%) Subhedral to anhedral crystals, light to medium green, simple and lamellar twinning

Alteration Minerals:

Chlorite (5%) Fine-grained, partially replacing hornblende, but also found around and in plagioclase

Opaque Minerals:

Hematite (2%) Euhedral to subhedral crystals, fine-grained, associated with chlorite-altered areas
Pyrite (trace) Subhedral, with rims of hematite
Magnetite (trace)

Texture:

Holocrystalline, equigranular, medium to locally fine-grained, poikilitic texture, overall the rock is pretty fresh.

Sample: 09-Bu-204

Lithology: Tonalite

Unit: Buriticá Stock

Primary Minerals:

Quartz (35%) Anhedral, medium-grained, , partially recrystallized to fine grains
Plagioclase (32%) Euhedral to subhedral, average 2-4 mm, zoned, simple and polysynthetic twinning, undulatory extinction
Hornblende (20%) Subhedral to euhedral, medium to dark green, pleochroic, simple twinning, partially altered to chlorite-epidote
Zircon (trace) Euhedral, prismatic, very fine-grained, as inclusion in plagioclase

Alteration Minerals:

Chlorite (5%) Subhedral to euhedral, very fine-grained, replacing mafic minerals
Sericite (5%) Euhedral to subhedral, very fine-grained, altering plagioclase
Epidote (2%) Subhedral, fine-grained, associated with chlorite

Opaque Minerals:

Magnetite (3%) Subhedral to anhedral, fine-grained, disseminated, concentrated around altered mafic minerals

Texture:

Holocrystalline, plagioclase coarser than quartz, medium-grained, moderate chlorite alteration of hornblende, weak sericite alteration of plagioclase, some recrystallization of quartz.

Sample: 09-Bu-205

Lithology: Plagioclase-Hornblende-Phyric Andesite

Unit: Buriticá Andesite

Primary Minerals:

Plagioclase (20%) Euhedral to subhedral crystals, stumpy lath-shaped, polysynthetic twinning, average 0.1-0.5 mm, up to 3 mm locally, some glomeroporphyritic aggregates
Hornblende (12%) Euhedral crystals, greenish brown color, easy 120° cleavage, average 0.1-0.5 mm, up to 3 mm locally

Apatite (trace) Euhedral crystals, fine-grained, prismatic, chadacrysts within hornblende and plagioclase

Groundmass (63%) Microcrystalline, plagioclase microliths

Alteration Minerals:

Chlorite (5%) Light green, replacing hornblende, associated with magnetite-rich zones

Magnetite (5%) Subhedral crystals, average 0.1 mm, disseminated throughout groundmass, concentrated near mafic minerals, secondary?

Epidote (trace) Very fine-grained

Opaque Minerals:

Pyrite (trace), Very fine-grained, disseminated

Chalcopyrite (trace) Anhedral, very fine-grained, disseminated

Calcite (trace) Late, infilling porosity

Texture:

Holocrystalline, porphyritic, locally glomeroporphyritic. Plagioclase phenocrysts are partially saussuritized. Overall the rock is pretty fresh.

Sample: 09-Bu-226

Lithology: Plagioclase-Pyroxene-Phyric Andesite

Unit: Buriticá Stock

Primary Minerals:

Plagioclase (15%) Euhedral to subhedral, average size 0.5-1.5 mm, locally forms glomeroporhs up to 2-3 mm, simple and polysynthetic twinning, undulatory extinction, moderately altered

Augite (10%) Euhedral to subhedral, stumpy, octagonal, 0.5-2.5 mm, locally form glomeroporhs up to 3 mm, simple twinning, strongly altered to chlorite-epidote-calcite

Groundmass (65%) Microcrystalline, plagioclase microliths

Alteration Minerals:

Chlorite (15%) Subhedral, fine to very fine-grained, replacing mafic minerals, filling porosity and along fractures

Epidote (5%) Subhedral, fine to very fine-grained, partially replacing mafic minerals

Calcite (2-3%) Anhedral, fine-grained, associated with chlorite, replacing mafic minerals

Quartz (1%) Anhedral, very fine-grained, associated with chlorite, filling fractures and porosity

Opaque Minerals:

Pyrite (3-4%) Anhedral to subhedral, fine to very fine-grained, associated with chlorite, mainly filling fractures and porosity, also disseminated throughout the rock

Chalcopyrite (trace) Anhedral, very fine-grained, disseminated

Magnetite (1%) Anhedral, very fine-grained, filling fractures and porosity and disseminated throughout the rocks

Texture:

Holocrystalline, porphyritic, locally glomeroporphyritic, microlithic groundmass, strong chlorite-epidote alteration, many chlorite-magnetite-pyrite±quartz-filled fractures (5%).

Sample: 09-Bu-234

Lithology: Plagioclase-Pyroxene-Hornblende-Phyric Andesite

Unit: Buriticá Andesite

Primary Minerals:

Plagioclase (16%) Euhedral to subhedral, lath-shaped, 0.3-2 mm, some crystals zoned, polysynthetic and simple twinning

Augite (15%) Euhedral to subhedral, stumpy, average size 0.3-1 mm, up to 5-6 mm, crystals are not at equilibrium with the magma (edges of crystals are not sharp, locally rounded), some have been sheared and fractured, partially to completely altered to chlorite-epidote

Hornblende (3-4%) Euhedral to subhedral, elongate, 0.4-2 mm, strongly pleochroic, simple twinning, crystals are not at equilibrium with the magma (edges of crystals are not sharp), less altered than augite

Groundmass (65%) Microcrystalline, lots of opaque minerals (likely magnetite)

Alteration Minerals:

Chlorite (15%) Anhedral to subhedral, very fine-grained, partially to completely replacing augite

Epidote (5%) Anhedral, fine-grained, partially replacing augite

Quartz (1%) Anhedral, fine-grained, associated with chlorite-rich zones, filling porosity

Biotite (trace) Anhedral, very fine-grained, only a few disseminated grains

Opaque Minerals:

Magnetite (3%) Anhedral, very fine-grained, disseminated

Pyrite (1-2%) Anhedral, fine to very fine-grained, associated with chlorite and located along fractures

Chalcopyrite (trace) Anhedral, very fine-grained, disseminated

Texture:

Holocrystalline, porphyritic, slightly porous (0.5-1%), phenocrysts seem not to be at equilibrium with the magma (xenoliths?), strong propylitic alteration.

Sample: 09-Bu-242

Lithology: Plagioclase-Hornblende-Pyroxene-Phyric Andesite

Unit: Buriticá Andesite

Primary Minerals:

Plagioclase (20%) Euhedral to subhedral, stumpy, lath-shaped, 0.2-3 mm, zoned, polysynthetic and simple twinning, undulatory extinction

Hornblende (15%) Euhedral, elongate, average size 0.1-0.5 mm, up to 8 mm, strongly pleochroic, simple twinning, fairly fresh, locally partially altered to chlorite

Augite (10%) Euhedral, stumpy, octagonal, 0.3-1 mm, simple twinning, almost completely altered to chlorite

Apatite (trace) Euhedral, prismatic, very fine-grained, chadacrysts within hornblende crystals

Groundmass (51%) Microcrystalline to cryptocrystalline

Alteration Minerals:

Chlorite (10%) Anhedral, replacing mafic minerals

Epidote (3-5%) Subhedral, granular, fine to very fine-grained, replacing mafic minerals

Quartz (trace) Anhedral, fine-grained, filling porosity

Calcite (trace) Anhedral, very fine-grained, associated with chlorite-epidote in augite replacement

Opaque Minerals:

Pyrite (4%) Subhedral, fine-grained, disseminated throughout the rock and along fractures

Chalcopyrite (trace) Anhedral, very fine-grained, disseminated

Texture:

Holocrystalline, porphyritic, weak trachytic texture developed, strong chlorite-epidote-calcite replacement of pyroxene.

Sample: 09-Bu-261

Lithology: Granite

Unit: Sabanalarga Batholith

Primary Minerals:

Quartz (40%) Anhedral to locally subhedral, 0.5-1.5 mm, irregular recrystallized edges, undulatory extinction, locally intragranular and transgranular fractures along a preferential orientation

Orthoclase (15%) Subhedral to euhedral, 2-4 mm, partially to completely replaced by sericite

Plagioclase (10%) Subhedral, 1-2 mm, polysynthetic twinning, partially replaced by epidote

Alteration Minerals:

Chlorite (17%) Anhedral, fine-grained, strongly pleochroic (green to yellow), occurs as patches, possibly where primary mafic minerals were located

Epidote (15%) Anhedral to subhedral, fine to very fine-grained, partially replacing plagioclase, filling fractures, and associated with chlorite-rich zones

Sericite (3-5%) Subhedral, very fine-grained, partially replacing orthoclase

Opaque Minerals:

Magnetite (0.5%) Anhedral, very fine-grained, associated with chlorite-rich zones

Pyrite (trace) Anhedral, very fine-grained, associated with chlorite-rich zones
Chalcopyrite (trace) Anhedral, very fine-grained, associated with chlorite-rich zones

Texture:

Massive, equigranular, quartz boundary-migration recrystallization, highly fractured along a preferential orientation, fractures filled with epidote, sigmoidal crystals along larger fractures.

Sample: 09-DH-3

Lithology: Andesite

Unit: Buriticá Andesite

Primary Minerals:

Intense phyllic/argillic alteration, no primary mineral nor texture preserved

Alteration Minerals:

Sericite (40%) Anhedral to euhedral, very fine-grained, needle-shaped, strong pervasive alteration, occurs as inclusions within adularia as well as disseminated throughout the rock

Quartz (20%) Anhedral, fine-grained, disseminated in groundmass, and filling porosity

Adularia (10%) Subhedral to anhedral, fine to very fine-grained, pervasive alteration, commonly with sericite needle inclusions

Opaque Minerals:

Pyrite (20%) Euhedral to subhedral, fine-grained, disseminated throughout the rock and along fractures

Sphalerite (1-2%) Anhedral, fine to very fine-grained, disseminated

Chalcopyrite (trace) Anhedral, very fine-grained, occurs as chalcopyrite disease

Texture:

Highly porous (10%), intense adularia/sericite alteration, no primary texture preserved, kaolinite was identified from XRD analysis but is too fine-grained to be identified here, it is possibly mixed with very fine sericite needles.

Sample: 09-M-1

Lithology: Mineralized Vein Margin (Andesite)

Unit: Buriticá Andesite

Primary Minerals:

No primary mineral left

Alteration Minerals:

Sericite (30%) Subhedral elongate crystals, very fine-grained, disseminated, altering adularia crystals

Quartz (15%) Anhedral crystals, very fine-grained, disseminated throughout the rock and locally clustered (possibly filling porosity)

Adularia (6%) Subhedral to euhedral crystals, average 0.3 mm, disseminated

Calcite (trace) Late infilling of porosity, located at the vein contact

Groundmass (29%) Very fine-grained, unable to identify

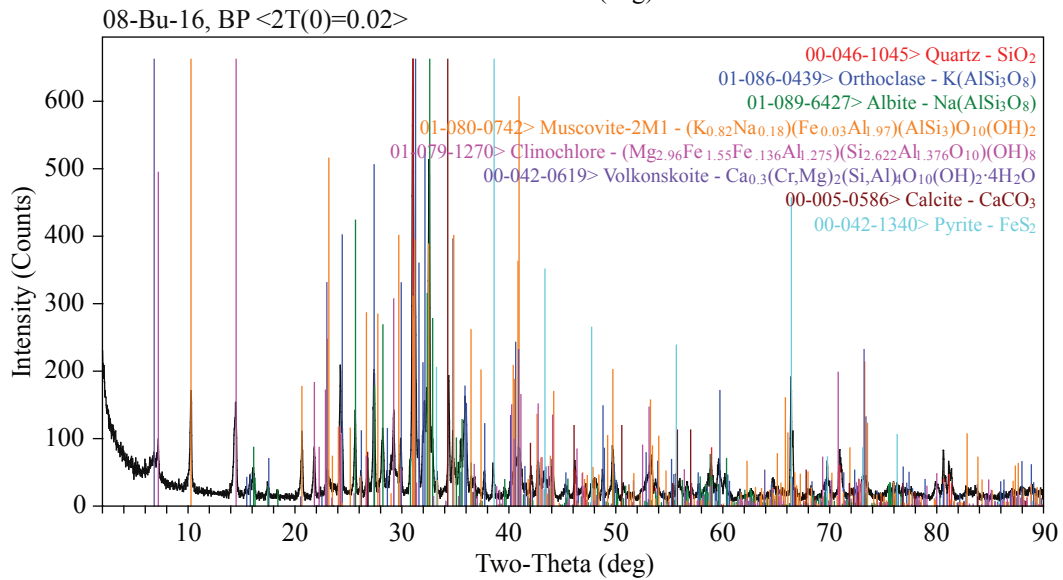
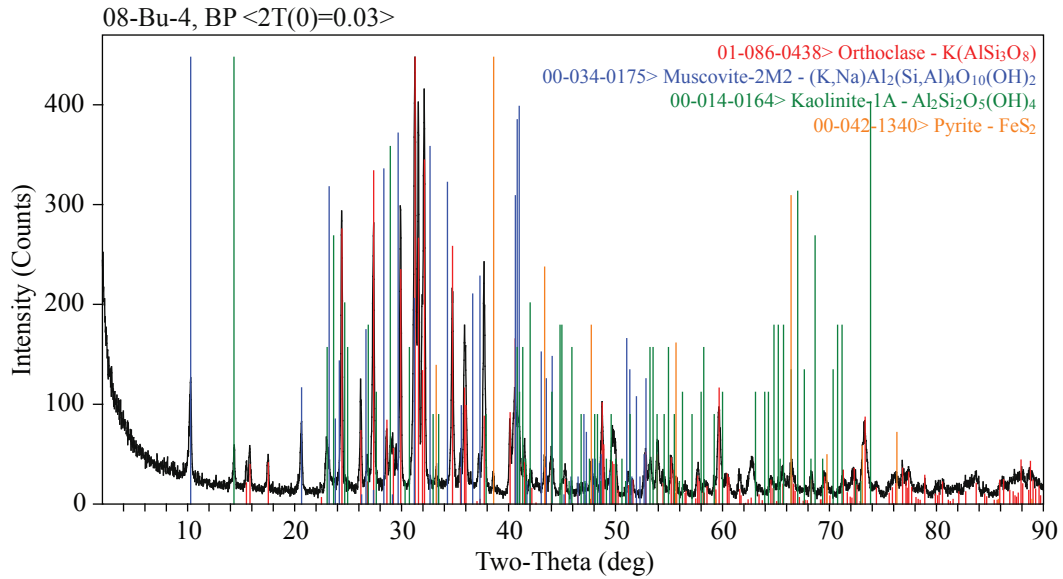
Opaque Minerals:

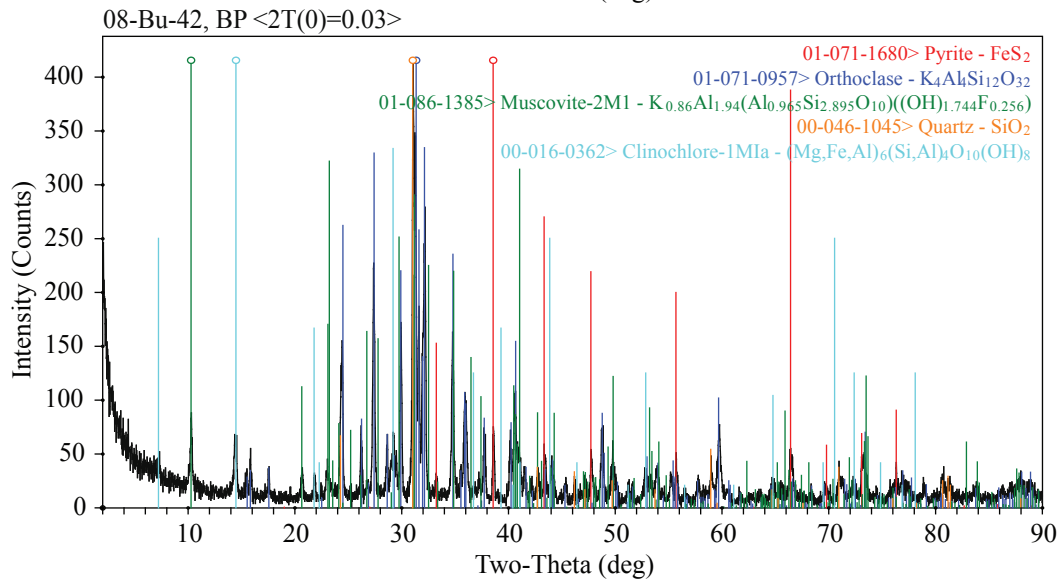
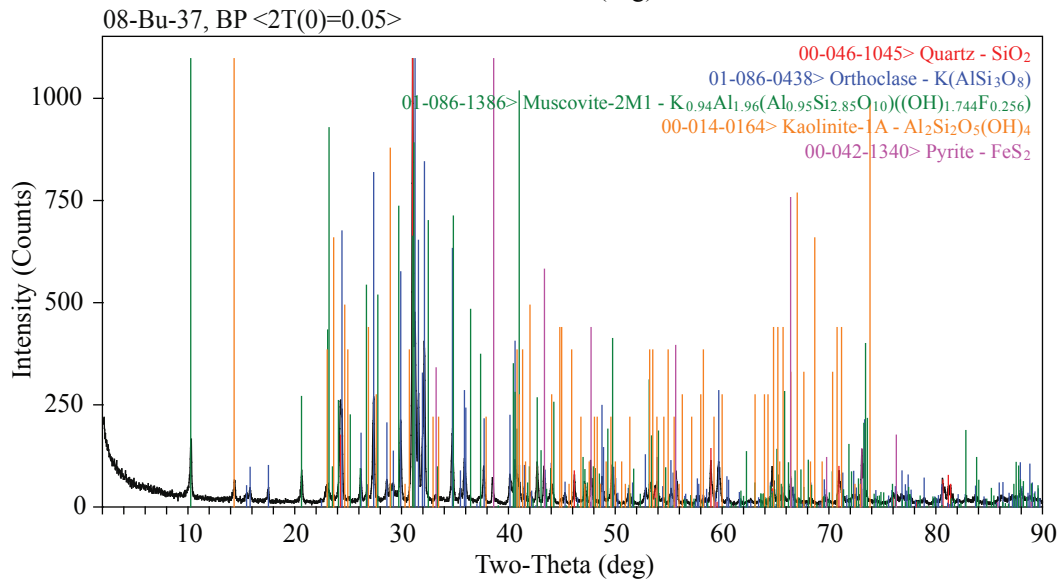
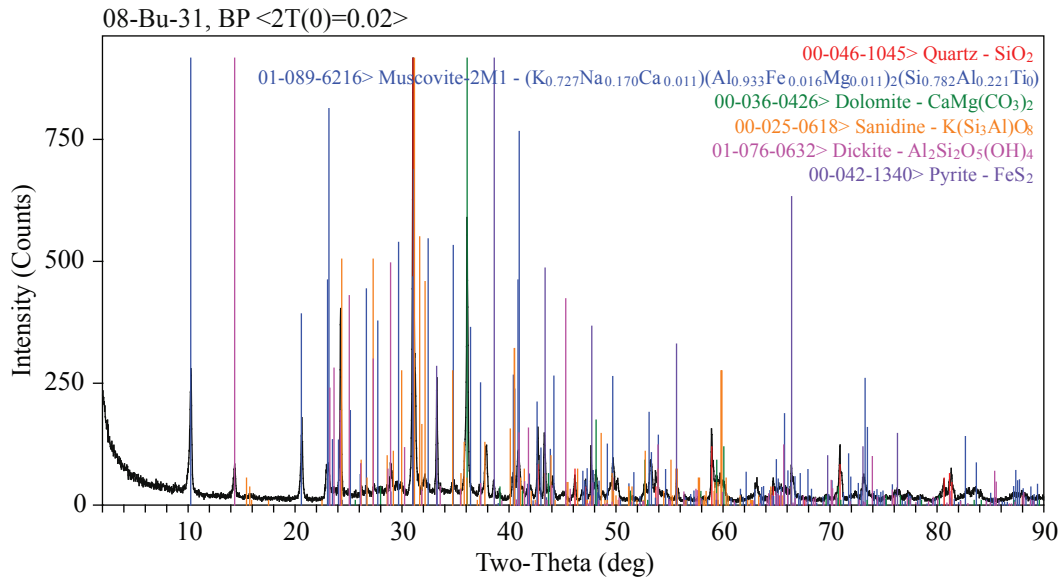
Pyrite (20%) Euhedral to subhedral crystals, fine-grained, disseminated

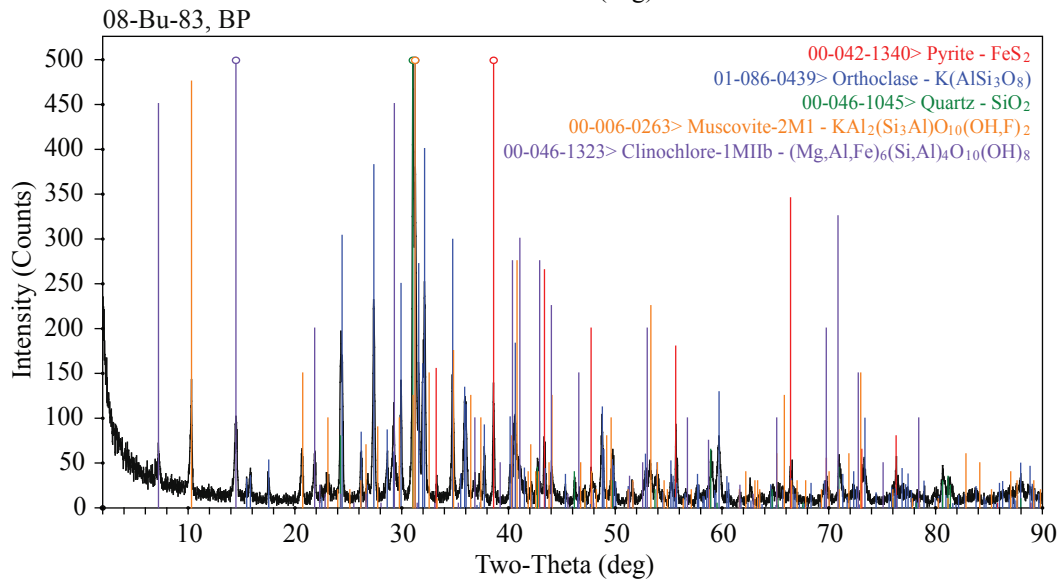
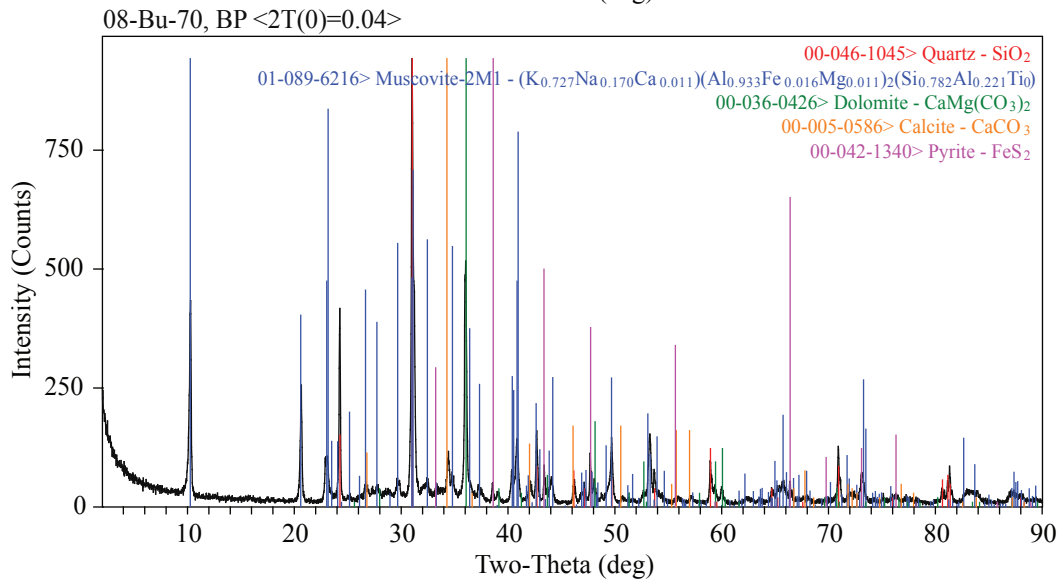
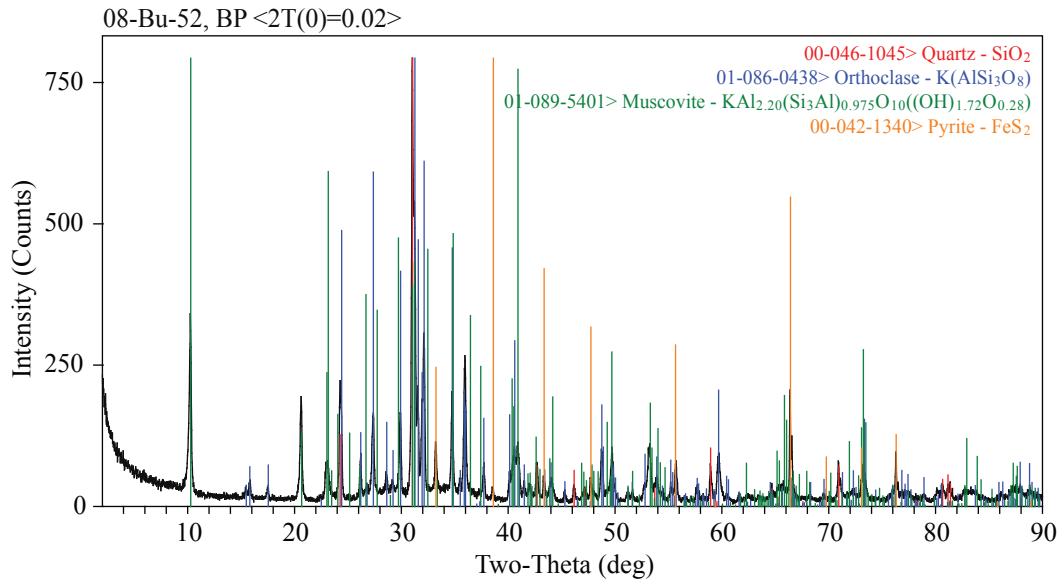
Texture:

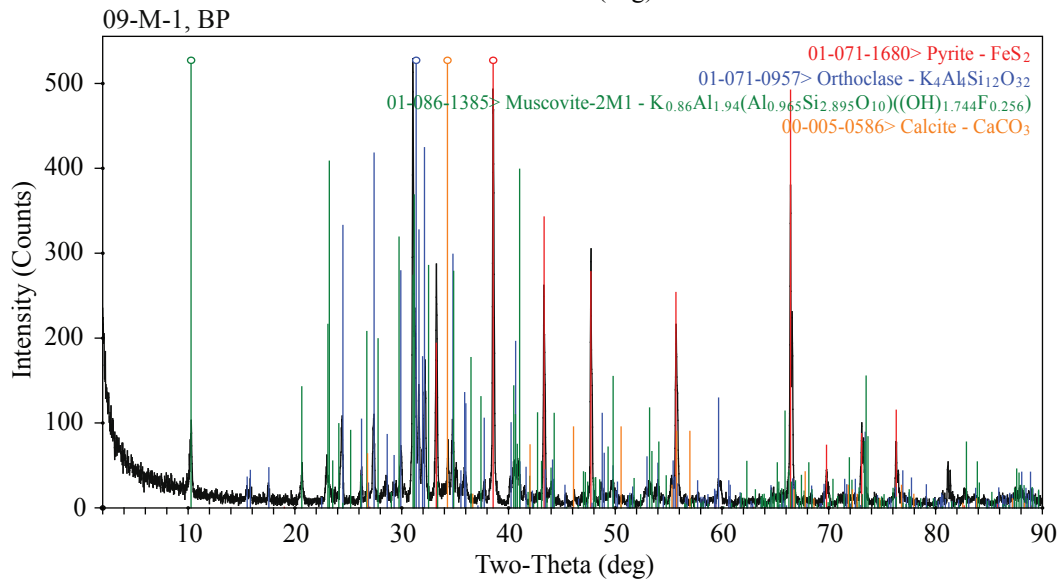
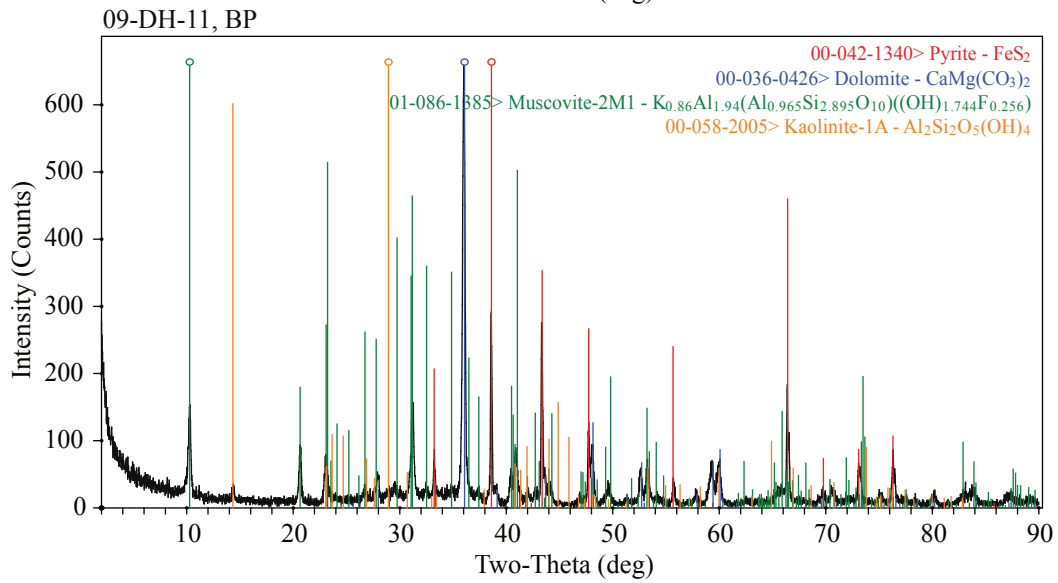
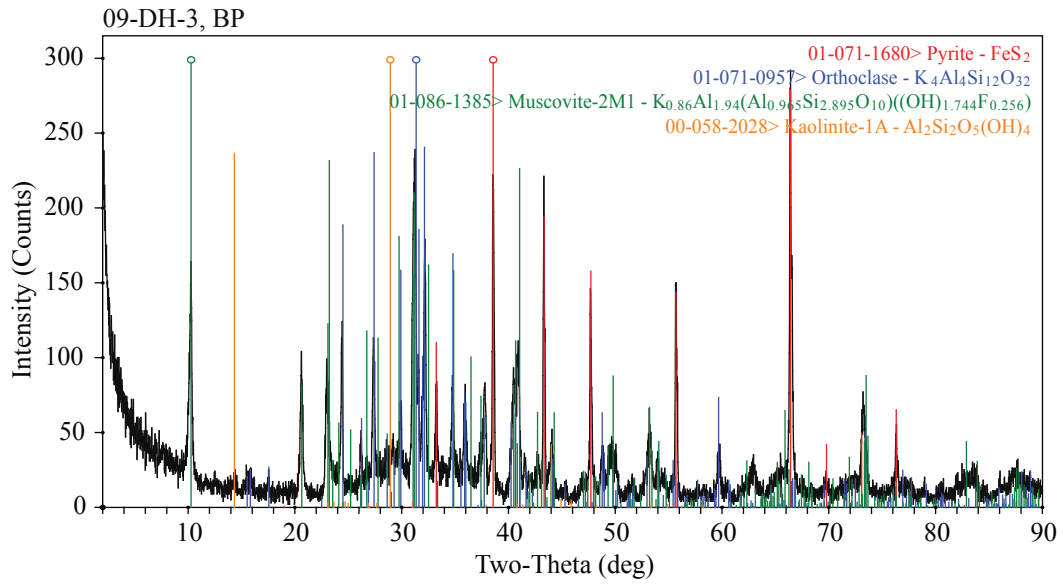
Intense phyllic alteration. No primary texture left. Sericite appears to be altering adularia crystals.

Appendix C: X-Ray Diffraction Data









Station ID	Collar Coordinate Easting ¹	Collar Coordinate Northing ¹	Collar Elevation (m)	Structure Type	Strike ²	Dip ³	Comment
09-Bu-14	399448	740589	1666	Joint	140	75	Joint set in sediments
09-Bu-15	399293	740586	1670	Vein	65	60	Previously mined vein hosted in andesite
				Joint	65	60	Joint set in andesite, parallel to mineralized structure
09-Bu-17	399188	740377	1664	Bedding	190	40	Calcareous mudstone, 2-4 cm-thick beds, way up unknown
				Z-fold hinge	298	58	1 m large parasitic Z-fold
09-Bu-19	398887	739887	1669	Fault	140	90	Fault in tonalite, 0.3-0.5 m-thick, west side up apparent movement
				Vein	214	48	Calcite-epidote vein, 2-5 cm-thick, close to the tonalite-sediment contact
	398950	739865	1669	Bedding	163	49	Calcareous mudstone-siltstone, 2-4 cm-thick beds, broken up and folded
				Z-fold hinge	277	37	0.5 m large parasitic Z-fold
09-Bu-23	399288	740257	1670	Vein	275	90	Previously mined vein in andesite, 10-15 cm-thick, pyrite-sphalerite-quartz-
				Joint	280	65	Joint set sub-parallel to the vein
09-Bu-44	399167	741587	1659	Fault	85	45	Small fault in tonalite
09-Bu-55	399120	738411	2034	Joint	50	42	Joint set in basalt
09-Bu-57	398996	738556	1651	Fault	300	55	Small fault in basalt
09-Bu-58	398982	738584	2095	Joint	220	35	Joint set in basalt
				Joint	90	65	Joint set in basalt
				Joint	10	45	Joint set in basalt
09-Bu-63	398406	740103	1647	Fault	220	35	Small fault in tonalite
09-Bu-87	399506	741484	1739	Fault	74	75	10-15 cm-thick fault in tonalite, gauge filling

Station ID	Collar Coordinate Easting ¹	Collar Coordinate Northing ¹	Collar Elevation (m)	Structure Type	Strike ²	Dip ³	Comment
09-Bu-89	399648	741274	1761	Fault	205	65	Small fault in andesite
				Fault	245	82	Small fault in andesite
				Joint	260	59	Joint set in andesite
09-Bu-95	399322	740910	1833	Fault	155	66	10 cm-thick fault in andesite
09-Bu-97	399426	740701	1867	Joint	85	55	Joint set in andesite
				Joint	5	65	Joint set in andesite
09-Bu-103	399100	740193	1930	Fault	160	57	Faulted tonalite(west)-andesite(east) contact
09-Bu-105	398980	739779	1934	Bedding	180	45	Calcareous Mudstone-siltstone, 2-4 cm-thick beds, way up unknown
	398965	739759	1934	Bedding	190	34	
09-Bu-107	398934	739629	1946	Fault	275	57	15-20 cm-thick fault zone in basalt, west side up apparent movement
09-Bu-110	398781	739522	1933	Fault	277	60	10-30 cm-thick fault zone in basalt
09-Bu-111	398877	739430	1933	Bedding	193	64	Thinly bedded calcareous mudstone-siltstone, way up to the north-west
	398862	739415	1933	Bedding	230	44	Thinly bedded calcareous mudstone-siltstone, way up to the north-west
	398847	739400	1933	Bedding	245	50	Thinly bedded calcareous mudstone-siltstone, way up to the north-west
09-Bu-113	398951	739271	1927	Bedding	253	50	10-30 cm-thick calcareous siltstone beds
	398951	739282	1927	Bedding	195	90	10-30 cm-thick calcareous siltstone beds
				Fault	214	74	Fault in siltstone
09-Bu-115	400084	743064	1557	Bedding	134	20	Thinly bedded mudstone
09-Bu-117	400148	743080	1570	Fault	95	70	Fault in basalt
09-Bu-118	400246	743008	1587	Fault	234	60	10 cm-thick fault gauge zone close to the sediment-basalt contact
				Joint	45	55	Joint set in basalt
09-Bu-119	400309	742981	1593	Fault	260	70	1 m-thick highly broken up zone in basalt

Station ID	Collar Coordinate Easting ¹	Collar Coordinate Northing ¹	Collar Elevation (m)	Structure Type	Strike ²	Dip ³	Comment
09-Bu-122	400709	742947	1513	Joint	295	56	Joint set in basalt
				Joint	296	37	Joint set in basalt
				Joint	30	39	Joint set in basalt
09-Bu-124	401018	743024	1437	Fault	226	45	10 cm-thick fault in basalt
				Fault	6	90	40 cm-thick fault in basalt, west side up apparent movement
				Vein	210	90	10-25 cm-thick quartz-epidote vein in basalt
				Vein	205	40	10 cm-thick quartz-epidote vein in basalt
09-Bu-126	400913	743031	1381	Joint	129	45	Joint set in basalt
				Joint	129	37	Joint set in basalt
09-Bu-130	401768	742217	893	Fault	190	65	Small fault in basalt
09-Bu-132	401529	742212	926	Fault	185	61	1 m-thick fault zone in basalt
				Joint	287	84	Joint set in basalt
09-Bu-136	401345	742334	991	Fault	190	90	2-2.5 m-thick fault zone with deformed basalt pillows in it
09-Bu-138	400969	742212	1054	Vein	45	70	10-15 cm-thick calcite-quartz-sphalerite-pyrite-chalcopyrite vein in basalt
09-Bu-140	400809	742220	1140	Fault	15	55	Fault in basalt
09-Bu-141	400782	742203	1140	Joint	355	28	Joint set in basalt
				Joint	336	52	Joint set in basalt
09-Bu-142	400768	742185	1139	Fault	184	79	Large sheared corridor, 12-13 m-thick, blocks of basalt and chert in sheared matrix, west side up apparent movement
	400768	742185	1139	Fault	205	90	Other measurement from the same sheared corridor
09-Bu-143	400710	742060	1152	Fault	330	82	1-2 m large fault in basalt
				Joint	74	76	Joint set in basalt

Station ID	Collar Coordinate Easting ¹	Collar Coordinate Northing ¹	Collar Elevation (m)	Structure Type	Strike ²	Dip ³	Comment
09-Bu-144	400517	742096	1177	Joint	68	40	Joint set in basalt
				Joint	76	75	Closely spaced joint set in basalt
				Joint	225	34	Joint set in basalt
09-Bu-145	400466	742088	1204	Joint	104	70	Joint set in basalt
				Joint	275	30	Joint set in basalt
09-Bu-147	400325	741817	1298	Vein	355	76	Set of closely spaced 1 cm-thick calcite veins in basalt
09-Bu-148	400316	741660	1308	Bedding	180	55	Chert, 5-10 cm-thick wavy beds, cut by a few calcite veinlets and pyrite veinlets
	400321	741755	1308	Bedding	161	41	Wavy bedding in chert
09-Bu-149	400372	741560	1350	Joint	146	61	Joint set in basalt
09-Bu-152	399058	739076	1913	Bedding	210	48	Mudstone, 3-15 cm-thick beds, parallel laminations, way up unknown
09-Bu-156	399174	738356	2033	Fault	330	50	Oldest, 2-5 cm-thick fault, moderate oxidation on each side over about 10 cm
				Fault	40	80	10-20 cm-thick fault zone with gauge filling, strong oxidation within the fault zone, offsets first fault by 1 m, dextral movement (northwest wall moves up/to the east)
				Fault	320	60	Youngest, very thin, offsets both fault by 0.75-0.80 m, dextral movement (west side move down/north)
09-Bu-168	398319	739155	2018	Fault	205	78	Fault zone in tonalite, strong argillic alteration / weathering associated with it
09-Bu-169	398280	739170	2017	Fault	55	90	Small fault in tonalite
09-Bu-171	397762	739828	2062	Fault	75	90	0.5 m-thick fault zone in tonalite

Station ID	Collar Coordinate Easting ¹	Collar Coordinate Northing ¹	Collar Elevation (m)	Structure Type	Strike ²	Dip ³	Comment
09-Bu-184	397463	740952	2075	Joint	75	85	Joint set in tonalite
09-Bu-213	397759	742464	1664	Joint	115	45	Joint set in basalt
				Joint	70	50	Joint set in basalt
09-Bu-217	397721	741849	1830	Joint	55	55	Joint set in tonalite
				Vein	135	50	10-15 cm-thick quartz-calcite-sphalerite-pyrite-chalcopyrite vein in tonalite
09-Bu-220	400391	741997	1239	Joint	255	70	Joint set in basalt
				Joint	72	54	Closely spaced joint set in basalt
				Joint	200	90	Joint set in basalt
				Joint	80	66	Joint set in basalt
09-Bu-221	400168	741909	1338	Joint	87	75	Joint set in basalt
				Joint	196	90	Joint set in basalt
				Joint	330	19	Joint set in basalt
09-Bu-238	400034	741100	1618	Joint	315	62	Joint set in andesite
				Joint	115	90	Joint set in andesite
09-Bu-239	399981	741047	1644	Joint	30	75	Joint set in andesite
09-Bu-244	399814	740896	1705	Joint	225	60	Joint set in andesite
09-Bu-253	401623	741503	957	Bedding	145	60	Calcareous siltstone, 10-20 cm-thick beds, parallel laminations, cut by many calcite veinlets
09-Bu-254	401531	740825	1039	Bedding	205	40	Calcareous siltstone, 10-20 cm-thick beds, parallel laminations, cut by many calcite veinlets
09-M-1	400035	741338	1484	Vein	245	72	San Antonio vein
09-M-2	400045	741349	1484	Vein	118	90	Centena vein
09-M-3	400066	741339	1484	Vein	110	81	Centena vein

Station ID	Collar Coordinate Easting ¹	Collar Coordinate Northing ¹	Collar Elevation (m)	Structure Type	Strike ²	Dip ³	Comment
09-M-4	400078	741335	1484	Vein	102	90	Centena vein
09-M-6	400114	741200	1484	Vein	90	90	Murcielagos vein
09-M-7	400091	741199	1484	Vein	250	90	Murcielagos vein
09-M-8	399970	741160	1484	Vein	66	90	Murcielagos vein
09-M-9	400011	741317	1484	Vein	75	80	San Antonio vein
09-M-10	399963	741310	1484	Vein	285	75	San Antonio vein
09-M-11	399970	741311	1484	Vein	90	65	San Antonio vein
09-M-12	399929	741303	1484	Vein	270	90	San Antonio vein
09-M-13	399919	741300	1484	Vein	270	90	San Antonio vein
09-M-14	399854	741281	1484	Vein	60	80	San Antonio vein

¹Collar coordinates are in WGS 84 / UTM zone 18N projection

²Trend in case of linear feature

³Plunge in case of linear feature

Element (unit)	Method (detec. Limit)	08-Bu-13	08-Bu-19	08-Bu-29	08-Bu-30	08-Bu-32	08-Bu-36	08-Bu-58	08-Bu-61	08-Bu-72	08-Bu-76	08-Bu-78	08-Bu-79	08-Bu-84	08-Bu-85	08-Bu-86	08-Bu-88
SiO ₂ %	FUS-ICP (0.01)	56.16	52.45	57.21	56.29	56.96	57.81	53.66	48.25	52.02	52.45	61.22	53.87	57.22	57.4	60.73	53.75
Al ₂ O ₃ %	FUS-ICP (0.01)	16.03	16.14	17	16.57	15.58	15.93	15.76	14.94	15.56	16.43	16.03	16.31	15.27	16.19	15.37	16.39
Fe ₂ O ₃ (T) %	FUS-ICP (0.01)	8.15	5.88	7.24	9.76	5.48	6.49	7.99	13.19	10.06	9.98	5.69	7.05	9.12	9.81	7.62	7.62
MnO %	FUS-ICP (0.001)	0.18	0.14	0.13	0.27	0.11	0.09	0.23	0.18	0.18	0.21	0.05	0.22	0.17	0.16	0.11	0.18
MgO %	FUS-ICP (0.01)	2.8	1.54	2.01	3.24	2.03	2.1	3.15	3.04	4.27	3.35	1.25	2.18	4.82	3.37	3.14	2.27
CaO %	FUS-ICP (0.01)	7.16	4.38	5.98	6.33	3.17	4.9	7.48	7.55	9.16	8.67	2.35	5.65	7.54	8.73	7.23	6.42
Na ₂ O %	FUS-ICP (0.01)	3.44	2.08	3.35	2.75	0.97	2.28	3.23	2.91	2.93	3.35	3.79	2.27	2.7	2.33	3.02	2.99
K ₂ O %	FUS-ICP (0.01)	3.05	7.67	4.41	2.81	7.89	4.2	4.22	4.14	3.5	2.83	6.3	5.75	0.11	0.51	0.54	3.09
TiO ₂ %	FUS-ICP (0.001)	0.70	0.47	0.61	0.81	0.52	0.51	0.72	0.82	0.84	0.79	0.50	0.60	0.51	0.57	0.44	0.64
P ₂ O ₅ %	FUS-ICP (0.01)	0.44	0.31	0.3	0.46	0.27	0.26	0.46	0.49	0.49	0.52	0.13	0.37	0.12	0.15	0.11	0.4
LOI %	FUS-ICP	0.67	6.82	1.12	1.35	5.76	3.51	3.2	4.81	1.8	0.26	3.41	5.01	2	0.67	0.98	5.6
Total %	FUS-ICP (0.01)	98.77	97.87	99.35	100.6	98.74	98.08	100.1	100.3	100.8	98.85	100.7	99.29	99.57	99.9	99.29	99.34
Au ppb	INAA (1)	26	178	51	15	39	41	12	45	< 1	20	18	6	< 1	< 1	< 1	< 1

Element (unit)	Method (detec. Limit)	08-Bu- 13	08-Bu- 19	08-Bu- 29	08-Bu- 30	08-Bu- 32	08-Bu- 36	08-Bu- 58	08-Bu- 61	08-Bu- 72	08-Bu- 76	08-Bu- 78	08-Bu- 79	08-Bu- 84	08-Bu- 85	08-Bu- 86	08-Bu- 88
Ag ppm	MULT INAA / TD-ICP (0.5)	< 0.5	3	< 0.5	< 0.5	< 0.5	0.8	< 0.5	0.6	< 0.5	< 0.5	< 0.5	< 0.5	< 0.5	< 0.5	< 0.5	< 0.5
As ppm	INAA (1)	2	39	12	9	7	13	15	23	17	5	15	22	2	< 1	< 1	2
Ba ppm	FUS-ICP (1)	1294	1671	3012	1365	1746	1513	1984	1645	1301	1093	1942	1115	129	201	250	1374
Be ppm	FUS-ICP (1)	2	2	2	2	2	2	2	2	2	2	2	2	1	< 1	< 1	2
Bi ppm	FUS-MS (0.1)	0.1	< 0.1	< 0.1	0.1	< 0.1	< 0.1	0.2	0.5	0.3	0.3	< 0.1	< 0.1	< 0.1	0.3	< 0.1	< 0.1
Br ppm	INAA (0.5)	2	1.5	2.6	< 0.5	1.5	0.9	< 0.5	1.9	< 0.5	3.3	2.7	< 0.5	< 0.5	< 0.5	< 0.5	1.2
Cd ppm	TD-ICP (0.5)	< 0.5	< 0.5	1.2	7.1	< 0.5	1.4	< 0.5	0.7	1	< 0.5	0.5	< 0.5	< 0.5	< 0.5	< 0.5	0.7
Co ppm	INAA (0.1)	13.7	12.5	7.8	22.1	12.8	10.4	9.1	32.6	21.1	21.1	11.4	12.8	27.7	25.5	21.2	15.1
Cr ppm	INAA (0.5)	13.4	10.4	8.7	22.3	30.2	28.8	17.7	14.2	63.7	20.1	6.6	12.7	101	44	49.4	13.5
Cs ppm	FUS-MS (0.1)	0.8	0.7	0.6	0.3	0.7	0.4	0.5	0.4	1	0.8	0.9	0.6	< 0.1	0.1	< 0.1	0.6
Cu ppm	TD-ICP (1)	26	21	16	64	8	43	51	173	29	139	13	24	14	116	17	34
Ga ppm	FUS-MS (1)	18	17	17	19	17	17	19	17	18	19	17	19	13	15	14	19

Element (unit)	Method (detec. Limit)	08-Bu- 13	08-Bu- 19	08-Bu- 29	08-Bu- 30	08-Bu- 32	08-Bu- 36	08-Bu- 58	08-Bu- 61	08-Bu- 72	08-Bu- 76	08-Bu- 78	08-Bu- 79	08-Bu- 84	08-Bu- 85	08-Bu- 86	08-Bu- 88
Ge ppm	FUS-MS (0.5)	1.6	1	1.4	1.5	1.7	1.1	1.4	1.3	1.3	1.5	0.8	1.5	1.2	1.6	1.4	1.3
Hf ppm	FUS-MS (0.1)	2.8	2.7	2.7	3	3.3	2.7	2.9	2.5	2.3	2.7	4.6	3.2	1.3	1.3	1.6	3.1
Hg ppm	INAA (1)	< 1	< 1	< 1	< 1	< 1	< 1	< 1	< 1	3	< 1	< 1	< 1	< 1	< 1	< 1	< 1
In ppm	FUS-MS (0.1)	< 0.1	< 0.1	< 0.1	< 0.1	< 0.1	< 0.1	< 0.1	< 0.1	< 0.1	< 0.1	< 0.1	< 0.1	< 0.1	< 0.1	< 0.1	< 0.1
Ir ppb	INAA (1)	< 1	7	< 1	< 1	< 1	< 1	< 1	< 1	< 1	< 1	< 1	< 1	< 1	< 1	< 1	< 1
Mo ppm	FUS-MS (2)	< 2	< 2	2	< 2	< 2	< 2	4	< 2	< 2	< 2	< 2	< 2	< 2	< 2	< 2	< 2
Nb ppm	FUS-MS (0.2)	5.9	5.1	5.9	6.9	6.8	6.4	6.4	5	5	6.6	8.4	6.9	2.4	3.2	2.8	6.6
Ni ppm	TD-ICP (1)	6	7	4	12	9	8	8	11	18	11	5	5	28	18	16	5
Pb ppm	TD-ICP (5)	5	6	14	< 5	6	14	< 5	< 5	7	9	< 5	8	< 5	< 5	< 5	6
Rb ppm	FUS-MS (2)	66	178	77	53	197	91	77	69	72	64	151	186	2	10	8	65
S %	TD-ICP (0.001)	0.04	4.8	0.09	0.05	4.01	0.99	0.36	2	0.09	0.16	4	0.93	0.01	0.01	0.00	0.01
Sb ppm	INAA (0.1)	1.7	6.8	3.8	2.7	8.4	4.6	14	10.8	4.7	1.3	2.9	4.1	0.3	0.1	0.3	3.9
Sc ppm	INAA (0.01)	16.9	7.59	9.3	17.9	10.2	10.3	17.1	19.2	24.5	16.5	7.83	13	33.1	30.2	24.6	13.9

Element (unit)	Method (detec. Limit)	08-Bu-13	08-Bu-19	08-Bu-29	08-Bu-30	08-Bu-32	08-Bu-36	08-Bu-58	08-Bu-61	08-Bu-72	08-Bu-76	08-Bu-78	08-Bu-79	08-Bu-84	08-Bu-85	08-Bu-86	08-Bu-88
Se ppm	INAA (0.5)	< 0.5	< 0.5	< 0.5	< 0.5	< 0.5	< 0.5	< 0.5	< 0.5	< 0.5	< 0.5	8.1	< 0.5	< 0.5	< 0.5	< 0.5	< 0.5
Sn ppm	FUS-MS (1)	14	< 1	< 1	1	2	1	2	12	2	2	< 1	< 1	1	1	< 1	2
Sr ppm	FUS-ICP (2)	926	263	881	859	325	848	894	860	911	993	473	577	173	205	201	1072
Ta ppm	FUS-MS (0.01)	0.4	0.3	0.4	0.4	0.5	0.4	0.4	0.3	0.3	0.4	0.6	0.4	0.1	0.2	0.2	0.4
Th ppm	FUS-MS (0.05)	3.66	3.66	3.63	3.5	4.62	4.31	4.14	3.44	2.98	3.11	6.17	4.37	0.55	0.85	0.68	3.93
U ppm	FUS-MS (0.05)	1.93	2.07	1.8	1.97	2.58	2.42	2.23	1.82	1.69	1.53	2.91	2.36	0.23	0.37	0.28	2.11
V ppm	FUS-ICP (5)	210	141	155	225	138	137	228	266	306	261	101	148	206	224	174	164
W ppm	INAA (1)	< 1	< 1	< 1	< 1	2	< 1	< 1	< 1	< 1	< 1	< 1	< 1	< 1	< 1	< 1	< 1
Y ppm	FUS-ICP (1)	20	17	17	22	16	19	19	19	19	22	16	20	11	13	10	25
Zn ppm	MULT INAA / TD-ICP (1)	84	55	133	785	60	135	48	85	80	128	82	100	69	56	51	110
Zr ppm	FUS-MS (1)	104	107	108	114	129	112	109	85	83	101	182	122	46	48	58	119
La ppm	FUS-MS (0.05)	20.8	23.6	16.5	20.5	21.8	28.2	23.5	18.9	18.1	19.7	18.7	29.2	5.21	12.5	4.53	21.2

Element (unit)	Method (detec. Limit)	08-Bu-13	08-Bu-19	08-Bu-29	08-Bu-30	08-Bu-32	08-Bu-36	08-Bu-58	08-Bu-61	08-Bu-72	08-Bu-76	08-Bu-78	08-Bu-79	08-Bu-84	08-Bu-85	08-Bu-86	08-Bu-88
Ce ppm	FUS-MS (0.1)	39.6	41.9	27.5	38.3	39.4	48	44.9	38.7	36.2	39.8	34.7	56.8	11.2	25.4	9.7	39.8
Pr ppm	FUS-MS (0.02)	5.37	4.9	3.08	5.27	5.14	5.49	5.93	5.26	5.05	5.51	4.52	7.2	1.55	3.16	1.37	5.62
Nd ppm	FUS-MS (0.05)	19.8	17.9	12	19.9	17.8	19	21.6	19.9	19.6	21.2	16	25.7	6.32	11.7	5.7	21
Sm ppm	FUS-MS (0.01)	4.45	4.09	2.89	4.39	3.72	4.14	4.74	4.4	4.38	4.83	3.35	5.3	1.58	2.6	1.48	4.69
Eu ppm	FUS-MS (0.005)	1.34	1.26	0.96	1.37	1.16	1.24	1.42	1.31	1.3	1.49	0.99	1.56	0.53	0.83	0.51	1.48
Gd ppm	FUS-MS (0.02)	4.15	3.83	3.12	4.19	3.35	3.8	4.13	4.05	4.01	4.47	2.99	4.38	1.73	2.39	1.68	4.48
Tb ppm	FUS-MS (0.01)	0.68	0.53	0.45	0.71	0.54	0.52	0.67	0.66	0.64	0.74	0.51	0.71	0.33	0.42	0.32	0.73
Dy ppm	FUS-MS (0.02)	3.96	2.89	2.63	4.34	3.23	3.01	3.79	3.88	3.77	4.42	3.09	4.15	2.07	2.6	2.07	4.38
Ho ppm	FUS-MS (0.01)	0.77	0.59	0.56	0.84	0.65	0.63	0.74	0.74	0.73	0.86	0.63	0.8	0.42	0.52	0.43	0.88
Er ppm	FUS-MS (0.01)	2.2	1.77	1.77	2.43	1.92	1.94	2.15	2.09	2.04	2.46	1.91	2.33	1.25	1.55	1.24	2.59
Tl ppm	FUS-MS (0.05)	0.65	1.03	0.92	0.86	2.22	0.1	0.96	0.81	0.93	1.35	0.51	1.61	0.07	0.21	0.13	1.06
Tm ppm	FUS-MS (0.005)	0.32	0.27	0.27	0.36	0.29	0.30	0.31	0.31	0.29	0.36	0.30	0.35	0.18	0.23	0.18	0.38
Yb ppm	FUS-MS (0.01)	2.03	1.77	1.76	2.34	1.95	1.93	1.95	1.92	1.82	2.3	2.04	2.23	1.19	1.42	1.15	2.37

Appendix E: Lithochemical Data Cont'd

Element (unit)	Method (detec. Limit)	08-Bu- 13	08-Bu- 19	08-Bu- 29	08-Bu- 30	08-Bu- 32	08-Bu- 36	08-Bu- 58	08-Bu- 61	08-Bu- 72	08-Bu- 76	08-Bu- 78	08-Bu- 79	08-Bu- 84	08-Bu- 85	08-Bu- 86	08-Bu- 88
Lu ppm	FUS-MS (0.002)	0.32	0.26	0.28	0.36	0.30	0.29	0.28	0.29	0.28	0.35	0.32	0.34	0.19	0.22	0.18	0.36
Mass grams		1.68	1.32	1.66	1.45	1.12	1.61	1.74	1.62	1.88	1.67	1.62	1.31	1.66	1.64	1.80	1.30

Element (unit)	Method (detec. Limit)	08-Bu- 93	08-Bu- 96	09-Bu- 47	09-Bu- 107	09-Bu- 139	09-Bu- 149	09-Bu- 172	09-Bu- 173	09-Bu- 177	09-Bu- 191	09-Bu- 204	09-Bu- 205	09-Bu- 226	09-Bu- 234	09-Bu- 242	09-Bu- 255	09-Bu- 261
SiO ₂ %	FUS-ICP (0.01)	54.7	56.13	64.3	52.51	50.63	49.47	50.88	72.88	51.15	64.38	69.71	54.08	51.36	53.64	52.41	68.05	65.23
Al ₂ O ₃ %	FUS-ICP (0.01)	15.06	14.81	13.61	16.97	13.58	14.28	15.58	13.35	14.36	15.12	14.39	17.06	15.48	14.32	16.03	13.5	14.02
Fe ₂ O ₃ (T) %	FUS-ICP (0.01)	8.34	5.47	6.38	6.25	12.66	12.27	9.64	2.66	11.77	5.93	4.83	7.48	11	10.3	8.86	4.9	6.58
MnO %	FUS-ICP (0.001)	0.29	0.21	0.10	0.15	0.21	0.19	0.15	0.03	0.16	0.11	0.10	0.25	0.22	0.19	0.18	0.12	0.12
MgO %	FUS-ICP (0.01)	4.53	3.65	1.95	1.99	6.95	7.75	6.53	0.61	7.05	2.4	1.23	2.44	6.51	6.05	3.23	1.66	1.98
CaO %	FUS-ICP (0.01)	7.28	9.84	5.43	7.96	9.66	10.93	9.9	4.12	9.74	6.27	4.42	7.58	4.75	8.61	8.15	3.27	4.84
Na ₂ O %	FUS-ICP (0.01)	3.05	3.6	3.25	2.45	2.66	2.25	2.4	3.93	2.76	3.08	3.53	3.3	4.76	2.57	2.81	3.82	3.6
K ₂ O %	FUS-ICP (0.01)	3.59	0.75	0.62	2.78	0.2	0.14	0.32	0.17	0.12	0.28	0.95	2.86	0.67	2.16	2.68	1.1	0.82
TiO ₂ %	FUS-ICP (0.001)	0.67	0.69	0.59	0.48	1.15	1.09	0.40	0.20	0.88	0.32	0.22	0.67	0.53	0.88	0.80	0.43	0.63
P ₂ O ₅ %	FUS-ICP (0.01)	0.4	0.35	0.15	0.31	0.1	0.08	0.05	0.04	0.07	0.04	0.04	0.4	0.1	0.48	0.4	0.12	0.18
LOI %	FUS-ICP	1.63	4.82	2.16	8.29	2.03	1.02	3.36	0.43	1.16	0.99	0.79	3.36	4.31	1.1	3.52	2.77	2.26
Total %	FUS-ICP (0.01)	99.54	100.3	98.53	100.2	99.83	99.47	99.19	98.42	99.22	98.93	100.2	99.48	99.69	100.3	99.08	99.75	100.3
Au ppb	INAA (1)	12	8	<1	<1	<1	<1	<1	<1	<1	<1	<1	<1	6	10	31	<1	<1

Element (unit)	Method (detec. Limit)	08-Bu- 93	08-Bu- 96	09-Bu- 47	09-Bu- 107	09-Bu- 139	09-Bu- 149	09-Bu- 172	09-Bu- 173	09-Bu- 177	09-Bu- 191	09-Bu- 204	09-Bu- 205	09-Bu- 226	09-Bu- 234	09-Bu- 242	09-Bu- 255	09-Bu- 261
Ag ppm	MULT INAA / TD-ICP (0.5)	0.6	< 0.5	< 0.5	< 0.5	< 0.5	< 0.5	< 0.5	< 0.5	< 0.5	< 0.5	< 0.5	0.8	< 0.5	< 0.5	1	< 0.5	< 0.5
As ppm	INAA (1)	53	54	< 1	1	< 1	< 1	< 1	< 1	< 1	3	1	6	17	24	38	< 1	< 1
Ba ppm	FUS-ICP (1)	1295	553	238	1421	41	65	107	82	24	80	242	1176	246	1096	2084	638	934
Be ppm	FUS-ICP (1)	2	2	< 1	2	< 1	< 1	< 1	< 1	< 1	< 1	< 1	1	< 1	1	1	< 1	< 1
Bi ppm	FUS-MS (0.1)	0.1	0.4	< 0.1	< 0.1	< 0.1	< 0.1	< 0.1	< 0.1	< 0.1	< 0.1	< 0.1	< 0.1	0.3	< 0.1	0.7	< 0.1	< 0.1
Br ppm	INAA (0.5)	1.5	< 0.5	< 0.5	0.7	< 0.5	< 0.5	0.7	1.1	< 0.5	1.6	0.9	< 0.5	< 0.5	< 0.5	1.2	< 0.5	< 0.5
Cd ppm	TD-ICP (0.5)	7.5	< 0.5	< 0.5	< 0.5	< 0.5	< 0.5	< 0.5	< 0.5	< 0.5	< 0.5	< 0.5	< 0.5	2.4	4.2	1	< 0.5	< 0.5
Co ppm	INAA (0.1)	31	11.4	15.5	12.4	45.4	45.3	36	4.2	40.8	14.8	11.5	15.2	35	24.6	26.1	12.3	14.2
Cr ppm	INAA (0.5)	94.4	65.4	38.6	13.4	130	267	167	29	242	22.7	7.1	20.3	67.6	194	25.7	15.2	29.9
Cs ppm	FUS-MS (0.1)	0.4	0.9	< 0.1	0.7	0.2	0.9	0.1	< 0.1	< 0.1	0.3	< 0.1	0.2	0.1	0.2	0.2	0.2	0.1
Cu ppm	TD-ICP (1)	148	58	71	55	191	166	66	68	92	6	12	63	100	41	63	4	48
Ga ppm	FUS-MS (1)	17	16	12	15	13	14	11	10	13	13	12	17	12	15	17	12	13

Element (unit)	Method (detec. Limit)	08-Bu- 93	08-Bu- 96	09-Bu- 47	09-Bu- 107	09-Bu- 139	09-Bu- 149	09-Bu- 172	09-Bu- 173	09-Bu- 177	09-Bu- 191	09-Bu- 204	09-Bu- 205	09-Bu- 226	09-Bu- 234	09-Bu- 242	09-Bu- 255	09-Bu- 261
Ge ppm	FUS-MS (0.5)	1.2	1.2	1.5	1.7	1.6	1.7	1.5	1.7	1.5	1.4	1.5	1.5	1.6	1.6	1.6	1.7	1.7
Hf ppm	FUS-MS (0.1)	2.6	1.4	2.6	2.3	1.7	1.5	0.6	2.5	1.2	1.7	2.8	3.2	0.7	2.4	2.4	3	3.4
Hg ppm	INAA (1)	< 1	< 1	< 1	< 1	< 1	< 1	< 1	< 1	< 1	< 1	< 1	< 1	< 1	< 1	< 1	< 1	< 1
In ppm	FUS-MS (0.1)	< 0.1	< 0.1	< 0.1	< 0.1	< 0.1	< 0.1	< 0.1	< 0.1	< 0.1	< 0.1	< 0.1	< 0.1	< 0.1	< 0.1	< 0.1	< 0.1	< 0.1
Ir ppb	INAA (1)	< 1	< 1	< 1	< 1	< 1	< 1	< 1	< 1	< 1	< 1	< 1	< 1	< 1	< 1	< 1	< 1	< 1
Mo ppm	FUS-MS (2)	3	< 2	< 2	< 2	< 2	< 2	< 2	< 2	< 2	< 2	< 2	< 2	< 2	< 2	< 2	< 2	< 2
Nb ppm	FUS-MS (0.2)	5.3	5	7.9	6.9	4.5	4.2	1.3	6.8	3.3	3.1	3.9	7.3	1.2	7.5	6.6	4.6	5.2
Ni ppm	TD-ICP (1)	40	17	12	5	74	105	32	3	77	12	6	9	24	39	11	5	9
Pb ppm	TD-ICP (5)	12	< 5	< 5	6	< 5	< 5	< 5	< 5	< 5	< 5	< 5	< 5	< 5	< 5	< 5	< 5	< 5
Rb ppm	FUS-MS (2)	78	12	7	58	3	3	5	< 1	1	4	13	60	12	40	45	17	13
S %	TD-ICP (0.001)	0.67	2.61	0.01	0.05	0.08	0.04	0.01	0.01	0.05	0.04	0.01	0.06	0.83	0.18	3.43	0.01	0.02
Sb ppm	INAA (0.1)	8.1	15.1	1.3	0.2	< 0.1	< 0.1	< 0.1	< 0.1	< 0.1	< 0.1	0.3	1.9	6.7	3.9	8.8	0.2	0.4
Sc ppm	INAA (0.01)	20.5	17.8	21.5	12.8	49.3	48	40.2	9.61	45.9	19.8	12.6	12	39.9	31.8	18.9	14.1	19.8

Element (unit)	Method (detec. Limit)	08-Bu- 93	08-Bu- 96	09-Bu- 47	09-Bu- 107	09-Bu- 139	09-Bu- 149	09-Bu- 172	09-Bu- 173	09-Bu- 177	09-Bu- 191	09-Bu- 204	09-Bu- 205	09-Bu- 226	09-Bu- 234	09-Bu- 242	09-Bu- 255	09-Bu- 261
Se ppm	INAA (0.5)	< 0.5	< 0.5	< 0.5	< 0.5	< 0.5	< 0.5	< 0.5	< 0.5	< 0.5	< 0.5	< 0.5	< 0.5	< 0.5	< 0.5	< 0.5	< 0.5	< 0.5
Sn ppm	FUS-MS (1)	1	< 1	4	1	1	1	< 1	4	1	2	2	2	< 1	3	2	2	3
Sr ppm	FUS-ICP (2)	849	921	163	657	92	101	150	163	108	197	164	941	245	636	724	155	281
Ta ppm	FUS-MS (0.01)	0.3	0.2	0.54	0.41	0.27	0.27	0.08	0.25	0.22	0.21	0.3	0.49	0.08	0.44	0.4	0.33	0.36
Th ppm	FUS-MS (0.05)	3.33	1.56	2.56	3.84	0.31	0.27	0.24	2.43	0.3	0.79	1.22	3.85	0.27	2.83	2.59	1.21	1.43
U ppm	FUS-MS (0.05)	1.97	0.99	0.89	2.21	0.08	0.07	0.06	0.65	0.07	0.33	0.42	1.94	0.09	1.5	1.55	0.54	0.62
V ppm	FUS-ICP (5)	215	271	149	157	389	382	236	27	328	103	61	185	282	302	243	71	124
W ppm	INAA (1)	< 1	< 1	< 1	< 1	< 1	< 1	< 1	< 1	< 1	< 1	< 1	< 1	< 1	< 1	< 1	< 1	< 1
Y ppm	FUS-ICP (1)	17	18	17	15	22	21	7	11	18	11	9	22	10	25	21	16	20
Zn ppm	MULT INAA / TD-ICP (1)	949	82	79	75	121	66	56	24	28	30	52	117	161	162	104	88	64
Zr ppm	FUS-MS (1)	94	51	112	110	65	58	24	111	51	68	119	146	28	106	107	130	143
La ppm	FUS-MS (0.05)	20.6	15.7	8.33	22.5	3.71	3.26	2.16	3.03	2.94	4.9	5.02	23.2	2.44	20	18.1	8.13	9.16

Element (unit)	Method (detec. Limit)	08-Bu- 93	08-Bu- 96	09-Bu- 47	09-Bu- 107	09-Bu- 139	09-Bu- 149	09-Bu- 172	09-Bu- 173	09-Bu- 177	09-Bu- 191	09-Bu- 204	09-Bu- 205	09-Bu- 226	09-Bu- 234	09-Bu- 242	09-Bu- 255	09-Bu- 261
Ce ppm	FUS-MS (0.1)	40	33.6	17.3	37.4	9.18	7.92	4.89	6.46	7.11	9.77	9.95	41.4	5.08	36.1	32.4	18	20.4
Pr ppm	FUS-MS (0.02)	5.35	4.76	2.26	4.24	1.35	1.16	0.67	0.91	1.04	1.28	1.26	5.26	0.77	4.67	4.23	2.49	2.88
Nd ppm	FUS-MS (0.05)	19.7	18.2	10.3	15.7	6.44	5.75	3.12	4.66	5.19	5.61	5.31	21.3	3.71	20.2	18	11.2	12.9
Sm ppm	FUS-MS (0.01)	4.2	4.15	2.62	3.17	2.25	1.96	0.86	1.56	1.69	1.6	1.34	4.79	1.16	4.66	4.09	2.75	3.37
Eu ppm	FUS-MS (0.005)	1.25	1.34	0.68	0.98	0.80	0.71	0.32	0.47	0.63	0.43	0.38	1.38	0.39	1.42	1.25	0.65	0.89
Gd ppm	FUS-MS (0.02)	3.54	3.61	2.95	2.87	3.16	2.72	1.01	1.96	2.36	1.8	1.51	4.16	1.6	4.89	3.83	2.84	3.43
Tb ppm	FUS-MS (0.01)	0.55	0.61	0.5	0.45	0.61	0.53	0.18	0.31	0.48	0.3	0.26	0.67	0.28	0.76	0.63	0.48	0.59
Dy ppm	FUS-MS (0.02)	3.19	3.58	3.12	2.65	4.04	3.49	1.25	1.97	3.11	1.96	1.65	3.97	1.83	4.39	3.67	3	3.75
Ho ppm	FUS-MS (0.01)	0.61	0.69	0.64	0.53	0.83	0.71	0.26	0.39	0.63	0.39	0.34	0.79	0.38	0.87	0.72	0.63	0.76
Er ppm	FUS-MS (0.01)	1.76	1.92	1.86	1.56	2.5	2.17	0.77	1.18	1.9	1.16	1.02	2.3	1.15	2.52	2.09	1.84	2.17
Tl ppm	FUS-MS (0.05)	1.07	0.2	< 0.05	0.25	< 0.05	< 0.05	< 0.05	< 0.05	< 0.05	< 0.05	0.06	0.28	0.15	0.16	0.23	< 0.05	< 0.05
Tm ppm	FUS-MS (0.005)	0.26	0.28	0.30	0.26	0.40	0.35	0.13	0.19	0.31	0.18	0.17	0.35	0.19	0.38	0.32	0.29	0.34
Yb ppm	FUS-MS (0.01)	1.62	1.75	1.93	1.79	2.6	2.35	0.83	1.31	2.09	1.21	1.18	2.49	1.23	2.42	2.18	1.97	2.36

Appendix E: Lithochemical Data Cont'd

Element (unit)	Method (detec. Limit)	08-Bu- 93	08-Bu- 96	09-Bu- 47	09-Bu- 107	09-Bu- 139	09-Bu- 149	09-Bu- 172	09-Bu- 173	09-Bu- 177	09-Bu- 191	09-Bu- 204	09-Bu- 205	09-Bu- 226	09-Bu- 234	09-Bu- 242	09-Bu- 255	09-Bu- 261
Lu ppm	FUS-MS (0.002)	0.25	0.26	0.31	0.26	0.37	0.34	0.13	0.20	0.31	0.19	0.19	0.37	0.18	0.36	0.32	0.29	0.35
Mass grams		1.72	1.65	1.62	1.46	1.83	1.72	1.62	1.30	1.55	1.21	1.45	1.47	1.46	1.52	1.31	1.36	1.73

08-Bu-16, Sericite, 11.80 mg, J = 0.001743 ± 0.18%4 amu discrimination = 1.0593 ± 0.57%, $^{40/39}\text{K}$ = 0.0205 ± 33.35%, $^{36/37}\text{Ca}$ = 0.000267 ± 1.87%, $^{39/37}\text{Ca}$ = 0.000691 ± 1.19%

Step	T (C)	t (min.)	^{36}Ar	^{37}Ar	^{38}Ar	^{39}Ar	^{40}Ar	% $^{40}\text{Ar}^*$	% ^{39}Ar rlsd	Ca/K	$^{40}\text{Ar}^*/^{39}\text{ArK}$	Age (Ma)	1 s.d.
1	455	12	0.671	0.085	0.480	8.19	211.934	12.1	0.6	0.3123728856	3.043497	9.55	0.78
2	500	12	0.410	0.087	0.269	7.876	133.414	15.1	0.6	0.3324715384	2.433189	7.64	0.46
3	540	12	0.342	0.116	0.249	11.756	125.387	25.5	0.8	0.2969851335	2.569573	8.06	0.19
4	580	12	0.409	0.418	0.408	22.155	168.256	33.9	1.6	0.5679056243	2.473430	7.76	0.15
5	620	12	0.562	1.693	0.779	43.467	246.379	38.0	3.1	1.1725943865	2.107211	6.61	0.11
6	660	12	1.115	4.252	0.977	56.252	456.973	31.1	4.0	2.2764061762	2.509522	7.87	0.15
7	700	12	0.890	6.390	1.199	73.373	449.275	46.7	5.3	2.6230359523	2.845635	8.93	0.12
8	750	12	0.670	1.244	1.538	105.483	453.261	59.9	7.6	0.3549619237	2.551046	8.00	0.09
9	810	12	0.279	0.170	1.954	141.843	431.463	83.2	10.2	0.0360697614	2.507606	7.87	0.07
10	880	12	0.343	0.182	2.427	174.417	520.506	83.6	12.5	0.0314039461	2.438299	7.65	0.07
11	1000	12	1.065	0.504	7.949	575.169	1713.4	82.8	41.2	0.0263715743	2.471195	7.75	0.07
12	1080	12	0.339	0.642	1.536	101.919	344.687	75.7	7.3	0.1895842086	2.460016	7.72	0.07
13	1180	12	0.198	0.502	0.603	34.819	140.826	81.4	2.5	0.433951896	2.441812	7.66	0.07
14	1400	12	0.454	1.439	0.779	38.57	253.706	75.7	2.8	1.1231951815	3.204009	10.05	0.12

Cumulative % ^{39}Ar rlsd = 100.0

Total gas age = 7.87 0.05

Plateau age = 7.73 0.06

(steps 9-13)

Isochron age = 7.73 0.13

(steps 10-13)

note: isotope beams in mV, rlsd = released, error in age includes J error, all errors 1 sigma

(^{36}Ar through ^{40}Ar are measured beam intensities, corrected for decay for the age calculations)

08-Bu-83, Sericite, 14.40 mg, J = 0.001737 ± 0.16%

4 amu discrimination = 1.0593 ± 0.57%, $^{40/39}\text{K}$ = 0.0205 ± 33.35%, $^{36/37}\text{Ca}$ = 0.000267 ± 1.87%, $^{39/37}\text{Ca}$ = 0.000691 ± 1.19%

Step	T (C)	t (min.)	^{36}Ar	^{37}Ar	^{38}Ar	^{39}Ar	^{40}Ar	% $^{40}\text{Ar}^*$	% ^{39}Ar rlsd	Ca/K	$^{40}\text{Ar}^*/^{39}\text{ArK}$	Age (Ma)	1 s.d.	
1	620	12	1.256	1.834	2.200	127.265	642.959	46.0	6.9	0.4427219939	2.323354	7.27	0.10	
2	670	12	0.672	3.516	1.584	107.193	467.192	61.3	5.8	1.0078523424	2.657949	8.31	0.09	
3	720	12	0.754	3.413	2.116	148.621	604.947	66.4	8.1	0.7055554408	2.694818	8.43	0.09	
4	770	12	0.414	0.236	2.548	182.209	581.973	81.7	9.9	0.0397860072	2.703154	8.45	0.08	
5	810	12	0.178	0.137	2.086	153.745	431.864	89.8	8.3	0.0273719744	2.499922	7.82	0.07	
6	850	12	0.150	0.115	1.510	107.637	305.613	88.5	5.8	0.0328188625	2.464668	7.71	0.07	
7	890	12	0.163	0.114	1.269	92.194	273.473	85.8	5.0	0.0379830763	2.487743	7.78	0.07	
8	930	12	0.278	0.155	2.040	146.269	439.738	84.9	7.9	0.0325511728	2.480692	7.76	0.07	
9	970	12	0.439	0.204	2.925	206.821	628.338	82.0	11.2	0.0302985939	2.452490	7.67	0.07	
10	1010	12	0.467	0.311	2.741	193.897	607.54	80.1	10.5	0.0492695635	2.468193	7.72	0.07	
11	1060	12	0.460	0.314	2.510	176.331	563.557	78.9	9.6	0.0547004755	2.474603	7.74	0.07	
12	1150	12	0.293	0.393	1.561	103.717	337.805	84.3	5.6	0.1163967295	2.470116	7.72	0.07	
13	1400	12	0.592	2.466	1.821	96.827	422.831	73.4	5.3	0.7824951757	2.641920	8.26	0.08	
Cumulative % ^{39}Ar rlsd =									100.0			Total gas age =	7.89	0.04
												Plateau age =	7.74	0.05
												(steps 5-12)		
												Isochron age =	7.89	0.06
												(steps 5-12)		

note: isotope beams in mV, rlsd = released, error in age includes J error, all errors 1 sigma
 (^{36}Ar through ^{40}Ar are measured beam intensities, corrected for decay for the age calculations)

09-Bu-191, Amphibole, 15.50 mg, J = 0.001743 ± 0.18%4 amu discrimination = 1.0593 ± 0.57%, $^{40/39}\text{K} = 0.0205 \pm 33.35\%$, $^{36/37}\text{Ca} = 0.000267 \pm 1.87\%$, $^{39/37}\text{Ca} = 0.000691 \pm 1.19\%$

Step	T (C)	t (min.)	^{36}Ar	^{37}Ar	^{38}Ar	^{39}Ar	^{40}Ar	% $^{40}\text{Ar}^*$	% ^{39}Ar rlsd	Ca/K	$^{40}\text{Ar}^*/^{39}\text{ArK}$	Age (Ma)	1 s.d.
1	750	12	1.309	0.419	0.589	0.297	413.03	12.0	0.8	44.7658937312	168.731651	465.12	21.51
2	850	12	0.228	0.561	0.136	0.133	71.707	14.2	0.3	137.525110672	71.435831	211.71	9.35
3	950	12	0.146	2.155	1.684	1.048	74.605	61.3	2.7	65.6532981849	34.471746	105.27	1.15
4	990	12	0.162	3.702	3.604	2.167	112.297	73.7	5.5	54.3626953128	33.169826	101.40	1.01
5	1020	12	0.137	4.313	5.122	2.835	124.396	83.8	7.2	48.325247883	32.454050	99.27	0.85
6	1040	12	0.146	5.977	7.520	3.693	145.763	85.9	9.4	51.4581753412	30.675171	93.97	0.78
7	1060	12	0.168	7.952	10.366	4.481	174.047	85.9	11.4	56.5067160374	30.888951	94.61	0.85
8	1080	12	0.130	7.879	10.226	4.061	151.352	91.4	10.4	61.8764135491	31.054866	95.10	0.93
9	1100	12	0.106	0.028	7.789	2.958	112.494	86.1	7.5	0.2964054755	27.989620	85.93	1.05
10	1120	12	0.066	2.327	2.959	1.189	51.654	100.0	3.0	62.426942637	29.548886	90.60	1.16
11	1140	12	0.070	1.081	1.252	0.583	36.927	89.9	1.5	59.0862746864	30.712695	94.08	1.48
12	1170	12	0.092	2.644	3.284	1.451	68.28	87.3	3.7	58.0484241058	31.417357	96.18	1.07
13	1210	12	0.128	3.645	4.411	1.896	91.375	79.1	4.8	61.301711351	31.743482	97.15	0.86
14	1400	12	0.635	22.888	29.202	12.398	552.154	85.5	31.6	58.8236560156	32.691988	99.98	0.83

Cumulative % ^{39}Ar rlsd = 100.0

Total gas age = 99.90 0.57

No plateau

No isochron

note: isotope beams in mV, rlsd = released, error in age includes J error, all errors 1 sigma

(^{36}Ar through ^{40}Ar are measured beam intensities, corrected for decay for the age calculations)

09-Bu-205, Amphibole, 8.00 mg, J = 0.001744 ± 0.18%4 amu discrimination = 1.0593 ± 0.57%, $^{40/39}\text{K} = 0.0205 \pm 33.35\%$, $^{36/37}\text{Ca} = 0.000267 \pm 1.87\%$, $^{39/37}\text{Ca} = 0.000691 \pm 1.19\%$

Step	T (C)	t (min.)	^{36}Ar	^{37}Ar	^{38}Ar	^{39}Ar	^{40}Ar	% $^{40}\text{Ar}^*$	% ^{39}Ar rlsd	Ca/K	$^{40}\text{Ar}^*/^{39}\text{ArK}$	Age (Ma)	1 s.d.
1	850	12	4.026	6.392	1.455	1.482	1186.86	6.0	1.1	143.3472822145	50.374365	151.91	14.38
2	950	12	0.086	0.549	0.280	0.461	25.35	8.9	0.3	38.383076155	1.526353	4.80	0.57
3	1020	12	0.072	0.746	0.453	1.690	25.631	63.8	1.2	14.1247274762	3.049739	9.57	0.25
4	1050	12	0.065	1.271	1.027	4.307	27.937	96.1	3.1	9.4294892921	2.320411	7.29	0.11
5	1080	12	0.085	3.811	2.587	13.900	53.419	90.4	9.9	8.7589973689	2.359344	7.41	0.08
6	1110	12	0.151	12.243	7.117	45.806	141.545	89.2	32.8	8.5382132098	2.449030	7.69	0.07
7	1140	12	0.143	14.873	5.237	54.539	156.518	93.9	39.0	8.711953175	2.427325	7.62	0.07
8	1170	12	0.083	1.847	1.659	5.653	35.208	72.4	4.0	10.4432887672	2.279884	7.16	0.13
9	1250	12	0.151	3.411	3.077	10.737	70.254	92.6	7.7	10.1533751453	2.849114	8.94	0.10
10	1400	12	0.265	0.281	0.203	1.277	86.768	23.7	0.9	7.0261936216	9.254806	28.89	0.75

Cumulative % ^{39}Ar rlsd = 100.0

Total gas age = 9.43 0.07

Plateau age = 7.59 0.08

(steps 5-7)

Isochron age = 7.41 0.20

(steps 3-7)

note: isotope beams in mV, rlsd = released, error in age includes J error, all errors 1 sigma

(^{36}Ar through ^{40}Ar are measured beam intensities, corrected for decay for the age calculations)

Ref #	Sample ID	Fill ¹ (%)	Visible Contents ² at 20°C	T _{m_{CO2}} (°C)	T _i (°C)	T _{m_{ice}} (°C)	Salinity ³ wt.% NaCl eq. (Bodnar, 1993)	T _{m_{Clath}} (°C)	Th _{L-V(L)} (°C)	Class ⁴	Host mineral
Bu F5	09-M-8	90	L+V	-	-	-3.0	4.96	-	286	P	Quartz
Bu F6	09-M-8	90	L+V	-	-	-2.9	4.80	-	284	P	Quartz
Bu F7	09-M-8	85	L+V	-	-	-2.9	4.80	-	283	P	Quartz
Bu F8	09-M-8	90	L+V	-	-	-3.0	4.96	-	281	P	Quartz
Bu F9	09-M-8	75	L+V	-	-	-2.9	4.80	-	280	P	Quartz
Bu F10	09-M-8	90	L+V	-	-	-3.0	4.96	-	279	P	Quartz
Bu F11	09-M-8	90	L+V	-	-	-3.1	5.11	-	282	P	Quartz
Bu F12	09-M-8	85	L+V	-	-	-3.7	6.01	-	296	P	Quartz
Bu F13	09-M-8	90	L+V	-	-	-3.6	5.86	-	274	P	Quartz
Bu F14	09-M-8	80	L+V	-	-	-2.5	4.18	-	299	P	Quartz
Bu F15	09-M-8	75	L+V	-	-	-2.9	4.80	-	296	P	Quartz
Bu F16	09-M-8	90	L+V	-	-	-3.7	6.01	-	299	P	Quartz
Bu F17	09-M-8	90	L+V	-	-	-3.5	5.71	-	281	P	Quartz
Bu F18	09-M-8	80	L+V	-	-	-5.3	8.28	-	302	P	Quartz
Bu F19	09-M-8	85	L+V	-	-	-5.5	8.55	-	305	P	Quartz
Bu F20	09-M-8	80	L+V	-	-	-4.7	7.45	-	319	P	Quartz
Bu F21	09-M-14	90	L+V	-	-	-4.4	7.02	-	296	P	Quartz
Bu F22	09-M-14	90	L+V	-	-	-3.8	6.16	-	276	P	Quartz
Bu F23	09-M-14	55	CO2+L+V	-56.3	-22.1	-3.9	6.30	-	381	P	Quartz
Bu F24	09-M-14	70	L+V	-	-	-4.9	7.73	-	311	P	Quartz
Bu F25	09-M-14	5	CO2+L+V	-56.4	-	-6.7	10.11	-	-	P	Quartz
Bu F26	09-M-14	80	L+V	-	-	-3.7	6.01	-	332	P	Quartz
Bu F27	09-M-14	70	L+V	-	-	-2.0	3.39	-	314	P	Brown Sphalerite

Ref #	Sample ID	Fill ¹ (%)	Visible Contents ² at 20°C	T _{m_{CO₂}} (°C)	T _i (°C)	T _{m_{ice}} (°C)	Salinity ³ wt.% NaCl eq. (Bodnar, 1993)	T _{m_{Clath}} (°C)	Th _{L-V(L)} (°C)	Class ⁴	Host mineral
Bu F28	09-M-14	90	L+V	-	-23.1	-2.9	4.80	-	292	P	Quartz
Bu F29	09-M-14	85	L+V	-	-	-3.1	5.11	-	332	P	Quartz
Bu F30	09-M-14	85	L+V	-	-	-3.6	5.86	-	326	P	Quartz
Bu F31	09-M-14	85	L+V	-	-	-3.8	6.16	-	331	P	Quartz
Bu F32	09-M-14	85	L+V	-	-	-3.3	5.41	-	329	P	Quartz
Bu F33	09-M-14	85	L+V	-	-	-3.7	6.01	-	316	P	Quartz
Bu F34	09-M-14	90	L+V	-	-	-3.5	5.71	-	320	P	Quartz
Bu F35	09-M-14	90	L+V	-	-	-5.4	8.41	-	289	P	Quartz
Bu F36	09-M-14	75	L+V	-	-23.7	-4.0	6.45	-	360	P	Quartz
Bu F37	09-M-14	85	L+V	-	-22.1	-3.8	6.16	-	325	P	Quartz
Bu F38	09-M-14	85	L+V	-	-	-3.6	5.86	-	332	P	Quartz
Bu F39	09-M-14	85	L+V	-	-	-4.5	7.17	-	310	P	Quartz
Bu F40	09-M-14	90	L+V	-	-	-3.6	5.86	-	281	P	Quartz
Bu F41	09-M-14	90	L+V	-	-	-3.0	4.96	-	290	P	Quartz
Bu F42	09-M-14	80	L+V	-	-	-1.3	2.24	-	219	P	Yellow Sphalerite
Bu F43	09-M-14	75	L+V	-	-	-2.3	3.87	-	281	P	Yellow Sphalerite
Bu F44	09-M-14	90	L+V	-	-23.7	-2.2	3.71	-	241	P	Yellow Sphalerite
Bu F45	09-M-14	90	L+V	-	-	-1.8	3.06	-	247	P	Yellow Sphalerite
Bu F46	09-M-14	90	L+V	-	-	-1.7	2.90	-	237	P	Yellow Sphalerite
Bu F47	09-M-14	90	L+V	-	-	-2.1	3.55	-	233	P	Yellow Sphalerite
Bu F48	09-M-14	85	L+V	-	-	-2.2	3.71	-	278	P	Yellow Sphalerite
Bu F49	09-M-14	90	L+V	-	-	-1.5	2.57	-	248	P	Yellow Sphalerite
Bu F50	09-M-14	90	L+V	-	-	-1.2	2.07	-	246	P	Yellow Sphalerite

Ref #	Sample ID	Fill ¹ (%)	Visible Contents ² at 20°C	T _{m_{CO2}} (°C)	T _i (°C)	T _{m_{ice}} (°C)	Salinity ³ wt.% NaCl eq. (Bodnar, 1993)	T _{m_{Clath}} (°C)	Th _{L-V(L)} (°C)	Class ⁴	Host mineral
Bu F51	09-M-14	90	L+V	-	-	-1.8	3.06	-	248	P	Yellow Sphalerite
Bu F52	09-M-14	90	L+V	-	-	-1.5	2.57	-	235	P	Yellow Sphalerite
Bu F53	09-M-14	85	L+V	-	-24.4	-3.4	5.56	-	286	P	Yellow Sphalerite
Bu F54	09-M-14	90	L+V	-	-	-2.0	3.39	-	238	P	Yellow Sphalerite
Bu F55	09-M-14	80	L+V	-	-	-2.1	3.55	-	230	P	Yellow Sphalerite
Bu F56	09-M-14	80	L+V	-	-	-3.2	5.26	-	281	P	Yellow Sphalerite
Bu F57	09-M-14	70	L+V	-	-	-2.3	3.87	-	232	P	Yellow Sphalerite
Bu F58	09-M-14	70	L+V	-	-24.2	-3.0	4.96	-	329	P	Yellow Sphalerite
Bu F59	09-M-14	80	L+V	-	-	-2.3	3.87	-	233	P	Yellow Sphalerite
Bu F60	09-M-14	90	L+V	-	-24.0	-1.5	2.57	-	233	P	Yellow Sphalerite
Bu F61	09-M-14	75	L+V	-	-24.5	-2.6	4.34	-	264	P	Yellow Sphalerite
Bu F62	09-M-14	70	L+V	-	-	-3.3	5.41	-	286	P	Brown Sphalerite
Bu F63	09-M-14	40	L+V	-	-	-4.1	6.59	-	347	P	Brown Sphalerite
Bu F64	09-M-14	70	L+V	-	-	-3.0	4.96	-	296	P	Brown Sphalerite
Bu F65	09-M-14	80	L+V	-	-	-3.3	5.41	-	309	P	Brown Sphalerite
Bu F66	09-M-14	40	L+V	-	-	-3.6	5.86	-	301	P	Brown Sphalerite
Bu F67	09-M-14	95	L+V	-	-	-3.1	5.11	-	281	P	Brown Sphalerite
Bu F68	09-M-14	90	L+V	-	-	-3.4	5.56	-	294	P	Brown Sphalerite
Bu F69	09-M-14	90	L+V	-	-	-3.6	5.86	-	311	P	Brown Sphalerite
Bu F70	09-M-14	85	L+V	-	-22.3	-2.7	4.49	-	276	P	Quartz
Bu F71	09-M-14	85	L+V	-	-24.0	-2.8	4.65	-	275	P	Quartz
Bu F72	09-M-14	85	L+V	-	-22.7	-2.7	4.49	-	276	P	Quartz
Bu F73	09-M-14	80	L+V	-	-	-2.9	4.80	-	276	P	Quartz

Ref #	Sample ID	Fill ¹ (%)	Visible Contents ² at 20°C	T _{m_{CO2}} (°C)	T _i (°C)	T _{m_{ice}} (°C)	Salinity ³ wt.% NaCl eq. (Bodnar, 1993)	T _{m_{Clath}} (°C)	Th _{L-V(L)} (°C)	Class ⁴	Host mineral
Bu F76	09-M-14	85	L+V	-	-	-2.5	4.18	-	279	P	Quartz
Bu F77	09-M-14	90	L+V	-	-25.2	-4.3	6.88	-	259	P	Quartz
Bu F78	09-M-14	90	L+V	-	-	-4.3	6.88	-	253	P	Quartz
Bu F79	09-M-14	90	L+V	-	-	-4.2	6.74	-	257	P	Quartz
Bu F80	09-M-14	90	L+V	-	-	-4.1	6.59	-	258	P	Quartz
Bu F81	09-M-14	90	L+V	-	-24.4	-3.3	5.41	-	276	P	Quartz
Bu F82	09-M-14	90	L+V	-	-	-3.7	6.01	-	258	P	Quartz
Bu F83	09-M-14	90	L+V	-	-25.4	-3.7	6.01	-	270	P	Quartz
Bu F84	09-M-14	90	L+V	-	-	-4.3	6.88	-	268	P	Quartz
Bu F85	09-M-13	85	L+V	-	-	-2.8	4.65	-	273	P	Quartz
Bu F86	09-M-13	85	L+V	-	-	-2.7	4.49	-	269	P	Quartz
Bu F87	09-M-13	85	L+V	-	-32.4	-3.2	5.26	-	267	P	Quartz
Bu F88	09-M-13	90	L+V	-	-22.3	-2.5	4.18	-	242	P	Quartz
Bu F89	09-M-13	85	L+V	-	-	-2.6	4.34	-	266	P	Quartz
Bu F90	09-M-13	90	L+V	-	-	-0.8	1.40	-	219	P	Quartz
Bu F91	09-M-13	90	L+V	-	-	-1.1	1.91	-	232	P	Quartz
Bu F92	09-M-13	90	L+V	-	-	-1.1	1.91	-	227	P	Quartz
Bu F93	09-M-13	80	L+V	-	-24.1	-3.2	5.26	-	263	P	Quartz
Bu F94	09-M-13	80	L+V	-	-	-3.2	5.26	-	282	P	Quartz
Bu F95	09-M-13	80	L+V	-	-	-3.2	5.26	-	275	P	Quartz
Bu F96	09-M-13	85	L+V	-	-	-0.2	0.35	-	232	P	Quartz
Bu F97	09-M-13	85	L+V	-	-	-1.8	3.06	-	237	P	Quartz
Bu F98	09-M-13	90	L+V	-	-31.1	-1.5	2.57	-	229	P	Quartz

Ref #	Sample ID	Fill ¹ (%)	Visible Contents ² at 20°C	Tm _{CO₂} (°C)	T _i (°C)	Tm _{ice} (°C)	Salinity ³ wt.% NaCl eq. (Bodnar, 1993)	Tm _{Clath} (°C)	Th _{L-V(L)} (°C)	Class ⁴	Host mineral
Bu F99	09-M-13	90	L+V	-	-30.5	-1.6	2.74	-	231	P	Quartz
Bu F100	09-M-13	90	L+V	-	-23.6	-3.1	5.11	-	236	P	Quartz
Bu F101	09-M-13	90	L+V	-	-	-3.1	5.11	-	237	P	Quartz
Bu F102	09-M-13	85	L+V	-	-27.2	-2.0	3.39	-	262	P	Quartz
Bu F103	09-M-13	80	L+V	-	-26.4	-1.6	2.74	-	252	P	Quartz
Bu F104	09-M-13	90	L+V	-	-	-2.3	3.87	-	266	P	Quartz
Bu F105	09-M-13	85	L+V	-	-	-3.7	6.01	-	263	P	Quartz
Bu F106	09-M-13	85	L+V	-	-	-1.6	2.74	-	249	P	Quartz
Bu F107	09-M-13	90	L+V	-	-25.0	-2.4	4.03	-	254	P	Quartz
Bu F108	09-M-13	90	L+V	-	-	-1.2	2.07	-	249	P	Quartz
Bu F109	09-M-13	90	L+V	-	-	-1.6	2.74	-	254	P	Quartz
Bu F110	09-M-13	90	L+V	-	-	-2.9	4.80	-	277	P	Quartz
Bu F111	09-M-13	90	L+V	-	-	-2.3	3.87	-	280	P	Quartz
Bu F112	09-M-13	90	L+V	-	-	-4.9	7.73	-	258	P	Quartz
Bu F113	09-M-13	85	L+V	-	-	-3.1	5.11	-	293	P	Quartz
Bu F114	09-M-13	85	L+V	-	-	-2.8	4.65	-	293	P	Quartz
Bu F115	09-M-13	85	L+V	-	-	-3.1	5.11	-	297	P	Quartz
Bu F116	09-M-13	80	L+V	-	-	-3.1	5.11	-	295	P	Quartz
Bu F117	09-M-13	85	L+V	-	-	-3.0	4.96	-	291	P	Quartz
Bu F118	09-M-13	85	L+V	-	-22.2	-3.1	5.11	-	278	P	Quartz
Bu F119	09-M-13	85	L+V	-	-	-1.3	2.24	-	247	P	Quartz
Bu F120	09-M-13	85	L+V	-	-22.2	-2.6	4.34	-	283	P	Quartz
Bu F121	09-M-13	85	L+V	-	-21.5	-1.8	3.06	-	248	P	Quartz

Ref #	Sample ID	Fill ¹ (%)	Visible Contents ² at 20°C	Tm _{CO₂} (°C)	T _i (°C)	Tm _{ice} (°C)	Salinity ³ wt.% NaCl eq. (Bodnar, 1993)	Tm _{Clath} (°C)	Th _{L-V(L)} (°C)	Class ⁴	Host mineral
Bu F122	09-M-13	85	L+V	-	-	-1.2	2.07	-	260	P	Quartz
Bu F123	09-M-13	90	L+V	-	-	-1.3	2.24	-	270	P	Quartz
Bu F124	09-M-13	85	L+V	-	-	-3.2	5.26	-	297	P	Quartz
Bu F125	09-M-13	85	L+V	-	-	-3.1	5.11	-	299	P	Quartz
Bu F126	09-M-13	80	L+V	-	-	-1.7	2.90	-	259	P	Quartz
Bu F127	09-M-13	90	L+V	-	-	-1.2	2.07	-	266	P	Quartz
Bu F128	09-M-13	90	L+V	-	-	-1.1	1.91	-	251	P	Quartz
Bu F129	09-M-13	90	L+V	-	-	-1.9	3.23	-	247	P	Quartz
Bu F130	09-M-13	80	L+V	-	-	-1.8	3.06	-	246	P	Quartz
Bu F131	09-M-13	90	L+V	-	-	-2.1	3.55	-	241	P	Quartz
Bu F132	09-M-13	85	L+V	-	-	-1.3	2.24	-	252	P	Quartz
Bu F133	09-M-9	90	L+V	-	-	-2.5	4.18	-	245	P	Quartz
Bu F134	09-M-9	90	L+V	-	-	-2.7	4.49	-	246	P	Quartz
Bu F135	09-M-9	90	L+V	-	-	-2.3	3.87	-	245	P	Quartz
Bu F136	09-M-9	90	L+V	-	-21.3	-2.3	3.87	-	244	P	Quartz
Bu F137	09-M-9	90	L+V	-	-	-3.2	5.26	-	240	P	Quartz
Bu F138	09-M-9	90	L+V	-	-	-2.5	4.18	-	245	P	Quartz
Bu F139	09-M-9	90	L+V	-	-23.7	-3.1	5.11	-	263	P	Quartz
Bu F140	09-M-9	90	L+V	-	-	-3.1	5.11	-	265	P	Quartz
Bu F141	09-M-9	85	L+V	-	-	-1.4	2.41	-	266	P	Quartz
Bu F142	09-M-9	90	L+V	-	-	-1.7	2.90	-	249	P	Quartz
Bu F143	09-M-9	85	L+V	-	-	-1.7	2.90	-	246	P	Quartz
Bu F144	09-M-9	90	L+V	-	-	-1.6	2.74	-	262	P	Quartz

Ref #	Sample ID	Fill ¹ (%)	Visible Contents ² at 20°C	T _{m_{CO₂}} (°C)	T _i (°C)	T _{m_{ice}} (°C)	Salinity ³ wt.% NaCl eq. (Bodnar, 1993)	T _{m_{Clath}} (°C)	Th _{L-V(L)} (°C)	Class ⁴	Host mineral
Bu F145	09-M-9	90	L+V	-	-	-3.1	5.11	-	250	P	Quartz
Bu F146	09-M-9	90	L+V	-	-	-3.1	5.11	-	248	P	Quartz
Bu F147	09-M-9	90	L+V	-	-	-1.7	2.90	-	250	P	Quartz
Bu F148	09-M-9	90	L+V	-	-	-2.9	4.80	-	302	P	Quartz
Bu F149	09-M-9	90	L+V	-	-	-2.6	4.34	-	242	P	Quartz
Bu F150	09-M-9	90	L+V	-	-	-2.3	3.87	-	230	P	Quartz
Bu F151	09-M-9	90	L+V	-	-	-2.3	3.87	-	231	P	Quartz
Bu F152	09-M-9	90	L+V	-	-	-2.3	3.87	-	234	P	Quartz
Bu F153	08-GL-2	80	L+V	-	-25.1	-2.6	4.34	-	282	P	Brown Sphalerite
Bu F154	08-GL-2	90	L+V	-	-24.2	-2.4	4.03	-	285	P	Brown Sphalerite
Bu F155	08-GL-2	85	L+V	-	-	-2.4	4.03	-	295	P	Brown Sphalerite
Bu F156	08-GL-2	90	L+V	-	-26.8	-2.7	4.49	-	277	P	Brown Sphalerite
Bu F157	08-GL-2	90	L+V	-	-	-2.7	4.49	-	282	P	Brown Sphalerite
Bu F158	08-GL-2	90	L+V	-	-24.7	-2.7	4.49	-	285	P	Brown Sphalerite
Bu F159	08-GL-2	90	L+V	-	-	-2.6	4.34	-	291	P	Brown Sphalerite
Bu F160	08-GL-2	90	L+V	-	-	-2.4	4.03	-	291	P	Brown Sphalerite
Bu F161	08-GL-2	80	L+V	-	-	-2.4	4.03	-	286	P	Brown Sphalerite
Bu F162	08-GL-2	85	L+V	-	-	-2.4	4.03	-	287	P	Brown Sphalerite
Bu F163	08-GL-2	85	L+V	-	-29.0	-2.7	4.49	-	285	P	Brown Sphalerite
Bu F164	08-GL-2	80	L+V	-	-	-2.2	3.71	-	286	P	Brown Sphalerite
Bu F165	08-GL-2	80	L+V	-	-	-4.6	7.31	-	320	P	Brown Sphalerite
Bu F166	08-GL-2	80	L+V	-	-	-4.8	7.59	-	-	P	Brown Sphalerite
Bu F167	08-GL-2	80	L+V	-	-	-4.6	7.31	-	273	P	Brown Sphalerite

Ref #	Sample ID	Fill ¹ (%)	Visible Contents ² at 20°C	T _{m_{CO2}} (°C)	T _i (°C)	T _{m_{ice}} (°C)	Salinity ³ wt.% NaCl eq. (Bodnar, 1993)	T _{m_{Clath}} (°C)	Th _{L-V(L)} (°C)	Class ⁴	Host mineral
Bu F168	08-GL-2	70	L+V	-	-	-3.5	5.71	-	316	P	Brown Sphalerite
Bu F169	08-GL-2	70	L+V	-	-31.7	-4.6	7.31	-	318	P	Brown Sphalerite
Bu F170	08-GL-2	60	L+V	-	-	-2.4	4.03	-	348	P	Brown Sphalerite
Bu F171	08-GL-2	70	L+V	-	-	-3.6	5.86	-	317	P	Brown Sphalerite
Bu F172	08-GL-2	70	L+V	-	-31.7	-3.5	5.71	-	316	P	Brown Sphalerite
Bu F173	08-GL-2	70	L+V	-	-	-2.3	3.87	-	329	P	Brown Sphalerite
Bu F174	08-GL-2	70	L+V	-	-31.5	-3.4	5.56	-	316	P	Brown Sphalerite
Bu F175	08-GL-2	60	L+V	-	-	-2.2	3.71	-	331	P	Brown Sphalerite
Bu F176	08-GL-2	70	L+V	-	-	-0.2	0.35	-	291	P	Quartz
Bu F177	08-GL-2	80	L+V	-	-	-0.5	0.88	-	291	P	Quartz
Bu F178	08-GL-2	70	L+V	-	-	-0.3	0.53	-	302	P	Quartz
Bu F179	08-GL-2	75	L+V	-	-26.7	-0.3	0.53	-	299	P	Quartz
Bu F180	08-GL-2	75	L+V	-	-23.0	-0.3	0.53	-	297	P	Quartz
Bu F182	08-GL-2	65	L+V	-	-	-2.3	3.87	-	320	P	Quartz
Bu F183	08-GL-2	65	L+V	-	-	-1.7	2.90	-	295	P	Quartz
Bu F184	08-GL-2	80	L+V	-	-	-0.5	0.88	-	290	P	Quartz
Bu F185	08-GL-2	85	L+V	-	-	-3.2	5.26	-	286	P	Quartz
Bu F186	08-GL-2	85	L+V	-	-26.1	-3.4	5.56	-	290	P	Quartz
Bu F187	08-GL-2	85	L+V	-	-	-2.4	4.03	-	292	P	Quartz
Bu F188	08-GL-2	70	L+V	-	-	-2.4	4.03	-	296	P	Quartz
Bu F193	09-M-4	90	L+V	-	-	-3.5	5.71	-	282	P	Yellow Sphalerite
Bu F194	09-M-4	80	L+V	-	-	-1.6	2.74	-	281	P	Yellow Sphalerite
Bu F195	09-M-4	90	L+V	-	-	-1.6	2.74	-	285	P	Yellow Sphalerite

Ref #	Sample ID	Fill ¹ (%)	Visible Contents ² at 20°C	T _{m_{CO2}} (°C)	T _i (°C)	T _{m_{ice}} (°C)	Salinity ³ wt.% NaCl eq. (Bodnar, 1993)	T _{m_{Clath}} (°C)	Th _{L-V(L)} (°C)	Class ⁴	Host mineral
Bu F196	09-M-4	90	L+V	-	-	-1.7	2.90	-	285	P	Yellow Sphalerite
Bu F197	09-M-4	90	L+V	-	-	-2.4	4.03	-	283	P	Yellow Sphalerite
Bu F198	09-M-4	90	L+V	-	-	-2.4	4.03	-	285	P	Yellow Sphalerite
Bu F199	09-M-4	95	L+V	-	-	-2.2	3.71	-	274	P	Yellow Sphalerite
Bu F200	09-M-4	90	L+V	-	-	-3.5	5.71	-	275	P	Yellow Sphalerite
Bu F201	09-M-4	90	L+V	-	-	-2.4	4.03	-	266	P	Yellow Sphalerite
Bu F202	09-M-4	90	L+V	-	-	-3.6	5.86	-	278	P	Yellow Sphalerite
Bu F203	09-M-4	85	L+V	-	-	-2.9	4.80	-	221	P	Yellow Sphalerite
Bu F204	09-M-12	85	L+V	-	-	-0.3	0.53	-	281	P	Quartz
Bu F205	09-M-12	85	L+V	-	-	-0.4	0.70	-	283	P	Quartz
Bu F206	09-M-12	85	L+V	-	-	-0.4	0.70	-	287	P	Quartz
Bu F207	09-M-12	85	L+V	-	-	-0.4	0.70	-	287	P	Quartz
Bu F208	09-M-12	70	L+V	-	-27.6	-3.3	5.41	-	290	P	Quartz
Bu F209	09-M-12	85	L+V	-	-	-3.6	5.86	-	292	P	Quartz
Bu F210	09-M-12	80	L+V	-	-	-2.7	4.49	-	299	P	Quartz
Bu F211	09-M-12	70	L+V	-	-	-3.4	5.56	-	295	P	Quartz
Bu F212	09-M-12	80	L+V	-	-	-2.2	3.71	-	290	P	Quartz
Bu F213	09-M-12	75	L+V	-	-		1.74	-	292	P	Quartz
Bu F214	09-M-12	80	L+V	-	-	-1.5	2.57	-	288	P	Quartz
Bu F215	09-M-12	85	L+V	-	-	-1.6	2.74	-	311	P	Quartz
Bu F216	09-M-12	90	L+V	-	-25.8	-22.2	23.83	-	257	P	Quartz
Bu F217	09-M-12	90	L+V	-	-	-22.3	23.89	-	246	P	Quartz
Bu F218	09-M-12	90	L+V	-	-25.3	-21.6	23.44	-	243	P	Quartz

Ref #	Sample ID	Fill ¹ (%)	Visible Contents ² at 20°C	T _{m_{CO₂}} (°C)	T _i (°C)	T _{m_{ice}} (°C)	Salinity ³ wt.% NaCl eq. (Bodnar, 1993)	T _{m_{Clath}} (°C)	Th _{L-V(L)} (°C)	Class ⁴	Host mineral
Bu F219	09-M-12	90	L+V	-	-	-21.0	23.05	-	264	P	Quartz
Bu F220	09-M-12	85	L+V	-	-	-22.2	23.83	-	261	P	Quartz
Bu F221	09-M-12	95	L+V	-	-	-21.6	23.44	-	199	P	Quartz
Bu F222	09-M-12	95	L+V	-	-25.3	-21.4	23.31	-	248	P	Quartz
Bu F223	09-M-12	95	L+V	-	-	-22.0	23.70	-	250	P	Quartz
Bu F224	09-M-12	95	L+V	-	-25.5	-21.9	23.63	-	255	P	Quartz
Bu F225	09-M-12	90	L+V	-	-25.8	-22.1	23.76	-	266	P	Quartz
Bu F226	09-M-12	90	L+V	-	-25.7	-21.9	23.63	-	254	P	Quartz
Bu F227	09-M-12	90	L+V	-	-	-22.4	23.95	-	256	P	Quartz
Bu F228	09-M-12	80	L+V	-	-22.7	-3.8	6.16	-	270	P	Quartz
Bu F229	09-M-12	85	L+V	-	-22.9	-4.1	6.59	-	287	P	Quartz
Bu F230	09-M-12	80	L+V	-	-22.9	-3.8	6.16	-	267	P	Quartz
Bu F231	09-M-12	85	L+V	-	-	-2.1	3.55	-	264	P	Quartz
Bu F232	09-M-12	85	L+V	-	-	-2.3	3.87	-	263	P	Quartz
Bu F238	09-M-12	80	L+V	-	-24.1	-4.7	7.45	-	276	P	Quartz
Bu F239	09-M-12	80	L+V	-	-	-4.4	7.02	-	275	P	Quartz
Bu F240	09-M-12	85	L+V	-	-	-4.2	6.74	-	271	P	Quartz
Bu F241	09-M-12	80	L+V	-	-23.3	-4.7	7.45	-	273	P	Quartz
Bu F242	09-M-12	80	L+V	-	-	-6.0	9.21	-	261	P	Quartz
Bu F243	09-M-12	80	L+V	-	-	-7.2	10.73	-	269	P	Quartz
Bu F244	09-M-12	80	L+V	-	-23.4	-5.0	7.86	-	272	P	Quartz
Bu F245	09-M-12	90	L+V	-	-23.4	-4.8	7.59	-	254	P	Quartz
Bu F247	09-M-12	75	L+V	-	-22.6	-4.8	7.59	-	312	P	Quartz

Ref #	Sample ID	Fill ¹ (%)	Visible Contents ² at 20°C	T _{m_{CO₂}} (°C)	T _i (°C)	T _{m_{ice}} (°C)	Salinity ³ wt.% NaCl eq. (Bodnar, 1993)	T _{m_{Clath}} (°C)	Th _{L-V(L)} (°C)	Class ⁴	Host mineral
Bu F248	09-M-12	85	L+V	-	-	-3.4	5.56	-	298	P	Quartz
Bu F249	09-M-12	80	L+V	-	-	-3.3	5.41	-	299	P	Quartz
Bu F250	09-M-12	80	L+V	-	-	-3.3	5.41	-	293	P	Quartz
Bu F251	09-M-12	85	L+V	-	-	-3.3	5.41	-	298	P	Quartz
Bu F252	09-M-12	85	L+V	-	-	-3.3	5.41	-	301	P	Quartz
Bu F253	09-M-12	75	L+V	-	-	-3.3	5.41	-	300	P	Quartz
Bu F254	09-M-12	75	L+V	-	-	-3.3	5.41	-	299	P	Quartz
Bu F255	09-M-12	80	L+V	-	-	-3.3	5.41	-	303	P	Quartz
Bu F261	09-M-1	85	L+V	-	-22.3	-2.8	4.65	-	261	P	Quartz
Bu F262	09-M-1	90	L+V	-	-	-2.8	4.65	-	257	P	Quartz
Bu F263	09-M-1	85	L+V	-	-	-2.5	4.18	-	302	P	Quartz
Bu F264	09-M-1	85	L+V	-	-	-2.6	4.34	-	266	P	Quartz
Bu F265	09-M-1	90	L+V	-	-	-2.4	4.03	-	256	P	Quartz
Bu F266	09-M-1	80	L+V	-	-22.6	-2.9	4.80	-	283	P	Quartz
Bu F267	09-M-1	80	L+V	-	-	-3.0	4.96	-	253	P	Quartz
Bu F268	09-M-1	80	L+V	-	-24.0	-3.2	5.26	-	309	P	Quartz
Bu F269	09-M-1	80	L+V	-	-	-3.5	5.71	-	315	P	Quartz
Bu F270	09-M-1	75	L+V	-	-23.4	-3.2	5.26	-	315	P	Quartz
Bu F271	09-M-1	80	L+V	-	-	-3.5	5.71	-	325	P	Quartz
Bu F272	09-M-1	80	L+V	-	-	-3.3	5.41	-	299	P	Quartz
Bu F273	09-M-1	80	L+V	-	-	-3.2	5.26	-	300	P	Quartz
Bu F274	09-M-1	80	L+V	-	-	-3.2	5.26	-	322	P	Quartz
Bu F275	09-M-1	75	L+V	-	-23.2	-3.2	5.26	-	316	P	Quartz

Ref #	Sample ID	Fill ¹ (%)	Visible Contents ² at 20°C	T _{m_{CO2}} (°C)	T _i (°C)	T _{m_{ice}} (°C)	Salinity ³ wt.% NaCl eq. (Bodnar, 1993)	T _{m_{Clath}} (°C)	Th _{L-V(L)} (°C)	Class ⁴	Host mineral
Bu F288	09-M-3	85	L+V	-	-	-1.8	3.06	-	255	P	Quartz
Bu F289	09-M-3	85	L+V	-	-26.0	-1.9	3.23	-	271	P	Quartz
Bu F290	09-M-3	85	L+V	-	-	-2.0	3.39	-	250	P	Quartz
Bu F291	09-M-3	85	L+V	-	-25.7	-1.9	3.23	-	249	P	Quartz
Bu F292	09-M-3	85	L+V	-	-	-1.9	3.23	-	270	P	Quartz
Bu F293	09-M-3	85	L+V	-	-	-1.9	3.23	-	246	P	Quartz
Bu F294	09-M-3	85	L+V	-	-	-1.9	3.23	-	246	P	Quartz
Bu F295	09-M-3	85	L+V	-	-	-2.0	3.39	-	271	P	Quartz
Bu F296	09-M-3	90	L+V	-	-	-1.9	3.23	-	271	P	Quartz
Bu F297	09-M-3	80	L+V	-	-	-2.0	3.39	-	245	P	Quartz
Bu F298	09-M-3	85	L+V	-	-	-1.9	3.23	-	248	P	Quartz
Bu F299	09-M-3	90	L+V	-	-	-1.9	3.23	-	269	P	Quartz
Bu F300	09-M-3	85	L+V	-	-	-1.9	3.23	-	253	P	Quartz
Bu F301	09-M-3	90	L+V	-	-	-1.8	3.06	-	248	P	Quartz
Bu F302	09-M-3	90	L+V	-	-	-1.9	3.23	-	250	P	Quartz

¹Fill % refers to the volume of liquid relative to other phases

²Visible contents abbreviations: L = H₂O liquid, V = H₂O vapor, CO₂ = CO₂ vapor

³Salinity measure in weight % NaCl equivalent